

ABSTRACT

MISHRA, AMIT. Tailored Mixed Metal Oxides for Chemical Looping Processes. (Under the direction of Dr. Fanxing Li).

There is a demand for efficient and environmentally friendly utilization of fossil fuels. Chemical looping is a potential route to accomplish this. Generally speaking, chemical looping utilizes the lattice oxygen of a metal oxide to oxidize a fuel through a two-step redox process to accomplish *in-situ* air separation. When applied to combustion of fuels, this leads to facile CO₂ capture and is termed chemical looping combustion (CLC). Typically, CLC is effective for gaseous fuels. Extension to solid fuels CLC calls for a metal oxide capable of producing gaseous oxygen, termed chemical looping with oxygen uncoupling (CLOU). Chemical looping can also be used to reform methane to syngas (CO + H₂), termed chemical looping reforming (CLR). Metal oxide design is critical to chemical looping. This study focuses on: 1) evaluation of CaMnO₃, Ca_{0.75}Sr_{0.25}MnO₃, CaMn_{0.75}Fe_{0.25}O₃, and BaMnO₃ through Density Functional Theory (DFT) for CLOU applications and experimental validation 2) extension of the CLOU ineffective material to CLR and coupling it with Ni/Fe dopants, 3) utilization of the CLOU candidates at low temperatures for CLR through Rh surface modification as well as a downstream reforming catalyst, and 4) use of the active lattice oxygen of spinel oxides substrates for coke prevention on NiO in the context of CLC.

DFT and DFT+U calculations showed the trend of energy of vacancy creation vs. metal oxide decreased as follows: BaMnO₃ > CaMnO₃ > Ca_{0.75}Sr_{0.25}MnO₃ > CaMn_{0.75}Fe_{0.25}O₃. Thermogravimetric analysis confirmed that i) BaMnO₃ has the lowest oxygen release and ii) doping CaMnO₃ increased the supply of oxygen. With CLOU capabilities of CaMnO₃, Ca_{0.75}Sr_{0.25}MnO₃, and CaMn_{0.75}Fe_{0.25}O₃ confirmed, they were tested in a fluidized bed reactor for

coal char combustion. Results from this experiment confirmed doping CaMnO_3 with Sr or Fe resulted in increased char conversions above 90% with CO_2 yield exceeding 75%.

With BaMnO_3 showing inadequate oxygen supply for complete combustion, it was tested for partial oxidation in CLR, $\text{BaMn}_x\text{B}_{1-x}\text{O}_3$ ($\text{B} = \text{Fe}$ or Ni) was evaluated as redox catalysts. Results showed BaMnO_3 has a high selectivity to CO (>85%), with Fe and Ni dopants slightly increasing syngas selectivity. These dopants also led to an increase in oxygen capacity. $\text{BaMn}_{0.5}\text{Fe}_{0.5}\text{O}_3$, in particular, showed exceptional syngas selectivity, exceeding 95% in fluidized bed experiments. H_2 TPR showed the BaMnO_3 class of materials possess more strongly bound oxygen leading to the higher selectivity.

Rh surface promotion of $\text{Ca}_x\text{A}_{1-x}\text{Mn}_x\text{B}_{1-x}\text{O}_3$ ($\text{A} = \text{Sr}$, $\text{B} = \text{Fe}$, $x = 0.95$ or 0.75) is expected to result in higher activity (oxygen extraction or methane conversion) and high syngas selectivity. Both were accomplished with Rh promoted CaMnO_3 , providing 20% CH_4 conversion and 71% syngas selectivity. Rh promoted $\text{Ca}_x\text{Sr}_{1-x}\text{MnO}_3$ ($x = 0.95$ or 0.75) led to a split between methane combustion and methane partial oxidation. Rh promoted $\text{CaMn}_x\text{Fe}_{1-x}\text{O}_3$ ($x = 0.95$ or 0.75) led to combustion of methane. However, notable activity was accomplished, with oxygen extraction between 2.2 – 4.0 wt.%. When coupled with a secondary reforming bed (Rh promoted Al_2O_3), syngas selectivity above 88% and methane conversion above 17% were achieved for all materials. Optimized redox times, temperature, and residence time led to a syngas yield above 70% when Rh- $\text{CaMn}_{0.75}\text{Fe}_{0.25}\text{O}_3$ was used.

While NiO has shown high rates of fuel conversion, it has commonly exhibited coke formation which can lead to deactivation. Literature has shown coke formation started to occur upon depletion of active lattice oxygen. NiFe_2O_4 , MgFe_2O_4 , and BaFe_2O_4 were investigated as active substrates for coke prevention of NiO . These substrates inhibited coke formation at all the

investigated NiO loadings. In comparison to MgAl_2O_4 supported NiO, BaFe_2O_4 supported NiO and NiFe_2O_4 supported NiO show similar oxygen release maxima (2.5 wt.%/min vs. 2.3-2.8 wt.% min). The phase transitions of $\text{NiFe}_2\text{O}_4 + 0.5\text{NiO}$ were investigated, showing that coke inhibition is associated with the slow decomposition of Fe_3O_4 .

© Copyright 2019 by Amit Mishra

All Rights Reserved

Tailored Mixed Metal Oxides for Chemical Looping Processes

by
Amit Mishra

A dissertation submitted to the Graduate Faculty of
North Carolina State University
in partial fulfillment of the
requirements for the degree of
Doctor of Philosophy

Chemical Engineering

Raleigh, North Carolina
2019

APPROVED BY:

Dr. Fanxing Li
Committee Chair

Dr. Erik Santiso

Dr. Greg Parsons

Dr. Jacob Eapen

DEDICATION

To my mother and father, Prativa and Banamber Mishra. Without their sacrifices, I would not be able to pursue this PhD.

BIOGRAPHY

Amit Mishra was born in Lake Charles, Louisiana on January 21st, 1991. Upon graduating high school, he attended Louisiana State University where he completed his Bachelors in Chemical Engineering in the Spring of 2013. In his undergraduate experience, he participated in two REUs (research experience for undergraduates) at the Petroleum Engineering Department at the University of Texas at Austin and the Chemical Engineering Department at the Colorado School of Mines. After graduation, he worked as an intern at Sasol in Westlake, Louisiana before attending North Carolina State University for his Ph.D. in Chemical and Biomolecular Engineering in the Fall of 2013. He joined the research groups of Dr. Fanxing Li and Dr. Erik Santiso in January of 2014, where he worked on developing the chemical looping processes for cleaner and more effecient conversion of fossil fuels.

ACKNOWLEDGMENTS

First, I would like to acknowledge my advisors, Dr. Fanxing Li and Dr. Erik Santiso for their guidance through this challenging process. Without their encouragement, patience, and wisdom I would not have been able to present this work. Additionally, their achievements and expectations have been a driving force for me throughout my Ph.D. career. I would also like to extend my thanks to past and present committee members: Dr. Parsons, Dr. Irving, and Dr. Eapen.

Next, I would like to thank all the group members I have worked with. This includes Dr. Arya Shafiefarhood, Dr. Nathan Galinsky, Dr. Feng He, Dr. Luke Neal, Dr. Junshe Zhang, Dr. Yang Liu, Donny Bhuana, Vasudev Haribal, Seif Yusuf, Yunfei Gao, Ryan Dudek, Dr. Jian Dou, Dr. Young-Min Chung, Dan Jackson, Emily Krystowczyk, Dr. Chen, Xin Tian, and Dr. Herskowitz, Dr. Tianyang Li, Dr. Nathan Duff, Dr. Mariah King, Dr. Laura Weiser, Dr. Chengxiang Liu, Dr. Deepti Srivastava, Amulya Pervaje, Christopher Walker, and Jennifer Clark. I would like to give special thanks to Dr. Arya Shafiefarhood for his mentorship during the early years of graduate school. I would also like to thank the undergraduates that I have worked with, Rory Bergen, Megan Boland, Todd Smith, Clay Hamill, and Felipe Bispo. Next, I would like to thank Jessica Yano, who has been a tremendous amount of support for me on a personal level throughout my graduate school career. Last and most importantly, I would like to give thanks to my family who have been a tremendous amount of support throughout my entire life and made me the individual I am today.

TABLE OF CONTENTS

LIST OF TABLES	x
LIST OF FIGURES	xi
Chapter 1: Introduction	1
1.1 Fossil Fuel Utilization and Greenhouse Gas Emissions	1
1.2 CO ₂ Capture Techniques and Their Impacts on Energy Efficiency.....	2
1.3 Valorization of Natural Gas	5
1.4 Chemical Looping as a Potentially Efficient Route to Fossil Fuel Utilization	6
1.4.1 Chemical Looping Combustion (CLC).....	7
1.4.2 Chemical Looping with Oxygen Uncoupling (CLOU)	8
1.4.3 Chemical Looping Reforming (CLR).....	9
1.5 Oxygen Carrier and Redox Catalyst Design	10
1.5.1 Transition Metal Oxide Oxygen Carriers	11
1.5.2 Mixed Metal Oxide Oxygen Carrier	12
1.5.3 Redox Catalyst Development	13
1.5.4 Surface Promotion of Redox Catalysts for Enhanced Selectivity and Activity.....	14
1.5.5 Density Functional Theory (DFT) for Oxygen Carrier Design	14
1.6 Summary	15
1.7 References	18

Chapter 2: Oxygen Vacancy Creation Energy in Mn-Containing Perovskites:

An Effective Indicator for Chemical Looping with Oxygen Uncoupling	31
2.1 Abstract	31
2.2 Introduction	32
2.3 Methods.....	36
2.3.1 Computational Methods.....	36
2.3.2 Experimental Oxygen Carrier Preparation.....	41
2.3.3 <i>In-Situ</i> XRD and Rietveld Refinement	41
2.3.4 Equilibrium Vacancy Characterization.....	42
2.4 Results and Discussion.....	43
2.4.1 Magnetic Spin State Calculations and Crystal Structure Validations.....	43
2.4.2 Effect of Strontium and Iron doping on the $\text{CaMnO}_{3-\delta}$ Vacancy Site	46
2.4.3 Oxygen Vacancy Formation in the Dilute Limit	48
2.4.4 Effect of the Hubbard U on Vacancy Creation Energies and Their Rankings	50
2.4.5 Bader Charge Analysis	52
2.4.6 Equilibrium Vacancy Concentrations and Char Conversion	53
2.4.7 Structural Characterization	56
2.5 Conclusions	60
2.6 References	62

Chapter 3: Perovskite-Structured $AM_nB_{1-x}O_3$ (A = Ca or Ba; B = Fe or Ni) Redox

Catalysts for Partial Oxidation of Methane	68
3.1 Abstract	68
3.2 Introduction	69
3.3 Experimental	71
3.3.1 Redox Catalyst Preparation.....	71
3.3.2 Redox Testing.....	72
3.3.3 Sample Characterization	73
3.4 Results and Discussion.....	74
3.4.1 Fresh Sample Characterizations.....	74
3.4.2 Material Screening.....	77
3.4.3 Surface Composition Effects	80
3.4.4 Effects of Parent Structure Stability	82
3.4.5 Cyclic Redox Studies.....	84
3.4.6 Fluidized Bed Testing.....	88
3.5 Conclusion.....	89
3.6 References	91

Chapter 4: Rh Promoted Perovskites for Exceptional “Low Temperature” Methane

Conversion to Syngas	95
4.1 Abstract	95

4.2	Introduction	95
4.2.1	Methods.....	98
4.2.2	Redox Catalyst Synthesis.....	98
4.2.3	Sample Characterization	99
4.2.4	Redox Testing.....	100
4.3	Results and Discussion.....	101
4.3.1	Effects of dopants and Rh promotion	101
4.3.2	Low temperature methane conversion using Rh promoted redox catalysts	104
4.3.3	Syngas yield enhancement via a sequential bed scheme	106
4.4	Conclusions	112
4.5	References	114

Chapter 5: Spinel Oxides as a Coke Resistant Support for NiO Based Oxygen Carriers

in Chemical Looping Combustion.....	119	
5.1	Abstract	119
5.2	Introduction	119
5.3	Experimental	122
5.3.1	Oxygen Carrier Synthesis	122
5.3.2	Phase Characterization.....	123
5.3.3	In-Situ Phase Characterization.....	123
5.3.4	Redox and Reaction Testing	124

5.4	Results and discussion.....	125
5.4.1	Spinel Oxides Selection and Redox Behavior	125
5.4.2	Active Spinel Oxides as Supports for Coke Inhibition.....	127
5.4.3	Reduction Pathway of NiFe ₂ O ₄ Supported NiO	131
5.4.4	Redox Stabilities of the Oxygen Carriers	137
5.4.5	Long Term Redox Stability of MgFe ₂ O ₄ and BaFe ₂ O ₄ supported Oxygen Carriers	139
5.5	Conclusion.....	140
5.6	References	142
Chapter 6: Conclusions and Future Work		147
6.1	Conclusions	147
6.2	Future Work	150
6.3	References	153
APPENDICES		154
Appendix A. Supplementary Information for Chapter 2.....		155
Appendix B. Supplementary Information for Chapter 4.....		169
Appendix C. Supplementary Information for Chapter 5.....		174

LIST OF TABLES

Table 1.1: Thermal efficiencies of power generation, with and without CO ₂ capture, with efficiency losses associated with each carbon capture technique listed ^{19,21,23,26,27}	5
Table 3.1: Abbreviation of Redox Catalysts	72
Table 3.2: Phase compositions identified in as-prepared redox catalysts	76
Table 3.3: Change in selectivity, coke, and CO yield for nickel doped redox catalysts from cycle 5 to 25	84
Table 3.4: Change in selectivity, coke, and CO yield for iron doped redox catalysts from cycle 5 to 25	86
Table 5.1: Peak Phenomena during H ₂ TPR in-Situ XRD (3% H ₂) of NiFe ₂ O ₄ + 0.5NiO	133
Table 5.2: Phase Transitions during H ₂ TPR in-Situ XRD (3% H ₂) of NiFe ₂ O ₄ + 0.5NiO....	134

LIST OF FIGURES

Figure 1.1:	Past and project worldwide energy consumption. Data provided by the U.S. Energy Information Administration ⁴	1
Figure 1.2	CO ₂ emissions in year 2015 and year 2030. Data provided by the U.S. Energy Information Administration ⁴	2
Figure 1.3:	Simplified Schematics for different CO ₂ capture techniques.....	3
Figure 1.4:	Simplified schematic of the chemical looping process. Besides air, H ₂ O, and CO ₂ can also be used as the oxidant.....	7
Figure 2.1:	(a) A simplified schematic of CLOU. MeO _y is more oxidized than MeO _x (y>x); (b) Equilibrium P _{O2} between 800-1000°C for various Cu, Mn, Co, Fe, and Ni oxides. The desired P _{O2} range is shaded in green.....	34
Figure 2.2:	Example of a cation shell in CaMn _{0.75} Fe _{0.25} O ₃ . Cations bonding to the oxygen (red) represent the cation shell. Gold is iron, purple is manganese, and blue is calcium.	39
Figure 2.3:	Energies of different magnetic spin states with respect to the minimum energy using DFT and DFT +U for a) BaMnO ₃ and b) CaMnO ₃ (40 atom supercell, AF: A-type antiferromagnetic, FM: Ferromagnetic, GAF: G-type antiferromagnetic).	45
Figure 2.4:	Unit cell distortion with respect to CaMnO ₃ found experimentally, through DFT, and DFT+U (40 atom supercell).....	45
Figure 2.5:	Energy of vacancy creation with respect to four sites with lower energy for a) CaMn _{0.75} Fe _{0.25} O _{3-δ} and b) Ca _{0.75} Sr _{0.25} MnO _{3-δ} . Graphical representation of the	

	oxygen site (red) and its shell is shown (gold is iron, blue is calcium, purple is manganese and green is strontium).	48
Figure 2.6:	Energy of vacancy creation for versus $1/\delta$ for a) $\text{BaMnO}_{3-\delta}$, b) $\text{CaMnO}_{3-\delta}$, c) $\text{CaMn}_{0.75}\text{Fe}_{0.25}\text{O}_{3-\delta}$, and d) $\text{Ca}_{0.75}\text{Sr}_{0.25}\text{MnO}_{3-\delta}$	50
Figure 2.7:	a) Energy of Vacancy Formation using the largest supercells and b) the energies with respect to $\text{CaMn}_{0.75}\text{Fe}_{0.25}\text{MnO}_{3-\delta}$ DFT and DFT+U.	52
Figure 2.8:	Change in Bader Charge, using DFT, after vacancy formation for different cation shells consisting of a) 4 cation and b) 5 cation shells. (40 atom supercell).	53
Figure 2.9:	δ' for $\text{CaMnO}_{3-\delta}$, $\text{Ca}_{0.75}\text{Sr}_{0.25}\text{MnO}_{3-\delta}$, and $\text{CaMn}_{0.75}\text{Fe}_{0.25}\text{O}_{3-\delta}$ using a) inert, b) $P_{\text{O}_2} = 0.01$ atm, and c) $P_{\text{O}_2} = 0.025$ atm in temperature range of 600-750°C.	55
Figure 2.10:	Results from char conversion experiments at 850°C from the 5 th cycle.	56
Figure 2.11:	Results of in-Situ XRD for a) CaMnO_3 , b) $\text{CaMn}_{0.75}\text{Fe}_{0.25}\text{O}_3$, and c) $\text{Ca}_{0.75}\text{Sr}_{0.25}\text{MnO}_3$. 2θ ranges of 32.5-34.5°, 47-49°, and 58.5-61.5° are shown. 0.025 atm P_{O_2} , 0.01 atm P_{O_2} , and Inert environments are applied for 56 minutes each at 750°C.	58
Figure 2.12:	Volume expansion normalized by oxygen non-stoichiometry found through both DFT and a combination of TGA and in-Situ XRD. A 40-atom unit ($\delta = 0.125$) was used for DFT calculations and experimental data at 750°C was used.	59
Figure 3.1:	XRD Spectra of (a) i. CMF and ii. CMN iii CM; (b). i. BMF25 ii. BMF50 and iii. BM; (c) i. BMN25 and ii. BMN50.	76

Figure 3.2: Product distributions from typical redox cycles of a) $\text{CaMn}_{0.8}\text{Ni}_{0.2}\text{O}_3$ and b) $\text{BaMn}_{0.75}\text{Ni}_{0.25}\text{O}_3$.	77
Figure 3.3: a) CO selectivity and b) yield for the redox catalysts (Cycle 10 of short term redox study, 10% CH_4 and 10% O_2 at 900°C).	80
Figure 3.4: Coke formation for the redox catalysts (Cycle 10 of short term redox study, 10% CH_4 and 10% O_2 at 900°C).	80
Figure 3.5: Surface Deviation of Redox Catalysts.	82
Figure 3.6: DTG of H_2 (20%) TPR (10°/min) of redox catalysts $\text{BaMn}_{0.75}\text{Ni}_{0.25}\text{O}_3$, BaMnO_3 , and $\text{CaMn}_{0.8}\text{Ni}_{0.2}\text{O}_3$.	83
Figure 3.7: DTG of TPD (5°/min) of redox catalysts $\text{BaMn}_{0.75}\text{Ni}_{0.25}\text{O}_3$, BaMnO_3 , and $\text{CaMn}_{0.8}\text{Ni}_{0.2}\text{O}_3$.	84
Figure 3.8: a) Gaseous product profile during the methane conversion stage at the 5 th cycle and b) 25 th cycle (10% CH_4 and 10% O_2 at 900°C) for $\text{BaMn}_{0.5}\text{Fe}_{0.5}\text{O}_3$.	87
Figure 3.9: a) XRD pattern of BMF50 i) 10 th cycle reduced and ii) oxidized phases after 10 th reduction.	87
Figure 3.10: CO Selectivity, CO yield, and coke during fixed bed experiments (10% CH_4 and 10% O_2 at 900°C).	87
Figure 3.11: a) Cycle 2 of $\text{BaMn}_{0.75}\text{Fe}_{0.25}\text{O}_3$, b) Cycle 5 of $\text{BaMn}_{0.75}\text{Fe}_{0.25}\text{O}_3$, c) Cycle 2 of $\text{BaMn}_{0.5}\text{Fe}_{0.5}\text{O}_3$, d) Cycle 5 of $\text{BaMn}_{0.5}\text{Fe}_{0.5}\text{O}_3$ (10% CH_4 and 10% O_2 at 900°C) during fixed bed experiments.	88
Figure 3.12: CO Selectivity and Methane conversion during fluidized bed experiments.	89

Figure 4.1:	DTG of a) unpromoted redox catalysts and b) promoted redox catalysts during CH ₄ – TPR. 10% CH ₄ (10 sccm CH ₄ , 90 sccm Ar) was used as the reducing gas. The sample was heated at 20oC/min. GHSV = 12000 hr ⁻¹	103
Figure 4.2:	Near surface enrichment of metal cations in Rh promoted Redox Catalysts. Results for Rh-CaMnO ₃ are from Shafiefarhood et. al. ²³ after oxidation of the fifth redox cycle.....	104
Figure 4.3:	a) CH ₄ conversion and O ²⁻ extraction and b) CO + H ₂ selectivity at 600°C with 15 minutes of reduction in 5% CH ₄ and 10 minutes of oxidation in 5.8% O ₂ . GHSV = 12000 hr ⁻¹	105
Figure 4.4:	a) DTG of Rh promoted redox catalysts during TPD. Ramping rate is 2°C/min and 180 sccm or argon was used. GHSV = 12000 hr ⁻¹ . b) TPD peak temperature vs. syngas selectivity during redox cycling.....	106
Figure 4.5:	CH ₄ conversion and syngas selectivity in the sequential bed chemical looping reforming scheme for promoted redox catalysts, shown as difference in conversion and selectivity over single bed. Reduction is 15 minutes long with 5% CH ₄ . Oxidation is 10 minutes long with 5.8% O ₂ at 600°C. GHSV = 12000 hr ⁻¹	108
Figure 4.6:	a) Instantaneous CH ₄ conversion and b) Instantaneous CO Selectivity of Rh - CaMnO ₃ , Rh - CaMn _{0.95} Fe _{0.05} O ₃ , Rh – Ca _{0.95} Sr _{0.05} MnO ₃ during dual bed experiments. Reduction is 15 minutes with 5% CH ₄ . Oxidation is 10 minutes long with 5.8% O ₂ at 600°C. GHSV = 12000 hr ⁻¹	109
Figure 4.7:	Syngas yields vs. oxygen extraction rate for Rh-CaMn _{0.95} Fe _{0.05} O ₃ and Rh-CaMn _{0.75} Fe _{0.25} O ₃ . Reduction is 15 minutes long with 5% CH ₄ . Oxidation is 10	

	minutes long with 5.8% O ₂ at 600°C. GHSV = 12000 hr ⁻¹ . Minutes 1.5-15 of reduction are shown.	110
Figure 4.8:	a) Effect of temperature and b) GHSV on syngas selectivity, CH ₄ conversion, and yield for Rh promoted CaMn _{0.75} Fe _{0.25} O ₃ , Ca _{0.75} Sr _{0.25} MnO ₃ , and CaMnO ₃ . Rh-CaMn _{0.75} Fe _{0.25} O ₃ and Rh-CaMn _{0.95} Fe _{0.05} O ₃ are oxidized for 5 minutes and reduced for 3 minutes. Rh-CaMnO ₃ is oxidized for 3 minutes and reduced for 5 minutes.	111
Figure 4.9:	CH ₄ conversion and syngas selectivity across all 50 cycles for Rh-CaMn _{0.75} Fe _{0.25} O ₃ . GHSV is 6000 hr ⁻¹ , temperature is 600°C, 5 minutes of oxidation and 3 minutes of reduction are used.	112
Figure 5.1:	a) Cumulative oxygen donation (capacity) from MgAl ₂ O ₄ , BaFe ₂ O ₄ , MgFe ₂ O ₄ , and NiFe ₂ O ₄ at 3, 15, and 40 mins and b) oxygen release rate of BaFe ₂ O ₄ , MgFe ₂ O ₄ , and NiFe ₂ O ₄ under during reduction in 10% CH ₄ at 900°C over 45 minutes.	127
Figure 5.2:	a) Oxygen donation (capacity) during reduction and oxidation and b) Oxygen release rate during reduction of MgAl ₂ O ₄ + 0.25NiO, BaFe ₂ O ₄ + 0.25NiO, MgFe ₂ O ₄ + 0.25NiO, and NiFe ₂ O ₄ + 0.25NiO. Reduction is under 10% CH ₄ and oxidation is under 10% O ₂ . All results are at 900°C.	129
Figure 5.3:	a) Weight during reduction and oxidation and b) DTG during reduction of BaFe ₂ O ₄ + 0.5NiO, MgFe ₂ O ₄ + 0.5NiO, and NiFe ₂ O ₄ + 0.5NiO. Reduction is under 10% CH ₄ and oxidation is under 10% O ₂ . All results are at 900°C.	131
Figure 5.4:	a) XRD of NiFe ₂ O ₄ , NiFe ₂ O ₄ + 0.25NiO, NiFe ₂ O ₄ + 0.5NiO, b) Detailed Scan of NiFe ₂ O ₄ + 0.5NiO in the 43-44°	132

Figure 5.5:	In-Situ XRD of NiFe ₂ O ₄ + 0.5NiO from 100-900°C under 3% H ₂ (total flow rate: 30 mL/min). Ramping rate to 500°C was at 10°C/min and ramping from 500°C to 900°C was at 2°C/min	135
Figure 5.6:	TPR under 3% H ₂ at 2°C/min.....	136
Figure 5.7:	a) oxygen donation (capacity) during reduction and b) oxygen gain during oxidation with 0.25NiO and c) oxygen donation (capacity) during reduction and d) oxygen gain during oxidation with 0.5NiO. Reduction is under 10% CH ₄ and oxidation is under 10% O ₂ . All results are at 900°C.....	139
Figure 5.8:	a) Oxygen donation (capacity) of MgFe ₂ O ₄ + 0.5NiO during cycles 2, 10, and 30, b) Weight of the oxygen carrier during a 30 cycle redox.....	140
Figure 6.1:	Schematic illustration of the vacancy formation energy with respect to the fermi energy. The solid blue lines represent the most favorable charge state and dotted blue lines correspond to formation energy define by equation 6.1. ...	151

Chapter 1: Introduction

1.1 Fossil Fuel Utilization and Greenhouse Gas Emissions

Fossil fuels are of paramount importance to power the society in the 21st century. In the United States alone, 900 million tons of coal and 28.3 trillion cubic feet of natural gas are consumed in 2015 according to the U.S. National Academy of Sciences¹. The most common use of fossil fuels is for energy production^{2,3}. Energy consumption has been rising steadily for the past two decades and is projected to increase to over 700 quadrillion BTUs by 2030⁴, as shown in Figure 1.1.

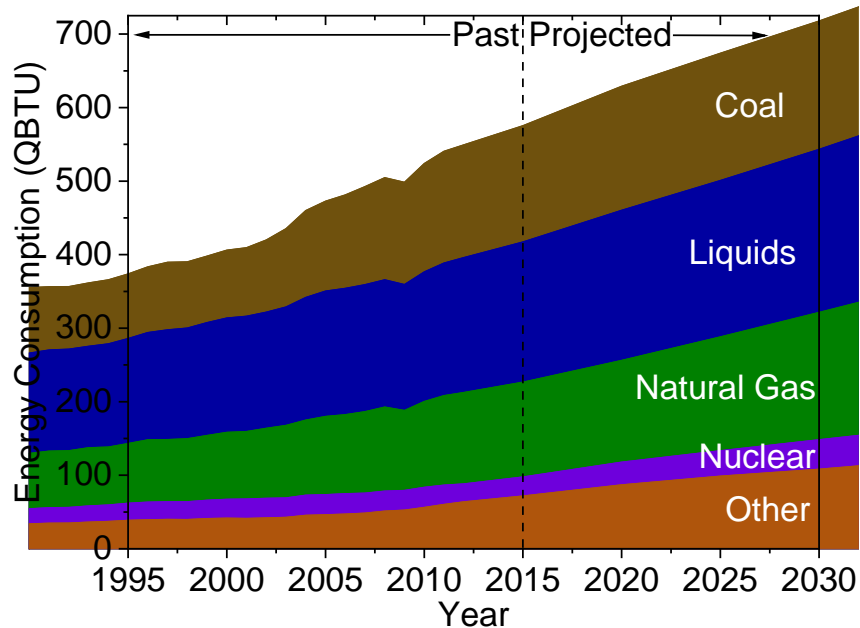


Figure 1.1: Past and project worldwide energy consumption. Data provided by the U.S. Energy Information Administration⁴.

Anthropogenic carbon emissions have been an unintended and unavoidable consequence of fossil fuel utilization. With rising energy consumptions, there has also been a rise in CO₂ emissions. The U.S. Energy Information Administration predicts the CO₂ emissions resulting from energy consumption in year 2030 to be over 16% higher than that in 2015⁴ (shown in Figure 1.2). Additionally, in 2015 these CO₂ emissions accounted for 94% of all anthropogenic CO₂ emissions

and 76% of all anthropogenic greenhouse gas emissions⁵. Even more importantly, the Intergovernmental Panel on Climate Change (IPCC) has estimated that human activities will have caused global warming of 1.5°C above pre-industrial levels by 2030⁶. As a result, there is a demand to engineer a sustainable solution to these issues. The national research council defined a sustainable processes as those which are “economically competitive and do not cause harm to the environment and health”³. As such, a potential solution to this problem will meet energy demands while efficiently capturing CO₂.

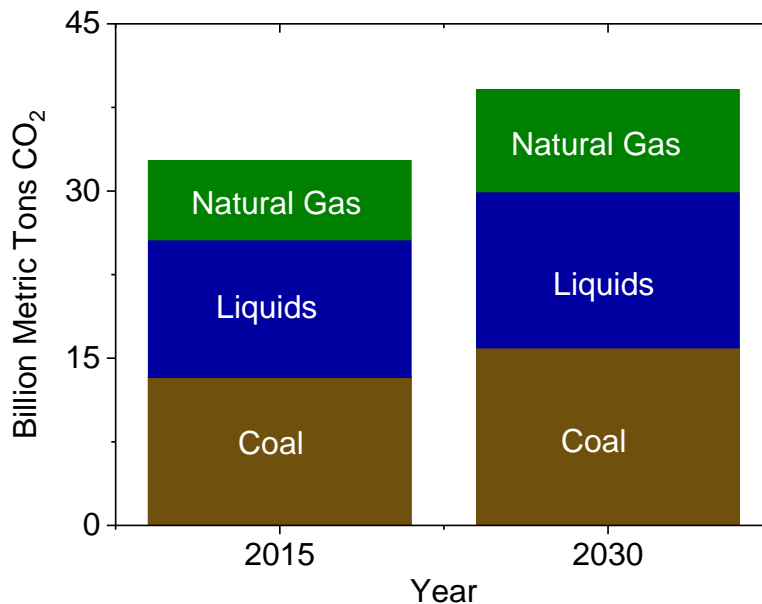


Figure 1.2 CO₂ emissions in year 2015 and year 2030. Data provided by the U.S. Energy Information Administration⁴.

1.2 CO₂ Capture Techniques and Their Impacts on Energy Efficiency

Currently, CO₂ capture can be achieved in three ways: post-combustion, pre-combustion, and oxy-combustion⁷⁻²⁷. In post combustion CO₂ capture, as the name suggests, CO₂ is separated downstream of the fossil fuel combustion. In pre-combustion, a fossil fuel is converted to H₂ and CO₂ where CO₂ is captured prior to H₂ being burned for power. In oxy fuel combustion, cryogenic

O₂ is combusted with a fossil fuel to produce a stream of H₂O and CO₂, where CO₂ can easily be separated. These processes are summarized in Figure 1.3.

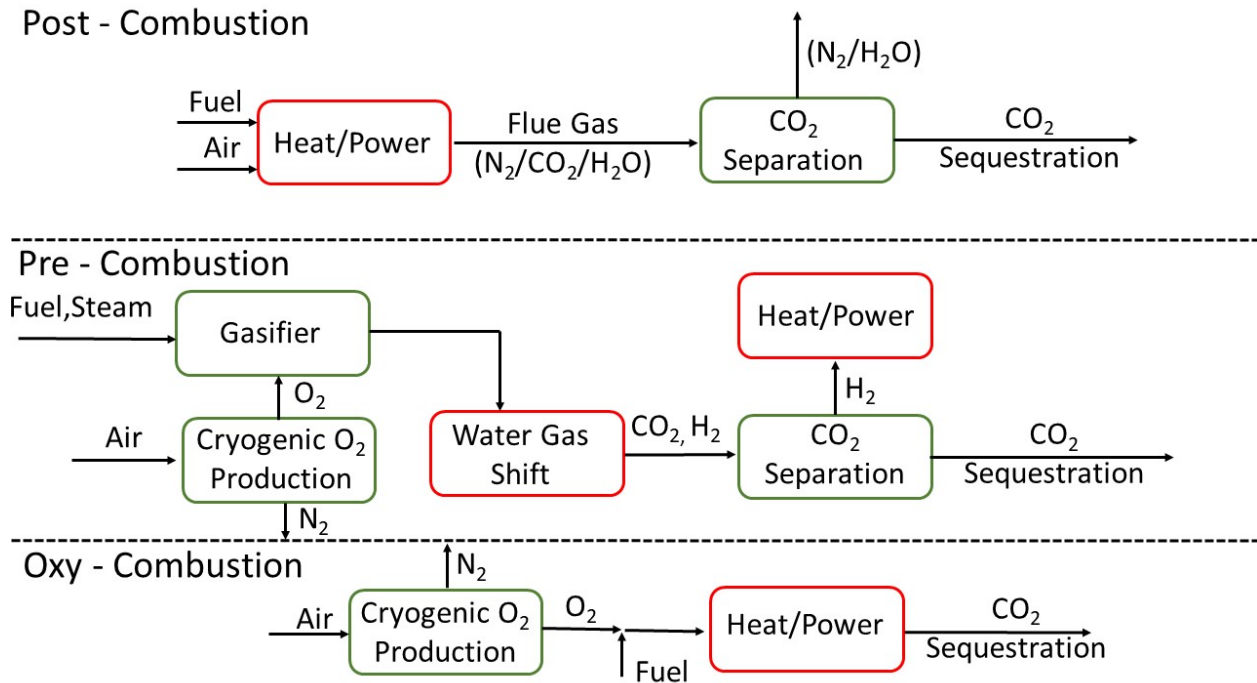


Figure 1.3: Simplified Schematics for different CO₂ capture techniques.

Of these processes, post combustion is the most readily implementable in current power plants, as most power plants use air for fuel combustion. This results in a variety of species in the flue gas including N₂, NO_x, CO₂, and H₂O. CO₂ capture from this flue gas is commonly accomplished through amine based scrubbing systems²⁰. However, there are challenges with this technology. Amine based scrubbing utilizes the reaction of CO₂ with a basic solvent such as monoethanolamine to form water soluble compounds and regeneration of the solvent requires significant amount of steam^{7-11,20}. As a result, there are significant losses in energy efficiency, consuming up to 30% parasitic energy. In pre-combustion technologies, cryogenic air separation and steam is used to gasify a fuel into CO, H₂, and CO₂ with water gas shift to follow, producing

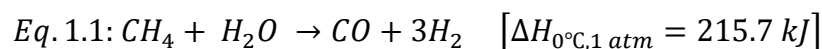
CO₂ and H₂. From here CO₂ can be separated and H₂ can be used for energy generation.^{7,13,14,16} However, pre-combustion CO₂ capture is not easily implementable in current power plants and it suffers from efficiency losses due to cryogenic air separation and CO₂ separation units. With oxy fuel combustion, cryogenic air separation is used produce pure O₂ which is subsequently reacted with fuel to produce power^{7,10,12,14,21,22}. The flue gas is rich in CO₂ and H₂O, where CO₂ can be easily removed because H₂O is easily condensable. However, this process requires energy intensive cryogenic air separation and is restricted in the amount of fuel that can be used, due to the high heats of reaction with pure O₂⁷. The efficiency losses that occur as a result of each CO₂ capture technique is listed in Table 1.1, for gas fired and coal fired power plants. From this table, it is obvious that current carbon capture techniques will have a major impact on the ability to provide economically sustainable energy generation. As will be discussed in later sections, chemical looping combustion offers a route towards power generation with facile CO₂ capture due to its ability to provide pure oxygen without cryogenic separation.

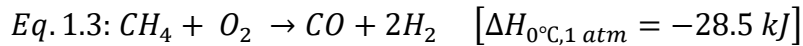
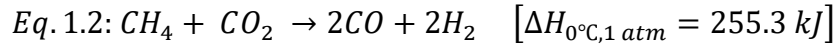
Table 1.1: Thermal efficiencies of power generation, with and without CO₂ capture, with efficiency losses associated with each carbon capture technique listed^{19,21,23,26,27}.

<i>CO₂ Capture Technology</i>	<i>Thermal Efficiency (% LHV)</i>	<i>Efficiency Loss (relative basis, %)</i>
Gas Fired		
<i>No Capture</i>	55.6-60	
<i>Post-Combustion</i>	47.4-50	10-15
<i>Pre-Combustion</i>	41.5-46	17-30
<i>Oxy Fuel Combustion</i>	44.7-48	14-25
Coal Fired		
<i>No Capture</i>	41-45	
<i>Post-Combustion</i>	30-34.8	15-33
<i>Pre-Combustion</i>	31.5-34	17-30
<i>Oxy Fuel Combustion</i>	35-35.4	14-22

1.3 Valorization of Natural Gas

While natural gas is predominantly used for energy production, there has been significant work to valorize natural gas. The largest constituent of natural gas is methane⁴ and methane conversion to syngas (CO + H₂) is a promising route towards valorization because it is the feedstock for the Fischer Tropsch process²⁸⁻³⁰. In this process, syngas is converted to liquid fuels (such as diesel) and chemicals (such as alcohols)²⁸⁻³⁰. Commonly investigated reforming techniques for methane conversion to syngas are steam reforming, dry reforming, and methane partial oxidation³¹⁻³³. These reactions are listed as equations 1.1, 1.2, and 1.3, respectively.





These processes require a heterogeneous catalyst for successful conversion of methane, due to the high binding energy of the C-H bond³⁴⁻³⁸. Presently steam reforming is the most common commercial method for syngas production in industry. However, there are drawbacks with steam reforming. It suffers from endothermicity and requires high amounts of steam, both of which result in energy penalties. While dry reforming does not require steam, coke formation and catalyst deactivation has been a commonly witnessed issue³⁹⁻⁴¹. Methane partial oxidation is promising because it will result in an exothermic reaction and provide a hydrogen to carbon monoxide ratio that is optimal for the Fischer Tropsch process. However, methane partial oxidation requires pure oxygen and cryogenic separation would result in noticeable energy penalties. In the later sections, chemical looping reforming is discussed as a promising alternative due to its ability to provide pure oxygen without the need for cryogenic separation.

1.4 Chemical Looping as a Potentially Efficient Route to Fossil Fuel Utilization

Chemical looping offers a potentially efficient route to fossil fuel utilization. In this process, a metal oxide undergoes a two-step redox process to provide pure oxygen for fossil fuel conversion⁴²⁻⁴⁵. The first step of this redox process is oxidation of the fuel through the lattice oxygen of a metal oxide in what is referred to as the reducer reactor. In the second step, the metal oxide is oxidized back to its original state through a gaseous oxidant in what is referred to as the oxidizer reactor. The chemical looping process is shown in Figure 1.4, with air as the gaseous oxidant. The metal oxide is typically referred to as an oxygen carrier in this process. The reactors in this system are interconnected with the oxygen carrier circulating between the two beds. There are two main advantages to this process: i) chemical looping can provide in-situ air separation and

ii) if designed properly, chemical looping can reduce the exergy loss and increase process efficiency⁴³. Chemical looping has most commonly been applied to combustion and uses air as the oxidant. However, this can be extended to any process where oxidation of a fossil fuel is required. In all chemical looping applications, a critical factor in the chemical looping scheme is oxygen carrier performance.

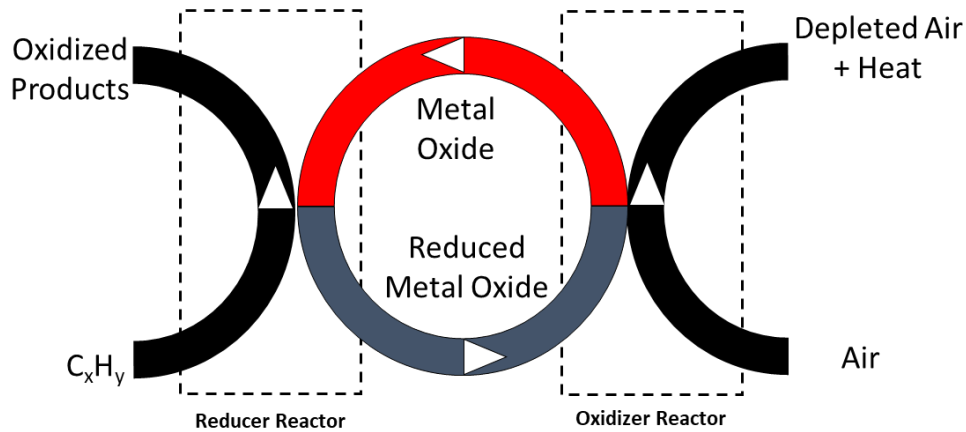
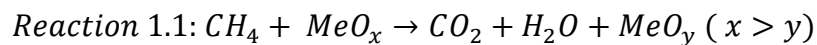


Figure 1.4: Simplified schematic of the chemical looping process. Besides air, H₂O, and CO₂ can also be used as the oxidant.

1.4.1 Chemical Looping Combustion (CLC)

In chemical looping combustion, the reducer reactor produces CO₂ and H₂O and the oxidizer reactor produces depleted air and heat for energy generation. The net of these reactions is combustion of fuel with air. However, the flue gas containing CO₂ only requires condensation of H₂O. Using CH₄ as an example of a solid fuel, the reactions in the reducer reactor and the oxidizer reactor are shown below (Reaction 1.1 and 1.2). MeO_x is used to represent an oxidized oxygen carrier and MeO_y is used to represent a reduced oxygen carrier.

Reducer Reactor:



Oxidizer Reactor:



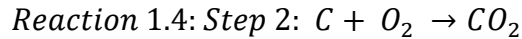
In essence, oxy-combustion is accomplished without the requirement of an air separation unit. In CLC, the reactor design requires proper circulation of the oxygen carrier between reducer and oxidizer reactor as well as excellent contact between the oxygen carrier and the fuel. This is typically accomplished using circulating fluidized beds^{46,47} and has been demonstrated in various pilot plants with sizes up to 1 MW_{th}⁴⁸⁻⁵⁰. The oxidizer reactor is more exothermic than the reducer reactor and operates at higher temperature⁴³. With this, the oxygen carrier can act as a heat transfer medium when circulating from the oxidizer reactor to the reducer reactor⁴³. As a result, a higher thermal efficiency can theoretically be achieved with CLC. For these reasons, chemical looping combustion provides a promising alternative to energy generation. CLC has traditionally been applied to gaseous fuels, such as natural gas or coal derived syngas⁵¹⁻⁵⁵. This can be applied to solid fuels as well, but there are kinetic limitations resulting from solid-solid reaction between the oxygen carrier and a solid fuel, such as coal.

1.4.2 Chemical Looping with Oxygen Uncoupling (CLOU)

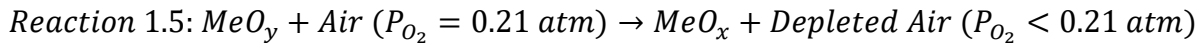
To adapt chemical looping for the conversion of solid fuels, chemical looping with oxygen uncoupling has been developed. While the process basics are the same as chemical looping, the oxygen carrier is designed to release gaseous oxygen in the reducer reactor⁵⁶⁻⁵⁸ and subsequently improve the kinetics of solid fuel conversion. The driving force for the oxygen release in the reducer reactor is the oxygen partial pressure. With a low partial pressure of oxygen, higher amounts of gaseous oxygen will “uncouple” from the oxygen carrier and react with a solid fuel. In this process, the ability of an oxygen carrier to uncouple oxygen is paramount to successful conversion of solid fuels. The reactions occurring in the reducer reaction and oxidizer reactor are

shown below (Reaction 1.3, 1.4, and 1.5) , where carbon is serving as an example of a solid fuel. MeO_x is used to represent an oxidized oxygen carrier and MeO_y is used to represent a reduced oxygen carrier.

Reducer Reactor



Oxidizer Reactor:



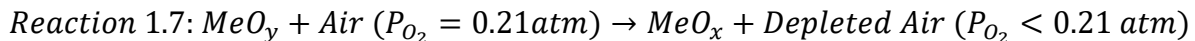
1.4.3 Chemical Looping Reforming (CLR)

Chemical looping reforming is another application of chemical looping. However, chemical looping reforming requires an oxygen carrier capable of selectively oxidizing methane to hydrogen and carbon monoxide^{44,59-61}. As such, the oxygen carrier is commonly referred to as a redox catalyst. In comparison to the aforementioned methane reforming techniques, chemical looping reforming accomplishes methane partial oxidation without an air separation unit. The ability of a redox catalyst to selectively oxidize a fuel is key to the success of chemical looping reforming. The reactions occurring in the reducer reactor and the oxidizer reactor are shown below (Reaction 1.6 and 1.7).

Reducer Reactor:



Oxidizer Reactor:



1.5 Oxygen Carrier and Redox Catalyst Design

As previously mentioned, the oxygen carrier plays a key role in success of chemical looping processes. Ideal oxygen carriers possess high oxygen capacity (i.e. amount of oxygen that is provided for fuel conversion), reaction kinetics, long term recyclability, mechanical stability, low environmental/health impacts, low cost, and selectivity to the desired products⁴²⁻⁴⁵. Transition metal oxides have most commonly been studied as oxygen carriers, due to their high oxygen capacities. This has included iron, nickel, cobalt, copper, and manganese oxides. Mixed metal oxides have also been explored because of the synergetic effect that can occur as a result of using more than one metal cation⁶²⁻⁶⁴. Mixed metal oxide design is particularly promising because the oxygen carrier design space is much larger. However, the use of a single “active” phase has encountered challenges such as low reaction kinetics, deactivation, and poor control over selectivity^{62,65,66}.

In order to counteract these shortcomings, a secondary phase is often employed as a support. This support phase is usually another metal oxide that does not contribute oxygen for fuel conversion, but provides stability or enhanced reaction rates. Most commonly this has been Al_2O_3 or TiO_2 , which are completely inert and provide stability⁶⁷⁻⁶⁹. However, this can also be mixed ionic electronic conductive substrates such as yttria-stabilized zirconia or lanthanum strontium ferrite^{70,71}. Surface promotion is another technique that can be employed to overcome challenges in oxygen carrier design, namely those of selectivity and activity. However, this is relatively unexplored and has only, to our knowledge, been studied for Rh promotion on select metal oxides^{72,73}. To date, hundreds of oxygen carriers/support combinations have been tested for chemical looping processes^{44,62,65,66,74-76}. In the next few sections oxygen carriers for CLC and CLOU will be discussed before moving onto redox catalysts for CLR.

1.5.1 Transition Metal Oxide Oxygen Carriers

Iron oxide has been an attractive oxygen carrier because of its high oxygen capacity, low cost, and low environmental impact. However, it suffers from low reactivity with carbonaceous fuels and low oxygen transport. Iron can accommodate different oxidation states, and Fe_2O_3 can be reduced to Fe_3O_4 , FeO , and Fe . Application of iron oxide for CLC in a circulating fluidized bed is typically limited to the transition from Fe_2O_3 to Fe_3O_4 . This is because the phase transitions of $\text{Fe}_3\text{O}_4/\text{FeO}$ and FeO/Fe have a low equilibrium partial pressure of oxygen, which results in CO and H_2 products⁷⁷.

A variety of inert supports have been used to enhance the mechanical stability of iron oxide. This has included Al_2O_3 , MgAl_2O_4 , SiO_2 , TiO_2 , and Zr based supports^{78–81}. In the case of Al_2O_3 and TiO_2 , this has led to the formation of FeAl_2O_4 and FeTiO_3 ^{82,83}. Typically iron oxide has shown deactivation due to sintering, and these supports have led to increased stability^{84–86}. In addition to inert supports, mixed ionic electronic conductors have been used as supports to improve activity through improved oxygen transport properties. This has included lanthanum strontium ferrite, barium cerium ferrite, and calcium titanium ferrite with activities increased up to 70 times^{70,87}.

Manganese oxide has, also, been explored due to its high oxygen capacity, low cost, and low environmental impact. Similar to iron oxide, it accommodates various oxidation states giving oxide phases of Mn_2O_3 , Mn_3O_4 , and MnO as well as metallic Mn . Manganese oxide also offers “oxygen uncoupling” capabilities for CLOU applications. However, Mn_2O_3 is an inaccessible phase in typical chemical looping operations because the partial pressure of oxygen in air is not sufficient for generation of this phase⁸⁸. As such, the transition of Mn_2O_3 to MnO is typically considered for CLC applications. Inert supports have been used for manganese oxide as well and

include TiO_2 , Al_2O_3 , SiO_2 , and MgAl_2O_4 ^{66,89,90}. However, mixed metal oxides phases are often formed, deeming them ineffective supports.

Copper oxide, while not offering multiple oxidation states, provides a high oxygen capacity and high activity at low costs and environmental impacts. Copper oxide also has oxygen uncoupling abilities for CLOU applications^{57,91,92}. However, agglomeration issues arise with this oxygen carrier, leading to defluidization in chemical looping operations⁶⁵. To alleviate these issues, impregnation of CuO on Al_2O_3 and MgAl_2O_4 has been studied^{91,92}. While this had led to pilot scale CLC operations, low loadings of CuO (15 wt.%) were required.

Nickel based oxygen carriers have been extensively studied because they possess high reactivity and excellent fuel conversion⁹³. However, there are concerns due to carbon formation, toxicity, high cost, and agglomeration. To address carbon formation and agglomeration, inert supports have been used. Most commonly, Al_2O_3 has been used^{69,94,95}. However, this resulted in the formation of NiAl_2O_4 which is inactive⁹⁶⁻⁹⁸. Other supports such as NiAl_2O_4 , MgAl_2O_4 , and YSZ have also been tested. However, the combination of coke resistance, desirable mechanical properties, and high activity were not achieved.

1.5.2 Mixed Metal Oxide Oxygen Carrier

With single metal oxides having limitations in chemical looping applications, mixed metal oxides have emerged as promising alternatives as oxygen carriers. This provides a limitless number of possible oxides, and possible applications. Iron has commonly been combined with other transition metals as it can improve the cost, toxicity, and oxygen capacity. This has included Cu-Fe and Mn-Fe combinations, where oxygen uncoupling properties are observed⁹⁹⁻¹⁰¹. Ni-Fe has also been investigated to minimize cost and toxicity issues¹⁰².

Perovskite oxides have emerged as promising mixed metal oxides, due to their unique properties. The general formula of perovskite oxides are $ABO_{3-\delta}$, where A and B are different metal cations and δ is oxygen non-stoichiometry, expressed as oxygen vacancies. Perovskites are highly tunable because they can accept a large number of different cations as well as combination of cations in either the A site of the B site. A semi-empirical factor called the “Goldschmidt tolerance factor” can be used to understand the stability of the oxides with different cations¹⁰³. This is expressed below, in equation 1.2, where an ideal cubic perovskite gives a tolerance factor of 1. r_a is the ionic radius of A site cation, r_b is the ionic radius of B site cation, and r_o is the ionic radius of oxygen.

$$Eq\ 1.2: t = \frac{r_a + r_o}{\sqrt{2}(r_b + r_o)}$$

Perovskites can also donate oxygen, without phase decomposition¹⁰⁴. For these reasons, perovskite oxides are very attractive for all chemical looping applications and recently there have been studies on them. Most notably this has included $La_{1-x}Sr_xFe_{1-y}Co_yO_{3-\delta}$, $La_{1-x}Sr_xFeO_3$, and $CaMnO_3$ ^{105–108}

1.5.3 Redox Catalyst Development

With redox catalysts requiring high product selectivity and high activity, redox catalyst success has been limited. Supported Ni based redox catalysts have shown the most success for CLR^{109–111}, with other Fe, Mn, and Cu based redox catalysts suffering from poor selectivity¹⁰⁹. These Ni based catalysts have included SiO_2 supported NiO ¹⁰⁹ and $MgAl_2O_4$ supported NiO ¹¹². However, the issues of carbon formation, toxicity, and cost are present. Perovskites have been investigated as redox catalysts and there has been success with perovskites such as $LaFeO_3$, $La_{1-x}Sr_xFeO_3$ ^{113,114}. However, these perovskites are costly and do not exhibit high oxygen capacities.

1.5.4 Surface Promotion of Redox Catalysts for Enhanced Selectivity and Activity

Oxygen carrier activity and selectivity can be enhanced by surface promotion with a catalytically active metal. Shafiefarhood reported that impregnation of 0.5 w.t.% Rh on CaMnO_3 and LaCeO_3 significantly enhanced their activity and syngas selectivity for methane partial oxidation⁷². Over 300°C decrease in the onset temperature for methane oxidation was observed. Moreover, Rh enriched on the oxide surface and decreased the apparent surface activation energy of methane by 95% for CaMnO_3 based oxygen carriers. The enhanced surface activity also led to significantly increased oxygen donation rate, resulting from the increased driving force for O^{2-} conduction. Rh promoted CaMnO_3 exhibited high activity and selectivity for methane POx for 100 cycles at 600°C. Palchelva et al. showed that Rh promotion on $\text{La}_{0.8}\text{Sr}_{0.2}(\text{Fe}_{0.8}\text{Co}_{0.2})_{1-x}\text{Ga}_x\text{O}_3$ led to 40% enhancement in CO selectivity under 10% CH_4 pulses at 600°C⁷³. Ni as a promoter for WO_3 based oxygen carriers for methane partial oxidation was reported by Chen et al¹¹⁵. Methane conversion and syngas yield increased by 2.7 fold upon Ni promotion within the region of high syngas selectivity at 800°C¹¹⁵. Doping low levels (~1%) of heteroatoms such as La on iron oxide was also reported to significantly improve the redox activity of the oxygen carrier¹¹⁶.

1.5.5 Density Functional Theory (DFT) for Oxygen Carrier Design

With a high number of possible oxygen carriers/redox catalysts existing, design principles are desired to guide the selection of the oxygen carrier/redox catalyst in a predictive manner. Describing properties of oxygen carriers and redox catalysts through quantum mechanical modeling is an attractive route to guiding the selection of oxygen carriers and redox catalysts. Density functional theory (DFT) has become a popular method, within quantum mechanical modeling to describe metals and metal oxides. Outside of chemical looping, density functional theory has emerged as a useful computational tool for describing properties of materials^{117,118},

catalysis^{119–123} and semiconductor design^{124–127} due to its computational efficiency¹²⁷. However, the application to chemical looping is relatively new and these studies are usually focused on explaining rather than predicting. A common example are the studies regarding the reaction of methane with iron oxide^{128–130}. For example, studies were carried out to explain methane oxidation on (0001) surface of α -Fe₂O₃ (hematite)^{129,130} as well as small clusters of iron oxides with different oxide supports¹²⁸. While these studies are valuable due to heavy application of iron oxide as an oxygen carrier, they lack predictive findings. Using DFT to predictively design oxygen carriers is most interesting for perovskites in the application of chemical looping with oxygen uncoupling. As mentioned in previous sections, oxygen carrier design for chemical looping with oxygen uncoupling has had limited success, but perovskites are a promising class of materials for this application. Oxygen donation in this process is governed by oxygen vacancy creation. As such, calculating the energy of oxygen vacancy creation in perovskites serve as promising route to predict the performance of perovskites for chemical looping with oxygen uncoupling. Using DFT to predict energies of oxygen vacancy creation is most traditionally used for semiconductor applications^{131–134}. More recently, there are studies on guiding the selection of materials using vacancy calculations for thermochemical applications, oxidation of hydrocarbons, or water splitting^{135–142}. While these studies have used a number of approximations to explore a large material space, they have had promising results and can serve as inspiration for designing oxygen carriers for chemical looping with oxygen uncoupling.

1.6 Summary

Redox catalyst and oxygen carrier design is critical to the success to chemical looping processes. Design of redox catalysts should be approached by (i) designing a metal oxide with suitable thermodynamics of oxygen release (equilibrium P_{O_2}); and/or (ii) designing a surface to

provide more kinetically favorable products. In this work, both of these approaches will be employed and density functional theory will be used to provide a thermodynamic understanding of promising perovskites before they are experimentally investigated for chemical looping with oxygen uncoupling and chemical looping reforming applications. Novel supports, which control oxygen release, will also be experimentally investigated for NiO.

In the second chapter, density functional theory will be employed for BaMnO_3 , CaMnO_3 , $\text{CaMn}_{0.75}\text{Fe}_{0.25}\text{O}_3$, and $\text{Ca}_{0.75}\text{Sr}_{0.25}\text{MnO}_3$ to investigate their capability for chemical looping with oxygen uncoupling. The energy of oxygen vacancy creation is used to indicate their capability for “oxygen uncoupling”. These calculations suggest that the ability to uncouple oxygen will follow the trend: $\text{CaMn}_{0.75}\text{Fe}_{0.25}\text{O}_3 > \text{Ca}_{0.75}\text{Sr}_{0.25}\text{MnO}_3 > \text{CaMnO}_3 > \text{BaMnO}_3$. This was confirmed by thermogravimetric experiments, particularly at low temperatures (less than 700°C). These results suggested that CaMnO_3 , $\text{Ca}_{0.75}\text{Sr}_{0.25}\text{MnO}_3$, $\text{CaMn}_{0.75}\text{Fe}_{0.25}\text{O}_3$ are capable of coal combustion. Comparison to coal char conversion experiments showed that amount of converted coal char is increased with strontium and iron doping of CaMnO_3 .

In chapter three, $\text{BaMn}_x\text{B}_{1-x}\text{O}_3$ ($\text{B} = \text{Ni}$ or Fe) are investigated chemical looping reforming with $\text{CaMn}_x\text{B}_{1-x}\text{O}_3$ ($\text{B} = \text{Ni}$ or Fe) investigated for comparison. Based on the findings of the previous chapter, it was suspected that BaMnO_3 as a base perovskite will lead to more selective products due to lower amounts of oxygen release. Temperature programmed hydrogen reduction and oxygen desorption experiments confirmed that BaMnO_3 as host perovskite resulted in more tightly bound oxygen. The selective conversion of methane using $\text{BaMn}_x\text{B}_{1-x}\text{O}_3$ ($\text{B} = \text{Ni}$ or Fe) was confirmed through differential bed experiments. In addition, BaMnO_3 was shown to be coke resistant, with Fe and Ni doping not resulting in significantly higher coke formation.

In chapter four, Rh promoted $\text{Ca}_x\text{A}_{1-x}\text{Mn}_y\text{B}_{1-y}\text{O}_3$ ($\text{A} = \text{Sr}$, $\text{B} = \text{Fe}$) was investigated as redox catalysts for low temperature methane conversion to syngas. With $\text{Ca}_x\text{A}_{1-x}\text{Mn}_y\text{B}_{1-y}\text{O}_3$ ($\text{A} = \text{Sr}$, $\text{B} = \text{Fe}$) being shown to have CLOU capabilities, Rh promotion was used to provide a more selective surface. In addition, Rh promotion was expected to provide a higher activity for methane conversion. High methane conversion and oxygen extraction from the redox catalyst was confirmed through fixed bed experiments. However, high selectivity was not found for all the redox catalysts. Rh promoted CaMnO_3 provided selective oxidation of methane. Rh promoted $\text{Ca}_x\text{Sr}_{1-x}\text{MnO}_3$ led to a combination of complete and selective oxidation of methane. Rh promoted $\text{CaMn}_y\text{Fe}_{1-y}\text{O}_3$ resulted in complete combustion of methane. A reforming catalyst was placed downstream of the redox catalyst to convert unselective products. Optimization of this scheme resulted in syngas yield above 70% at 600°C and 700°C.

In chapter five, MgFe_2O_4 , NiFe_2O_4 , and BaFe_2O_4 are investigated as substrates for NiO. NiO suffers from coking because it can only provide oxygen over a short period of time. It is hypothesized that using these spinel oxides as substrates can aid in coke formation because they will provide oxygen over long periods of time. $\text{MgFe}_2\text{O}_4 + x\text{NiO}$, $\text{NiFe}_2\text{O}_4 + x\text{NiO}$, and $\text{BaFe}_2\text{O}_4 + x\text{NiO}$ ($x = 0.25, 0.5$) were investigated in redox cycling and these materials did not show any signs of coke (carbon deposition) and reduction of the supports showed they provide sustained oxygen release during the entirety of the reduction half cycle. In addition, BaFe_2O_4 and NiFe_2O_4 supported NiO were shown to be capable of converting methane as rapidly as inert supported NiO.

1.7 References

1. Fossil Fuels — The National Academies <http://needtoknow.nas.edu/energy/energy-sources/fossil-fuels/> (accessed Nov 3, 2018).
2. Abas, N.; Kalair, A.; Khan, N. Review of Fossil Fuels and Future Energy Technologies. *Futures* **2015**, *69*, 31–49.
3. Stangland, E. E. Shale Gas Implications for C2-C3 Olefin Production: Incumbent and Future Technology. *Annual Review of Chemical and Biomolecular Engineering* **2018**, *9* (1), 341–364.
4. International Energy Outlook 2016 - Energy Information Administration <https://www.eia.gov/outlooks/archive/ieo16/> (accessed Nov 4, 2018).
5. What are the energy-related carbon dioxide emissions from fossil fuels for the United States and the world? - FAQ - U.S. Energy Information Administration (EIA) <https://www.eia.gov/tools/faqs/faq.php?id=79&t=11> (accessed Nov 5, 2018).
6. Figueroa, J. D.; Fout, T.; Plasynski, S.; McIlvried, H.; Srivastava, R. D. Advances in CO₂ Capture Technology—The U.S. Department of Energy’s Carbon Sequestration Program. *International Journal of Greenhouse Gas Control* **2008**, *2* (1), 9–20.
7. Horn, F. L.; Steinberg, M. Control of Carbon Dioxide Emissions from a Power Plant (and Use in Enhanced Oil Recovery). *Fuel* **1982**, *61* (5), 415–422.
8. Herzog, H.; Golomb, D.; Zemba, S. Feasibility, Modeling and Economics of Sequestering Power Plant CO₂ Emissions in the Deep Ocean. *Environmental Progress* **1991**, *10* (1), 64–74.
9. Nakayama, S.; Noguchi, Y.; Kiga, T.; Miyamae, S.; Maeda, U.; Kawai, M.; Tanaka, T.; Koyata, K.; Makino, H. Pulverized Coal Combustion in O₂/CO₂ Mixtures on a Power Plant for CO₂ Recovery. *Energy Conversion and Management* **1992**, *33* (5), 379–386.
10. Sander, M. T.; Mariz, C. L. The Fluor Daniel® Econamine FG Process: Past Experience and Present Day Focus. *Energy Conversion and Management* **1992**, *33* (5), 341–348.
11. Anheden, M.; Yan, J.; Smedt, G. D. Denitrogenation (or Oxyfuel Concepts). *Oil & Gas Science and Technology - Rev. IFP* **2005**, *60* (3), 485–495.
12. Stiegel, G. J.; Ramezan, M. Hydrogen from Coal Gasification: An Economical Pathway to a Sustainable Energy Future. *International Journal of Coal Geology* **2006**, *65* (3), 173–190.
13. Wall, T. F. Combustion Processes for Carbon Capture. *Proceedings of the Combustion Institute* **2007**, *31* (1), 31–47.

14. Davison, J. Performance and Costs of Power Plants with Capture and Storage of CO₂. *Energy* **2007**, *32* (7), 1163–1176.
15. Descamps, C.; Bouallou, C.; Kanniche, M. Efficiency of an Integrated Gasification Combined Cycle (IGCC) Power Plant Including CO₂ Removal. *Energy* **2008**, *33* (6), 874–881.
16. Pehnt, M.; Henkel, J. Life Cycle Assessment of Carbon Dioxide Capture and Storage from Lignite Power Plants. *International Journal of Greenhouse Gas Control* **2009**, *3* (1), 49–66.
17. Ciferno, J. P.; Fout, T. E.; Jones, A. P.; Murphy, J. T. Capturing Carbon from Existing Coal-Fired Power Plants. *Chemical Engineering Progress; New York* **2009**, *105* (4), 33–41.
18. Nord, L. O.; Anantharaman, R.; Bolland, O. Design and Off-Design Analyses of a Pre-Combustion CO₂ Capture Process in a Natural Gas Combined Cycle Power Plant. *International Journal of Greenhouse Gas Control* **2009**, *3* (4), 385–392.
19. Rochelle, G. T. Amine Scrubbing for CO₂ Capture. *Science* **2009**, *325* (5948), 1652–1654.
20. Kanniche, M.; Gros-Bonnivard, R.; Jaud, P.; Valle-Marcos, J.; Amann, J.-M.; Bouallou, C. Pre-Combustion, Post-Combustion and Oxy-Combustion in Thermal Power Plant for CO₂ Capture. *Applied Thermal Engineering* **2010**, *30* (1), 53–62.
21. Toftegaard, M. B.; Brix, J.; Jensen, P. A.; Glarborg, P.; Jensen, A. D. Oxy-Fuel Combustion of Solid Fuels. *Progress in Energy and Combustion Science* **2010**, *36* (5), 581–625.
22. Finkenrath, M. Cost and Performance of Carbon Dioxide Capture from Power Generation. **2011**.
23. Markewitz, P.; Kuckshinrichs, W.; Leitner, W.; Linssen, J.; Zapp, P.; Bongartz, R.; Schreiber, A.; E. Müller, T. Worldwide Innovations in the Development of Carbon Capture Technologies and the Utilization of CO₂. *Energy & Environmental Science* **2012**, *5* (6), 7281–7305.
24. Rubin, E. S.; Mantripragada, H.; Marks, A.; Versteeg, P.; Kitchin, J. The Outlook for Improved Carbon Capture Technology. *Progress in Energy and Combustion Science* **2012**, *38* (5), 630–671.
25. E. Boot-Handford, M.; C. Abanades, J.; J. Anthony, E.; J. Blunt, M.; Brandani, S.; Dowell, N. M.; R. Fernández, J.; Ferrari, M.-C.; Gross, R.; P. Hallett, J.; et al. Carbon Capture and Storage Update. *Energy & Environmental Science* **2014**, *7* (1), 130–189.

26. Leung, D. Y. C.; Caramanna, G.; Maroto-Valer, M. M. An Overview of Current Status of Carbon Dioxide Capture and Storage Technologies. *Renewable and Sustainable Energy Reviews* **2014**, *39*, 426–443.
27. Khodakov, A. Y.; Chu, W.; Fongarland, P. Advances in the Development of Novel Cobalt Fischer–Tropsch Catalysts for Synthesis of Long-Chain Hydrocarbons and Clean Fuels. *Chem. Rev.* **2007**, *107* (5), 1692–1744.
28. Dry, M. E. Fischer–Tropsch Reactions and the Environment. *Applied Catalysis A: General* **1999**, *189* (2), 185–190.
29. Dry, M. E. The Fischer–Tropsch Process: 1950–2000. *Catalysis Today* **2002**, *71* (3), 227–241.
30. Iulianelli, A.; Liguori, S.; Wilcox, J.; Basile, A. Advances on Methane Steam Reforming to Produce Hydrogen through Membrane Reactors Technology: A Review. *Catalysis Reviews* **2016**, *58* (1), 1–35.
31. LeValley, T. L.; Richard, A. R.; Fan, M. The Progress in Water Gas Shift and Steam Reforming Hydrogen Production Technologies – A Review. *International Journal of Hydrogen Energy* **2014**, *39* (30), 16983–17000.
32. Edwards, J. H.; Maitra, A. M. The Chemistry of Methane Reforming with Carbon Dioxide and Its Current and Potential Applications. *Fuel Processing Technology* **1995**, *42* (2), 269–289.
33. Li, D.; Nakagawa, Y.; Tomishige, K. Methane Reforming to Synthesis Gas over Ni Catalysts Modified with Noble Metals. *Applied Catalysis A: General* **2011**, *408* (1), 1–24.
34. Nieva, M. A.; Villaverde, M. M.; Monzón, A.; Garetto, T. F.; Marchi, A. J. Steam-Methane Reforming at Low Temperature on Nickel-Based Catalysts. *Chemical Engineering Journal* **2014**, *235*, 158–166.
35. Pakhare, D.; Spivey, J. A Review of Dry (CO₂) Reforming of Methane over Noble Metal Catalysts. *Chemical Society Reviews* **2014**, *43* (22), 7813–7837.
36. Barroso-Quiroga, M. M.; Castro-Luna, A. E. Catalytic Activity and Effect of Modifiers on Ni-Based Catalysts for the Dry Reforming of Methane. *International Journal of Hydrogen Energy* **2010**, *35* (11), 6052–6056.
37. Nematollahi, B.; Rezaei, M.; Khajenoori, M. Combined Dry Reforming and Partial Oxidation of Methane to Synthesis Gas on Noble Metal Catalysts. *International Journal of Hydrogen Energy* **2011**, *36* (4), 2969–2978.

38. Barroso-Quiroga, M. M.; Castro-Luna, A. E. Catalytic Activity and Effect of Modifiers on Ni-Based Catalysts for the Dry Reforming of Methane. *International Journal of Hydrogen Energy* **2010**, *35* (11), 6052–6056.
39. Wang, C.; Sun, N.; Zhao, N.; Wei, W.; Sun, Y.; Sun, C.; Liu, H.; Snape, C. E. Coking and Deactivation of a Mesoporous Ni–CaO–ZrO₂ Catalyst in Dry Reforming of Methane: A Study under Different Feeding Compositions. *Fuel* **2015**, *143*, 527–535.
40. de Sousa, F. F.; de Sousa, H. S. A.; Oliveira, A. C.; Junior, M. C. C.; Ayala, A. P.; Barros, E. B.; Viana, B. C.; Filho, J. M.; Oliveira, A. C. Nanostructured Ni-Containing Spinel Oxides for the Dry Reforming of Methane: Effect of the Presence of Cobalt and Nickel on the Deactivation Behaviour of Catalysts. *International Journal of Hydrogen Energy* **2012**, *37* (4), 3201–3212.
41. Adánez, J.; Abad, A. Chemical-Looping Combustion: Status and Research Needs. *Proceedings of the Combustion Institute* **2018**.
42. Fan, L.; Wiley, A. J.; Fan, L. *Chemical Looping Systems for Fossil Energy Conversions* *Chemical Looping Systems for Fossil Energy Conversions*.
43. Tang, M.; Xu, L.; Fan, M. Progress in Oxygen Carrier Development of Methane-Based Chemical-Looping Reforming: A Review. *Applied Energy* **2015**, *151*, 143–156.
44. Lyngfelt, A. Chemical-Looping Combustion of Solid Fuels – Status of Development. *Applied Energy* **2014**, *113*, 1869–1873.
45. Kronberger, B.; Johansson, E.; Löffler, G.; Mattisson, T.; Lyngfelt, A.; Hofbauer, H. A Two-Compartment Fluidized Bed Reactor for CO₂ Capture by Chemical-Looping Combustion. *Chemical Engineering & Technology* **2004**, *27* (12), 1318–1326.
46. Lyngfelt, A.; Leckner, B.; Mattisson, T. A Fluidized-Bed Combustion Process with Inherent CO₂ Separation; Application of Chemical-Looping Combustion. *Chemical Engineering Science* **2001**, *56* (10), 3101–3113.
47. Ohlemüller, P.; Busch, J.-P.; Reitz, M.; Ströhle, J.; Epple, B. Chemical-Looping Combustion of Hard Coal: Autothermal Operation of a 1 MWth Pilot Plant. *J. Energy Resour. Technol* **2016**, *138* (4), 042203.
48. Kolbitsch, P.; Bolhàr-Nordenkamp, J.; Pröll, T.; Hofbauer, H. Operating Experience with Chemical Looping Combustion in a 120kW Dual Circulating Fluidized Bed (DCFB) Unit. *International Journal of Greenhouse Gas Control* **2010**, *4* (2), 180–185.
49. Pröll, T.; Bolhàr-Nordenkamp, J.; Kolbitsch, P.; Hofbauer, H. Syngas and a Separate Nitrogen/Argon Stream via Chemical Looping Reforming – A 140kW Pilot Plant Study. *Fuel* **2010**, *89* (6), 1249–1256.

50. Consonni, S.; Lozza, G.; Pelliccia, G.; Rossini, S.; Saviano, F. Chemical-Looping Combustion for Combined Cycles With CO₂ Capture. **2004**, 321–331.
51. Johansson, E.; Mattisson, T.; Lyngfelt, A.; Thunman, H. Combustion of Syngas and Natural Gas in a 300 W Chemical-Looping Combustor. *Chemical Engineering Research and Design* **2006**, *84* (9), 819–827.
52. Kronberger, B.; Lyngfelt, A.; Löffler, G.; Hofbauer, H. Design and Fluid Dynamic Analysis of a Bench-Scale Combustion System with CO₂ Separation–Chemical-Looping Combustion. *Ind. Eng. Chem. Res.* **2005**, *44* (3), 546–556.
53. Mattisson, T.; Lyngfelt, A.; Cho, P. The Use of Iron Oxide as an Oxygen Carrier in Chemical-Looping Combustion of Methane with Inherent Separation of CO₂. *Fuel* **2001**, *80* (13), 1953–1962.
54. Mattisson, T.; García-Labiano, F.; Kronberger, B.; Lyngfelt, A.; Adánez, J.; Hofbauer, H. Chemical-Looping Combustion Using Syngas as Fuel. *International Journal of Greenhouse Gas Control* **2007**, *1* (2), 158–169.
55. Mattisson, T.; Lyngfelt, A.; Leion, H. Chemical-Looping with Oxygen Uncoupling for Combustion of Solid Fuels. *International Journal of Greenhouse Gas Control* **2009**, *3* (1), 11–19.
56. Mattisson, T.; Leion, H.; Lyngfelt, A. Chemical-Looping with Oxygen Uncoupling Using CuO/ZrO₂ with Petroleum Coke. *Fuel* **2009**, *88* (4), 683–690.
57. Shulman, A.; Cleverstam, E.; Mattisson, T.; Lyngfelt, A. Manganese/Iron, Manganese/Nickel, and Manganese/Silicon Oxides Used in Chemical-Looping With Oxygen Uncoupling (CLOU) for Combustion of Methane. *Energy Fuels* **2009**, *23* (10), 5269–5275.
58. de Diego, L. F.; Ortiz, M.; Adánez, J.; García-Labiano, F.; Abad, A.; Gayán, P. Synthesis Gas Generation by Chemical-Looping Reforming in a Batch Fluidized Bed Reactor Using Ni-Based Oxygen Carriers. *Chemical Engineering Journal* **2008**, *144* (2), 289–298.
59. de Diego, L. F.; Ortiz, M.; García-Labiano, F.; Adánez, J.; Abad, A.; Gayán, P. Hydrogen Production by Chemical-Looping Reforming in a Circulating Fluidized Bed Reactor Using Ni-Based Oxygen Carriers. *Journal of Power Sources* **2009**, *192* (1), 27–34.
60. Rydén, M.; Lyngfelt, A.; Mattisson, T. Synthesis Gas Generation by Chemical-Looping Reforming in a Continuously Operating Laboratory Reactor. *Fuel* **2006**, *85* (12), 1631–1641.

61. Intiaz, Q.; Hosseini, D.; Müller, C. R. Review of Oxygen Carriers for Chemical Looping with Oxygen Uncoupling (CLOU): Thermodynamics, Material Development, and Synthesis. *Energy Technology* **2013**, *1* (11), 633–647.
62. Yuan, C.; Wu, H. B.; Xie, Y.; Lou, X. W. (David). Mixed Transition-Metal Oxides: Design, Synthesis, and Energy-Related Applications. *Angewandte Chemie International Edition* **2014**, *53* (6), 1488–1504.
63. B. Gawande, M.; K. Pandey, R.; V. Jayaram, R. Role of Mixed Metal Oxides in Catalysis Science—Versatile Applications in Organic Synthesis. *Catalysis Science & Technology* **2012**, *2* (6), 1113–1125.
64. Adanez, J.; Abad, A.; Garcia-Labiano, F.; Gayan, P.; de Diego, L. F. Progress in Chemical-Looping Combustion and Reforming Technologies. *Progress in Energy and Combustion Science* **2012**, *38* (2), 215–282.
65. Adánez, J.; de Diego, L. F.; García-Labiano, F.; Gayán, P.; Abad, A.; Palacios, J. M. Selection of Oxygen Carriers for Chemical-Looping Combustion. *Energy Fuels* **2004**, *18* (2), 371–377.
66. de Diego, L. F.; Gayán, P.; García-Labiano, F.; Celaya, J.; Abad, A.; Adánez, J. Impregnated CuO/Al₂O₃ Oxygen Carriers for Chemical-Looping Combustion: Avoiding Fluidized Bed Agglomeration. *Energy Fuels* **2005**, *19* (5), 1850–1856.
67. Zhang, Y.; Doroodchi, E.; Moghtaderi, B. Chemical Looping Combustion of Ultra Low Concentration of Methane with Fe₂O₃/Al₂O₃ and CuO/SiO₂. *Applied Energy* **2014**, *113*, 1916–1923.
68. Dueso, C.; Abad, A.; García-Labiano, F.; de Diego, L. F.; Gayán, P.; Adánez, J.; Lyngfelt, A. Reactivity of a NiO/Al₂O₃ Oxygen Carrier Prepared by Impregnation for Chemical-Looping Combustion. *Fuel* **2010**, *89* (11), 3399–3409.
69. Neal, L.; Shafieifarhood, A.; Li, F. Effect of Core and Shell Compositions on MeOx@LaySr_{1-y}FeO₃ Core–Shell Redox Catalysts for Chemical Looping Reforming of Methane. *Applied Energy* **2015**, *157*, 391–398.
70. Ishida, M.; Jin, H. A Novel Chemical-Looping Combustor without NO_x Formation. *Ind. Eng. Chem. Res.* **1996**, *35* (7), 2469–2472.
71. Shafieifarhood, A.; Zhang, J.; Michael Neal, L.; Li, F. Rh-Promoted Mixed Oxides for “Low-Temperature” Methane Partial Oxidation in the Absence of Gaseous Oxidants. *Journal of Materials Chemistry A* **2017**, *5* (23), 11930–11939.
72. Palcheva, R.; Olsbye, U.; Palcut, M.; Rauwel, P.; Tyuliev, G.; Velinov, N.; Fjellvåg, H. H. Rh Promoted La_{0.75}Sr_{0.25}(Fe_{0.8}Co_{0.2})_{1-x}GaxO_{3-δ} Perovskite Catalysts:

Characterization and Catalytic Performance for Methane Partial Oxidation to Synthesis Gas. *Applied Surface Science* **2015**, *357*, 45–54.

73. Nandy, A.; Loha, C.; Gu, S.; Sarkar, P.; Karmakar, M. K.; Chatterjee, P. K. Present Status and Overview of Chemical Looping Combustion Technology. *Renewable and Sustainable Energy Reviews* **2016**, *59*, 597–619.
74. Adanez, J.; García-Labiano, F.; de Diego, L. F.; Gayán, P.; Celaya, J.; Abad, A. - Characterization of Oxygen Carriers for Chemical-Looping Combustion. In *Greenhouse Gas Control Technologies 7*; Rubin, E. S., Keith, D. W., Gilboy, C. F., Wilson, M., Morris, T., Gale, J., Thambimuthu, K., Eds.; Elsevier Science Ltd: Oxford, 2005; pp 105–113.
75. Kang, K.-S.; Kim, C.-H.; Bae, K.-K.; Cho, W.-C.; Kim, S.-H.; Park, C.-S. Oxygen-Carrier Selection and Thermal Analysis of the Chemical-Looping Process for Hydrogen Production. *International Journal of Hydrogen Energy* **2010**, *35* (22), 12246–12254.
76. Jerndal, E.; Mattisson, T.; Lyngfelt, A. Thermal Analysis of Chemical-Looping Combustion. *Chemical Engineering Research and Design* **2006**, *84* (9), 795–806.
77. Corbella, B. M.; Palacios, J. M. Titania-Supported Iron Oxide as Oxygen Carrier for Chemical-Looping Combustion of Methane. *Fuel* **2007**, *86* (1), 113–122.
78. Mattisson, T.; Johansson, M.; Lyngfelt, A. Multicycle Reduction and Oxidation of Different Types of Iron Oxide Particles Application to Chemical-Looping Combustion. *Energy Fuels* **2004**, *18* (3), 628–637.
79. Fan, L.-S.; Li, F. Chemical Looping Technology and Its Fossil Energy Conversion Applications. *Ind. Eng. Chem. Res.* **2010**, *49* (21), 10200–10211.
80. Jerndal, E.; Leion, H.; Axelsson, L.; Ekvall, T.; Hedberg, M.; Johansson, K.; Källén, M.; Svensson, R.; Mattisson, T.; Lyngfelt, A. Using Low-Cost Iron-Based Materials as Oxygen Carriers for Chemical Looping Combustion. *Oil Gas Sci. Technol. – Rev. IFP Energies nouvelles* **2011**, *66* (2), 235–248.
81. Yang, S.; Kim, K.; Baek, J.-I.; Kim, J.-W.; Lee, J. B.; Ryu, C. K.; Lee, G. Spinel Ni(Al,Fe)2O4 Solid Solution as an Oxygen Carrier for Chemical Looping Combustion <http://pubs.acs.org/doi/abs/10.1021/ef300712u> (accessed Nov 8, 2018).
82. Karimi, E.; Forutan, H. R.; Saidi, M.; Rahimpour, M. R.; Shariati, A. Experimental Study of Chemical-Looping Reforming in a Fixed-Bed Reactor: Performance Investigation of Different Oxygen Carriers on Al2O3 and TiO2 Support <http://pubs.acs.org/doi/abs/10.1021/ef5003765> (accessed Nov 8, 2018).

83. Cuadrat, A.; Abad, A.; Adánez, J.; de Diego, L. F.; García-Labiano, F.; Gayán, P. Behavior of Ilmenite as Oxygen Carrier in Chemical-Looping Combustion. *Fuel Processing Technology* **2012**, *94* (1), 101–112.
84. Bleeker, M. F.; Veringa, H. J.; Kersten, S. R. A. Deactivation of Iron Oxide Used in the Steam-Iron Process to Produce Hydrogen. *Applied Catalysis A: General* **2009**, *357* (1), 5–17.
85. Adánez, J.; Cuadrat, A.; Abad, A.; Gayán, P.; Diego, L. F. de; García-Labiano, F. Ilmenite Activation during Consecutive Redox Cycles in Chemical-Looping Combustion <http://pubs.acs.org/doi/abs/10.1021/ef900856d> (accessed Nov 8, 2018).
86. Chen, Y.; Galinsky, N.; Wang, Z.; Li, F. Investigation of Perovskite Supported Composite Oxides for Chemical Looping Conversion of Syngas. *Fuel* **2014**, *134*, 521–530.
87. Zafar, Q.; Abad, A.; Mattisson, T.; Gevert, B.; Strand, M. Reduction and Oxidation Kinetics of Mn₃O₄/Mg–ZrO₂ Oxygen Carrier Particles for Chemical-Looping Combustion. *Chemical Engineering Science* **2007**, *62* (23), 6556–6567.
88. Cho, P.; Mattisson, T.; Lyngfelt, A. Comparison of Iron-, Nickel-, Copper- and Manganese-Based Oxygen Carriers for Chemical-Looping Combustion. *Fuel* **2004**, *83* (9), 1215–1225.
89. Tobias Mattisson, *; Anders Järnäs, ‡ and; Lyngfelt†, A. Reactivity of Some Metal Oxides Supported on Alumina with Alternating Methane and Oxygen Application for Chemical-Looping Combustion <http://pubs.acs.org/doi/abs/10.1021/ef020151i> (accessed Nov 8, 2018).
90. Adánez-Rubio, I.; Gayán, P.; Abad, A.; Diego, L. F. de; García-Labiano, F.; Adánez, J. Evaluation of a Spray-Dried CuO/MgAl₂O₄ Oxygen Carrier for the Chemical Looping with Oxygen Uncoupling Process <http://pubs.acs.org/doi/abs/10.1021/ef3002229> (accessed Nov 8, 2018).
91. Arjmand, M.; Azad, A.-M.; Leion, H.; Lyngfelt, A.; Mattisson, T. Prospects of Al₂O₃ and MgAl₂O₄-Supported CuO Oxygen Carriers in Chemical-Looping Combustion (CLC) and Chemical-Looping with Oxygen Uncoupling (CLOU) <http://pubs.acs.org/doi/abs/10.1021/ef201329x> (accessed Nov 8, 2018).
92. Mattisson, T.; Johansson, M.; Lyngfelt, A. The Use of NiO as an Oxygen Carrier in Chemical-Looping Combustion. *Fuel* **2006**, *85* (5), 736–747.
93. Gayán, P.; Dueso, C.; Abad, A.; Adanez, J.; de Diego, L. F.; García-Labiano, F. NiO/Al₂O₃ Oxygen Carriers for Chemical-Looping Combustion Prepared by Impregnation and Deposition–Precipitation Methods. *Fuel* **2009**, *88* (6), 1016–1023.

94. Shen, L.; Wu, J.; Gao, Z.; Xiao, J. Reactivity Deterioration of NiO/Al₂O₃ Oxygen Carrier for Chemical Looping Combustion of Coal in a 10kWth Reactor. *Combustion and Flame* **2009**, *156* (7), 1377–1385.
95. Masaru Ishida, *; Hongguang Jin, and; Okamoto, T. Kinetic Behavior of Solid Particle in Chemical-Looping Combustion: Suppressing Carbon Deposition in Reduction <http://pubs.acs.org/doi/abs/10.1021/ef970041p> (accessed Nov 8, 2018).
96. Hongguang Jin; Toshihiro Okamoto, and; Ishida*, M. Development of a Novel Chemical-Looping Combustion: Synthesis of a Solid Looping Material of NiO/NiAl₂O₄ <http://pubs.acs.org/doi/abs/10.1021/ie9803265> (accessed Nov 8, 2018).
97. Guo, J.; Lou, H.; Zheng, X. The Deposition of Coke from Methane on a Ni/MgAl₂O₄ Catalyst. *Carbon* **2007**, *45* (6), 1314–1321.
98. Ksepko, E.; Siriwardane, R. V.; Tian, H.; Simonyi, T.; Sciazko, M. Effect of H₂S on Chemical Looping Combustion of Coal-Derived Synthesis Gas over Fe–Mn Oxides Supported on Sepiolite, ZrO₂, and Al₂O₃ <http://pubs.acs.org/doi/abs/10.1021/ef201441k> (accessed Nov 8, 2018).
99. Lambert, A.; Delquié, C.; Clémeneçon, I.; Comte, E.; Lefebvre, V.; Rousseau, J.; Durand, B. Synthesis and Characterization of Bimetallic Fe/Mn Oxides for Chemical Looping Combustion. *Energy Procedia* **2009**, *1* (1), 375–381.
100. Siriwardane, R.; Tian, H.; Simonyi, T.; Poston, J. Synergetic Effects of Mixed Copper–Iron Oxides Oxygen Carriers in Chemical Looping Combustion. *Fuel* **2013**, *108*, 319–333.
101. Marcus Johansson, *; Tobias Mattisson, ‡ and; Lyngfelt‡, A. Creating a Synergy Effect by Using Mixed Oxides of Iron- and Nickel Oxides in the Combustion of Methane in a Chemical-Looping Combustion Reactor <http://pubs.acs.org/doi/abs/10.1021/ef060068l> (accessed Nov 8, 2018).
102. Kieslich, G.; Sun, S.; K. Cheetham, A. An Extended Tolerance Factor Approach for Organic–Inorganic Perovskites. *Chemical Science* **2015**, *6* (6), 3430–3433.
103. Vieten, J.; Bulfin, B.; Senholdt, M.; Roeb, M.; Sattler, C.; Schmücker, M. Redox Thermodynamics and Phase Composition in the System SrFeO_{3–δ} — SrMnO_{3–δ}. *Solid State Ionics* **2017**, *308*, 149–155.
104. Galinsky, N.; Mishra, A.; Zhang, J.; Li, F. Ca_{1–x}A_xMnO₃ (A=Sr and Ba) Perovskite Based Oxygen Carriers for Chemical Looping with Oxygen Uncoupling (CLOU). *Applied Energy* **2015**, *157*, 358–367.

105. Onreabroy, W.; Papato, K.; Rujijanagul, G.; Pengpat, K.; Tunkasiri, T. Study of Strontium Ferrites Substituted by Lanthanum on the Structural and Magnetic Properties. *Ceramics International* **2012**, *38*, S415–S419.
106. Hallberg, P.; Jing, D.; Rydén, M.; Mattisson, T.; Lyngfelt, A. Chemical Looping Combustion and Chemical Looping with Oxygen Uncoupling Experiments in a Batch Reactor Using Spray-Dried $\text{CaMn}_{1-x}\text{M}_x\text{O}_{3-\delta}$ (M = Ti, Fe, Mg) Particles as Oxygen Carriers <http://pubs.acs.org/doi/abs/10.1021/ef3013618> (accessed Nov 8, 2018).
107. Galinsky, N. L.; Huang, Y.; Shafiefarhood, A.; Li, F. Iron Oxide with Facilitated O_2 –Transport for Facile Fuel Oxidation and CO_2 Capture in a Chemical Looping Scheme <http://pubs.acs.org/doi/abs/10.1021/sc300177j> (accessed Nov 8, 2018).
108. Qamar Zafar, *; Tobias Mattisson, ‡ and; Gevert†, B. Integrated Hydrogen and Power Production with CO_2 Capture Using Chemical-Looping Reforming Redox Reactivity of Particles of CuO, Mn_2O_3 , NiO, and Fe_2O_3 Using SiO_2 as a Support <http://pubs.acs.org/doi/abs/10.1021/ie048978i> (accessed Nov 8, 2018).
109. Ortiz, M.; de Diego, L. F.; Abad, A.; García-Labiano, F.; Gayán, P.; Adánez, J. Hydrogen Production by Auto-Thermal Chemical-Looping Reforming in a Pressurized Fluidized Bed Reactor Using Ni-Based Oxygen Carriers. *International Journal of Hydrogen Energy* **2010**, *35* (1), 151–160.
110. Rydén, M.; Johansson, M.; Lyngfelt, A.; Mattisson, T. NiO Supported on Mg–ZrO₂ as Oxygen Carrier for Chemical-Looping Combustion and Chemical-Looping Reforming. *Energy & Environmental Science* **2009**, *2* (9), 970–981.
111. Magnus Rydén; Anders Lyngfelt; Tobias Mattisson. Chemical-Looping Combustion and Chemical-Looping Reforming in a Circulating Fluidized-Bed Reactor Using Ni-Based Oxygen Carriers <http://pubs.acs.org/doi/abs/10.1021/ef800065m> (accessed Nov 8, 2018).
112. Zheng, Y.; Li, K.; Wang, H.; Tian, D.; Wang, Y.; Zhu, X.; Wei, Y.; Zheng, M.; Luo, Y. Designed Oxygen Carriers from Macroporous LaFeO_3 Supported CeO_2 for Chemical-Looping Reforming of Methane. *Applied Catalysis B: Environmental* **2017**, *202*, 51–63.
113. Rydén, M.; Lyngfelt, A.; Mattisson, T.; Chen, D.; Holmen, A.; Bjørgum, E. Novel Oxygen-Carrier Materials for Chemical-Looping Combustion and Chemical-Looping Reforming; $\text{La}_x\text{Sr}_{1-x}\text{Fe}_y\text{Co}_{1-y}\text{O}_{3-\delta}$ Perovskites and Mixed-Metal Oxides of NiO, Fe_2O_3 and Mn_3O_4 . *International Journal of Greenhouse Gas Control* **2008**, *2* (1), 21–36.
114. Chen, S.; Zeng, L.; Tian, H.; Li, X.; Gong, J. Enhanced Lattice Oxygen Reactivity over Ni-Modified WO_3 -Based Redox Catalysts for Chemical Looping Partial Oxidation of Methane <http://pubs.acs.org/doi/abs/10.1021/acscatal.7b00436> (accessed Nov 8, 2018).

115. Qin, L.; Cheng, Z.; Guo, M.; Xu, M.; Fan, J. A.; Fan, L.-S. Impact of 1% Lanthanum Dopant on Carbonaceous Fuel Redox Reactions with an Iron-Based Oxygen Carrier in Chemical Looping Processes <http://pubs.acs.org/doi/abs/10.1021/acsenergylett.6b00511> (accessed Nov 8, 2018).
116. Balog, R.; Jørgensen, B.; Nilsson, L.; Andersen, M.; Rienks, E.; Bianchi, M.; Fanetti, M.; Lægsgaard, E.; Baraldi, A.; Lizzit, S.; et al. Bandgap Opening in Graphene Induced by Patterned Hydrogen Adsorption. *Nature Materials* **2010**, *9* (4), 315–319.
117. Greeley, J.; Mavrikakis, M. Alloy Catalysts Designed from First Principles. *Nat. Mater.* **2004**, *3* (11), 810–815.
118. Nørskov, J. K.; Bligaard, T.; Rossmeisl, J.; Christensen, C. H. Towards the Computational Design of Solid Catalysts. *Nature Chemistry* **2009**, *1* (1), 37–46.
119. Byskov, L. S.; Nørskov, J. K.; Clausen, B. S.; Topsøe, H. DFT Calculations of Unpromoted and Promoted MoS₂-Based Hydrodesulfurization Catalysts. *Journal of Catalysis* **1999**, *187* (1), 109–122.
120. Nolan, M.; Parker, S. C.; Watson, G. W. The Electronic Structure of Oxygen Vacancy Defects at the Low Index Surfaces of Ceria. *Surface Science* **2005**, *595* (1), 223–232.
121. Blakemore, J. D.; Schley, N. D.; Balcells, D.; Hull, J. F.; Olack, G. W.; Incarvito, C. D.; Eisenstein, O.; Brudvig, G. W.; Crabtree, R. H. Half-Sandwich Iridium Complexes for Homogeneous Water-Oxidation Catalysis. *J. Am. Chem. Soc.* **2010**, *132* (45), 16017–16029.
122. Zhao, Y.; Schultz, N. E.; Truhlar, D. G. Design of Density Functionals by Combining the Method of Constraint Satisfaction with Parametrization for Thermochemistry, Thermochemical Kinetics, and Noncovalent Interactions. *J. Chem. Theory Comput.* **2006**, *2* (2), 364–382.
123. Giannozzi, P.; de Gironcoli, S.; Pavone, P.; Baroni, S. Ab Initio Calculation of Phonon Dispersions in Semiconductors. *Phys. Rev. B* **1991**, *43* (9), 7231–7242.
124. Zhang, G.-X.; Tkatchenko, A.; Paier, J.; Appel, H.; Scheffler, M. Van Der Waals Interactions in Ionic and Semiconductor Solids. *Phys. Rev. Lett.* **2011**, *107* (24), 245501.
125. Kresse, G.; Hafner, J. Ab Initio Molecular-Dynamics Simulation of the Liquid-Metal–Amorphous-Semiconductor Transition in Germanium. *Phys. Rev. B* **1994**, *49* (20), 14251–14269.
126. Le Bahers, T.; Rérat, M.; Sautet, P. Semiconductors Used in Photovoltaic and Photocatalytic Devices: Assessing Fundamental Properties from DFT. *J. Phys. Chem. C* **2014**, *118* (12), 5997–6008.

127. Hafner, J. Ab-Initio Simulations of Materials Using VASP: Density-Functional Theory and Beyond. *Journal of Computational Chemistry* **2008**, 29 (13), 2044–2078.
128. Qin, W.; Wang, Y.; Dong, C.; Zhang, J.; Chen, Q.; Yang, Y. The Synergetic Effect of Metal Oxide Support on Fe₂O₃ for Chemical Looping Combustion: A Theoretical Study. *Applied Surface Science* **2013**, 282, 718–723.
129. Cheng, Z.; Qin, L.; Guo, M.; A. Fan, J.; Xu, D.; Fan, L.-S. Methane Adsorption and Dissociation on Iron Oxide Oxygen Carriers: The Role of Oxygen Vacancies. *Physical Chemistry Chemical Physics* **2016**, 18 (24), 16423–16435.
130. Tang, J.-J.; Liu, B. Reactivity of the Fe₂O₃(0001) Surface for Methane Oxidation: A GGA + U Study. *J. Phys. Chem. C* **2016**, 120 (12), 6642–6650.
131. Kohan, A. F.; Ceder, G.; Morgan, D.; Van de Walle, C. G. First-Principles Study of Native Point Defects in ZnO. *Phys. Rev. B* **2000**, 61 (22), 15019–15027.
132. Van de Walle, C. G.; Neugebauer, J. First-Principles Calculations for Defects and Impurities: Applications to III-Nitrides. *Journal of Applied Physics* **2004**, 95 (8), 3851–3879.
133. Janotti, A.; Van de Walle, C. G. Oxygen Vacancies in ZnO. *Appl. Phys. Lett.* **2005**, 87 (12), 122102.
134. Castleton, C. W. M.; Höglund, A.; Mirbt, S. Managing the Supercell Approximation for Charged Defects in Semiconductors: Finite-Size Scaling, Charge Correction Factors, the Band-Gap Problem, and the Ab Initio Dielectric Constant. *Phys. Rev. B* **2006**, 73 (3), 035215.
135. Maiti, D.; A. Daza, Y.; M. Yung, M.; N. Kuhn, J.; R. Bhethanabotla, V. Oxygen Vacancy Formation Characteristics in the Bulk and across Different Surface Terminations of La (1-x) Sr x Fe (1-y) Co y O (3-δ) Perovskite Oxides for CO₂ Conversion. *Journal of Materials Chemistry A* **2016**, 4 (14), 5137–5148.
136. Su, H.-Y.; Sun, K. DFT Study of the Stability of Oxygen Vacancy in Cubic ABO₃ Perovskites. *J Mater Sci* **2015**, 50 (4), 1701–1709.
137. L. Muhich, C.; D. Ehrhart, B.; A. Witte, V.; L. Miller, S.; N. Coker, E.; B. Musgrave, C.; W. Weimer, A. Predicting the Solar Thermochemical Water Splitting Ability and Reaction Mechanism of Metal Oxides: A Case Study of the Hercynite Family of Water Splitting Cycles. *Energy & Environmental Science* **2015**, 8 (12), 3687–3699.
138. Muñoz-García, A. B.; Ritzmann, A. M.; Pavone, M.; Keith, J. A.; Carter, E. A. Oxygen Transport in Perovskite-Type Solid Oxide Fuel Cell Materials: Insights from Quantum Mechanics. *Acc. Chem. Res.* **2014**, 47 (11), 3340–3348.

139. Kotomin, E. A.; Mastrikov, Y. A.; Kuklja, M. M.; Merkle, R.; Roytburd, A.; Maier, J. First Principles Calculations of Oxygen Vacancy Formation and Migration in Mixed Conducting $\text{Ba}_{0.5}\text{Sr}_{0.5}\text{Co}_{1-y}\text{Fe}_y\text{O}_{3-\delta}$ Perovskites. *Solid State Ionics* **2011**, *188* (1), 1–5.
140. Greeley, J.; Jaramillo, T. F.; Bonde, J.; Chorkendorff, I.; Nørskov, J. K. Computational High-Throughput Screening of Electrocatalytic Materials for Hydrogen Evolution. In *Materials for Sustainable Energy*; Co-Published with Macmillan Publishers Ltd, UK, 2010; pp 280–284.
141. Lee, Y.-L.; Kleis, J.; Rossmeisl, J.; Morgan, D. Ab Initio Energetics of $\text{LaB}_3\text{O}_{11}$ ($\text{B}=\text{Mn}$, Fe, Co, and Ni) for Solid Oxide Fuel Cell Cathodes. *Phys. Rev. B* **2009**, *80* (22), 224101.
142. Rossmeisl, J.; Qu, Z.-W.; Zhu, H.; Kroes, G.-J.; Nørskov, J. K. Electrolysis of Water on Oxide Surfaces. *Journal of Electroanalytical Chemistry* **2007**, *607* (1), 83–89.

Chapter 2: Oxygen Vacancy Creation Energy in Mn-Containing Perovskites: An Effective Indicator for Chemical Looping with Oxygen Uncoupling

2.1 Abstract

Chemical looping with oxygen uncoupling (CLOU) is a novel process for carbon dioxide capture from coal combustion. Designing a metal oxide oxygen carrier with suitable oxygen release and uptake properties represents one of the most critical aspects for CLOU. The current work aims to correlate oxygen vacancy creation energy of metal oxide oxygen carriers with their oxygen uptake and release properties. Oxygen vacancy creation energy of $\text{CaMnO}_{3-\delta}$, $\text{Ca}_{0.75}\text{Sr}_{0.25}\text{MnO}_{3-\delta}$, $\text{CaMn}_{0.75}\text{Fe}_{0.25}\text{O}_{3-\delta}$, and $\text{BaMnO}_{3-\delta}$ were determined through density functional theory calculations and correlated with their oxygen release and uptake properties. The effect of the Hubbard U correction on the ground state magnetic configurations and vacancy formation energies was investigated along with the effect of coordination environment of the oxygen in the lattice. It was determined that, while Hubbard U affects the absolute values of vacancy formation energies, it only slightly changes the relative differences in vacancy formation energies between the investigated Mn-containing perovskites to any significant extent. A ranking based on oxygen vacancy creation energy among the various oxides is possible without the use of Hubbard U. Comparisons with experimental data confirm that the energy of vacancy formation for these oxides is an effective indicator for their oxygen donation properties in CLOU: oxygen carrier materials with lower vacancy formation energies can release their lattice oxygen more readily. Thermogravimetric analysis indicates increased oxygen release with decreasing oxygen vacancy formation energy when oxygen non-stoichiometry, relative to oxygen pretreatment, is less than $\delta'=0.023$. Higher activities for coal char combustion were also observed. Additionally, volume change upon oxygen vacancy creation was calculated using DFT and compared to experimental

results obtained through a combination of *in-situ* XRD and thermogravimetric analysis. The simplified DFT strategy is shown to accurately predict the enhancement of the volume expansion by iron doping and suppression of the volume expansion by strontium. These findings indicate that DFT calculations and oxygen vacancy creation energies in Mn-containing perovskites can be an effective indicator for their CLOU properties and can potentially be used as a design parameter for oxygen carrier development and optimizations.

2.2 Introduction

Given the steady increase in global energy consumption and stricter environmental regulations, there is an urgent demand for advanced energy conversion technologies for efficient carbonaceous fuel conversion and CO₂ capture.^{1,2} As the most energy intensive step for CO₂ capture, CO₂ separation from combustion flue gas has attracted significant attention in research and development.³⁻⁹ Although notable progress has been made to reduce the energy penalty for CO₂ separation, state-of-the-art monoethylamine (MEA) based separation processes in coal-fired power plants still consume up to 30% parasitic energy.¹⁰ An alternative approach to avoid CO₂ separation is to use gaseous oxygen for coal combustion to generate an exhaust gas stream with concentrated CO₂. However, existing oxygen generation systems, which are based on cryogenic air separation, are both energy and capital intensive.¹¹ Chemical Looping with Oxygen Uncoupling (CLOU) offers a potentially attractive alternative to cryogenic air separation.¹¹⁻¹⁴ In this process, as illustrated in Figure 2.1a, a metal oxide releases its lattice oxygen into the gas phase for fossil fuel combustion in a fuel reactor. The oxygen depleted metal oxide is then re-oxidized to its original state in an air reactor. As such, oxygen is separated from the air by solid metal oxide particles, which act as “oxygen carriers”, at temperatures and pressures close to those for fossil fuel combustion. The CLOU process enables facile oxygen separation by circulating the oxygen

carrier particles between the two reactors. Since the energy consumption for oxygen carrier circulation is significantly smaller than that associated with cryogenic air separation, the CLOU process has an excellent potential to efficiently capture CO₂ from fossil fuel combustion.¹¹

Oxygen carrier performance is one of the most critical factors affecting commercial viability of the CLOU process. From a thermodynamic standpoint, the metal oxide-based oxygen carrier should spontaneously release oxygen from its lattice under the low oxygen partial pressure (P_{O2}) environment in the fuel reactor. Meanwhile, the depleted oxygen carrier should be re-oxidizable in the air reactor. From a practical standpoint, a typical operating temperature range of 800 – 1,000°C is required for fast fuel combustion and reduction-oxidation (redox) kinetics without causing significant challenges over oxygen carrier physical integrity.¹¹ Based on these oxygen carrier design criteria, a “desired P_{O2} range” can be determined, as shown in Figure 2.1b. The upper limit of the desired P_{O2} range corresponds to the requirement to regenerate the oxygen carrier assuming 10% excess air (corresponding to ~90% conversion of air) is used to re-oxidize the oxygen carrier in an air reactor operated at near atmospheric pressure.¹⁵ The lower optimal P_{O2} limit is estimated based on 1% of the equilibrium oxygen partial pressure of CuO decomposition to Cu₂O at 800°C, since CuO has been shown to have suitable CLOU properties and fast fuel combustion kinetics.^{16–18} A suitable oxygen carrier should exhibit equilibrium P_{O2} within the desired equilibrium P_{O2} range inside of the typical operating temperature window of 800°-1000°C.

Figure 2.1b also illustrates the equilibrium P_{O2} for temperatures in the range 800-1000°C of the most commonly investigated oxides. As can be seen, none of these oxide redox pairs except for CuO/Cu₂O possess desirable properties for CLOU. For instance, the equilibrium oxygen partial pressures for manganese oxides are either too high or too low. Although the Co₃O₄/CoO redox

pair exhibits suitable redox properties within a tight temperature window of 800-835°C, cobalt oxides' toxicity and high cost make it unsuitable for chemical looping.¹⁹

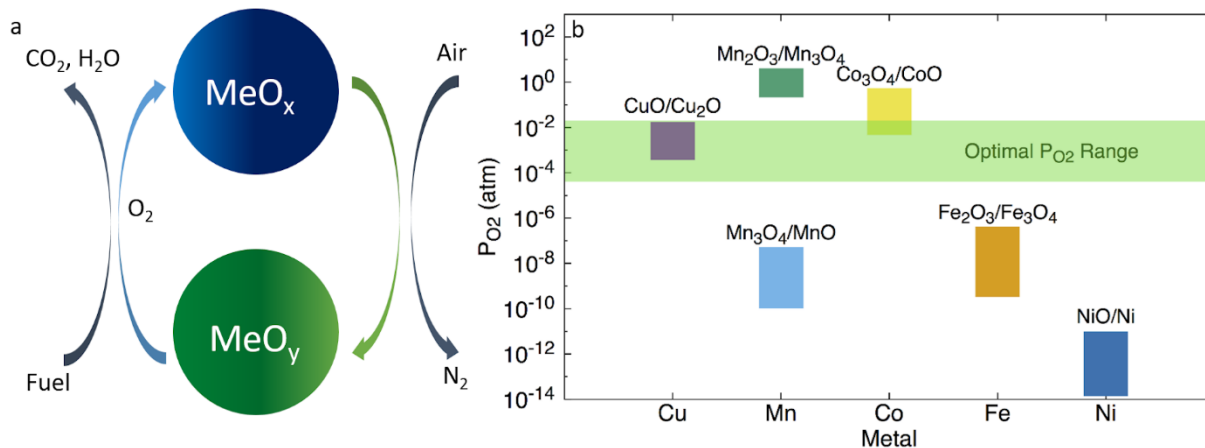


Figure 2.1: (a) A simplified schematic of CLOU. MeO_y is more oxidized than MeO_x ($y > x$); (b) Equilibrium P_{O_2} between 800-1000°C for various Cu, Mn, Co, Fe, and Ni oxides. The desired P_{O_2} range is shaded in green.

While copper oxides are promising for CLOU, they face several challenges including agglomeration and defluidization due to the low melting point of metallic copper.¹⁶⁻¹⁸ In contrast to limited options in monometallic oxides, mixed oxides offer a significantly enlarged material design space with potentially tunable redox properties. For instance, manganese-containing mixed metal oxides, including Mn-Fe, Mn-Si, Mn-Mg, Mn-containing ores, and perovskites have been extensively investigated due to their low cost and abundance.²⁰⁻²⁴ Although these studies have resulted in promising oxygen carrier materials, their performances are less than optimal. For instance, the oxygen carrying capacities of such mixed metal oxides are generally limited compared to CuO based oxygen carriers.²⁰⁻²⁴ Moreover, high operating temperatures ($>950^\circ C$) are often required for effective coal conversion due mainly to the slow oxygen release kinetics. Although further improvements in oxygen capacity and redox kinetics are possible, effective

oxygen carrier design and optimization principles are highly desirable in order to avoid the cumbersome, trial-and-error type of oxygen carrier development strategy.

Using Density Functional Theory (DFT) as a computational tool, the present study aims to identify a relatively simple and computationally efficient descriptor that correlates with the CLOU properties of mixed oxides. Previous studies have shown the effectiveness of DFT in predicting thermochemical redox properties for processes such as water splitting, CO₂ conversion, and air separation^{25–27}. Our study indicates that the energy of oxygen vacancy formation is a potentially effective indicator for CLOU performance in Mn-containing perovskites. In particular, we examined three promising CLOU materials, CaMnO_{3-δ}, Ca_{0.75}Sr_{0.25}MnO_{3-δ}, and CaMn_{0.75}Fe_{0.25}O_{3-δ}, and one ineffective CLOU material, BaMnO_{3-δ}, for comparison.^{28–30} This study represents an attempt to establish a correlation between oxygen vacancy formation and CLOU properties. In order to obtain reliable simulation results, the effects of spin ordering, finite size effects (i.e. vacancy creation in the dilute limit), effect of the Hubbard U correction, and coordination environments of oxygen vacancy sites were considered in calculating the vacancy formation energy of the abovementioned perovskite materials. The analysis on coordination environments includes change in Bader charge of those coordination environments after vacancy formation, providing insights into coordination environments that facilitate oxygen vacancy formation. The calculated oxygen vacancy formation energies were compared to experimentally determined oxygen non-stoichiometry and rates for coal-char combustion. These results confirm energy of vacancy creation as an effective descriptor for CLOU performance, and it can potentially be used for efficient screening and optimization of oxygen carriers in CLOU applications.

2.3 Methods

2.3.1 Computational Methods

We carried out geometry optimizations using the spin-polarized generalized gradient approximation (GGA) and the projector augmented wave (PAW)^{31,32} approach with the Perdew-Burke-Ernzerhof (PBE)³³ exchange correlation functional as implemented in the Vienna *Ab initio* Simulation Package (VASP).³⁴⁻³⁷ We considered the following structures: orthorhombic $\text{CaMnO}_{3-\delta}$, hexagonal $\text{BaMnO}_{3-\delta}$, orthorhombic $\text{Ca}_{0.75}\text{Sr}_{0.25}\text{MnO}_{3-\delta}$, and orthorhombic $\text{CaMn}_{0.75}\text{Fe}_{0.25}\text{O}_{3-\delta}$. All structures were converged with respect to the k-point mesh and plane-wave cutoff (<0.01 eV/atom). For $\text{CaMnO}_{3-\delta}$ and doped $\text{CaMnO}_{3-\delta}$ structures we used a mesh density corresponding to a $2 \times 4 \times 4$ mesh for a 40-atom supercell using a Monkhorst-Pack grid. For $\text{BaMnO}_{3-\delta}$ we used a mesh density corresponding to a $2 \times 2 \times 2$ mesh for an 80-atom supercell using a Γ -centered grid. The system sizes were chosen to accommodate different possible spin configurations. We tested $\text{CaMnO}_{3-\delta}$ and $\text{BaMnO}_{3-\delta}$ for energetic stability under various magnetic configurations using spin polarized calculations. For the doped materials, we used the stable spin ordering for $\text{CaMnO}_{3-\delta}$. Figure A.5 illustrates the initial spin configurations used for the antiferromagnetic states. A-type antiferromagnetic (AF) corresponds to the direction of the spin changing in a single direction and g-type antiferromagnetic (GAF) corresponds to the direction of the spin changing in the direction of all three lattice vectors. For a-type antiferromagnetic states the direction of the spin will be denoted as such: AF-100 for spin direction changing along the lattice vector a , AF-010 for spin direction changing along lattice vector b , and AF-001 for spin direction changing along lattice vector c . We also considered the ferromagnetic state (F), where all spins point in the same direction. We used a cutoff energy of 425 eV for all systems, which we found sufficient to reach convergence (<0.01 eV/atom), as shown in Table A.1. The energy to create an oxygen vacancy

was calculated for several vacancy concentrations by varying the number of crystal unit cells in the simulation supercell, and removing a single oxygen in each supercell size. The energy to create an oxygen vacancy is represented by equation 2.1⁶⁸:

$$Eq. 2.1: \Delta E_{vacancy}^q = E_{defect,supercell}^q - E_{pristine,supercell} - \mu_O + qE_F + E_{corr}$$

Here, $\Delta E_{vacancy}^q$ is the energy to create an oxygen vacancy, associated with a charge state q . $E_{defect,supercell}^q$ is the energy of a supercell with an oxygen defect (with charge q), μ_O is the chemical potential of the removed oxygen atom, E_F is the Fermi Energy (referenced to the valance band maximum of the bulk), and E_{corr} is the electrostatic correction term, which is necessary when q is nonzero⁶⁸. The Fermi energy can range from zero to the band gap energy, and the energy to create an oxygen vacancy will need to be minimized with respect to the charge state q . In semiconductor and insulator materials, the defect can typically assume various charge states, depending on the Fermi Energy. This is further discussed in Chapter 6. A simplified equation for finding the energy to create an oxygen vacancy is shown in equation 2.2, where a neutral oxygen vacancy ($q = 0$) is assumed and the chemical potential of the removed oxygen atom is half of an isolated diatomic oxygen molecule (E_{O_2}). It should be noted that, when the goal is finding accurate vacancy formation energies, care should be taken in considering different charge states, and this will require more accurate exchange-correlation functionals. The use of equation 2.2 is meant for initial studies of the energy of oxygen vacancy formation in the context of CLOU.

$$[Eq. 2.2] \Delta E_{vacancy} = E_{defect,supercell} + \frac{1}{2}E_{O_2} - E_{pristine,supercell}$$

Using equation 2.2 as the definition of oxygen vacancy formation, we tested various system sizes to find the energy of vacancy formation at infinite dilution. By varying the system size, the oxygen non-stoichiometry (represented as δ) changes, giving the energy of vacancy formation as a function of δ . The energy of vacancy formation at infinite dilution is defined as the energy of

vacancy formation for a sufficiently large supercell size, such that the vacancy formation energy remains unchanged when the supercell is further enlarged. At infinite dilution, the defective supercell is expected to be altered only in the vicinity of the defect. Therefore, inducing an oxygen defect is not expected to affect lattice parameters. For this reason, the fully relaxed pristine supercell lattice parameters were used for the defective supercell. For $\text{BaMnO}_{3-\delta}$, we used system sizes of 80, 160, and 320 atoms, consistent with the $P6_3/mmc$ space group.³⁹ For orthorhombic $\text{CaMnO}_{3-\delta}$, $\text{Ca}_{0.75}\text{Sr}_{0.25}\text{MnO}_{3-\delta}$ and $\text{CaMn}_{0.75}\text{Fe}_{0.25}\text{O}_{3-\delta}$ we used system sizes of 40, 80, and 160 atoms, consistent with the $Pnma$ space group.⁴⁰ We created strontium and iron-doped systems by replacing a calcium or manganese atom in a 20-atom supercell, respectively. Larger supercells were replicates of this 20-atom supercell. For $\text{BaMnO}_{3-\delta}$, the choice of oxygen site for vacancy formation was trivial, as there is a single oxygen type due to symmetry. For orthorhombic $\text{CaMnO}_{3-\delta}$, which has two different oxygen types, we found the energy of oxygen vacancy creation for both sites. For $\text{Ca}_{0.75}\text{Sr}_{0.25}\text{MnO}_{3-\delta}$ and $\text{CaMn}_{0.75}\text{Fe}_{0.25}\text{O}_{3-\delta}$, we used a 40-atom unit cell to determine which oxygen was easiest to remove, as, to our knowledge, there are no experimentally derived structures. In order to find the unique oxygen sites in these materials, we determined the coordination environment around each oxygen by defining unique “shells” of local cations surrounding each oxygen site based on the elements and distances from the nearest neighbors to the oxygen site. These shells contained either four or five cations. Figure 2.2 shows an example of a cation shell in $\text{CaMn}_{0.75}\text{Fe}_{0.25}\text{O}_{3-\delta}$, illustrated by bonds between oxygen and neighboring cations. We obtained the energy of vacancy formation for each unique oxygen site, based on the cation shell, in a 40-atom supercell, providing information for which site corresponds to the easiest vacancy formation. Oxygen vacancy linear clustering was not considered, as it is typically seen at vacancy concentrations that would exceed the ones seen in CLOU^{41–46}. In addition, vacancy

ordering in CaMnO_3 starts to disappear at 300°C^{47} , which is well below our experimental temperature.

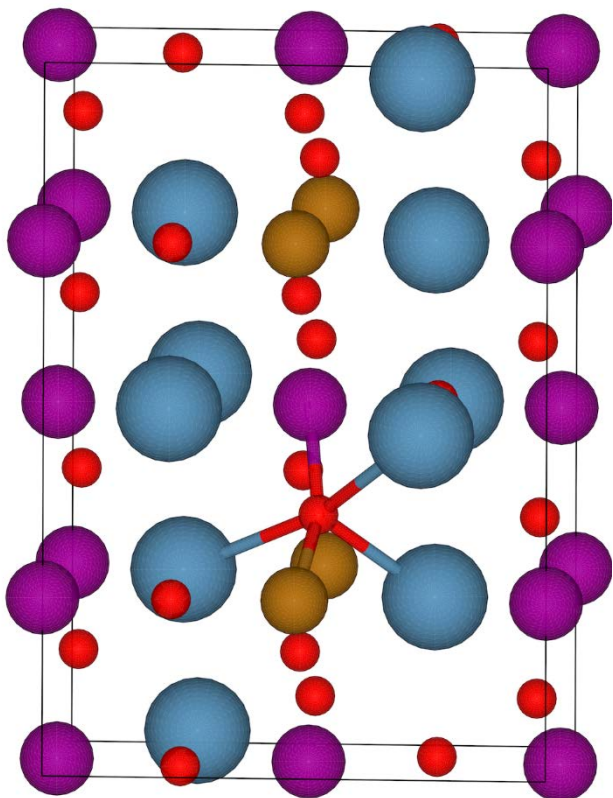


Figure 2.2: Example of a cation shell in $\text{CaMn}_{0.75}\text{Fe}_{0.25}\text{O}_3$. Cations bonding to the oxygen (red) represent the cation shell. Gold is iron, purple is manganese, and blue is calcium.

In our calculations, we obtained energies with and without the use of the Hubbard U correction, which is used to correct an error associated with strongly correlated materials (namely those containing transition metals), where highly correlated orbitals tend to delocalize due to DFT's poor description of exchange energies.⁴⁸ Given the additional complexity of obtaining accurate values of the Hubbard U constant in order to use this correction, we aimed to ascertain whether the trends in energy of oxygen vacancy formation are preserved when the correction is not used, and how sensitive the trends are to the value of U used. Avoiding the need to estimate accurate U values would enable faster screening of different materials. In the calculations with the

Hubbard U correction, we used values for the Hubbard U parameters from the Materials Project database⁴⁹ according to Dudarev et al.⁵⁰, which were fitted to reproduce heats of reduction for manganese and iron oxide (U is 3.9 eV for Mn and 5.3 eV for Fe). In the results, we use “DFT” to denote Density Functional Theory calculations without the Hubbard U correction, and “DFT+U” for those with the correction.

Additional calculations were also conducted to evaluate the effect of vacancy creation on the volume expansion of the oxides, and the results were compared with experimental data. While the volume change of a supercell should be negligible at the infinite dilution, large values of oxygen non-stoichiometry will lead to volume expansion. Considering this, we calculated the volume expansion in 40-atom supercells, corresponding to $\delta = 0.125$. This oxygen non-stoichiometry is close to the upper limit of non-stoichiometry that was found in our TGA experiments.

We also conducted a Bader charge analysis (without the Hubbard U correction), to find the change in Bader charge of the cations shells after vacancy creation, which serves as a descriptor for electron delocalization. This is defined by equation 2.3. Bader charge analysis is a method to separate charges between atoms, making the Bader charge analogous to the oxidation state. This makes it suitable for describing electron delocalization by partitioning charge by cation shell. Electron delocalization is expected to be related to vacancy creation energies due to the ionic nature of the metal oxides, and is expected to indicate the ability of a material and its coordination environments to create an oxygen vacancy. This will possibly establish a trend between ability to delocalize electrons and energy of oxygen vacancy formation. The method for finding the Bader charge is described in the literature.⁵¹ A large Δ Bader will correspond to a large amount of electron delocalization.

$$\begin{aligned}
 [Eq. 2.3] \Delta Bader (Defect - Pristine) \\
 = \sum_{\text{cation shell cations}} Bader Charge_{\text{defect}} - Bader Charge_{\text{pristine}}
 \end{aligned}$$

2.3.2 Experimental Oxygen Carrier Preparation

We used a sol-gel method to prepare the aforementioned perovskites.⁵² We dissolved stoichiometric amounts of metal nitrates, *e.g.* $\text{Ca}(\text{NO}_3)_2 \cdot 4\text{H}_2\text{O}$ and $\text{Mn}(\text{NO}_3)_2 \cdot 4\text{H}_2\text{O}$ for CaMnO_3 , in deionized water. Next we added citric acid (CA, Sigma Aldrich) at a molar ratio of 2.5:1 to the total amount of metal cations, heated the solution to 50°C and held this temperature for 30 minutes. This results in a mixed-metal citric acid complex with good dispersion of metal ions. We then added ethylene glycol (EG, Sigma Aldrich) at a molar ratio of 1.5:1 to the moles of citric acid at 80°C until a gel formed. This gel was dried in an oven at slightly above boiling temperature of water to remove any moisture. Finally, we sintered the sample at 1200 °C for proper phase formation. We used X-ray powder diffraction (XRD) to characterize the crystalline phases present in each sample. The XRD pattern was obtained using a Rigaku SmartLab X-ray diffractometer with CuK_α ($\lambda = .1542$) radiation operating at 40 kV and 44 mA. Scanning was conducted in a step-wise approach with a step size of 0.1° over a 2θ range of 20–80° and a scan time of 4.5s at each step. We used the HighScore Plus[®] software for phase matching. XRD patterns with the corresponding phases are shown in Figure A.2.

2.3.3 *In-Situ* XRD and Rietveld Refinement

The XRD pattern for Rietveld refinement of as-prepared oxygen carriers was collected on a PANalytical Empyrean diffractometer under CuK_α radiation from a sealed tube generator at 45kV and 40mA, with PIXcel1D detector at room temperature. Measurement was taken under a Bragg-Brentano configuration using a spinning sample stage over a 2θ range of 20–100° at 0.01° step size and 4.5s per step. Data was analyzed and refined using GSAS-II software package⁵³. A

plot of the experimental diffraction pattern, the fit for Rietveld refinement, and the difference is shown in the Figure A.3.

Diffraction patterns on (partially) reduced oxygen carriers was also collected on the PANalytical Empyrean diffractometer and used to find unit cell volumes of the reduced oxygen carriers through fitting of the diffraction patterns. A $\text{CuK}\alpha$ radiation from a sealed tube generator at 45kV and 40mA was used with a XRK900 stage. Each scan was 6.3 minutes long and used a 2θ range of 20–100°. Three reducing environments were used: $\text{P}_{\text{O}_2} = 0.01$ atm, $\text{P}_{\text{O}_2} = 0.025$ atm, and inert (5.0 Argon). Nine scans were taken at each reducing environment, measuring the change in diffraction pattern upon equilibration with the reducing environment. This amounted to 56 minutes and was sufficient for an equilibrated diffraction pattern.

2.3.4 Equilibrium Vacancy Characterization

We measured the equilibrium vacancy concentrations through oxygen uncoupling in a Thermogravimetric Analyzer (TGA, TA Instruments SDT-Q600) under reducing environments of $\text{P}_{\text{O}_2} = 0.01, 0.025$ atm, and Inert prepared by blending argon (5.0 grade) with oxygen (extra dry grade). We used reducing environments between 600 and 750°C with isotherms maintained at 25°C increments. We removed any adsorbates by pretreating the samples with 20% oxygen at 1000°C for 90 minutes. 20% oxygen was used during ramping (10°C/min) to 1000°C and cooling (10°C/min) to 100°C as well. We allowed the weight to equilibrate in the oxidizing environment for 30 minutes, and used the weight after equilibration as the initial weight of the oxygen carrier. After this step, we switched the oxidizing environment to a reducing environment and increased the temperature to 600°C. Equilibrium measurements for $\text{P}_{\text{O}_2} = 0.01$ atm and $\text{P}_{\text{O}_2} = 0.025$ environments were taken at every 25°C until 750°C, with sufficient time (the thermogravimetric curves are shown in supplemental text as Figure A.9 and A.10) allowed for an equilibrated weight.

Equilibrium measurements for the inert environment was taken at 600, 700, and 750°C. For all experiments, if a differential weight change were less than 0.02 wt%/min, equilibrium was deemed to have been reached. In these materials, the oxygen non-stoichiometry is typically represented as δ . All reported non-stoichiometry (δ) from these experiments are relative to the weight at 100°C after pretreatment and will be reported as δ' .

2.4 Results and Discussion

2.4.1 Magnetic Spin State Calculations and Crystal Structure Validations

To accurately estimate the energy of vacancy creation, it is desirable to determine the lowest energy spin ordering. While typical operating temperatures for CLOU are higher than the Neel temperature of these perovskites^{54,55}, the DFT calculations are performed at 0 K and may exhibit spin ordering. CaMnO_{3- δ} and BaMnO_{3- δ} have been shown, in the experimental literature, to exhibit antiferromagnetic ordering at low temperatures.^{54,55} Comparing this to the ground states predicted by our calculations provides a way to test the validity of our model. To this aim, we calculated the energies of pristine CaMnO_{3- δ} and BaMnO_{3- δ} structures using a-type antiferromagnetic, g-type antiferromagnetic, and ferromagnetic spin states. We used a spin-polarized calculation without initialized moments to determine which atom should be used as the site to localize the spins. This resulted in the spin being highly localized on the manganese atom. Therefore, manganese (and iron in CaMn_{0.75}Fe_{0.25}O_{3- δ}) atoms were used as the sites for spin ordering in the rest of the calculations. Since symmetry of manganese atoms is the same in both *a* and *c* directions, spin ordering with respect to two axes, i.e. *a/c* and *b*, were considered for a-type antiferromagnetic spin ordering. The energies for the different spin states obtained using both DFT and DFT+U are shown in Figure 2.3 for 80-atom systems of CaMnO_{3- δ} and BaMnO_{3- δ} , with the lowest energy taken as the reference. In agreement with experimental data from the literature³⁹,

both DFT and DFT+U predicted g-type antiferromagnetic as the ground state for $\text{BaMnO}_{3-\delta}$. The magnetic moment predicted by DFT ($2.47 \mu_{\text{B}}$) deviated slightly from the experimental value ($3 \pm 0.3 \mu_{\text{B}}$)³⁹, whereas the DFT+U prediction ($2.98 \mu_{\text{B}}$) was very close. G-type antiferromagnetic spin ordering will be used for $\text{BaMnO}_{3-\delta}$ in the rest of the study to maintain consistency with these findings. In the case of $\text{CaMnO}_{3-\delta}$, DFT predicts g-type antiferromagnetic ordering whereas DFT+U predicts ferromagnetic ordering. Interestingly, the experimentally determined ground state was g-type antiferromagnetic⁵⁵, which is consistent with the prediction from DFT *without* the Hubbard U correction (DFT+U predicted a slightly lower energy for a-type antiferromagnetic as illustrated in Figure 2.3). In addition, DFT yields a better prediction of the moment of the manganese atom ($2.55 \mu_{\text{B}}$ vs. $2.69 \mu_{\text{B}}$ from experimental data), and is nearly identical to previous *ab initio* studies^{56–58} while DFT+U predicts a moment of $3.1 \mu_{\text{B}}$. For the remainder of the study the spin ordering was used as follows, to maintain internal consistency with these findings: ferromagnetic spin ordering was adopted in DFT calculations of $\text{CaMnO}_{3-\delta}$, whereas g-type antiferromagnetic spin ordering was used in DFT+U calculations of $\text{CaMnO}_{3-\delta}$. The spin states used for doped $\text{CaMnO}_{3-\delta}$, i.e. $\text{Ca}_{0.75}\text{Sr}_{0.25}\text{MnO}_{3-\delta}$ and $\text{CaMn}_{0.75}\text{Fe}_{0.25}\text{O}_{3-\delta}$, were assumed to be identical to those of $\text{CaMnO}_{3-\delta}$. In addition to comparing magnetic moments with previous experiments and simulations, we compared the lattice parameters predicted by our calculations with experimental values for $\text{CaMnO}_{3-\delta}$ (our experimental results via Rietveld refinement) and $\text{BaMnO}_{3-\delta}$ (literature report).³⁹ The complete results are shown in Tables A.4-A.8. For $\text{CaMnO}_{3-\delta}$, $\text{BaMnO}_{3-\delta}$, and $\text{CaMn}_{0.75}\text{Fe}_{0.25}\text{O}_{3-\delta}$, the DFT calculations produced a closer match to the experimental lattice parameters, whereas DFT+U calculations provide better values for $\text{Ca}_{0.75}\text{Sr}_{0.25}\text{MnO}_{3-\delta}$. The relative differences in unit cell volumes between experimental and simulation results were all less than 4%. Figure 2.4 illustrates the experimentally determined unit

cell distortions of $\text{CaMn}_{0.75}\text{Fe}_{0.25}\text{O}_{3-\delta}$ and $\text{Ca}_{0.75}\text{Sr}_{0.25}\text{MnO}_{3-\delta}$ compared to undoped $\text{CaMnO}_{3-\delta}$, as well as those predicted by DFT and DFT+U. Both experimental and computational results indicate increased lattice distortion upon strontium substitution. However, DFT over-predicted such distortion whereas the DFT+U results match experimental data more closely for both of the doped materials. The octahedral bond distortion predicted by DFT+U matches experimental data closely as well, as shown in supplemental Table A.15. To summarize, both DFT and DFT+U provide reasonable predictions of the perovskite lattice parameters and spin states. Moreover, DFT+U provided a more accurate prediction than DFT only in some cases. As such, both DFT and DFT+U were adopted in the following sections.

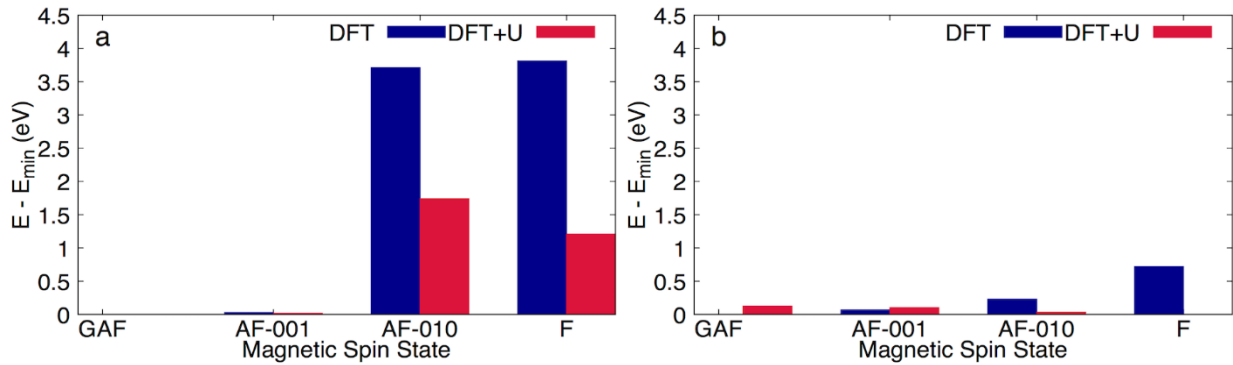


Figure 2.3: Energies of different magnetic spin states with respect to the minimum energy using DFT and DFT +U for a) BaMnO₃ and b) CaMnO₃ (40 atom supercell, AF: A-type antiferromagnetic, FM: Ferromagnetic, GAF: G-type antiferromagnetic).

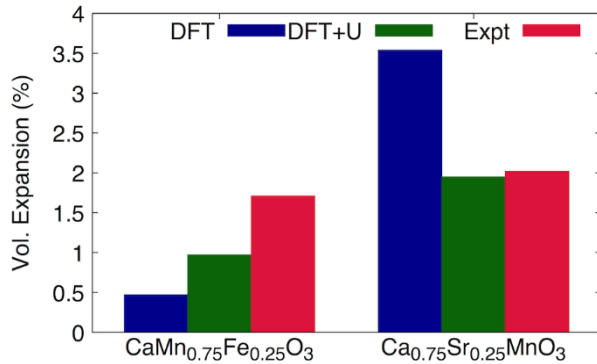


Figure 2.4: Unit cell distortion with respect to CaMnO₃ found experimentally, through DFT, and DFT+U (40 atom supercell).

2.4.2 Effect of Strontium and Iron doping on the $\text{CaMnO}_{3-\delta}$ Vacancy Site

Since the CLOU process involves oxygen vacancy formation (in the fuel reactor) and elimination (in the air reactor), the energy of vacancy creation was investigated as a descriptor for mixed oxides' CLOU properties. It is also noted that energy of vacancy creation can vary with the concentration of oxygen vacancies. To estimate the energy of vacancy creation in the dilute limit for a bulk crystal, it is important to identify the most loosely bound oxygen. In the case of $\text{CaMnO}_{3-\delta}$ and $\text{BaMnO}_{3-\delta}$, this is straightforward since, due to the crystal symmetries, there are only two and one unique lattice oxygen types, respectively. However, in the construction of $\text{Ca}_{0.75}\text{Sr}_{0.25}\text{MnO}_{3-\delta}$ and $\text{CaMn}_{0.75}\text{Fe}_{0.25}\text{O}_{3-\delta}$ supercells will lead to a structure slightly distorted from that of $\text{CaMnO}_{3-\delta}$. Therefore, it is no longer accurate to assume two unique lattice oxygen locations. Without prior knowledge regarding the symmetry of lattice oxygen atoms, the coordination environments of various lattice oxygen atoms were determined in a 40-atom supercell. The unique coordination environments for oxygen can then be identified and extended to larger supercells. Such an approach is more computationally efficient than screening every oxygen atom in a given supercell. The local coordination environment for a lattice oxygen anion was described using its nearest cation neighbors (cation shell) and the radial distances from the lattice oxygen site. Four unique O^{2-} sites/cation shells were identified for $\text{CaMn}_{0.75}\text{Fe}_{0.25}\text{O}_{3-\delta}$ and eight oxygen sites/cation shells were determined for $\text{Ca}_{0.75}\text{Sr}_{0.25}\text{MnO}_{3-\delta}$. Figure 2.5 shows the energy of vacancy creation as well as a graphical representation of the cation shells for $\text{CaMn}_{0.75}\text{Fe}_{0.25}\text{O}_{3-\delta}$ and $\text{Ca}_{0.75}\text{Sr}_{0.25}\text{MnO}_{3-\delta}$. Out of the eight unique lattice oxygen locations for $\text{Ca}_{0.75}\text{Sr}_{0.25}\text{MnO}_{3-\delta}$, only the four corresponding to lower energy of vacancy formation are shown in Figure 2.5. The coordination environments and energy of vacancy formation of all the oxygen vacancy types are provided in Tables A.2 and A.3. Cation shells within the crystal are also shown in Figures A.5 and A.6. The coordination

environments for lattice oxygen obtained using DFT+U were nearly identical to those obtained from DFT ($< 0.03 \text{ \AA}$ difference in cation-anion distances). However, DFT+U predicts lower energies of vacancy creation. Moreover, the ordering of vacancy creation energies among the different lattice oxygens also changed slightly, as shown in Figure 2.5. In the iron-doped material, the creation of two additional oxygen sites can be explained by iron creating an extra possible neighbor for each of the two distinct oxygen types in $\text{CaMnO}_{3-\delta}$. However, strontium distorts the lattice structure to a larger extent, resulting in six additional nearest-neighbor configurations. This enhanced distortion is expected, due to a large ionic radius of strontium compared to calcium ($\text{Sr}/\text{Ca} = 1.16$), in comparison to 1.08 for Mn/Fe. These results indicate that iron doping and strontium doping affect oxygen vacancy formation in different ways. We hypothesize that iron doping decreases the energy of vacancy formation by affecting the B-site cation and O^{2-} bonding strength, as indicated by site 1 and 3 having the lowest energies of vacancy formation, which correspond to an iron cation in the local cation shell. Strontium, however, is in the A-site, and we hypothesize that it affects oxygen vacancy formation through a physical distortion in the structure. While the increased distortion of the unit cell is expected to favor oxygen vacancy creation, the effect with respect to differences between different cations shells (O^{2-} sites) is not clear. DFT predicts the two sites with lowest energy of vacancy formation to be 2a and 5 whereas DFT+U predicts to the two sites with lowest energy to be 2a and 2b, with site 5 being very energetically close to 2b ($\sim 0.03 \text{ eV}$ difference). Nonetheless, the oxygen site with the lowest energy of oxygen vacancy formation was chosen for finding the energy of oxygen vacancy formation in the dilute limit in each case. For $\text{CaMn}_{0.75}\text{Fe}_{0.25}\text{O}_3$, we used sites 1 and 3 with DFT and DFT+U, and for $\text{Ca}_{0.75}\text{Sr}_{0.25}\text{MnO}_3$ we used sites 2a and 5 with DFT and 2a, 2b, and 5 with DFT+U.

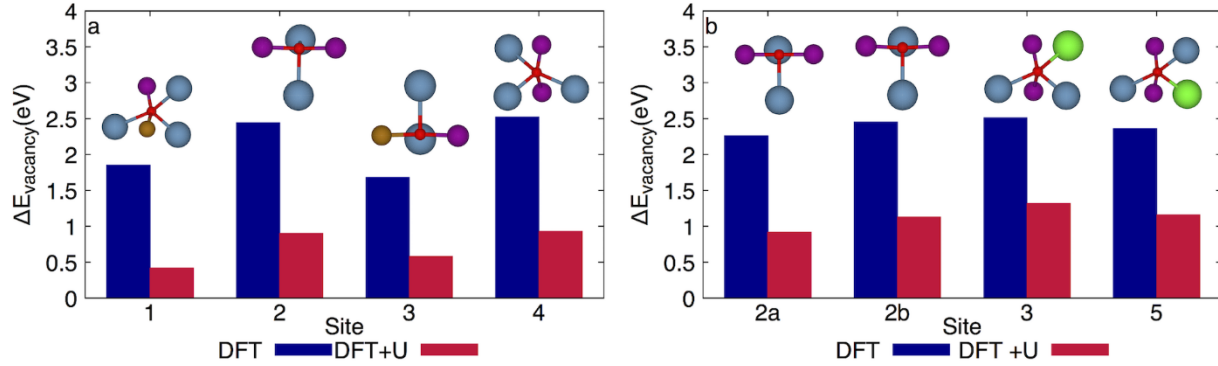


Figure 2.5: Energy of vacancy creation with respect to four sites with lower energy for a) $\text{CaMn}_{0.75}\text{Fe}_{0.25}\text{O}_{3-\delta}$ and b) $\text{Ca}_{0.75}\text{Sr}_{0.25}\text{MnO}_{3-\delta}$. Graphical representation of the oxygen site (red) and its shell is shown (gold is iron, blue is calcium, purple is manganese and green is strontium).

2.4.3 Oxygen Vacancy Formation in the Dilute Limit

Having examined choice of oxygen sites and spin ordering on the estimated energy of vacancy formation, we obtained the vacancy formation energies in the dilute limit for all the materials studied. We carried out these calculations at increasing supercell sizes, *i.e.* increasing values of $1/\delta$ (where δ is the oxygen non-stoichiometry), in order to obtain the limit at which defect-defect interactions do not affect the results. The energy of vacancy formation vs. $1/\delta$ obtained from these calculations is shown in Figure 2.6 for all four materials, including the values for the relevant oxygen sites identified in the previous section. The energy of vacancy formation reached the dilute limit in our calculations for $\text{CaMnO}_{3-\delta}$, $\text{Ca}_{0.75}\text{Sr}_{0.25}\text{MnO}_{3-\delta}$, and $\text{BaMnO}_{3-\delta}$, as the energy to create a vacancy becomes independent of δ for the larger values of $1/\delta$ considered. A previous DFT+U study, which investigated the thermoelectric properties and vacancy ordering behaviors of $\text{CaMnO}_{3-\delta}$, reported an energy of vacancy formation of 2.09 eV for $\text{CaMnO}_{3-\delta}$.⁵⁶ This differs from our DFT+U results (1.51 eV). The difference is likely to result from a combination of different U values adopted (4 eV v.s. 3.9 eV) and a higher vacancy concentration. For $\text{CaMn}_{0.75}\text{Fe}_{0.25}\text{O}_{3-\delta}$ we were unable to reach the dilute limit using our available computing resources. Despite this, the results at $1/\delta = 32$ appear sufficient to establish the trend in the

material's ability to donate oxygen as a CLOU substrate. Averaging the energy of vacancy formation of Site 1 and 3 in $\text{CaMn}_{0.75}\text{Fe}_{0.25}\text{O}_{3-\delta}$ at $1/\delta = 32$ results in a value of 1.43 eV using DFT, and 0.17 eV using DFT+U. The results in Figure 2.6 indicate that $\text{CaMnO}_{3-\delta}$ will donate oxygen more readily than $\text{BaMnO}_{3-\delta}$, as it has a substantially lower vacancy formation energy. This agrees with the results found in the experimental literature²⁸. The trend is the same regardless of the oxygen type chosen for $\text{CaMnO}_{3-\delta}$, as they are almost identical. While the dopants are different, it is expected that a B-site dopant will have a larger effect than an A-site dopant on the energy of vacancy formation, due to its greater interaction with oxygen. Our results indicate that the materials considered can be ranked, in terms of the thermodynamic ease of oxygen donation, as $\text{CaMn}_{0.75}\text{Fe}_{0.25}\text{O}_{3-\delta} > \text{Ca}_{0.75}\text{Sr}_{0.25}\text{MnO}_{3-\delta} > \text{CaMnO}_{3-\delta} > \text{BaMnO}_{3-\delta}$. This trend remains the same with and without the use of the Hubbard U correction. With the results from DFT+U at the largest supercell size, we have shown the predicted equilibrium P_{O_2} range during reduction and oxidation for these four materials in Figure A.4, for comparison with Figure 2.1b. This further illustrates that vacancy formation energy will predict equilibrium P_{O_2} trends.

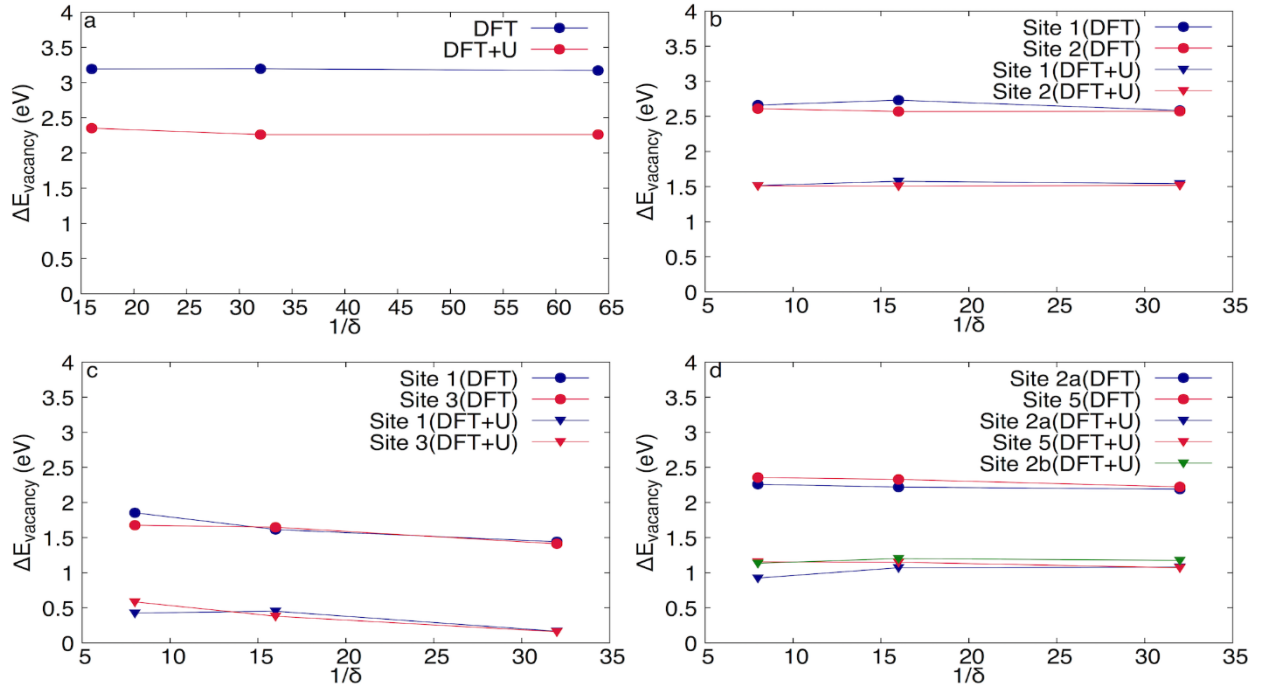


Figure 2.6: Energy of vacancy creation for versus $1/\delta$ for a) BaMnO_{3-δ}, b) CaMnO_{3-δ}, c) CaMn_{0.75}Fe_{0.25}O_{3-δ}, and d) Ca_{0.75}Sr_{0.25}MnO_{3-δ}.

2.4.4 Effect of the Hubbard U on Vacancy Creation Energies and Their Rankings

The Hubbard U correction, which compensates for the limitations of DFT in describing highly correlated transition metals where exact exchange is an issue⁴⁸, can impact the values of the oxygen vacancy formation energy, as shown in the previous sections. As shown in Figure 2.6, implementation of Hubbard U results in lowered vacancy formation energy by 0.94 – 1.26 eV compared to DFT without U in all cases. This implies that DFT and DFT+U may lead to similar results in terms of relative differences in vacancy formation energies between the oxygen carrier materials investigated. Since predicting the ease of oxygen release on a relative basis would be very useful for oxygen carrier screening and optimization purposes, it is possible that such information, which is correlated with the difference in vacancy formation energy, can be well approximated from DFT without U correction. While the U correction can still provide more accurate results on the absolute values of the vacancy creation energy, the ability to efficiently

determine the *relative* performance of oxygen carriers without U can be advantageous from a material-screening standpoint. This section aims to determine whether: a) the trend of vacancy creation energies versus material is unaffected by implementation of Hubbard U and/or b) the relative difference in vacancy creation energies between materials is larger than the possible errors associated with not using a material/site specific Hubbard U. There are different approaches in the literature to estimate the Hubbard U parameter, including the linear response method^{59,60}, fitting to experimental heats of formation⁶¹, and using a higher level of ab-initio theory where exact exchange is included^{62,63}. In this study we used Hubbard U values reported by the Materials Project, which are non site-specific⁴⁹. The method used by Materials Project fit enthalpies of oxidation for binary oxides using U as the fitting parameter, according to Wang et al.⁶¹ This method was also utilized in other studies^{64,65}. Figure 2.7a shows the energy of vacancy formation calculated using the largest supercell (320 atoms for BaMnO_{3-δ}, and 160 atoms for Ca_{0.75}Sr_{0.25}MnO_{3-δ}, CaMn_{0.75}Fe_{0.25}O_{3-δ}, CaMnO_{3-δ}) using both DFT and DFT+U. As shown in the figure, both DFT and DFT+U predict decreasing vacancy creation energy for Ca_{0.75}Sr_{0.25}MnO_{3-δ}, CaMn_{0.75}Fe_{0.25}O_{3-δ}, CaMnO_{3-δ}, and BaMnO_{3-δ}. The minimum difference between two materials in vacancy creation energy for the DFT+U results was 0.37 eV (CaMnO_{3-δ} and Ca_{0.75}Sr_{0.25}MnO_{3-δ}). While the choice of Hubbard U value may lead to a change in the predicted trend of vacancy creation energy versus material, our results indicate that this would require a relatively large change in Hubbard U. We found this by carrying out a sensitivity analysis (shown in Appendix A and Figure A.1), examining the change in vacancy creation energy upon a change in Hubbard U. This indicated that a change in ranking would occur when the U value is varied by more than 1 eV. Such a large uncertainty in the U value is highly unlikely. For instance, the U values for CaMnO₃, BaMnO₃, and SrMnO₃ were determined to be 3.0, 2.7, and 2.8 as reported in a previous literature based on PBEsol+U

fitted with higher level of ab-initio theories (including exact exchange)⁶⁶. This shows that the ranking of metal oxides for oxygen vacancy creation energy is unlikely to be sensitive to the implementation of the choice of Hubbard U parameter. Figure 2.7b further illustrates the differences in vacancy creation energy using $\text{CaMn}_{0.75}\text{Fe}_{0.25}\text{O}_{3-\delta}$ as the reference material based on both DFT and DFT+U results. This shows that the discrepancies between DFT and DFT+U range between 0.16 and 0.32 eV. Based on these findings, we conclude that either DFT or DFT+U with non site-specific U parameter can be sufficient to determine the relative ease of vacancy formation. This also suggests that we can potentially use DFT without Hubbard U correction for the purpose of comparing the relative redox properties of various oxides.

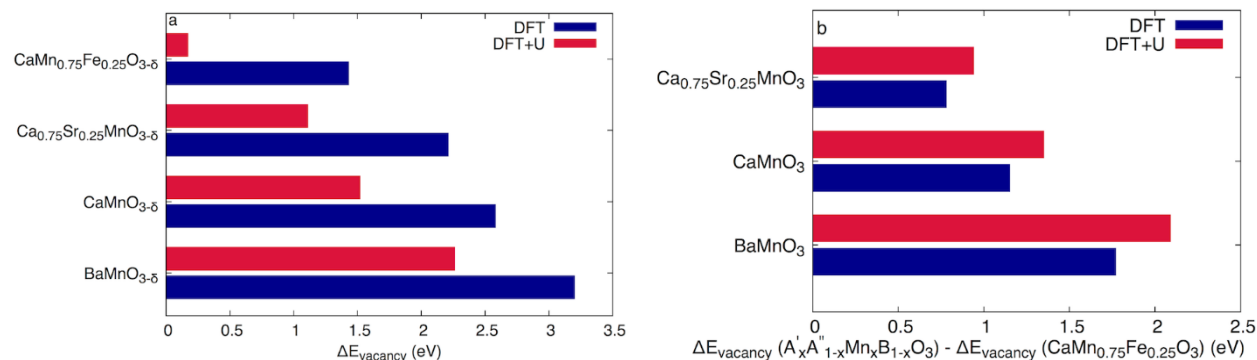


Figure 2.7: a) Energy of Vacancy Formation using the largest supercells and b) the energies with respect to $\text{CaMn}_{0.75}\text{Fe}_{0.25}\text{MnO}_{3-\delta}$ DFT and DFT+U.

2.4.5 Bader Charge Analysis

The ability of the oxide material to redistribute electrons after vacancy formation can correlate to the ease of vacancy formation. Therefore, we examined the amount of electron delocalization after vacancy formation in a 40-atom supercell for $\text{CaMnO}_{3-\delta}$, $\text{CaMn}_{0.75}\text{Fe}_{0.25}\text{O}_{3-\delta}$, and $\text{Ca}_{0.75}\text{Sr}_{0.25}\text{MnO}_{3-\delta}$. Electron delocalization is likely to have an important role in the process of creating an oxygen vacancy. In CaMnO_3 or doped CaMnO_3 materials, there are either four or five cation neighbors making up a cation shell. We determined the change in Bader charge for these

shells, which can serve as a descriptor for electron delocalization, as it is analogous to the oxidation state. For $\text{CaMnO}_{3-\delta}$, there is a single four-cation shell and a single five-cation shell, corresponding to sites 1 and 2. However, for $\text{CaMn}_{0.75}\text{Fe}_{0.25}\text{O}_{3-\delta}$ and $\text{Ca}_{0.75}\text{Sr}_{0.25}\text{MnO}_{3-\delta}$, as discussed above, there are a variety of shells. The amount of delocalization, examined across all the four-cation and-five cation shells, is shown in Figure 2.8. These results show that $\text{CaMn}_{0.75}\text{Fe}_{0.25}\text{O}_{3-\delta}$ has the smallest change in Bader charge in its cation shells, suggesting a large amount of the electron delocalization into the rest of the lattice. $\text{Ca}_{0.75}\text{Sr}_{0.25}\text{MnO}_{3-\delta}$ also has a smaller change in Bader charge, compared to $\text{CaMnO}_{3-\delta}$. From this analysis, we find that the material that better distributes the electron after vacancy formation has a lower vacancy formation energy, with electron delocalization ranked as: $\text{CaMn}_{0.75}\text{Fe}_{0.25}\text{O}_{3-\delta} > \text{Ca}_{0.75}\text{Sr}_{0.25}\text{MnO}_{3-\delta} > \text{CaMnO}_{3-\delta}$. However, the trend is not clear from site to site within a material. This suggests that the ability of a material to delocalize electrons is not a useful descriptor for determining which oxygen site is favorable for vacancy formation, but rather to find which material is more favorable for oxygen vacancy formation in general.

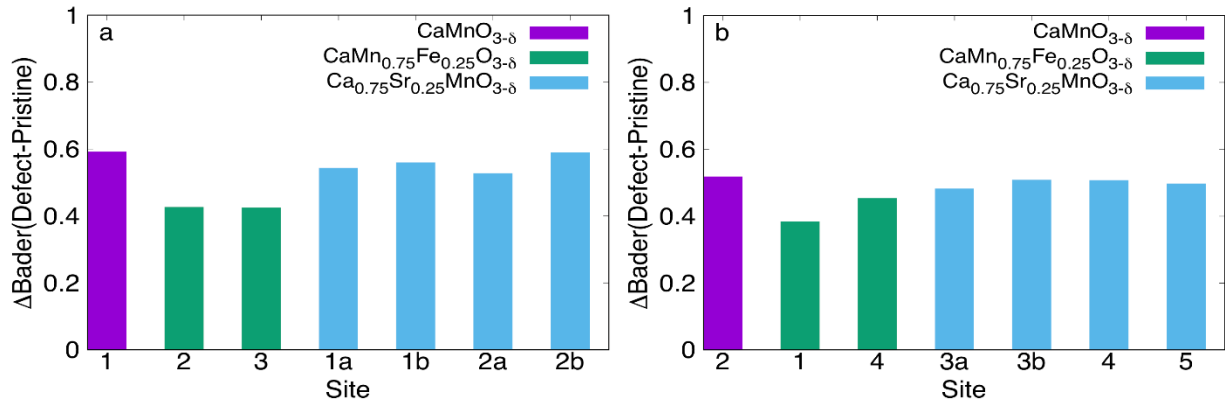


Figure 2.8: Change in Bader Charge, using DFT, after vacancy formation for different cation shells consisting of a) 4 cation and b) 5 cation shells. (40 atom supercell).

2.4.6 Equilibrium Vacancy Concentrations and Char Conversion

The estimated energy of vacancy formation can be used a predictor for the equilibrium vacancy concentration, and effectiveness for char conversion. As previously discussed, we

anticipate oxygen non-stoichiometry to follow the trend of: $\text{CaMn}_{0.75}\text{Fe}_{0.25}\text{O}_{3-\delta} > \text{Ca}_{0.75}\text{Sr}_{0.25}\text{MnO}_{3-\delta} > \text{CaMnO}_{3-\delta}$. Equilibrium oxygen non-stoichiometry on a relative basis (denoted as δ') was experimentally measured in the temperature range of 600-750°C in 25°C increments for two different partial pressures of oxygen (0.01 and 0.025 atm). Additionally, δ' s were experimentally measured under an inert environment (5.0 Argon). Although the oxygen non-stoichiometry (δ') reported in this section is relative to the weight of the sample after oxygen pretreatment, as opposed to an absolute oxygen non-stoichiometry (δ), the trends for δ and δ' are intrinsically consistent since they always differ by the oxygen non-stoichiometry in the pretreated sample, δ_0 . Measurements were only taken at 600, 700, and 750°C due to the long time required for equilibrium values under an inert environment. Oxygen non-stoichiometry for $\text{CaMnO}_{3-\delta}$, $\text{Ca}_{0.75}\text{Sr}_{0.25}\text{MnO}_{3-\delta'}$ and $\text{CaMn}_{0.75}\text{Fe}_{0.25}\text{O}_{3-\delta'}$ are shown for these sets of conditions are shown in Figure 2.9. When δ' is less than 0.023, the oxygen non-stoichiometry follows the order $\text{CaMn}_{0.75}\text{Fe}_{0.25}\text{O}_{3-\delta'} > \text{Ca}_{0.75}\text{Sr}_{0.25}\text{MnO}_{3-\delta'} > \text{CaMnO}_{3-\delta}$. When δ' is above 0.023, however, the oxygen non-stoichiometry follows $\text{Ca}_{0.75}\text{Sr}_{0.25}\text{MnO}_{3-\delta'} > \text{CaMn}_{0.75}\text{Fe}_{0.25}\text{O}_{3-\delta'} > \text{CaMnO}_{3-\delta}$. These results show that oxygen vacancy creation energy is correlated with the oxygen non-stoichiometry found in these experiments at lower values of δ' . This corresponds to conditions where the temperature or oxygen partial pressure is relatively low. With increasing temperature or decreasing oxygen partial pressure, however, the energy of vacancy formation becomes less accurate as a predictor for a material's oxygen uncoupling ability. This can occur for a number of reasons: the assumption of a neutral oxygen vacancy, a breakdown of the approximation of infinite vacancy dilution, as well as entropic effects becoming significant at higher temperatures. Experimental literature has shown that there is higher configurational entropy in Sr-substituted $\text{CaMnO}_{3-\delta}$ vs. $\text{CaMnO}_{3-\delta}$.⁶⁷

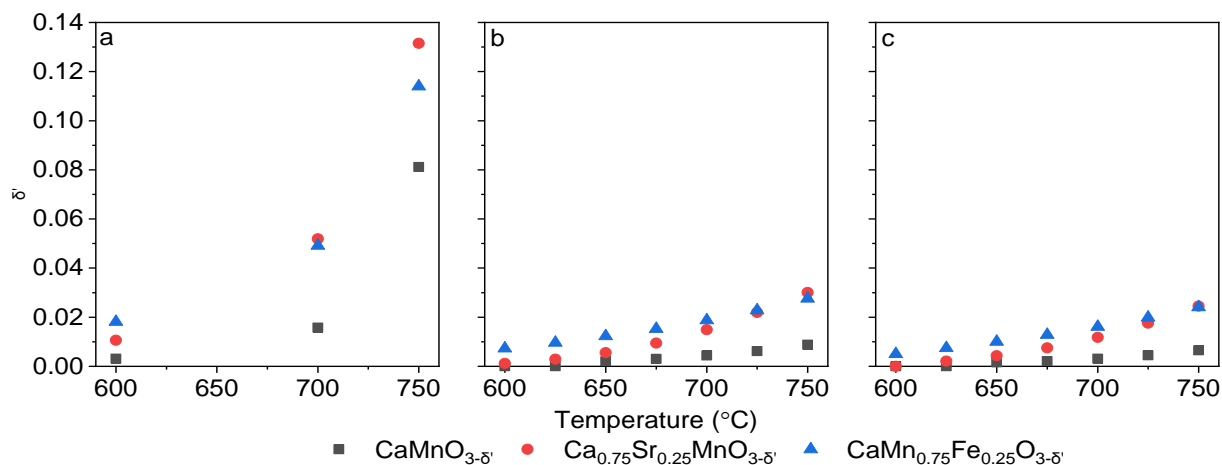


Figure 2.9: δ' for $\text{CaMnO}_{3-\delta}$, $\text{Ca}_{0.75}\text{Sr}_{0.25}\text{MnO}_{3-\delta}$, and $\text{CaMn}_{0.75}\text{Fe}_{0.25}\text{O}_{3-\delta}$ using a) inert, b) $P_{\text{O}_2} = 0.01$ atm, and c) $P_{\text{O}_2} = 0.025$ atm in temperature range of 600-750°C.

Nonetheless, these results predict that both Sr and Fe dopants will lead to enhanced CLOU properties and hence char conversion. Results from char conversion experiments on $\text{CaMnO}_{3-\delta}$, $\text{CaMn}_{0.75}\text{Fe}_{0.25}\text{O}_{3-\delta}$, and $\text{CaMn}_{0.95}\text{Fe}_{0.05}\text{O}_{3-\delta}$, with further details provided in our previous publications,^{28,29} are summarized in Figure 2.10. A lower Fe doping level was used since $\text{CaMn}_{0.95}\text{Fe}_{0.05}\text{O}_{3-\delta}$ exhibited similar redox properties as $\text{CaMn}_{0.75}\text{Fe}_{0.25}\text{O}_{3-\delta}$ based on experimental studies²⁹. The CO_2 yield is defined as the char conversion multiplied by the CO_2 selectivity. Both Sr and Fe doping resulted in an increase in char conversion and CO_2 yield compared to the undoped samples. These results correlate well with the lower oxygen vacancy creation energy for the Sr and Fe doped samples. Although char conversion and CO_2 yield is affected by various factors in addition to oxygen vacancy creation energy, this qualitative comparison demonstrates the usefulness of oxygen vacancy creation energies in predicting an oxygen carriers' char conversion capability. This indicates that a reduced vacancy formation energy correlates with faster oxygen release from these oxides. These results suggest that the energy of vacancy formation at the dilute limit derived from DFT is a useful descriptor to rank materials for CLOU applications. This is true even when the Hubbard U parameter is not applied and our simplified description of a vacancy

site is applied to doped structures. A more accurate prediction of the energy of vacancy creation at higher temperatures is possible by using phonon calculations or experimental methods, as in previous studies.⁶⁷ However, these calculations and experimental studies are beyond the scope of the present investigation.

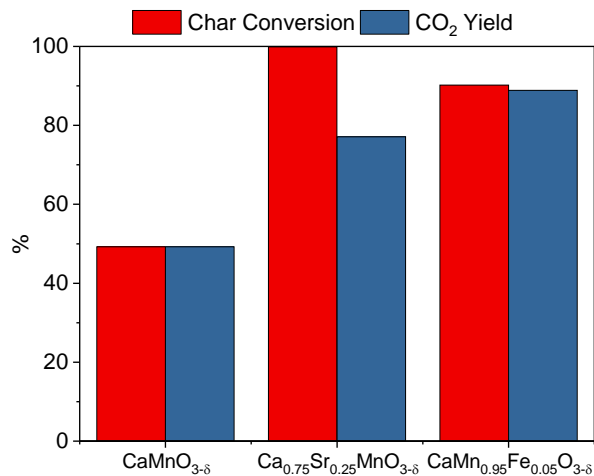


Figure 2.10: Results from char conversion experiments at 850°C from the 5th cycle.

2.4.7 Structural Characterization

In addition to predicting relative CLOU performance, vacancy formation calculations are expected to predict the volume expansion due to formation of vacancies. *In-Situ* XRD was used to investigate the volume expansion for CaMnO_{3-δ}, Ca_{0.75}Sr_{0.25}MnO_{3-δ}, and CaMn_{0.75}Fe_{0.25}O_{3-δ} at 750°C using 2.5% O₂, 1% O₂, and inert environments. The unit cell volume is expected to increase with decreasing oxygen concentration, through the formation of vacancies. A combination of these results and TGA can provide a volume expansion per non-stoichiometric unit. To eliminate the effect of thermal expansion, comparisons were made for oxides with different oxygen vacancy concentrations under isothermal conditions. Figure 2.11 shows the results of *in-situ* XRD, highlighting the peaks with largest intensity (around 33.5, 48, and 60°). It is clear from the figure

that any peak shift that occurs by switching from 2.5% to 1% O₂ is extremely slight, with the peak shift from switching from 1% O₂ to inert being significantly more noticeable. The lattice parameters for these calculations are shown in Tables A.9-A.14.

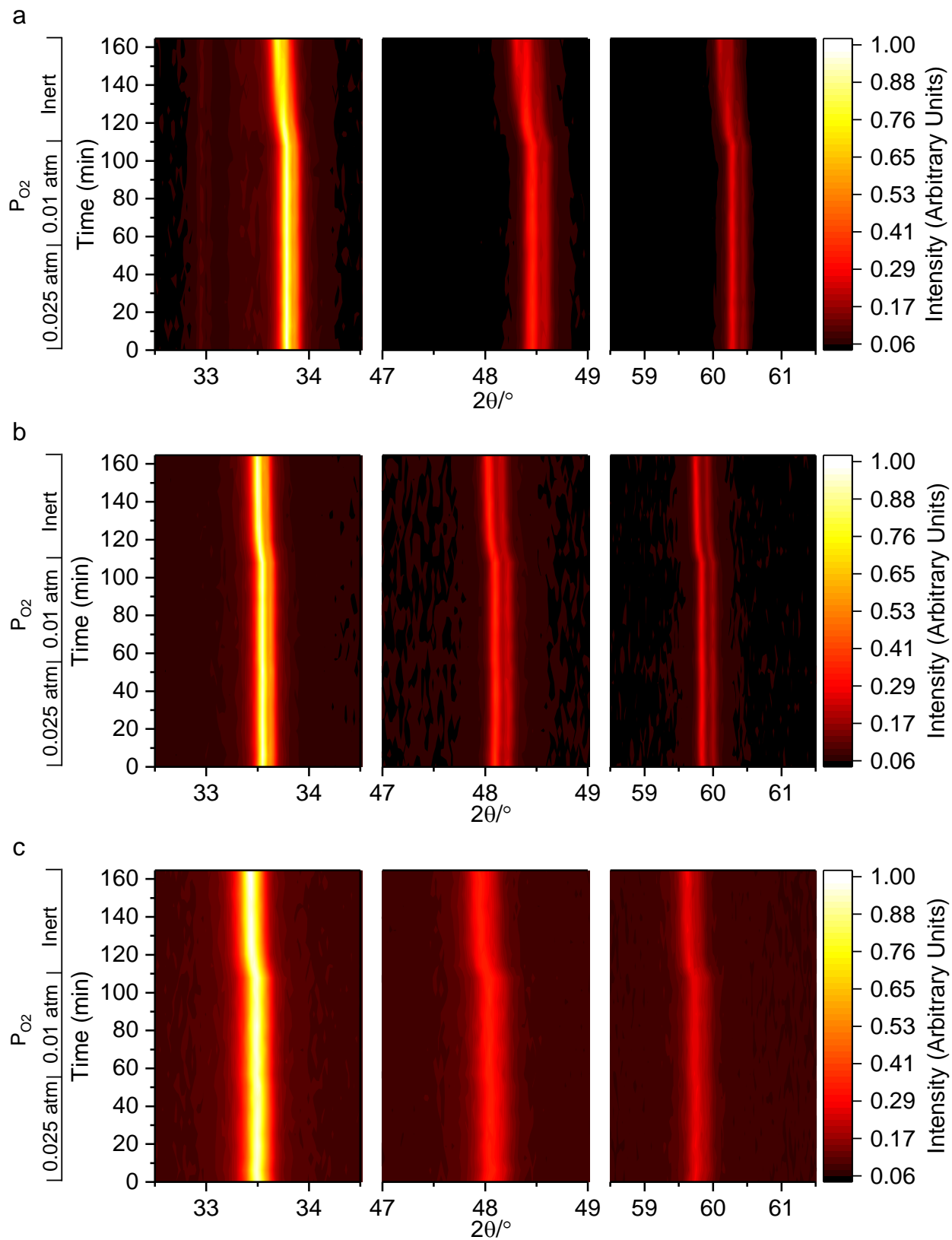


Figure 2.11: Results of in-Situ XRD for a) CaMnO_3 , b) $\text{CaMn}_{0.75}\text{Fe}_{0.25}\text{O}_3$, and c) $\text{Ca}_{0.75}\text{Sr}_{0.25}\text{MnO}_3$. 2θ ranges of $32.5\text{-}34.5^\circ$, $47\text{-}49^\circ$, and $58.5\text{-}61.5^\circ$ are shown. $0.025\text{ atm } P_{\text{O}_2}$, $0.01\text{ atm } P_{\text{O}_2}$, and Inert environments are applied for 56 minutes each at 750°C .

Since both TGA and *in-situ* XRD showed slight differences between 1% and 2.5% O₂ environments, they were averaged and used as the reference value in calculating volume expansion per unit δ upon switching to the inert environment. The experimental volume expansion is shown in Figure 2.12 together with the volume expansion found from our DFT calculations with a 40-atom unit cell. Energetically favorable oxygen sites for vacancy formation were the only ones considered. Each site was weighted equally in calculating the volume expansion. Both DFT and experimental results show iron-doping increases volume expansion upon vacancy formation, whereas strontium suppresses volume expansion. While the discrepancies in quantitative prediction can possibly be resolved using a higher level of theory, these results show that trends can be predicted using PAW pseudopotentials and a PBE exchange correlation functional are again consistent with experimental results. This further highlights the usefulness of the simplified simulation strategy in this study.

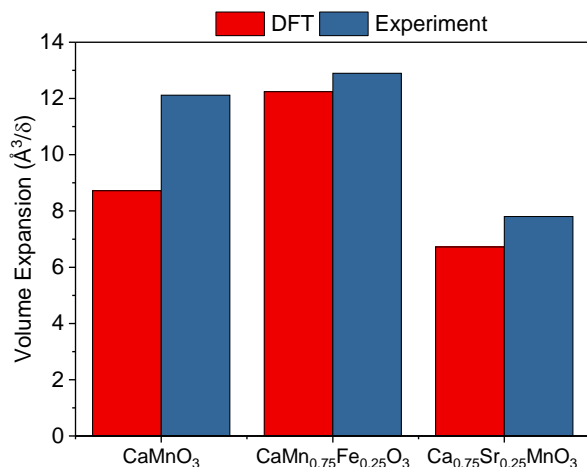


Figure 2.12: Volume expansion normalized by oxygen non-stoichiometry found through both DFT and a combination of TGA and *in-Situ* XRD. A 40-atom unit ($\delta = 0.125$) was used for DFT calculations and experimental data at 750°C was used.

2.5 Conclusions

Chemical looping with oxygen uncoupling (CLOU) offers the potential for efficient combustion of coal with *in-situ* carbon dioxide capture. Metal oxide based oxygen carrier design is a key aspect of this process. This study aimed to correlate oxygen vacancy creation energy with oxygen uptake and release properties for a number of Mn-containing oxygen carriers, i.e. BaMnO₃, CaMnO₃, Ca_{0.75}Sr_{0.25}MnO₃, and CaMn_{0.75}Fe_{0.25}O₃. In addition to showing this correlation, key findings were made in regard to the effect of Hubbard U and coordination environment on oxygen vacancy creation energy. Results showed that, while incorporating the Hubbard U correction can increase the accuracy of the vacancy creation energy calculations when compared to regular DFT, it did not significantly change the energies relative to each other among the mixed oxides investigated. As such, relative ranking of vacancy creation energy among these materials was unaffected by inclusion of Hubbard U. Specifically, the energy of vacancy formation follows this trend: BaMnO₃ > CaMnO₃ > Ca_{0.75}Sr_{0.25}MnO₃ > CaMn_{0.75}Fe_{0.25}O₃. Experimental results indicate that this ranking was effective for indicating oxygen donation properties in CLOU, with lower vacancy creation energies leading to increased oxygen release (change in oxygen non-stoichiometry for a given decrease in P_{O2} and/or increase in temperature) and higher activity for char combustion. For instance, thermogravimetric experiments confirm the abovementioned trend in oxygen carrying capacity, when the oxygen non-stoichiometry (δ') is less than 0.023. Furthermore, fluidized bed experiments at 850°C showed an increase in oxygen donation and coal char conversion upon doping of CaMnO₃ with Sr or Fe, confirming that the energy of vacancy formation can be a useful indicator for mixed oxides' CLOU capabilities, specifically oxygen carrying capacity. The simplified DFT calculation in the current study also accurately predicted

the trends of volume change of the (doped) perovskite oxides upon vacancy formation when compared to experimental results obtained from *in-situ* XRD and TGA.

2.6 References

1. Hansen, J.; Sato, M. Greenhouse Gas Growth Rates. *Proc. Natl. Acad. Sci. U. S. A.* **2004**, *101* (46), 16109–16114.
2. US EPA, E. Inventory of US Greenhouse Gas Emissions and Sinks: 1990-2016. **2018**.
3. Figueroa, J. D.; Fout, T.; Plasynski, S.; McIlvried, H.; Srivastava, R. D. Advances in CO₂ Capture Technology—The U.S. Department of Energy’s Carbon Sequestration Program. *Int. J. Greenh. Gas Control* **2008**, *2* (1), 9–20.
4. Kerr, H. R. Capture and Separation Technology Gaps and Priority Research Needs. *Carbon Dioxide Capture Storage Deep Geol. Form. - Results Co₂ Capture Proj. Vols 1 2 Vol 1 - Capture Sep. Carbon Dioxide Combust. Vol 2 - Geol. Storage* **2005**, 655–660.
5. Li, B.; Duan, Y.; Luebke, D.; Morreale, B. Advances in CO₂ Capture Technology: A Patent Review. *Appl. Energy* **2013**, *102*, 1439–1447.
6. Wang, M.; Joel, A. S.; Ramshaw, C.; Eimer, D.; Musa, N. M. Process Intensification for Post-Combustion CO₂ Capture with Chemical Absorption: A Critical Review. *Appl. Energy* **2015**, *158*, 275–291.
7. Abanades, J. C.; Arias, B.; Lyngfelt, A.; Mattisson, T.; Wiley, D. E.; Li, H.; Ho, M. T.; Mangano, E.; Brandani, S. Emerging CO₂ Capture Systems. *Int. J. Greenh. Gas Control* **2015**, *40*, 126–166.
8. Pérez-Vega, R.; Abad, A.; García-Labiano, F.; Gayán, P.; de Diego, L. F.; Adánez, J. Coal Combustion in a 50kWth Chemical Looping Combustion Unit: Seeking Operating Conditions to Maximize CO₂ Capture and Combustion Efficiency. *Int. J. Greenh. Gas Control* **2016**, *50*, 80–92.
9. Demirel, Y.; Matzen, M.; Winters, C.; Gao, X. Capturing and Using CO₂ as Feedstock with Chemical Looping and Hydrothermal Technologies. *Int. J. Energy Res.* **2015**, *39* (8), 1011–1047.
10. Rochelle, G. T. Amine Scrubbing for CO₂ Capture. *Science* **2009**, *325* (5948), 1652–1654.
11. Fan, L.-S. *Chemical Looping Systems for Fossil Energy Conversions*; Wiley, 2011.
12. Boot-Handford, M. E.; Abanades, J. C.; Anthony, E. J.; Blunt, M. J.; Brandani, S.; Dowell, N. M.; Fernández, J. R.; Ferrari, M.-C.; Gross, R.; Hallett, J. P.; et al. Carbon Capture and Storage Update. *Energy Environ. Sci.* **2013**, *7* (1), 130–189.

13. Zhou, Z.; Han, L.; Nordness, O.; Bollas, G. M. Continuous Regime of Chemical-Looping Combustion (CLC) and Chemical-Looping with Oxygen Uncoupling (CLOU) Reactivity of CuO Oxygen Carriers. *Appl. Catal. B Environ.* **2015**, *166–167*, 132–144.
14. Azimi, G.; Mattisson, T.; Leion, H.; Rydén, M.; Lyngfelt, A. Comprehensive Study of Mn–Fe–Al Oxygen-Carriers for Chemical-Looping with Oxygen Uncoupling (CLOU). *Int. J. Greenh. Gas Control* **2015**, *34*, 12–24.
15. Haribal, V. P.; Neal, L. M.; Li, F. Oxidative Dehydrogenation of Ethane under a Cyclic Redox Scheme – Process Simulations and Analysis. *Energy* **2017**, *119*, 1024–1035.
16. Gayan, P.; Adanez-Rubio, I.; Abad, A.; de Diego, L. F.; Garcia-Labiano, F.; Adanez, J. Development of Cu-Based Oxygen Carriers for Chemical-Looping with Oxygen Uncoupling (CLOU) Process. *Fuel* **2012**, *96* (1), 226–238.
17. Abad, A.; Adanez-Rubio, I.; Gayan, P.; Garcia-Labiano, F.; de Diego, L. F.; Adanez, J. Demonstration of Chemical-Looping with Oxygen Uncoupling (CLOU) Process in a 1.5 KW(Th) Continuously Operating Unit Using a Cu-Based Oxygen-Carrier. *Int. J. Greenh. Gas Control* **2012**, *6*, 189–200.
18. Mattisson, T.; Leion, H.; Lyngfelt, A. Chemical-Looping with Oxygen Uncoupling Using CuO/ZrO₂ with Petroleum Coke. *Fuel* **2009**, *88* (4), 683–690.
19. Mattisson, T. Materials for Chemical-Looping with Oxygen Uncoupling. *Int. Sch. Res. Not.* **2013**, *2013*, e526375.
20. Azimi, G.; Leion, H.; Mattisson, T.; Lyngfelt, A. Chemical-Looping with Oxygen Uncoupling Using Combined Mn-Fe Oxides, Testing in Batch Fluidized Bed. *Energy Procedia* **2011**, *4*, 370–377.
21. Azimi, G.; Leion, H.; Rydén, M.; Mattisson, T.; Lyngfelt, A. Investigation of Different Mn–Fe Oxides as Oxygen Carrier for Chemical-Looping with Oxygen Uncoupling (CLOU). *Energy Fuels* **2013**, *27* (1), 367–377.
22. Shafiefarhood, A.; Stewart, A.; Li, F. Iron-Containing Mixed-Oxide Composites as Oxygen Carriers for Chemical Looping with Oxygen Uncoupling (CLOU). *Fuel* **2015**, *139*, 1–10.
23. Arjmand, M.; Hedayati, A.; Azad, A.-M.; Leion, H.; Ryden, M.; Mattisson, T. Ca_xLa_{1-x}Mn_{1-y}MY₃O_{3-δ} (M = Mg, Ti, Fe, or Cu) as Oxygen Carriers for Chemical-Looping with Oxygen Uncoupling (CLOU). *Energy Fuels* **2013**, *27* (8), 4097–4107.
24. Taylor, D. D.; Schreiber, N. J.; Levitas, B. D.; Xu, W.; Whitfield, P. S.; Rodriguez, E. E. Oxygen Storage Properties of La_{1-x}Sr_xFeO_{3-δ} for Chemical-Looping Reactions—An In Situ Neutron and Synchrotron X-Ray Study. *Chem. Mater.* **2016**, *28* (11), 3951–3960.

25. Lau, C. Y.; Dunstan, M. T.; Hu, W.; Grey, C. P.; Scott, S. A. Large Scale in Silico Screening of Materials for Carbon Capture through Chemical Looping. *Energy Environ. Sci.* **2017**, *10* (3), 818–831.
26. Muhich, C. L.; Ehrhart, B. D.; Witte, V. A.; Miller, S. L.; Coker, E. N.; Musgrave, C. B.; Weimer, A. W. Predicting the Solar Thermochemical Water Splitting Ability and Reaction Mechanism of Metal Oxides: A Case Study of the Hercynite Family of Water Splitting Cycles. *Energy Environ. Sci.* **2015**, *8* (12), 3687–3699.
27. Maiti, D.; Hare, B. J.; Daza, Y. A.; Ramos, A. E.; Kuhn, J. N.; Bhethanabotla, V. R. Earth Abundant Perovskite Oxides for Low Temperature CO₂ Conversion. *Energy Environ. Sci.* **2018**.
28. Galinsky, N.; Mishra, A.; Zhang, J.; Li, F. Ca_{1-x}A_xMnO₃ (A = Sr and Ba) Perovskite Based Oxygen Carriers for Chemical Looping with Oxygen Uncoupling (CLOU). *Appl. Energy* **2015**, *157*, 358–367.
29. Galinsky, N.; Sendi, M.; Bowers, L.; Li, F. CaMn_{1-x}B_xO_{3-δ} (B = Al, V, Fe, Co, and Ni) Perovskite Based Oxygen Carriers for Chemical Looping with Oxygen Uncoupling (CLOU). *Appl. Energy* **2016**, *174*, 80–87.
30. Hallberg, P.; Jing, D.; Rydén, M.; Mattisson, T.; Lyngfelt, A. Chemical Looping Combustion and Chemical Looping with Oxygen Uncoupling Experiments in a Batch Reactor Using Spray-Dried CaMn_{1-x}M_xO_{3-δ} (M = Ti, Fe, Mg) Particles as Oxygen Carriers. *Energy Fuels* **2013**, *27* (3), 1473–1481.
31. Kresse, G.; Joubert, D. From Ultrasoft Pseudopotentials to the Projector Augmented-Wave Method. *Phys. Rev. B* **1999**, *59* (3), 1758–1775.
32. Blöchl, P. E. Projector Augmented-Wave Method. *Phys. Rev. B* **1994**, *50* (24), 17953–17979.
33. Perdew, J. P.; Burke, K.; Ernzerhof, M. Generalized Gradient Approximation Made Simple. *Phys. Rev. Lett.* **1996**, *77* (18), 3865–3868.
34. Kresse, G.; Furthmüller, J. Efficient Iterative Schemes for Ab Initio Total-Energy Calculations Using a Plane-Wave Basis Set. *Phys. Rev. B* **1996**, *54* (16), 11169–11186.
35. Kresse, G.; Furthmüller, J. Efficiency of Ab-Initio Total Energy Calculations for Metals and Semiconductors Using a Plane-Wave Basis Set. *Comput. Mater. Sci.* **1996**, *6* (1), 15–50.
36. Kresse, G.; Hafner, J. \textit{Ab Initio} Molecular Dynamics for Liquid Metals. *Phys. Rev. B* **1993**, *47* (1), 558–561.

37. Kresse, G.; Hafner, J. *Ab Initio* Molecular-Dynamics Simulation of the Liquid-Metal/amorphous-Semiconductor Transition in Germanium. *Phys. Rev. B* **1994**, *49* (20), 14251–14269.
38. Kröger, F. A.; Vink, H. J. Relations between the Concentrations of Imperfections in Crystalline Solids. In *Solid State Physics*; Turnbull, F. S. and D., Ed.; Academic Press, 1956; Vol. 3, pp 307–435.
39. Christensen, A. N.; Ollivier, G. Hydrothermal and High-Pressure Preparation of Some BaMnO₃ Modifications and Low-Temperature Magnetic Properties of BaMnO₃(2H). *J. Solid State Chem.* **1972**, *4* (1), 131–137.
40. Melo Jorge, M. E.; Correia dos Santos, A.; Nunes, M. R. Effects of Synthesis Method on Stoichiometry, Structure and Electrical Conductivity of CaMnO_{3-δ}. *Int. J. Inorg. Mater.* **2001**, *3* (7), 915–921.
41. Takeda, Y.; Kanno, K.; Takada, T.; Yamamoto, O.; Takano, M.; Nakayama, N.; Bando, Y. Phase Relation in the Oxygen Nonstoichiometric System, SrFeO_x (2.5 ≤ x ≤ 3.0). *J. Solid State Chem.* **1986**, *63* (2), 237–249.
42. Poepelmeier, K. R.; Leonowicz, M. E.; Scanlon, J. C.; Longo, J. M.; Yelon, W. B. Structure Determination of CaMnO₃ and CaMnO_{2.5} by X-Ray and Neutron Methods. *J. Solid State Chem.* **1982**, *45* (1), 71–79.
43. Reller, A.; Jefferson, D.; Thomas, J.; Beyerlein, R.; Poepelmeier, K. Three New Ordering Schemes for Oxygen Vacancies in CaMnO_{3-x} Superlattices Based on Square-Pyramidal Co-Ordination of Mn³⁺. *J. Chem. Soc. Chem. Commun.* **1982**, *0* (24), 1378–1380.
44. Reller, A.; Jefferson, D. A.; Thomas, J. M.; Uppal, M. K. Oxygen Vacancy Ordering in a Selective Oxidation Catalyst: Calcium Manganese Oxide (CaMnO_{2.8}). *J. Phys. Chem.* **1983**, *87* (6), 913–914.
45. Vidyasagar, K.; Reller, A.; Gopalakrishnan, J.; Ramachandra Rao, C. N. Oxygen Vacancy Ordering in Superlattices of the Two Novel Oxides, La₂Ni₂O₅ and La₂Co₂O₅, Prepared by Low Temperature Reduction of the Parent Perovskites. *J. Chem. Soc. Chem. Commun.* **1985**, *0* (1), 7–8.
46. Kruidhof, H.; Bouwmeester, H. J. M.; v. Doorn, R. H. E.; Burggraaf, A. J. Influence of Order-Disorder Transitions on Oxygen Permeability through Selected Nonstoichiometric Perovskite-Type Oxides. *Solid State Ion.* **1993**, *63–65*, 816–822.
47. Dubinin, S. F.; Loshkareva, N. N.; Teploukhov, S. G.; Sukhorukov, Y. P.; Balbashov, A. M.; Arkhipov, V. E.; Parkhomenko, V. D. Ordering of Oxygen Vacancies in a CaMnO_{3-δ} Perovskite Single Crystal. *Phys. Solid State* **2005**, *47* (7), 1267–1272.

48. Anisimov, V. I.; Zaanen, J.; Andersen, O. K. Band Theory and Mott Insulators: Hubbard U Instead of Stoner I. *Phys. Rev. B* **1991**, *44* (3), 943–954.
49. Jain, A.; Ong, S. P.; Hautier, G.; Chen, W.; Richards, W. D.; Dacek, S.; Cholia, S.; Gunter, D.; Skinner, D.; Ceder, G.; et al. Commentary: The Materials Project: A Materials Genome Approach to Accelerating Materials Innovation. *APL Mater.* **2013**, *1* (1), 011002.
50. Dudarev, S. L.; Botton, G. A.; Savrasov, S. Y.; Humphreys, C. J.; Sutton, A. P. Electron-Energy-Loss Spectra and the Structural Stability of Nickel Oxide: An LSDA+U Study. *Phys. Rev. B* **1998**, *57* (3), 1505–1509.
51. Tang, W.; Sanville, E.; Henkelman, G. A Grid-Based Bader Analysis Algorithm without Lattice Bias. *J. Phys. Condens. Matter* **2009**, *21* (8), 084204.
52. Kakihana, M.; Yoshimura, M. Synthesis and Characteristics of Complex Multicomponent Oxides Prepared by Polymer Complex Method. *Bull. Chem. Soc. Jpn.* **1999**, *72* (7), 1427–1443.
53. Toby, B. H.; Von Dreele, R. B. GSAS-II: The Genesis of a Modern Open-Source All Purpose Crystallography Software Package. *J. Appl. Crystallogr.* **2013**, *46* (2), 544–549.
54. Adkin, J. J.; Hayward, M. A. BaMnO_{3-x} Revisited: A Structural and Magnetic Study. *Chem. Mater.* **2007**, *19* (4), 755–762.
55. Fawcett, I. D.; Sunstrom; Greenblatt, M.; Croft, M.; Ramanujachary, K. V. Structure, Magnetism, and Properties of Ruddlesden–Popper Calcium Manganates Prepared from Citrate Gels. *Chem. Mater.* **1998**, *10* (11), 3643–3651.
56. Molinari, M.; Tompsett, D. A.; Parker, S. C.; Azough, F.; Freer, R. Structural, Electronic and Thermoelectric Behaviour of CaMnO₃ and CaMnO(3- δ). *J. Mater. Chem. A* **2014**, *2* (34), 14109–14117.
57. Nguyen, T. T.; Bach, T. C.; Pham, H. T.; Pham, T. T.; Nguyen, D. T.; Hoang, N. N. Magnetic State of the Bulk, Surface and Nanoclusters of CaMnO₃: A DFT Study. *Phys. B Condens. Matter* **2011**, *406* (19), 3613–3621.
58. Cardoso, C.; Borges, R. P.; Gasche, T.; Godinho, M. Ab-Initio Calculations of the Ruddlesden–Popper Phases CaMnO₃, CaO(CaMnO₃) and CaO(CaMnO₃)₂. *J. Phys. Condens. Matter* **2008**, *20* (3), 035202.
59. Kulik, H. J.; Cococcioni, M.; Scherlis, D. A.; Marzari, N. Density Functional Theory in Transition-Metal Chemistry: A Self-Consistent Hubbard U Approach. *Phys. Rev. Lett.* **2006**, *97* (10), 103001.

60. Cococcioni, M.; de Gironcoli, S. Linear Response Approach to the Calculation of the Effective Interaction Parameters in the LDA+U Method. *Phys. Rev. B* **2005**, *71* (3), 035105.
61. Wang, L.; Maxisch, T.; Ceder, G. Oxidation Energies of Transition Metal Oxides within the $\text{GGA}+\text{U}$ Framework. *Phys. Rev. B* **2006**, *73* (19), 195107.
62. Muñoz-García, A. B.; Ritzmann, A. M.; Pavone, M.; Keith, J. A.; Carter, E. A. Oxygen Transport in Perovskite-Type Solid Oxide Fuel Cell Materials: Insights from Quantum Mechanics. *Acc. Chem. Res.* **2014**, *47* (11), 3340–3348.
63. Mosey, N. J.; Liao, P.; Carter, E. A. Rotationally Invariant Ab Initio Evaluation of Coulomb and Exchange Parameters for DFT+U Calculations. *J. Chem. Phys.* **2008**, *129* (1), 014103.
64. Lee, Y.-L.; Gadre, M. J.; Shao-Horn, Y.; Morgan, D. Ab Initio GGA+U Study of Oxygen Evolution and Oxygen Reduction Electrocatalysis on the (001) Surfaces of Lanthanum Transition Metal Perovskites LaBO_3 (B = Cr, Mn, Fe, Co and Ni). *Phys. Chem. Chem. Phys.* **2015**, *17* (33), 21643–21663.
65. Lee, Y.-L.; Kleis, J.; Rossmeisl, J.; Morgan, D. Ab Initio. *Phys. Rev. B* **2009**, *80* (22), 224101.
66. Hong, J.; Stroppa, A.; Íñiguez, J.; Picozzi, S.; Vanderbilt, D. Spin-Phonon Coupling Effects in Transition-Metal Perovskites: A DFT + U and Hybrid-Functional Study. *Phys. Rev. B* **2012**, *85* (5), 054417.
67. Bulfin, B.; Vieten, J.; Starr, D. E.; Azarpira, A.; Zachäus, C.; Hävecker, M.; Skorupska, K.; Schmücker, M.; Roeb, M.; Sattler, C. Redox Chemistry of CaMnO_3 and $\text{Ca}_{0.8}\text{Sr}_{0.2}\text{MnO}_3$ Oxygen Storage Perovskites. *J. Mater. Chem. A* **2017**, *5* (17), 7912–7919.
68. Van de Walle, C. G.; Neugebauer, J. First-Principles Calculations for Defects and Impurities: Applications to III-Nitrides. *J. Appl. Phys.* **2004**, *95* (8), 3851–3879. <https://doi.org/10.1063/1.1682673>.

Chapter 3: Perovskite-Structured $AMn_xB_{1-x}O_3$ (A = Ca or Ba; B = Fe or Ni) Redox

Catalysts for Partial Oxidation of Methane

3.1 Abstract

Methane is one the simplest and most abundant organic compound on earth¹. Methane reforming offers the versatility to produce value-added fuels and chemicals. Unlike typical reforming processes, which suffer from efficiency losses associated with endothermic reforming reactions and/or oxygen/steam generation, chemical looping reforming (CLR) utilizes redox properties of an oxygen carrier, a.k.a. redox catalyst, to partially oxidize methane into syngas with its lattice oxygen. The reduced redox catalyst is subsequently regenerated with air, providing *in-situ* air separation with minimal energy penalty.

The performance of the CLR process is highly dependent upon the redox catalyst. In the current study, CLR performances and underlying mechanisms for perovskite-structured redox catalysts with a general formula of $AMn_xB_{1-x}O_3$ (A = Ca or Ba; B = Fe or Ni) are reported. $CaMnO_3$ and $BaMnO_3$ perovskites are worth investigating due to their desirable redox properties and relatively low cost. $BaMn_xB_{1-x}O_3$ (B = Fe or Ni) are shown to be more selective and coke-resistant for methane partial oxidation when compared to $CaMn_xB_{1-x}O_3$ (B = Fe or Ni) based redox catalysts. While undoped $BaMnO_3$ exhibited high selectivity towards syngas, addition of B-site dopants such as Ni or Fe leads to higher oxygen carrying capacity without significantly impacting coke-resistance of the redox catalysts. In contrast, nickel doped $CaMnO_3$ is significantly more prone to coke formation. As a low cost and environmentally benign option, a $BaMn_xFe_{1-x}O_3$ based redox catalyst was tested for CLR operations in a fluidized bed reactor. > 95% syngas selectivity was observed with no signs of deactivation over 20 cycles.

3.2 Introduction

Methane is the simplest and one of the most abundant organic compound on earth¹. As an alternative for combustion based approaches, methane reforming offers the advantage to produce value-added fuels and chemicals such as hydrogen, hydrocarbons, and alcohols²⁻⁷. In conventional methane reforming processes, methane is converted to syngas in the presence of gaseous oxidants such as steam, oxygen, and/or carbon dioxide. These processes, however, suffer from efficiency losses due to endothermic steam/CO₂ reforming reactions as well as energy consumption for steam or oxygen generation⁷⁻¹². Therefore, novel process schemes that can reduce such energy penalties are highly desirable from both environmental and process economics viewpoints. Compared to conventional reforming processes, the chemical looping reforming (CLR) strategy offers a unique approach for methane partial oxidation in absence of gaseous oxidant¹³⁻¹⁶. In such a process, a redox-active metal oxide, a.k.a. redox catalyst or oxygen carrier, is used to incorporate gaseous oxygen from the air into its lattice. In a subsequent step, the active lattice oxygen in the redox catalyst is released for methane partial oxidation and syngas generation. Using the redox catalyst as the reaction intermediate, the two-step cyclic process provides *in-situ* air separation with minimal energy penalty. In addition, safety issues encountered with CH₄/O₂ mixture in the conventional methane partial oxidation schemes is avoided.

A critical factor affecting the effectiveness of the CLR scheme is the performance of the redox catalyst. Satisfactory redox catalysts possess high redox activity, long-term chemical and physical stabilities, and excellent syngas selectivity. In addition, they should be cost-effective, environmentally benign, and highly resistant towards coke formation. Lewis & Gilliland explored the use of CuO based redox catalysts for syngas generation nearly 60 years ago. The non-selective nature of CuO, however, resulted in poor syngas selectivity¹⁷. It was not until the early 2000s that

the CLR concept was re-investigated in detail¹⁸. Early studies found Pt doped Ce₂O₃ to be an effective redox catalyst for methane partial oxidation^{19,20}. A number of other CeO₂ containing redox catalysts, including those with Al₂O₃, SiO₂, and MgO supports and mixed cerium oxides with Fe, Mn, Cu, and Ni, were also found to be active and selective²¹. Compared to ceria containing redox catalysts, first row transition metal oxides offer the promise of being less expensive with higher oxygen carrying capacities^{14,15,21–28}. Using NiO based redox catalysts, Proll et al. demonstrated the feasibility of the CLR concept²². Syngas yield in excess of 60% was achieved in a 120 kW_{th} circulating fluidized bed (CFB) reactor. The key challenge with respect to NiO based redox catalysts, however, resides in their toxicity and lack of coke resistance. Mn and Fe based redox catalysts have also been explored^{7,12,14,15,21,23,24,26–28}. In general, supported Mn and Fe oxides are less selective than their NiO counterparts. He et al. reported a composite La_{0.8}Sr_{0.2}FeO₃ supported iron oxide for syngas and hydrogen generation in a two-step redox process with high activity and exceptional H₂ yield^{29,30}. The syngas selectivity for methane partial oxidation; however, was limited to approximately 70%. In their recent studies, Shafiefarhood et al. and Neal et al. investigated a Fe₂O₃@La_xSr_{1-x}FeO₃ core-shell redox catalyst^{31–34}, which achieved 94% syngas selectivity with minimal coke formation. Such a high selectivity was realized through tailoring surface composition of the redox catalyst and careful control of reduction and regeneration conditions.

In addition to first-row transition metal oxides, perovskites with a general formula of ABO₃ offer many unique properties that are potentially suitable for CLR applications. These properties include high oxygen anion (O²⁻) mobility, structural stability, and tunable redox properties. For instance, pure and A-site doped LaFeO₃ and LaMnO₃ have been investigated for methane reforming purposes^{35–40}. These redox catalysts exhibit high syngas selectivity. However, the use

of a rare-earth metal (La) as the primary A-site material as well as poor coke resistance limits their feasibility for commercial applications. In the current study, we report the CLR performances and underlying mechanisms for perovskite materials with a general formula of $AMn_xB_{1-x}O_3$ (A = Ca or Ba; B = Fe or Ni). $CaMnO_3$ and $BaMnO_3$ are both perovskites that are worthwhile investigating because they possess reasonable oxygen carrying capacity and present relatively low cost. Our studies indicate that $CaMnO_3$ based redox catalysts generally exhibits low selectivity. Doping increases selectivity but decreases coke resistance of $CaMnO_3$ based redox catalysts. In the case of nickel doping, this is attributed to surface Ni. To compare, catalysts with a general formula of $BaMn_xB_{1-x}O_3$ (B = Fe or Ni) are determined to be suitable for partial oxidation of methane. In these catalysts, the presence of Fe and Ni dopants are found to enhance the oxygen carrying capacity of the redox catalysts without negatively affecting their coke-resistance. Such redox catalysts are compared to $CaMn_xB_{1-x}O_3$ (B = Fe or Ni) based redox catalysts, which exhibit relatively low syngas selectivity and coke-resistance.

3.3 Experimental

3.3.1 Redox Catalyst Preparation

A sol-gel method was used to prepare the aforementioned perovskites. Stoichiometric amounts of metal nitrates, e.g. $Ba(NO_3)_2$, $Mn(NO_3)_2 \cdot 4H_2O$, and $Ni(NO_3)_2 \cdot 6H_2O$ (Sigma Aldrich), were dissolved in deionized water. Citric acid (CA, Sigma Aldrich) was then added (CA: total cations =2.5) and the solution was heated at 50°C for 30 minutes. This results in a mixed-metal citric acid complex with good dispersion of metal ions. Ethylene glycol (EG, Sigma Aldrich) was then added (EG: CA ratio of 1.5) at 80°C until a gel forms. This gel was dried in an oven at slightly above boiling temperature to remove any moisture. Finally, the sample was sintered at 1200°C for proper phase formation. The samples used in the current study are listed below in Table 3.1.

Table 3.1: Abbreviation of Redox Catalysts.

Catalyst Name	Composition
BM	BaMnO₃
BMN25	BaMn_{.75}Ni_{.25}O₃
BMN50	BaMn_{.5}Ni_{.5}O₃
BMF25	BaMn_{.75}Fe_{.25}O₃
BMF50	BaMn_{.5}Fe_{.5}O₃
CM	CaMnO₃
CMN	CaMn_{.8}Ni_{.2}O₃
CMF	CaMn_{.8}Fe_{.2}O₃

3.3.2 Redox Testing

Initial reactivity studies were conducted in a SETARAM SETSYS Evolution Thermal Gravimetric Analyzer (TGA) with reactant gases delivered from a computer controlled gas-mixing panel. The initial tests were conducted at 900°C. Reduction and oxidation steps were performed in 10% methane (5.0 grade) and 10% oxygen (extra dry grade) respectively with helium (5.0 grade) as the inert gas. The total gas flow rate during these steps was 200 mL/min to remove external mass transfer resistance. Short term redox studies were conducted over 10 cycles with oxidation and reduction steps of 20 minutes followed by 5 minutes of purge. Based on short term redox studies, promising samples were used for long term redox studies and fixed bed redox studies. The long term redox studies used 10 minute reduction and oxidation steps, as such a duration was deemed appropriate based on the short term redox studies. 20 mg of the redox catalyst with a particle size below 150 microns was used for both short and long term studies. A quadrupole mass spectrometer (QMS, MKS Cirrus II) was used to measure the products of the reduction and oxidation steps. A set of calibrations was applied to the signals obtained from the QMS. Production of CO, CO₂, and H₂ was calculated by integrating the calibrated signals of CO and CO₂, and H₂.

CO and CO₂ produced during regeneration of the redox catalyst were used to quantify coke formation. H₂O was calculated using a hydrogen mass balance. Selectivity was calculated using the total amount of CO produced during the reforming step.

Additional redox testing was also conducted in a 4 mm ID u-tube reactor loaded with 100mg of catalyst to simulate a fixed bed. These tests were conducted at 900°C with 100 sccm total gas flow rate. Reduction and oxidation were performed in 10% methane (5.0 grade) and 10% oxygen (extra dry grade), respectively, balanced by helium (5.0 grade) as the inert gas. The reduction time used was 20 minutes and the oxidation time was 10 minutes. These times were determined to be sufficient for a completion of syngas production and removal of any carbon species.

Fluidized bed redox experiments were conducted at 800°C using a reducing gas of 3.2 mL/min methane (5.0 grade) and oxidizing gas of 6.8 mL/min H₂O during cycles 1-15 and 4.7 mL/min during cycles 16-20 H₂O. The carrier gas for both reducing and oxidizing steps was 200 mL/min of N₂.

3.3.3 Sample Characterization

Several characterization techniques were used to analyze the surface, structural, and reactive properties of the redox catalysts. X-ray powder diffraction (XRD) was used to identify the crystalline phases present in each sample. The XRD pattern was obtained using a Rigaku SmartLab X-ray diffractometer with CuK_α ($\lambda = .1542$) radiation operating at 40kV and 44mA. Scanning was conducted in a step-wise approach with a step size of 0.1° over 2 θ range of 20–80° and a scan time of 4.5s at each step. HighScore Plus[®] software was used for phase matching. Surface areas of the samples were determined using a Micromeritics ASAP 2020 physi-chemisorption system with Krypton as the adsorption gas.

X-Ray photoelectron spectroscopy (XPS) was used to analyze surface compositions and oxidation states of fresh and reduced samples. Reduced samples were prepared using a 2 cycle redox experiment with hydrogen as the reducing gas (5.0 Grade). Methane was not used as carbon deposition can affect surface measurements. The XPS system consists of a Thermo-Fisher Alpha 110 hemispherical energy analyzer, a Thermo-Fischer XR3, 300W dual-anode X-Ray source, and a chamber with a base pressure of 1×10^{-9} torr. Survey spectra used a pass of 100eV, and narrow scan spectra are taken with a pass energy of 20eV. A Mg anode was used for all analysis.

Hydrogen (5.0 Grade) TPR was conducted using a TGA (TA SDT Q600) with 20% hydrogen balance helium or argon (5.0 grade) at a total flowrate of 200 sccm and a ramp rate of 10°C/min to 900°C. Temperature programmed desorption (TPD) was conducted in the same TGA in either helium or argon (5.0 grade) at a ramping rate of 5°C/min to 900°C from 100°C. The weight and differential thermogravimetry (DTG) of the redox catalyst was measured to determine the amount of oxygen release. The sample was pre-treated with 20% oxygen at 900°C as well as during cooling to 100°C.

3.4 Results and Discussion

3.4.1 Fresh Sample Characterizations

Resulting from the high temperature sintering step, all samples exhibited low BET surface areas. For instance, surface areas of as-prepared $\text{BaMn}_{0.5}\text{Ni}_{0.5}\text{O}_3$, BaMnO_3 , and CaMnO_3 are 0.85, 0.76, and 1.22 m^2/g , respectively. XRD spectra of as-prepared samples are shown in Figure 3.1. Since the crystal structures for most of the doped samples are not available in the database, comparing XRD patterns of doped BaMnO_3 and CaMnO_3 redox catalysts with pure BaMnO_3 and CaMnO_3 can provide initial evidences of doping effect.

Table 3.2 presents the primary and secondary phases determined by fitting the XRD spectra using the HighScore[®] software. Secondary phases are those associated with peaks that cannot be fully accounted for by the primary peaks, although they often provide worse fit with XRD spectra than primary phases. We note that XRD spectra for most doped samples investigated in the current study are not included in the database. Therefore, less than perfect fittings are often observed. Iron doped BaMnO₃ redox catalysts have the best match with BaMn_{0.7}Fe_{0.3}O₃. This indicates that iron dopants successfully integrated into the BaMnO₃ parent structure. In the case of nickel doped BaMnO₃, most of the peaks were associated with BaMnO₃. Unidentified peaks were also seen at $2\theta \approx 28^\circ$ and 31° . They are likely to result from Ni doping in the BaMnO₃ parent structure since crystal structure of the doped sample is not available in the database. The slight shift of 2θ angles when compared to undoped BaMnO₃ also indicates the incorporation of a fraction of Ni cation into the perovskite structure. However, some of the remaining peaks, albeit insignificant, were associated with NiO, suggesting Ni cations were not fully integrated into the nickel doped redox catalysts. This, however, does not affect the use of the resulting oxide as redox catalysts for CLR.

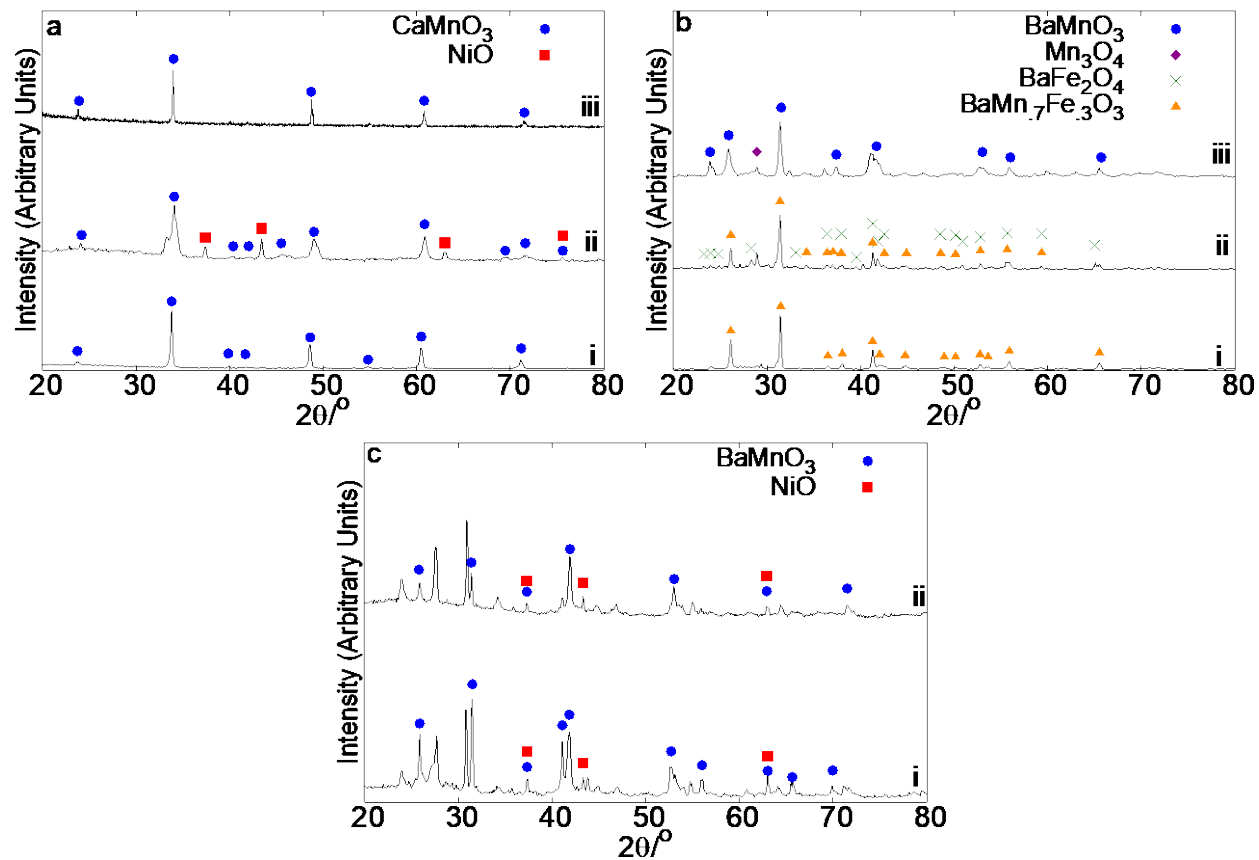


Figure 3.1: XRD Spectra of (a) i. CMF and ii. CMN iii CM; (b). i. BMF25 ii. BMF50 and iii. BM; (c) i. BMN25 and ii. BMN50.

Table 3.2: Phase compositions identified in as-prepared redox catalysts

Catalyst	Primary Phase	Secondary Phase
BMN25	BaMnO ₃	NiO
BMN50	BaMnO ₃	NiO
BMF25	BaMn ₇ Fe ₃ O ₃	None
BMF50	BaMn ₇ Fe ₃ O ₃	BaFe ₂ O ₄
BM	BaMnO ₃	None
CMN	CaMnO ₃	NiO
CMF	CaMnO ₃	None
CM	CaMnO ₃	None

3.4.2 Material Screening

Initial characterization of the redox catalysts was conducted by exposing them for 10 redox cycles using the TGA under a differential bed mode. Since the bulk and surface properties of the redox catalysts can change during redox reactions, redox catalysts can exhibit multiple reaction stages when reacted with methane, as reported by Neal et al.^{31,33,34} Figure 3.2 shows product gas concentration profiles as a function of time for both $\text{CaMn}_{0.8}\text{Ni}_{0.2}\text{O}_3$ and $\text{BaMn}_{0.75}\text{Ni}_{0.25}\text{O}_3$. As can be seen, $\text{CaMn}_{0.8}\text{Ni}_{0.2}\text{O}_3$ exhibited a reaction scheme that is notably different that of the $\text{BaMn}_{0.75}\text{Ni}_{0.25}\text{O}_3$ redox catalyst. For $\text{CaMn}_{0.8}\text{Ni}_{0.2}\text{O}_3$, concurrent production of CO and CO₂ was first observed as the redox catalyst is reduced. This was followed by significant coke formation as evidenced by a significant increase of H₂/(CO+CO₂) ratio and sample weight gain shown by the TGA. Coke formation was also confirmed by the significant amount of CO₂ formed during the oxidation stage, as shown in Figure 3.2a. In comparison, $\text{BaMn}_{0.75}\text{Ni}_{0.25}\text{O}_3$ exhibited high CO₂ selectivity at the beginning of the reaction, as evidenced by the small CO₂ peak. This is followed with an “auto-activation” region with high syngas selectivity. Unlike $\text{CaMn}_{0.8}\text{Ni}_{0.2}\text{O}_3$, coke formation was minimal during the methane- $\text{BaMn}_{0.75}\text{Ni}_{0.25}\text{O}_3$ reaction.

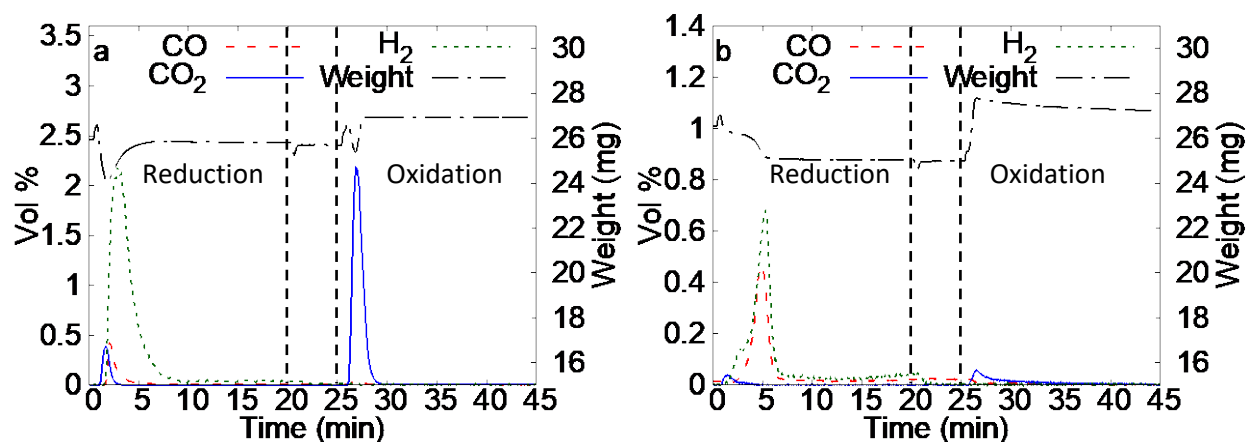


Figure 3.2: Product distributions from typical redox cycles of a) $\text{CaMn}_{0.8}\text{Ni}_{0.2}\text{O}_3$ and b) $\text{BaMn}_{0.75}\text{Ni}_{0.25}\text{O}_3$.

Figure 3.3a summarizes the selectivity to CO (S_{CO}), as defined as $\frac{100 \cdot \sum CO (reduction)}{\sum CO_x (reduction)}$, for all the redox catalysts. It can be seen that BaMnO₃ doped samples outperformed CaMnO₃ doped samples. This suggests that a BaMnO₃ parent structure promoted selective oxidation of CH₄ to CO. In addition, the effect of dopant on syngas selectivity was not significant for BaMnO₃ based redox catalysts. For instance, BaMnO₃ shows a CO selectivity of 90%. All nickel doped samples exhibited selectivity of 93% ± 0.5%. In comparison, iron doped samples exhibited a selectivity of 95.2% ± 0.5%. The insignificant effect of Ni/Fe doping can be explained provided that the catalyst surface is enriched with A-site metal cations. Such a phenomena was reported for BaZrO₃, where a preferential surface aggregation of Ba was observed.⁴¹ Further discussion of dopant effects on surface and bulk properties of the redox catalyst is provided in section 3.4.3. It is also noted that the presence of Ni and Fe dopants had more pronounced effects on the selectivity of redox catalysts with a CaMnO₃ parent structure. For instance, CaMnO₃ samples with Ni and Fe dopants exhibited over 20% higher selectivity when compared with the undoped sample. This can be explained by the formation of reduced Ni or Fe phase on the surface of the CaMnO₃ oxides. The presence of metallic Ni or Fe phases, which are known to be active for methane activation, can lead to improved syngas selectivity. A similar effect has been reported for Pt doped CaTiO₃ catalyst for CO oxidation.⁴² Iron doped BaMnO₃, however, showed the highest selectivity (~95%) and exhibited properties that are desirable over a pure BaMnO₃ catalyst. Figure 3.3b summarizes the yield of CO, expressed as: $\frac{\sum_{reduction} CO (mmole)}{Catalyst\ weight (g)}$. Even though the selectivity of the BaMn_xB_{1-x}O₃ redox catalysts remained relatively unchanged with Ni or Fe doping, the yield of CO increased with doping. The increase in CO yield resulted from increased amount of active lattice oxygen from the doped catalyst. In fact, Ni and Fe dopants can destabilize the BaMnO₃ parent structure,

thereby increasing the amount of usable lattice oxygen. Iron doping, in particular, exhibited this effect: $\text{BaMn}_{0.75}\text{Fe}_{0.25}\text{O}_3$ and $\text{BaMn}_{0.5}\text{Fe}_{0.5}\text{O}_3$ showed the highest CO yields.

Besides CO selectivity, resistance towards coke formation represents another important performance parameter for redox catalysts. The amount of coke formation is determined by integrating the amount of CO and CO_2 formed during the oxidation of reduced redox catalyst. Since coke formation tends to occur upon depletion of active lattice oxygen³¹, each catalyst is reduced for 20 minutes to allow complete reduction and to determine the maximum coke formation. Figure 3.4 summarizes the amount of coke formation for the redox catalysts investigated in the current study. When compared to MgAl_2O_4 supported Fe and Ni oxides which exhibit > 430 mg/g catalyst coke formation⁴³, all the perovskite based redox catalysts exhibited significantly improved coke-resistance. Dopant effect on catalyst coke-resistance exhibited similar trends as that for CO selectivity, i.e. Ni or Fe dopants have insignificant effect on coke-resistance for $\text{BaMn}_x\text{B}_{1-x}\text{O}_3$ based redox catalysts whereas Ni doping in a CaMnO_3 parent structure lead to significantly weakened coke-resistance. This again indicates that A-site metal cation may be enriched on the surface of the redox catalyst for the $\text{BaMn}_x\text{B}_{1-x}\text{O}_3$ system. Overall, $\text{BaMn}_{0.75}\text{Fe}_{0.25}\text{O}_3$ exhibited the highest coke-resistance, forming merely 4 mg of coke on each gram of the redox catalyst.

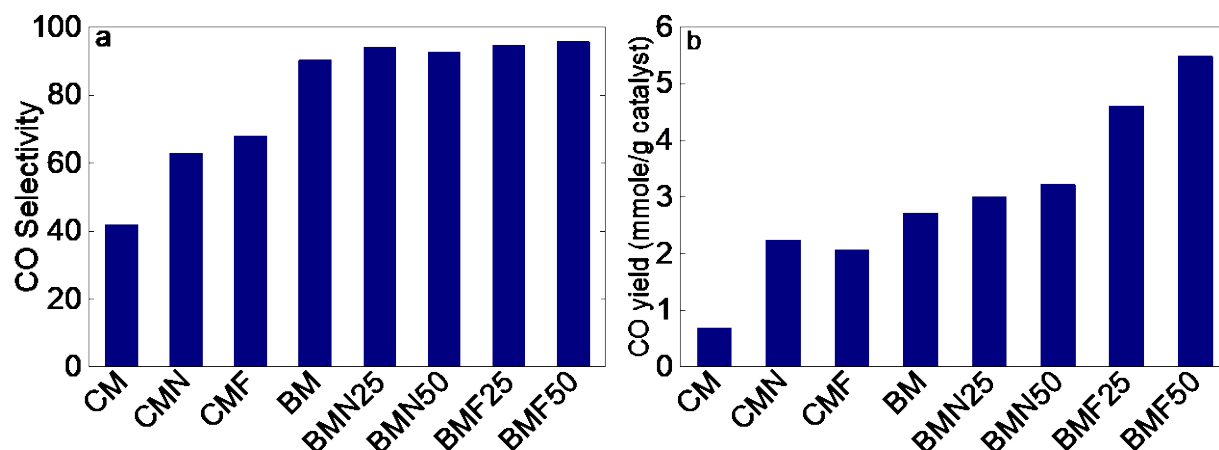


Figure 3.3: a) CO selectivity and b) yield for the redox catalysts (Cycle 10 of short term redox study, 10% CH₄ and 10% O₂ at 900°C).

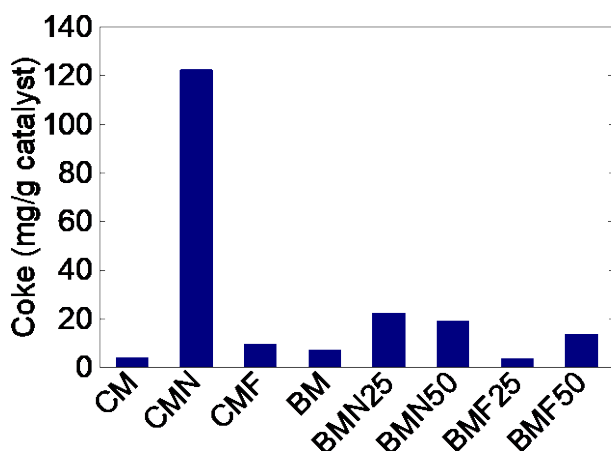


Figure 3.4: Coke formation for the redox catalysts (Cycle 10 of short term redox study, 10% CH₄ and 10% O₂ at 900°C).

3.4.3 Surface Composition Effects

Presence of reduced Ni on redox catalyst surfaces is anticipated to enhance the catalyst's activity for methane activation and CO selectivity. In the meantime, it can lead to increased coke formation. Such effects are apparent for redox catalysts with a CaMnO₃ parent structure (Figure 3.3 and Figure 3.4). In contrast, Ni doping in a BaMnO₃ parent structure exhibited insignificant

impact on CO selectivity and coke formation. As discussed earlier, this may point to a significantly different surface metal composition when compared to the bulk, i.e. Ni dopant is significantly underrepresented on the surface. Compositions of outermost layers for many mixed oxides have been reported to deviate from its bulk stoichiometry⁴⁴. To investigate this phenomenon, near surface compositions of as-prepared BaMn_{0.5}Ni_{0.5}O₃ (Fresh BMN50) and CaMn_{0.75}Ni_{0.25}O₃ (Fresh CMN25) and reduced BaMn_{0.5}Ni_{0.5}O₃ (Reduced BMN50) and CaMn_{0.75}Ni_{0.25}O₃ (Reduced CMN25) are examined using XPS. While more surface sensitive techniques such as low-energy ion scattering (LEIS) are desirable, XPS provided a convenient approach to determine elemental compositions within 1 – 3 nm from the surface. Surface deviation is shown in Figure 3.5 and is calculated as follows (Equation 1.3):

$$Eq. 1.3: SD: \frac{\textit{Measured Near Surface Concentration}}{\textit{Stoichiometric Concentration}}$$

As can be seen, the surface is over-expressed with A-site cations for all samples. In comparison, Ni is under-represented by an SD below 0.5 for all samples. While the as-prepared samples have similar degrees of surface deviation (SD), reduced CaMn_{0.75}Ni_{0.25}O₃ exhibited five times the surface deviation for Ni when compared to BaMn_{0.5}Ni_{0.5}O₃. In contrast, barium and oxygen were enriched by an SD of 1.22 in BaMn_{0.5}Ni_{0.5}O₃. This indicated that the surface of doped BaMnO₃ samples, when reduced, is practically covered with BaO. This is consistent with the observation that Ni and Fe doping had insignificant effects on CO selectivity and coke formation for BaMnO₃ based redox catalysts. The dopants, however, can change the bulk properties of the perovskite, allowing more lattice oxygen to be released during the redox cycles.

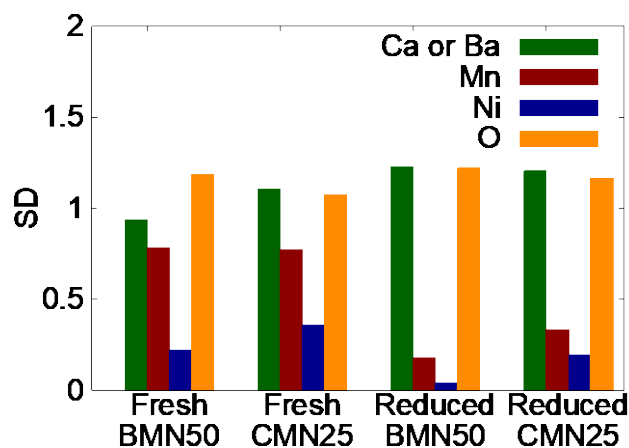


Figure 3.5: Surface Deviation of Redox Catalysts.

3.4.4 Effects of Parent Structure Stability

Another interesting observation is that all redox catalysts with a BaMnO_3 parent structure exhibited significantly higher CO selectivity when compared to those with a CaMnO_3 structure. Recent studies of a $\text{La}_x\text{Sr}_{1-x}\text{FeO}_3$ containing redox catalyst indicated that electrophilic surface oxygen species, which may evolve from lattice oxygen species in the bulk, play an important role for non-selective oxidation of methane.³⁴ Therefore, stability of parent structure, which affects the evolution of lattice oxygen to electrophilic oxygen species, can play a role in the selectivity of the redox catalysts. TPR and TPD experiments are therefore conducted to investigate such relationships. Figure 3.6 illustrates the H_2 -TPR results for $\text{CaMn}_{0.8}\text{Ni}_{0.2}\text{O}_3$, BaMnO_3 , and $\text{BaMn}_{0.75}\text{Ni}_{0.25}\text{O}_3$. These results indicate that all the active lattice oxygen species are removed from $\text{CaMn}_{0.8}\text{Ni}_{0.2}\text{O}_3$ below 700°C , where TPR peaks occurred at 425°C and 575°C . In contrast, the TPR peak temperatures for $\text{BaMn}_{0.75}\text{Ni}_{0.25}\text{O}_3$ and BaMnO_3 appeared around $400 - 550^\circ\text{C}$, 700°C , and 825°C . The higher reduction peaks for BaMnO_3 based samples indicate that lattice oxygen are more tightly bonded in such a structure when compared with CaMnO_3 . This could contribute to higher selectivity observed for the BaMnO_3 based redox catalysts. The three peaks of BaMnO_3 are consistent with Mn changing oxidation states in the following order: $4+ \rightarrow 3+ \rightarrow 8/3+ \rightarrow 2+$. The

two extra peaks seen in $\text{BaMn}_{0.75}\text{Ni}_{0.25}\text{O}_3$ are likely to result from oxidation state change for Ni either in the perovskite structure or as separate NiO/Ni phases as indicated by XRD Figure 3.1).

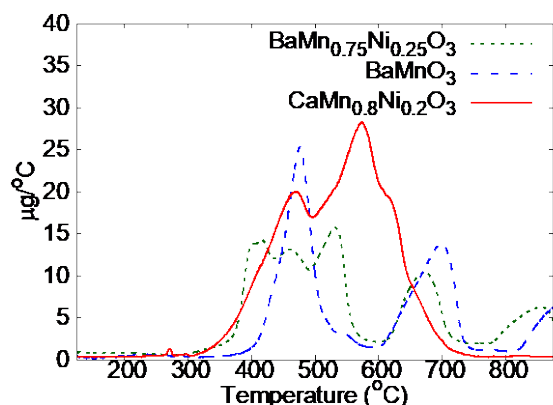


Figure 3.6: DTG of H_2 (20%) TPR ($10^\circ/\text{min}$) of redox catalysts $\text{BaMn}_{0.75}\text{Ni}_{0.25}\text{O}_3$, BaMnO_3 , and $\text{CaMn}_{0.8}\text{Ni}_{0.2}\text{O}_3$.

To supplement H_2 -TPR experiments, temperature programmed desorption is conducted to measure the amount of oxygen that can evolve from the redox catalyst under an inert, non-reducing atmosphere. Shafiefarhood et al.³⁴ showed surface oxygen species contributed to deep oxidation. DTG results of these TPD experiments are shown in Figure 3.7. These experiments showed little to no oxygen desorption with BaMnO_3 structured redox catalysts. However, $\text{CaMn}_{0.8}\text{Ni}_{0.2}\text{O}_3$ showed noticeably higher amount of oxygen desorption. Since the desorption of gaseous oxygen from a perovskite lattice occurs through lattice oxygen evolution to surface oxygen species ($\text{O}^{2-} \rightarrow \text{O}^- \rightarrow \text{O}_2^{2-} \rightarrow \text{O}_2$), one would anticipate that the non-selective oxygen species on CaMnO_3 based redox catalyst surface would be far more abundant than that on BaMnO_3 based redox catalysts. Once again, these findings are consistent with the higher amount of deep oxidation seen in CaMnO_3 based redox catalysts.

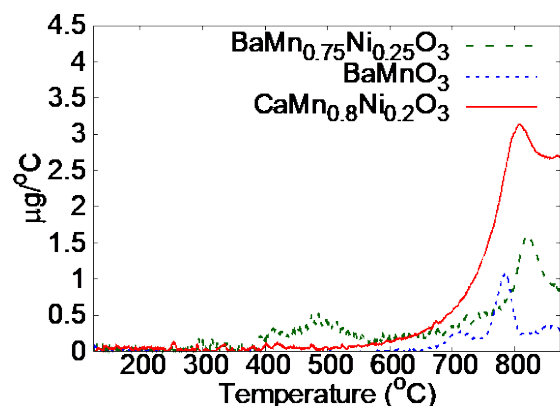


Figure 3.7: DTG of TPD (5°/min) of redox catalysts BaMn_{0.75}Ni_{0.25}O₃, BaMnO₃, and CaMn_{0.8}Ni_{0.2}O₃.

3.4.5 Cyclic Redox Studies

Another important factor for a redox catalyst is its recyclability. The recyclability of the catalysts are tested with 10 minutes reduction/oxidation half cycles. Table 3.3 summarizes the change in CO selectivity, yield, and coke formation for nickel doped BaMn_{1-x}Ni_xO₃ redox catalysts from cycle 5 to 25. Both Ni doped catalysts showed stability, with BaMn_{0.75}Ni_{0.25}O₃ performing exceptionally well: both selectivity and CO yield showed almost no decline within 25 cycles. BaMn_{0.5}Ni_{0.5}O₃ also showed marginal decline in selectivity and CO yield. We note that the CO yields shown in Table 3.3 are slightly different from those in Figure 3.3 due to slight differences in operating conditions.

Table 3.3: Change in selectivity, coke, and CO yield for nickel doped redox catalysts from cycle 5 to 25.

	BMN2	BMN2	BMN5	BMN5
	5	5	0	0
Cycle Number	5	25	5	25
S _{co} (%)	92.0	91.9	93.1	92.5
Coke (mg/g catalyst)	6.4	6.6	7.2	9.5
CO yield (mmol/g catalyst)	3.2	3.1	5.2	4.8

Long term redox studies were also conducted for iron doped catalysts, with the results summarized in Table 3.4. In contrast to nickel doped catalysts, iron doped catalysts showed signs of deactivation. Both $\text{BaMn}_{0.75}\text{Fe}_{0.25}\text{O}_3$ and $\text{BaMn}_{0.5}\text{Fe}_{0.5}\text{O}_3$ showed a decrease in selectivity and CO yield. This is seen as a result of the reaction slowing down with cycling and can be illustrated in Figure 3.8. The notable decrease in coke formation can also be explained by the slower reduction kinetics, i.e. the presence of active lattice oxygen tends to retard coke formation reactions such as Boudouard reaction and methane decomposition.

While nickel doped BaMnO_3 redox catalysts exhibit desirable performance, they may not be applicable industrially due to their inherent toxicity and relatively high cost. In comparison, iron doped BaMnO_3 would be advantageous from both cost and environmental sustainability standpoints. It is therefore desirable to determine the underlying cause for deactivation of the iron doped redox catalysts. The loss of redox activity for iron doped BaMnO_3 redox catalysts can result from two possible mechanisms: (i) lack of phase regenerability: a redox catalyst underwent irreversible phase change during the reduction reaction. One would anticipate a drop in redox activity if the reduced phases cannot be reoxidized to form the original phases of the redox catalyst; (ii) sintering: severe loss of surface area and pore volume lead to deactivation for oxygen carriers with low ionic and/or electronic conductivity. To determine the phase regenerability of the redox catalyst, XRD analysis was performed on $\text{BaMn}_{0.5}\text{Fe}_{0.5}\text{O}_3$ (Figure 3.9). As can be seen, BaMnO_3 was fully regenerated after oxidation. It is therefore concluded that the reduced iron doped BaMnO_3 redox catalysts can be fully regenerated to their original phases when oxidized. Therefore, lack of phase regenerability is not likely to be the cause of deactivation. Further observation of the cycled redox catalyst sample indicated significant aggregation of the solids particles, this indicated sintering and loss of surface area. We note that the iron based redox catalyst

has the highest oxygen carrying capacity among the all the redox catalyst samples (Figure 3.3b). Therefore, one would anticipate significant heat release during the regeneration reaction. The large heat release coupled with the ineffectiveness for heat removal in a packed bed and relatively low melting point of reduced iron (~1,200°C) can lead to significant sintering of the redox catalyst sample. To confirm this, we performed cyclic redox experiment with a U-tube fixed bed reactor operated under an integral bed mode. Results of the integral bed experiment are shown in Figure 3.11. The results indicated that iron doped catalysts maintained high performance as redox catalysts under fixed bed operations, with the exception of BMF25 having its selectivity slightly lowered. However, deactivation remained with both selectivity and CO yield decreasing. It is apparent that the reduction rates became slower as evidenced by the decrease of CO yield from cycle 2 to cycle 5. In addition, cycle 2 showed completion of reaction stage 3 (the highly selective reaction region) while cycle 5 does not (Figure 3.10). Inspection of the post-experiment samples again confirmed sintering of the redox catalyst, which is the likely cause of deactivation.

Table 3.4: Change in selectivity, coke, and CO yield for iron doped redox catalysts from cycle 5 to 25.

	BMF25	BMF25	BMF50	BMF50
Cycle Number	5	25	5	25
S_{co} (%)	88.2	76.4	95.1	86.9
Coke (mg/g catalyst)	1.2	1.2	10.5	1.3
CO yield (mmol/g catalyst)	2.7	0.9	6.8	3.63

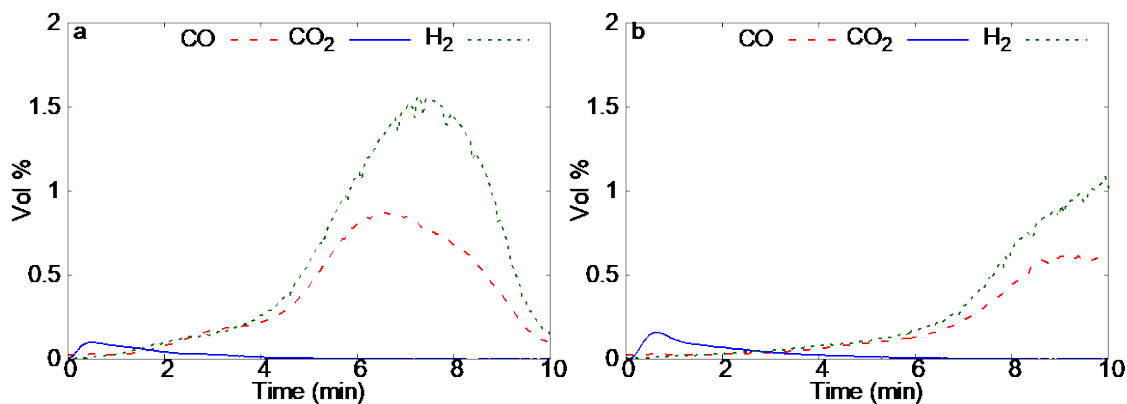


Figure 3.8: a) Gaseous product profile during the methane conversion stage at the 5th cycle and b) 25th cycle (10% CH₄ and 10% O₂ at 900°C) for BaMn_{0.5}Fe_{0.5}O₃.

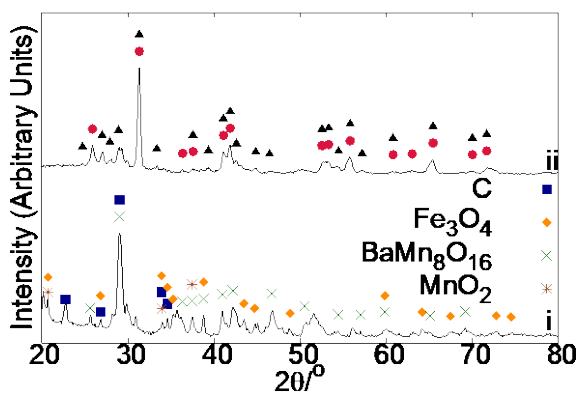


Figure 3.9: a) XRD pattern of BMF50 i) 10th cycle reduced and ii) oxidized phases after 10th reduction.

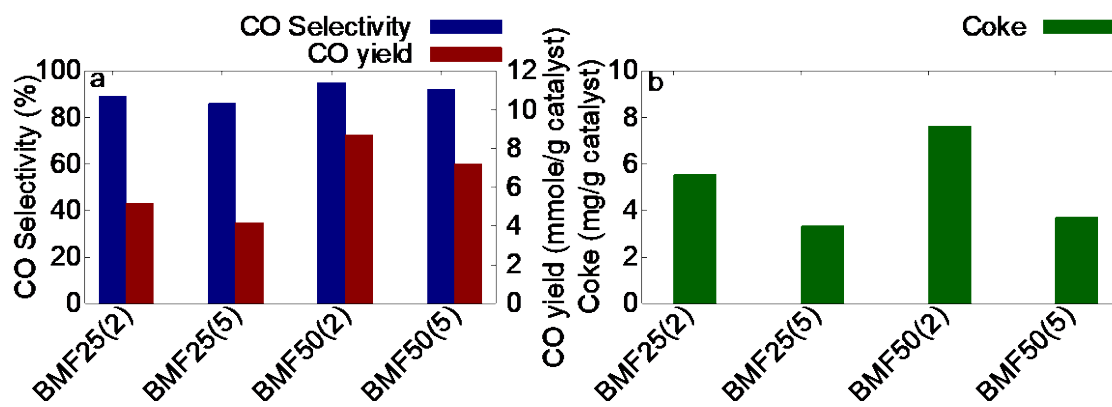


Figure 3.10: CO Selectivity, CO yield, and coke during fixed bed experiments (10% CH₄ and 10% O₂ at 900°C).

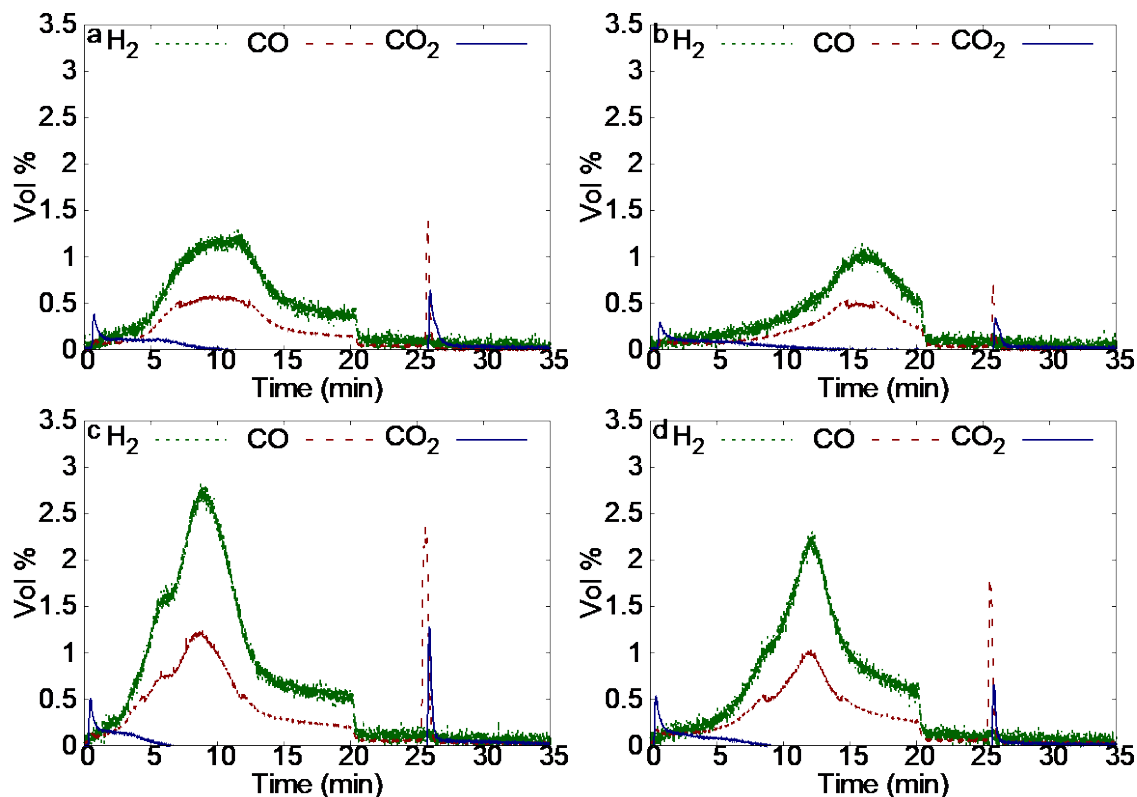


Figure 3.11: a) Cycle 2 of $\text{BaMn}_{0.75}\text{Fe}_{0.25}\text{O}_3$, b) Cycle 5 of $\text{BaMn}_{0.75}\text{Fe}_{0.25}\text{O}_3$, c) Cycle 2 of $\text{BaMn}_{0.5}\text{Fe}_{0.5}\text{O}_3$, d) Cycle 5 of $\text{BaMn}_{0.5}\text{Fe}_{0.5}\text{O}_3$ (10% CH_4 and 10% O_2 at 900°C) during fixed bed experiments.

3.4.6 Fluidized Bed Testing

Investigation of a fluidized bed application will gauge the effect of sintering and determine the applicability of iron doped BaMnO_3 redox catalysts. Sintering is expected to be minimized because of excellent gas-solid heat transfer in fluidized beds. To further minimize sintering, the sample is partially regenerated with steam to reduce the rate and degree of regeneration for the redox catalysts. This helps to lower the heat released during the regeneration stage. As can be seen from Figure 3.12, the redox catalyst maintained excellent recyclability over 20 cycles. CO selectivity as high as 95% was achieved with average methane conversion exceeding 95%. The high recyclability of the $\text{BaMn}_{0.5}\text{Fe}_{0.5}\text{O}_3$ catalyst in the fluidized bed mode with limited regeneration again confirms that sintering is likely to be the primary cause of the deactivation. In addition, a fluidized bed operating mode is potentially suitable for chemical looping reforming of

methane using iron doped BaMnO₃ based redox catalysts. Other approaches to increase the sintering resistance of BaMn_{1-x}Fe_xO₃ based redox catalysts include improving its lattice oxygen conductivity through doping or inclusion of a compatible secondary phase, as discussed in our previous article⁴³.

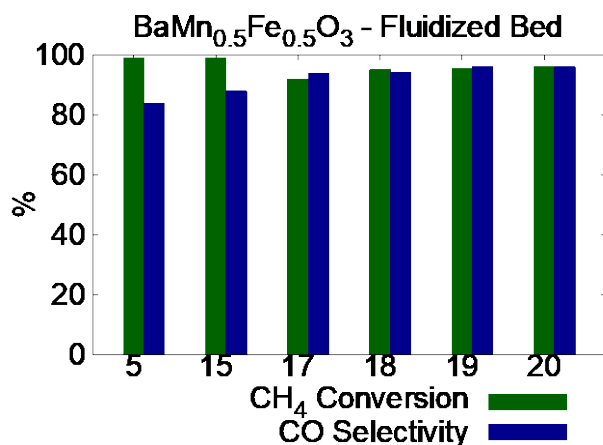


Figure 3.12: CO Selectivity and Methane conversion during fluidized bed experiments.

3.5 Conclusion

The current study investigates redox catalysts with a general formula of AMn_xB_{1-x}O₃ (A = Ca or Ba; B = Fe or Ni) for chemical looping reforming of methane. Redox catalysts with a BaMnO₃ parent structure exhibited considerably higher syngas selectivities when compared to CaMnO₃ based redox catalyst. Moreover, BaMn_xB_{1-x}O₃ based redox catalysts are more coke-resistant for methane partial oxidation than CaMn_xB_{1-x}O₃. While undoped BaMnO₃ also exhibited high selectivity towards syngas, addition of B-site dopants leads to higher oxygen carrying capacity (and hence syngas yield) without significantly impacting coke-resistance. In contrast, nickel doped CaMnO₃ is significantly more prone for coke formation. The higher coke-resistance of the BaMnO₃ based redox catalysts can be explained by a BaO terminated surface which minimizes the exposure of metallic Ni or Fe, thereby inhibiting the methane cracking and

Boudouard reactions. When compared with BaMnO_3 based redox catalyst, CaMnO_3 contains significantly higher amounts of loosely bound oxygen species, as indicated by TPR and TPD experiments. The facile evolution of such oxygen species into non-selective, electrophilic oxygen species under the reaction conditions can explain the lower syngas selectivity for CaMnO_3 based redox catalysts.

Among $\text{BaMn}_x\text{B}_{1-x}\text{O}_3$ based redox catalysts, $\text{BaMn}_{0.5}\text{Fe}_{0.5}\text{O}_3$ exhibits the highest syngas selectivity and oxygen carrying capacity. The catalyst, however, deactivates over multiple redox cycles in fixed bed testing. It was determined that sintering of the redox catalyst, resulting from the lack of heat dissipation in the fixed bed, is the cause of deactivation. However, high syngas selectivity, methane conversion, and long term stability was achieved in a fluidized bed using steam as the oxidant. It is therefore concluded that $\text{BaMn}_x\text{B}_{1-x}\text{O}_3$ based redox catalysts, especially those with Fe as B-site dopants, can potentially be effective for chemical looping reforming of methane. However, care must be taken to prevent excessive sintering of the redox catalysts during redox operations.

3.6 References

1. BP Statistical Review of World Energy June 2015, <http://www.bp.com/en/global/corporate/energy-economics/statistical-review-of-world-energy/natural-gas-review-by-energy-type/natural-gas-production.html>, (accessed December 2015).
2. Van der Laan, G. P. & Beenackers, A. Kinetics and selectivity of the Fischer-Tropsch synthesis: A literature review. *Catal. Rev.-Sci. Eng.* **41**, 255–318 (1999).
3. Tijm, P. J. A., Waller, F. J. & Brown, D. M. Methanol technology developments for the new millennium. *Appl. Catal. -Gen.* **221**, 275–282 (2001).
4. Lange, J. P. & Tijm, P. J. A. Processes for converting methane to liquid fuels: Economic screening through energy management. *Chem. Eng. Sci.* **51**, 2379–2387 (1996).
5. Fox, J. The Different Catalytic Routes for Methane Valorization - an Assessment. *Catal. Rev.-Sci. Eng.* **35**, 169–212 (1993).
6. Enger, B. C., Lodeng, R. & Holmen, A. A review of catalytic partial oxidation of methane to synthesis gas with emphasis on reaction mechanisms over transition metal catalysts. *Appl. Catal. -Gen.* **346**, 1–27 (2008).
7. York, A. P. E., Xiao, T. C. & Green, M. L. H. Brief overview of the partial oxidation of methane to synthesis gas. *Top. Catal.* **22**, 345–358 (2003).
8. Rostrup-Nielsen, J. R., Sehested, J. & Nørskov, J. K. in *Advances in Catalysis Volume 47*, 65–139 (Academic Press, 2002).
9. Ross, J. R. H. Natural gas reforming and CO₂ mitigation. *Catal. Today* **100**, 151–158 (2005).
10. <http://www.iea.org/publications/freepublications/publication/hydrogen.pdf>.
11. Tsang, S. C., Claridge, J. B. & Green, M. L. H. Recent advances in the conversion of methane to synthesis gas. *Catal. Today* **23**, 3–15 (1995).
12. Adanez, J., Abad, A., Garcia-Labiano, F., Gayan, P. & de Diego, L. F. Progress in Chemical-Looping Combustion and Reforming technologies. *Prog. Energy Combust. Sci.* **38**, 215–282 (2012).
13. Fan, L.-S. *Chemical Looping Systems for Fossil Energy Conversions*. (Wiley, 2011).
14. Thursfield, A., Murugan, A., Franca, R. & Metcalfe, I. S. Chemical looping and oxygen permeable ceramic membranes for hydrogen production – a review. *Energy Environ. Sci.* **5**, 7421–7459 (2012).

15. Murugan, A., Thursfield, A. & Metcalfe, I. S. A chemical looping process for hydrogen production using iron-containing perovskites. *Energy Environ. Sci.* **4**, 4639–4649 (2011).
16. Ryden, M., Lyngfelt, A. & Mattisson, T. Synthesis gas generation by chemical-looping reforming in a continuously operating laboratory reactor. *Fuel* **85**, 1631–1641 (2006).
17. Lewis, W. K., Gilliland, E. R. & Reed, W. A. Reaction of Methane with Copper Oxide in a Fluidized Bed. *Ind. Eng. Chem.* **41**, 1227–1237 (1949).
18. Mattisson, T. & Lyngfelt, A. Applications of chemical-looping combustion with capture of CO₂. (2001).
19. Otsuka, K., Wang, Y., Sunada, E. & Yamanaka, I. Direct Partial Oxidation of Methane to Synthesis Gas by Cerium Oxide. *J. Catal.* **175**, 152–160 (1998).
20. Otsuka, K., Ushiyama, T. & Yamanaka, I. Partial Oxidation of Methane Using the Redox of Cerium Oxide. *Chem. Lett.* **22**, 1517–1520 (1993).
21. Zafar, Q., Mattisson, T. & Gevert, B. Integrated Hydrogen and Power Production with CO₂ Capture Using Chemical-Looping Reforming Redox Reactivity of Particles of CuO, Mn₂O₃, NiO, and Fe₂O₃ Using SiO₂ as a Support. *Ind. Eng. Chem. Res.* **44**, 3485–3496 (2005).
22. Pröll, T., Bolhàr-Nordenkamp, J., Kolbitsch, P. & Hofbauer, H. Syngas and a separate nitrogen/argon stream via chemical looping reforming – A 140 kW pilot plant study. *Fuel* **89**, 1249–1256 (2010).
23. Mendiara, T. *et al.* Evaluation of different oxygen carriers for biomass tar reforming (I): Carbon deposition in experiments with toluene. *Fuel* **90**, 1049–1060 (2011).
24. Mendiara, T., Johansen, J. M., Utrilla, R., Jensen, A. D. & Glarborg, P. Evaluation of different oxygen carriers for biomass tar reforming (II): Carbon deposition in experiments with methane and other gases. *Fuel* **90**, 1370–1382 (2011).
25. Bhavsar, S., Najera, M. & Vesper, G. Chemical Looping Dry Reforming as Novel, Intensified Process for CO₂ Activation. *Chem. Eng. Technol.* **35**, 1281–1290 (2012).
26. Najera, M., Solunke, R., Gardner, T. & Vesper, G. Carbon capture and utilization via chemical looping dry reforming. *Chem. Eng. Res. Des.* **89**, 1533–1543 (2011).
27. Cleeton, J. P. E., Bohn, C. D., Müller, C. R., Dennis, J. S. & Scott, S. A. Clean hydrogen production and electricity from coal via chemical looping: Identifying a suitable operating regime. *Int. J. Hydrog. Energy* **34**, 1–12 (2009).

28. Bohn, C. D. *et al.* Production of Very Pure Hydrogen with Simultaneous Capture of Carbon Dioxide using the Redox Reactions of Iron Oxides in Packed Beds. *Ind. Eng. Chem. Res.* **47**, 7623–7630 (2008).
29. Galinsky, N. L., Huang, Y., Shafieifarhood, A. & Li, F. Iron Oxide with Facilitated O₂–Transport for Facile Fuel Oxidation and CO₂ Capture in a Chemical Looping Scheme. *ACS Sustain. Chem. Eng.* **1**, 364–373 (2013).
30. He, F. & Li, F. Hydrogen production from methane and solar energy – Process evaluations and comparison studies. *Int. J. Hydrog. Energy* **39**, 18092–18102 (2014).
31. Neal, L. M., Shafieifarhood, A. & Li, F. Dynamic Methane Partial Oxidation Using a Fe₂O₃@La_{0.8}Sr_{0.2}FeO_{3-δ} Core–Shell Redox Catalyst in the Absence of Gaseous Oxygen. *ACS Catal.* **4**, 3560–3569 (2014).
32. Shafieifarhood, A., Galinsky, N., Huang, Y., Chen, Y. & Li, F. Fe₂O₃@La_xSr_{1-x}FeO₃ Core–Shell Redox Catalyst for Methane Partial Oxidation. *ChemCatChem* **6**, 790–799 (2014).
33. Neal, L., Shafieifarhood, A. & Li, F. Effect of core and shell compositions on MeOx@La_ySr_{1-y}FeO₃ core–shell redox catalysts for chemical looping reforming of methane. *Appl. Energy* **157**, 391–398 (2015).
34. Shafieifarhood, A., Hamill, J. C., Neal, L. M. & Li, F. Methane Partial Oxidation using FeO_x@La_{0.8}Sr_{0.2}FeO_{3-δ} Core-Shell Catalyst - Transient Pulse Studies. *Phys. Chem. Chem. Phys.* (2015). doi:10.1039/C5CP05583K
35. Ryden, M. *et al.* Novel oxygen-carrier materials for chemical-looping combustion and chemical-looping reforming; La_xSr_{1-x}Fe_yCo_{1-y}O_{3-δ} perovskites and mixed-metal oxides of NiO, Fe₂O₃ and Mn₃O₄. *Int. J. Greenh. Gas Control* **2**, 21–36 (2008).
36. He, F. *et al.* The use of La_{1-x}Sr_xFeO₃ perovskite-type oxides as oxygen carriers in chemical-looping reforming of methane. *Fuel* **108**, 465–473 (2013).
37. Evdou, A., Zaspalis, V. & Nalbandian, L. La_{1-x}Sr_xFeO_{3-δ} perovskites as redox materials for application in a membrane reactor for simultaneous production of pure hydrogen and synthesis gas. *Fuel* **89**, 1265–1273 (2010).
38. Zhao, K. *et al.* Three-dimensionally ordered macroporous LaFeO₃ perovskites for chemical-looping steam reforming of methane. *Int. J. Hydrog. Energy* **39**, 3243–3252 (2014).
39. Mihai, O., Chen, D. & Holmen, A. Catalytic Consequence of Oxygen of Lanthanum Ferrite Perovskite in Chemical Looping Reforming of Methane. *Ind. Eng. Chem. Res.* **50**, 2613–2621 (2011).

40. Xiaoping, D. & Changchun, Y. Nano-Perovskite-Based (LaMO₃) Oxygen Carrier for Syngas Generation by Chemical-Looping Reforming of Methane. *Chin. J. Catal.* **32**, 1411–1417 (2011).
41. Wachs, I. E. & Routray, K. Catalysis Science of Bulk Mixed Oxides. *ACS Catal.* **2**, 1235–1246 (2012).
42. Tanaka, H. *et al.* Self-regenerating Rh- and Pt-based perovskite catalysts for automotive-emissions control. *Angew. Chem.-Int. Ed.* **45**, 5998–6002 (2006).
43. Galinsky, N. L., Shafiefarhood, A., Chen, Y., Neal, L. & Li, F. Effect of support on redox stability of iron oxide for chemical looping conversion of methane. *Appl. Catal. B Environ.* **164**, 371–379 (2015).
44. Merzlikin, S. V. *et al.* Anomalous Surface Compositions of Stoichiometric Mixed Oxide Compounds. *Angew. Chem. Int. Ed.* **49**, 8037–8041 (2010).

Chapter 4: Rh Promoted Perovskites for Exceptional “Low Temperature” Methane Conversion to Syngas

4.1 Abstract

By utilizing lattice oxygen of a reducible metal oxide (a.k.a. redox catalyst), chemical looping reforming (CLR) partially oxidizes methane to syngas without gaseous oxygen. Subsequent to methane partial oxidation (POx), the reduced metal oxide is re-oxidized with air to complete the two-step redox cycle. In essence, CLR accomplishes methane POx without the need for an air separation unit, offering a potentially more efficient route for syngas production. This study investigates Rh promoted and iron/strontium doped CaMnO_3 as redox catalysts at relatively low temperatures ($<700\text{ }^\circ\text{C}$). These redox catalysts take advantage of Rh promoter for methane activation as well as the high redox activity of iron/strontium doped CaMnO_3 . It was determined that Sr and Fe doped CaMnO_3 are highly active for methane conversion, showing lattice oxygen extraction of 2.2-4.5 wt.% at $600\text{ }^\circ\text{C}$. However, the syngas selectivities are relatively low. To further increase the syngas selectivity and yield, a reforming catalyst was placed downstream of the chemical looping bed. Under such a sequential bed scheme, 88-96% syngas selectivity was demonstrated for the redox catalysts. Optimization of the reaction conditions showed that sequential bed composed of Rh promoted $\text{CaMn}_{0.75}\text{Fe}_{0.25}\text{O}_3$ with a downstream reforming catalyst bed is capable of achieving syngas yields above 70% at $600\text{ }^\circ\text{C}$. The relatively low operating temperature and elimination of air separation unit makes the redox catalysts and the sequential bed scheme a potentially attractive option for methane conversion.

4.2 Introduction

Methane is the simplest and the most abundant organic compounds on earth^{1,2}. Compared to other fossil fuels such as coal and petroleum, methane also has lower CO_2 emissions³. These

have led to increased interests in methane valorization. One potential route to produce value added products from methane is the indirect, syngas (CO and H₂) route. Syngas can be converted to liquid fuels or methanol through the well-established commercial processes⁴⁻⁷. Traditionally, syngas is produced from methane by steam reforming and/or partial oxidation (POx) of methane⁸. These reactions have efficiency losses due to the endothermic dry and steam reforming reactions⁷. As an alternative approach, chemical looping reforming (CLR) offers the potential to circumvent these losses through a metal oxide capable of methane partial oxidation (a.k.a redox catalyst) through its lattice oxygen as part of a redox process⁹⁻¹². This is a two-step process, where the first step is selective oxidation of methane through the lattice oxygen of a metal oxide and the second step is replenishment of lattice oxygen by re-oxidation in air. This accomplishes methane partial oxidation, an exothermic reaction, without the requirement for cryogenic air separation.

The capability of the redox catalyst to achieve high methane conversion and high syngas selectivity is crucial to the success of the CLR process. Earlier studies generally focused on redox catalysts composed of a primary transition metal oxide for oxygen storage with a secondary metal oxide for enhanced structural stability and/or oxygen extraction rates¹³⁻¹⁷. Typically, the primary oxides are composed those of iron, manganese, or nickel. Unfortunately, redox catalysts composed of these transition metal oxides have encountered challenges. Nickel based redox catalysts suffer from toxicity concerns^{18,19}. Iron and manganese oxides, while benign and cheap, have not shown promising activity or selectivity^{9,10}. As an alternative, recent studies have investigated mixed metal oxides as redox catalysts in the context of chemical looping²⁰⁻²². In particular, the perovskite class of mixed metal oxides have demonstrated promising CLR results^{14,23-28}. Both iron and manganese containing perovskites have exhibited selectivity to syngas or carbon monoxide above 90%^{25,26}. However, the methane conversions reported in these studies are generally low (<2% among those

reported conversion numbers in fixed bed experiments). As such, higher methane conversion and syngas yield are still desired. Another limitation related to most CLR studies is the high operating temperature (mostly at 800°C or above)^{9,10,29-31}. Higher operating temperature can lead to increased heat loss and cost of materials of construction. This is particularly the case for the CLR system which uses more than one reactors.

A few recent studies, however, have brought to light the usefulness of rhodium surface promotion in activating methane. Most notably, Shafiefarhood et. al. has shown Rh promoted CaMnO_3 is active at 600°C, with a CO selectivity of 80%³². With unpromoted CaMnO_3 being active for chemical looping combustion³³⁻³⁵, Shafiefarhood attributed the increased selectivity and activity to facile methane activation facilitated by rhodium. Palchelva et. al.³⁶ also reported similar phenomena, with Rh promotion on $\text{La}_{0.8}\text{Sr}_{0.2}(\text{Fe}_{0.8}\text{Co}_{0.2})_{1-x}\text{Ga}_x\text{O}_3$ leading to a 40% increase (on an absolute basis) in CO selectivity at 600°C. However, the CH_4 conversion shown by Shafiefarhood et. al.³² was low at 600°C (<1%) and results shown by Palchelva et. al.³⁶ were produced using experiments with sharp pulse of methane, which is not representative of cyclic chemical looping operations.

With this in mind, this study aims to develop redox catalysts for improved syngas yield from methane CLR at low temperatures. We sought to accomplish this through rhodium promotion of perovskite oxides that are highly active at lower temperatures. Galinsky et. al. has reported increased CLOU activity at temperatures below 700°C through strontium and iron doping of CaMnO_3 ^{37,38}. Further improvement of redox activity and lattice oxygen utilization can potentially be achieved on these doped perovskites through Rh promotion. As such, Rh promoted $\text{Ca}_x\text{A}_{1-x}\text{Mn}_x\text{B}_{1-x}\text{O}_3$ (A = Sr, B = Fe, x = 0.95 or 0.75) are investigated in this study.

Our results indicate that all the redox catalysts are highly active at 600°C or lower, with iron substituted samples resulting in complete combustion of methane and strontium doped samples resulting in a split between complete combustion and partial oxidation products. To address the low selectivity (and high activity) of the doped redox catalysts, a secondary reforming bed was integrated downstream of the CLR redox catalyst bed. More than 88% syngas selectivity was demonstrated for all the redox catalysts under this sequential bed scheme. Moreover, single-pass syngas yield in excess of 70% was achieved at 600 °C in a sequential bed composed of Rh promoted $\text{CaMn}_{0.75}\text{Fe}_{0.25}\text{O}_3$ with a downstream reforming catalyst bed, marking one of the highest syngas yields report to date within this relatively low temperature range.

4.2.1 Methods

4.2.2 Redox Catalyst Synthesis

A modified pechini method was used to prepare the unpromoted redox catalysts. Stoichiometric amounts of metal nitrates, *e.g.* $\text{Ca}(\text{NO}_3)_2$, $\text{Mn}(\text{NO}_3)_2 \cdot 4\text{H}_2\text{O}$, $\text{Sr}(\text{NO}_3)_2$, and $\text{Mn}(\text{NO}_3)_2 \cdot 4\text{H}_2\text{O}$ (Sigma Aldrich), were dissolve in deionized water. Next, citric acid (CA, Sigma Aldrich) was added at a molar ratio of 2.5:1 to the total amount of metal cations and the solution was heated to 50°C and held at this temperature for 30 minutes. This results in a mixed-metal citric acid complex with good dispersion of metal ions. Ethylene glycol (EG, Sigma Aldrich) was added next at a molar ratio of 1.5:1 to the moles of citric acid at 80°C until a gel formed. This gel was dried in an oven at slightly above 100°C to remove any moisture. Finally, the dried sample was sintered at 950°C for 8 hours. The unpromoted perovskites follow the general formula: $\text{Ca}_x\text{A}_{1-x}\text{Mn}_x\text{B}_{1-x}\text{O}_3$ (A = Sr, B = Fe, x = 0.95 or 0.75)

Incipient wetness was used for Rh promotion to ensure surface enrichment. The redox catalysts were prepared by promotion of $\text{Ca}_x\text{A}_{1-x}\text{Mn}_x\text{B}_{1-x}\text{O}_3$ (A = Sr, B = Fe, x = 0.95 or 0.75) at

0.5 wt.%. The reforming catalyst was prepared by Rh promotion of Al_2O_3 at 0.4 wt%. Rhodium nitrate (Sigma Aldrich) was first dissolved in deionized water, with the solution added to $\text{Ca}_x\text{A}_{1-x}\text{Mn}_x\text{B}_{1-x}\text{O}_3$ ($A = \text{Sr}$, $B = \text{Fe}$, $x = 0.95$ or 0.75) and Al_2O_3 in sequential steps until the desired amount of Rh is reached. The impregnated sample was dried for 4 hours and annealed again for 6 hours at 950°C . After annealing, the particles were crushed with a mortar and pestle and sieved for a particle size between 70-300 μm . For the remainder of the paper, the redox catalysts will be abbreviated as $\text{Rh-Ca}_x\text{A}_{1-x}\text{Mn}_x\text{B}_{1-x}\text{O}_3$ ($A = \text{Sr}$, $B = \text{Fe}$, $x = 0.95$ or 0.75). Phase confirmation is shown for unpromoted and promoted redox catalysts in Figure B.1.

4.2.3 Sample Characterization

Characterization techniques were used to analyze the structural and reactive properties of the redox catalysts. X-ray powder diffraction was used to identify the crystalline phases present in each sample. The XRD pattern was obtained using the Empyrean PANalytical diffractometer with $\text{CuK}\alpha$ radiation operating at 45 kV and 40 mA. A 2θ range of 20 - 80° is used with a step size 0.0263° holding each step for 0.24 seconds at each step. HighScore Plus© software was used for phase matching.

The XPS system consists of a Thermo-Fisher Alpha 110 hemispherical energy analyzer, a Thermo-Fischer XR3, 300 W dual-anode X-ray source, and a chamber with a base pressure of 1×10^{-9} Torr. Survey spectra used a pass energy of 100 eV, and narrow scan spectra were taken with a pass energy of 20 eV. An Al anode was used for all analyses. The spectral energies were calibrated to an adventitious C 1s peak of 284.6 eV

Methane (5.0 grade) temperature programmed reduction (TPR) was conducted using a TGA (TA SDT Q600) with 10% CH_4 at an overall flow rate of 200 sccm and a ramp rate of $20^\circ\text{C}/\text{min}$ to 900°C . Argon (5.0 grade) was used as the carrier gas. The weight and differential

thermogravimetric (DTG) results were obtained to determine the effect of doping and Rh promotion on reducibility of the redox catalyst. This was conducted for all redox catalysts, promoted and unpromoted.

Temperature programmed oxygen (5.0 grade) desorption (TPD) was conducted using a TGA (TA SDT Q600). 20% O₂ at an overall flowrate of 200 sccm was used to pretreat and remove any adsorbed hydroxyl or carbonate species. Argon (5.0 grade) was used as the carrier gas. The pretreatment steps were heating at 20°C/min to 600°C, holding an isotherm at 600°C, cooling at 10°C/min to 100°C, and finally holding an isotherm at 100°C for 60 minutes. After pretreatment, injection of oxygen was stopped and an additional isotherm at 100°C was maintained for 60 minute to ensure oxygen was properly purged before ramping. The sample was ramped to 900°C at 2°C/min and weight loss and DTG was used to determine the availability of loosely bound oxygen.

4.2.4 Redox Testing

Redox tests were conducted in single and sequential bed configurations to examine the redox catalysts in CLR and sequential bed CLR applications, respectively. All configurations used quartz U-tube (4 mm ID) reactors. The single bed configuration consisted of a single U-tube loaded with the redox catalyst, simulating standard chemical looping reforming. In the sequential bed configuration, a secondary U-tube was loaded with the reforming catalyst and placed downstream of the U-tube loaded with the redox catalyst. Either 230 mg or 460 mg of the redox catalyst and 25 mg of the reforming catalyst was used. Argon (Grade 5.0) was used as the carrier gas, a mixture of methane in argon (Grade 5.0, 25% methane) was blended with the carrier gas during reduction, and pure O₂ (Grade 5.0) was blended with the carrier gas during oxidation. During reduction, the methane concentration was 5% and during oxidation the oxygen concentration was 5.8%. An overall flow rate of either 50 or 100 sccm was used during reduction to keep the overall gas hourly

space velocity constant at 12000 across redox catalysts. The flow rate during the oxidation half cycle corresponded to either 42.5 or 85 sccm depending on redox catalyst loading. Initial redox testing was at 600°C.

A quadrupole mass spectrometer (QMS, MKS Cirrus II) was used to measure the products of the reduction and oxidation steps. A set of calibrations was applied to the signals obtained from the QMS. Calibrations for H₂, CO, CO₂, and CH₄ were obtained immediately after a redox experiment. H₂O was calculated using a hydrogen mass balance. O₂ extraction is calculated using CO, CO₂, and H₂O production. Mass balance on carbon species was balanced within 10%. Unless specifically mentioned, the results are from 10th cycle of a 10-cycle experiment, as obtained calibrations will be most accurate for the last cycle. All reported data are from redox catalysts that were already cycled 100+ times for a thorough break in.

4.3 Results and Discussion

4.3.1 Effects of dopants and Rh promotion

We sought to characterize the effect of dopant and Rh promotion on the reduction temperature through CH₄ TPR. In Figure 4.1a, DTG is shown for as-prepared, unpromoted redox catalysts. Aside from Ca_{0.95}Sr_{0.05}MnO₃, which exhibited a reduction onset temperature of 500°C, all other samples started to reduce at 550°C. An additional reduction peak occurred in all the samples at higher temperatures, where their peaks appeared between 750°C and 850°C. DTG for Rh promoted redox catalysts is shown in Figure 4.1b. Rh-Ca_{0.75}Sr_{0.25}MnO₃ showed a sharp peak at 375°C, and the remaining Rh promoted redox catalysts showed sharp peaks around 450°C. For all redox catalysts, this reduction ended before 600°C, which was selected as the temperature for most isothermal redox experiments. Additional reduction of Rh promoted redox catalysts occurred above 650°C. The first peak for promoted and unpromoted samples finishes at 5 wt.% or less

(shown in Figure B.2). Phase decomposition for these materials typically occurs when a larger weight loss is observed, as CaMnO_3 is capable of reduction to $\text{CaMnO}_{2.5}$ ³⁹ and strontium and iron doping inhibits phase change^{37,38}. As such, the results from CH_4 -TPR indicate that the first peak is a result of vacancy formation and the second peak is a result of phase decomposition. The most notable difference between unpromoted and Rh promoted redox catalysts is that Rh promotion led to significantly lower reduction temperature as well as more rapid reduction. With Rh known to promote methane activation⁴⁰⁻⁴², this peak is associated with rapid removal of lattice oxygen due to activated methane. This reduction is not likely to correspond to the reduction of Rh_2O_3 , because weight loss attributed to reduction of Rh_2O_3 would only account for less than 0.1 wt%. Additionally, unpromoted and promoted samples showed very similar XRD patterns (Figures B.1).

TPR results also showed minor signs of carbon deposition or carbonate formation in select samples. In $\text{Rh-Ca}_{0.75}\text{Sr}_{0.25}\text{MnO}_3$ and $\text{Rh-Ca}_{0.95}\text{Sr}_{0.05}\text{MnO}_3$, weight gain was present at 760°C and 790°C, respectively. Weight gain was also seen in CaMnO_3 around 725°C. While carbon deposition can lead to deactivation, their amounts are small and the onset temperatures are higher than the proposed operating temperatures in the current study.

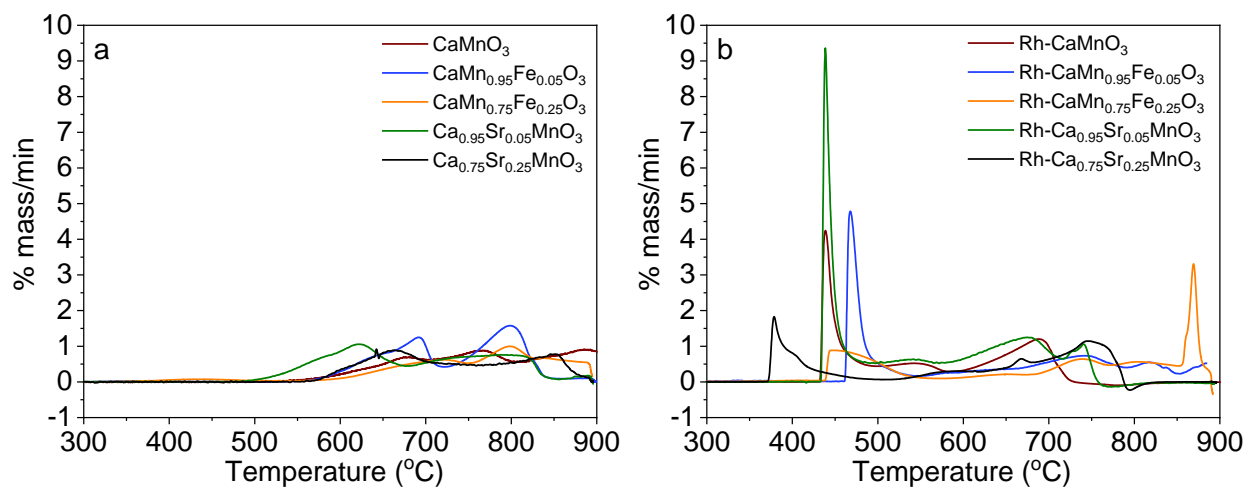


Figure 4.1: DTG of a) unpromoted redox catalysts and b) promoted redox catalysts during CH₄ – TPR. 10% CH₄ (10 sccm CH₄, 90 sccm Ar) was used as the reducing gas. The sample was heated at 20°C/min. GHSV = 12000 hr⁻¹.

Since Rh cations cannot be readily incorporated into the CaMnO₃ structure³², lower activation temperature is likely to be a result of Rh surface enrichment and its subsequent facilitation of methane activation. This was investigated with XPS. Figure 4.2 summarizes the near surface concentrations of all the metal cations relative to their averaged bulk compositions. A value higher than unity indicates surface enrichment whereas smaller values indicates suppression. All redox catalysts showed surface enrichment of Rh above 2.9, or >290% overrepresentation of Rh on the surface based on XPS. Rh-CaMn_{0.75}Fe_{0.25}O₃ showed the highest surface enrichment at 7.0 and Rh-Ca_{0.95}Sr_{0.05}MnO₃ showed the lowest surface enrichment at 2.9. The near surface enrichment of Rh is the most notable feature in Figure 4.2 and is associated with the weight loss seen below 500°C in CH₄-TPR. Strontium was the only other metal that showed surface enrichment. This is expected as strontium has shown a tendency to preferentially enrich on the surface of perovskites^{43,44}.

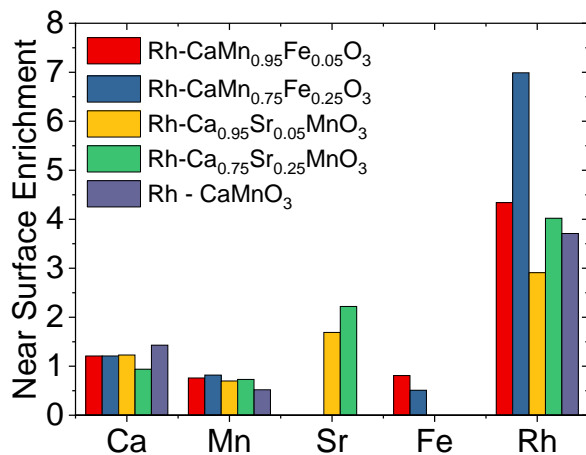


Figure 4.2: Near surface enrichment of metal cations in Rh promoted Redox Catalysts. Results for Rh-CaMnO₃ are from Shafiefarhood et. al.²³ after oxidation of the fifth redox cycle.

4.3.2 Low temperature methane conversion using Rh promoted redox catalysts

Having shown Rh-Ca_xA_{1-x}Mn_xB_{1-x}O₃ (A = Sr, B = Fe, x = 0.95 or 0.75) is active at low temperatures, these redox catalysts were examined for methane partial oxidation. Results for CH₄ conversion and O₂ extraction at 600°C are shown in Figure 4.3a. Rh-CaMn_{0.95}Fe_{0.05}O₃ and Rh-CaMnO₃ exhibited the highest amounts of oxygen extraction at 4.5 wt.% and 4.1 wt.%, respectively. All other dopant combinations resulted in an oxygen extraction between 2.2-3.0 wt.%. CH₄ conversion is highest with Rh-CaMnO₃ at 20%. All other redox catalysts showed a CH₄ conversion below 12.5%. Although Rh-CaMn_{0.95}Fe_{0.05}O₃ resulted in the highest amount of O₂ extraction, CH₄ conversion was below 10%. Results for CO and H₂ selectivity are shown in Figure 4.3b. Rh-CaMnO₃ exhibits 81% CO selectivity and 65% H₂ selectivity. Rh-CaMn_{0.75}Fe_{0.25}O₃ and Rh-CaMn_{0.95}Fe_{0.05}O₃ did not show any CO selectivity and less than 10% H₂ selectivity. Rh-Ca_{0.75}Sr_{0.25}MnO₃ and Rh-Ca_{0.95}Sr_{0.05}MnO₃ showed intermediate amounts of CO and H₂ selectivity. This indicates that the dopants have significant effects on product selectivity as well as oxygen removal; Both Fe and Sr doping led to over oxidation of the syngas. It should also be noted that

these results are stable with respect to cycling since all redox catalysts were cycled 100 times, before data was collected and reported in Figure 4.3.

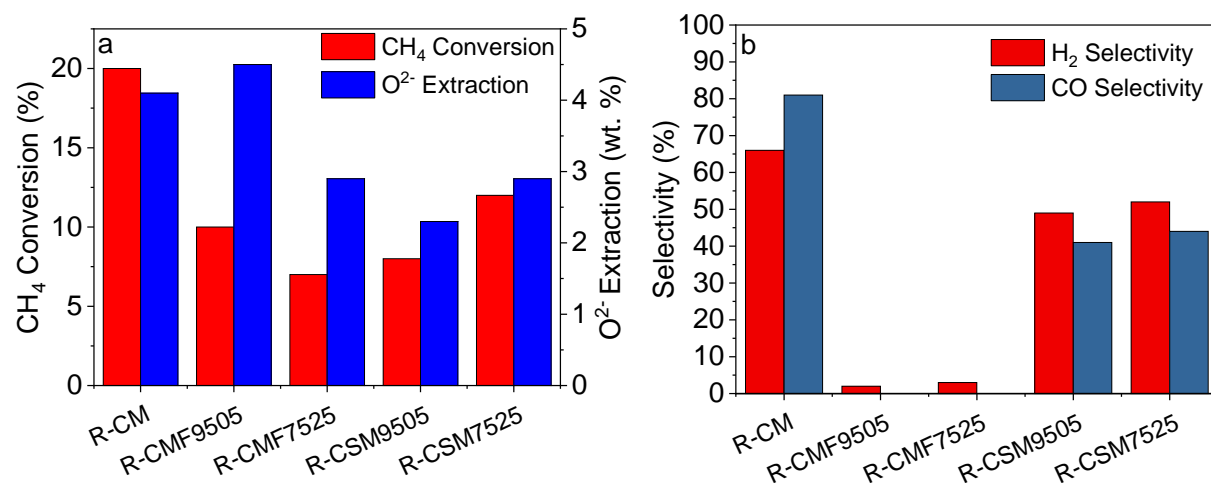


Figure 4.3: a) CH₄ conversion and O₂⁻ extraction and b) CO + H₂ selectivity at 600°C with 15 minutes of reduction in 5% CH₄ and 10 minutes of oxidation in 5.8% O₂. GHSV = 12000 hr⁻¹.

One possible explanation of the difference in product selectivity is the availability of loosely bound oxygen since such oxygen species are believed to be highly non-selective^{20,45–47}. Temperature programmed oxygen desorption (TPD) was conducted to determine the amount of oxygen that can be spontaneously removed from the lattice. DTG of this experiment is shown in Figure 4.4a for Rh promoted redox catalysts. Peak positions of Rh-CaMnO₃, Rh-Ca_{0.95}Sr_{0.05}MnO₃, Rh-Ca_{0.75}Sr_{0.25}MnO₃, Rh-CaMn_{0.75}Fe_{0.25}O₃, and Rh-CaMn_{0.95}Fe_{0.05}O₃ are 790°C, 755°C, 698°C, 405°C, and 370°C respectively. In general, this shows strontium lowers the oxygen desorption temperature whereas iron doping further enhances oxygen release at even lower temperatures. Weight during TPD is shown in Figure B.2. Comparing weight loss at 600°C, Rh-CaMnO₃ did not show any signs of weight loss, Rh – Ca_{0.95}Sr_{0.05}MnO₃ and Rh – Ca_{0.75}Sr_{0.25}MnO₃ showed 0.05% weight loss, Rh – CaMn_{0.95}Fe_{0.05}O₃ showed 0.4% weight loss, and Rh-CaMn_{0.75}Fe_{0.25}O₃ showed 0.63% weight loss. This indicates strontium increases the amount of readily available oxygen and iron further increases the amount of oxygen available at 600°C. This was consistent with studies

by Galinsky et. al. and Mishra et. al.^{35,37,38} where the effect of iron and strontium was investigated on unpromoted CaMnO_3 . In Figure 4.4b, the TPD peak temperature is shown with respect to syngas selectivity. From this, it can be seen that an increase in TPD peak temperature correlates well with an increase in syngas selectivity. As such, this result indicates that that syngas selectivity can be correlated with the O_2 release temperature from the perovskite redox catalysts.

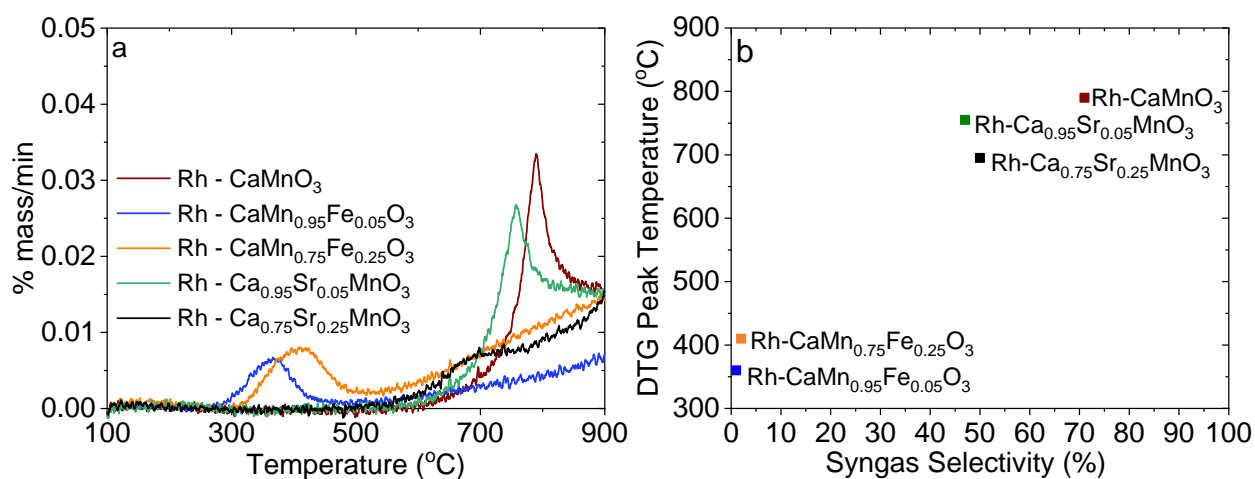


Figure 4.4: a) DTG of Rh promoted redox catalysts during TPD. Ramping rate is $2^\circ\text{C}/\text{min}$ and 180 sccm of argon was used. GHSV = 12000 hr^{-1} . b) TPD peak temperature vs. syngas selectivity during redox cycling.

4.3.3 Syngas yield enhancement via a sequential bed scheme

Utilization of highly active and unselective redox catalysts

While CaMnO_3 showed higher syngas selectivity, it is important to recognize an important function of the redox catalysts is to donate oxygen. In this aspect, iron doped sample exhibited the best overall performance although it demonstrated the lowest syngas selectivity. Although the latter is undesirable for CLR, the complete oxidation products, i.e. CO_2 and H_2O , are known to be active for methane reforming. In the following section, these redox catalysts will be investigated in a sequential bed chemical looping reforming scheme, where a reforming bed was placed

downstream of a redox catalyst with the aim to convert both unreacted methane and CO₂/H₂O for improved syngas yields.

Rh (0.4 wt.%) promoted Al₂O₃ was used as the secondary reforming bed in a sequential bed chemical looping reforming scheme to increase methane conversion and selectivity of syngas through dry and steam reforming reactions. Improvements in CH₄ conversion and syngas selectivity over single bed results are shown in Figure 4.5 for promoted redox catalysts, along with a schematic illustrating both single and sequential bed schemes. In all cases, the sequential bed chemical looping reforming scheme increased CH₄ conversion by at least 17% (on an absolute basis). The largest increase in CH₄ conversion occurred with Rh-CaMn_{0.95}Fe_{0.05}O₃, with a difference of 29% (absolute basis). The results indicated that this is a result of the high oxygen extraction and low methane conversion occurring in the first bed. The sequential bed chemical looping reforming scheme was also effective in producing syngas, with all cases showing syngas selectivity above 88%. This was most notable with Rh-CaMn_{0.95}Fe_{0.05}O₃ and Rh-CaMn_{0.75}Fe_{0.25}O₃, where syngas selectivity increase by 94% and 87%, respectively.

These results demonstrate the usefulness of Rh-Ca_xA_{1-x}Mn_xB_{1-x}O₃ (A = Sr, B = Fe, x = 0.95 or 0.75) as an oxygen source in the sequential bed chemical looping reforming scheme. This concept is exemplified when comparing Rh-CaMnO₃ and Rh-CaMn_{0.95}Fe_{0.05}O₃. Under chemical looping reforming, Rh-CaMnO₃ converted twice as much methane (20% vs 10%) and was much more selective (71% vs 1%). However, in the sequential bed chemical looping reforming scheme they had similar amounts of CH₄ conversion (41% vs. 39%) and syngas selectivity (91% vs. 95%). This is directly attributed to possessing similar amounts of oxygen extraction (4.1 wt.% vs 4.5 wt.%).

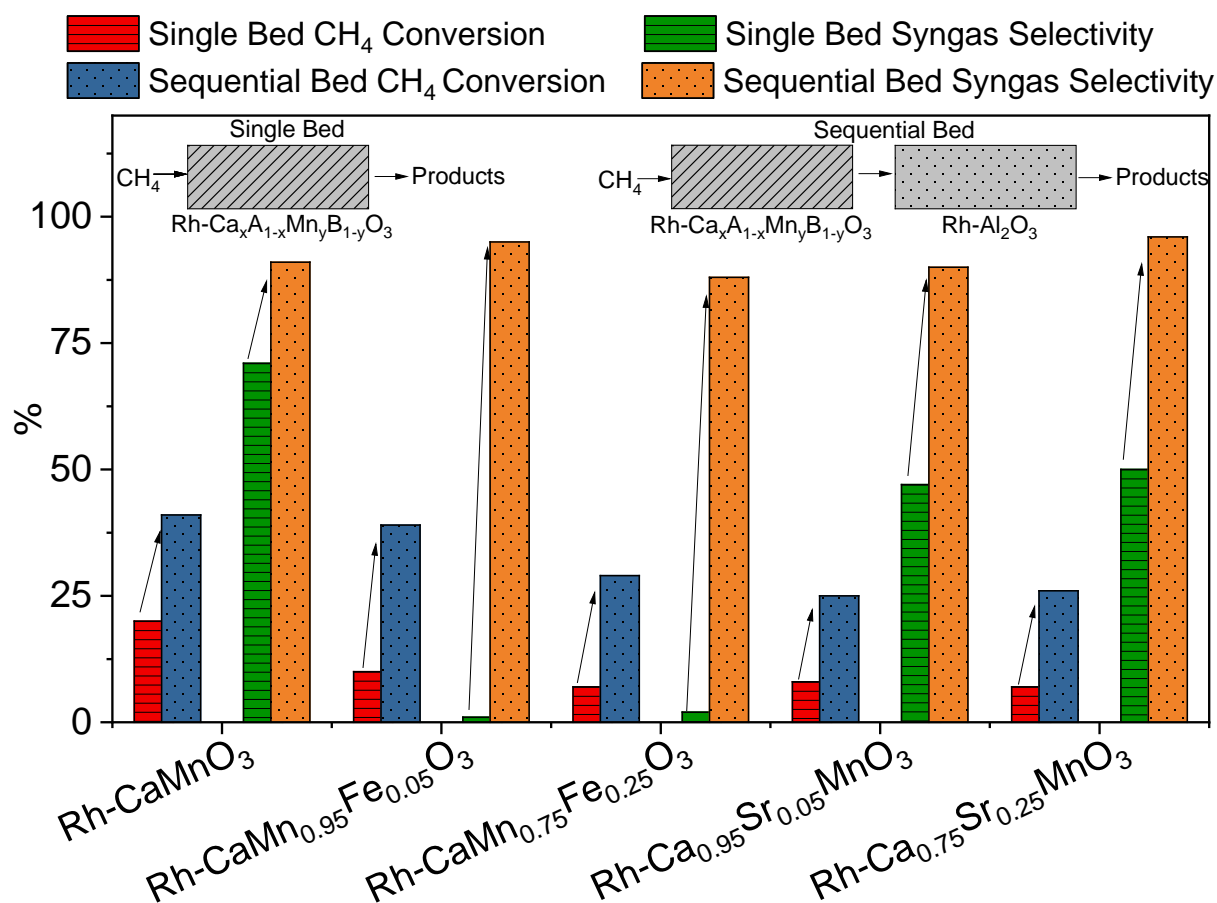


Figure 4.5: CH₄ conversion and syngas selectivity in the sequential bed chemical looping reforming scheme for promoted redox catalysts, shown as difference in conversion and selectivity over single bed. Reduction is 15 minutes long with 5% CH₄. Oxidation is 10 minutes long with 5.8% O₂ at 600°C. GHSV = 12000 hr⁻¹.

To shed light on the behavior of these redox catalysts with respect to oxidation state of the redox catalyst, CH₄ conversion and CO selectivity are examined as a function of time in the sequential bed CLR scheme. The instantaneous CH₄ conversion is shown in Figure 4.6a, when Rh-CaMnO₃, Rh-CaMn_{0.95}Fe_{0.05}O₃, and Rh-CaMn_{0.95}Fe_{0.05}O₃ is used. CH₄ conversion in all cases decreased with respect to time. However, the nature of this decrease was different depending on the redox catalyst. When Rh-CaMnO₃ and Rh-Ca_{0.95}Sr_{0.05}MnO₃ are used, a sudden decrease in CH₄ conversion occurred at 7 and 4.5 minutes, respectively. With Rh-CaMnO₃, CH₄ conversion dropped from 60% to 29%. With Rh-Ca_{0.95}Sr_{0.05}MnO₃, CH₄ conversion dropped from 55% to 20%.

In contrast, Rh-CaMn_{0.95}Fe_{0.05}O₃ displayed a gradual decrease in CH₄ conversion from 60% to 30%. Instantaneous CO selectivity is shown in Figure 4.6b. Rh-CaMnO₃ and Rh-Ca_{0.95}Sr_{0.05}MnO₃ showed a sudden increase in CO selectivity at 7 and 4.5 minutes, respectively. For Rh-CaMnO₃, CO selectivity increase from 90% to 98%. With Rh-Ca_{0.95}Sr_{0.05}MnO₃, CO selectivity increased from 85% to 97%. Rh-CaMn_{0.95}Fe_{0.05}O₃ showed a slow increase in CO selectivity across the entire reduction. It should be noted that syngas selectivity was above 75% in across the entire reduction for Rh-CaMn_{0.95}Fe_{0.05}O₃, suggesting selectivity is not significantly affected by the oxidation state of Rh-CaMn_{0.95}Fe_{0.05}O₃. The step change in CO selectivity for Rh-CaMnO₃ and Rh-Ca_{0.95}Sr_{0.05}MnO₃ corresponded to the step change seen for CH₄ conversion. In Figure B.4, all promoted redox catalysts are shown and the reduction behavior of Rh-Ca_{0.75}Sr_{0.25}MnO₃ and Rh-CaMn_{0.75}Fe_{0.25}O₃ was very similar to Rh-Ca_{0.95}Sr_{0.05}MnO₃ and CaMn_{0.95}Fe_{0.05}O₃, respectively.

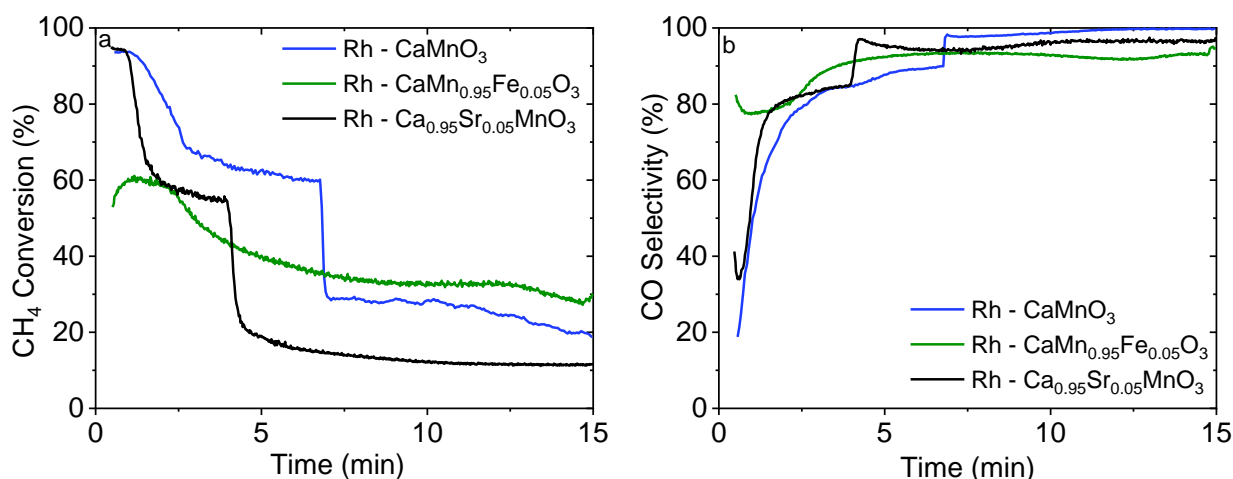


Figure 4.6: a) Instantaneous CH₄ conversion and b) Instantaneous CO Selectivity of Rh - CaMnO₃, Rh - CaMn_{0.95}Fe_{0.05}O₃, Rh - Ca_{0.95}Sr_{0.05}MnO₃ during dual bed experiments. Reduction is 15 minutes with 5% CH₄. Oxidation is 10 minutes long with 5.8% O₂ at 600°C. GHSV = 12000 hr⁻¹.

Examining syngas yield with respect to oxygen extraction rate can help elucidate the relationship between oxygen extraction and syngas yield. In Figure 4.7, syngas yield was shown as a function of oxygen extraction rate for Fe doped redox catalysts. In general, a higher oxygen

extraction will lead to a higher syngas yield. This result indicates that, in the presence of a reforming bed, increased supply of oxygen would lead to increased syngas productivity so long as methane is not the limiting reactant. We note, however, syngas yield can also be affected by the redox catalyst, even at similar oxygen extraction rates.

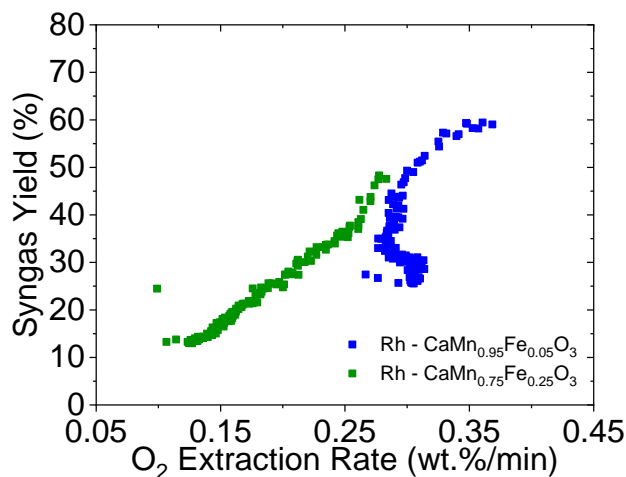


Figure 4.7: Syngas yields vs. oxygen extraction rate for Rh-CaMn_{0.95}Fe_{0.05}O₃ and Rh-CaMn_{0.75}Fe_{0.25}O₃. Reduction is 15 minutes long with 5% CH₄. Oxidation is 10 minutes long with 5.8% O₂ at 600°C. GHSV = 12000 hr⁻¹. Minutes 1.5-15 of reduction are shown.

Syngas yield optimization

Attempts were made to improve syngas yield by varying the operating conditions such as residence time, redox step durations, and reaction temperature. Modifying the reduction and oxidation time is particularly interesting due to the previously discussed differences in the reduction behavior of Rh-CaMnO₃ and Fe doped Rh-CaMnO₃. While they show differences across time, the first five minutes of reduction display higher amounts of methane conversion and oxygen extraction. However, the syngas selectivity is lower in this region. Varying oxidation state can potentially address this by finding a region where there is a balance between high CH₄ conversion and syngas selectivity. This being said, Rh-CaMnO₃, Rh-CaMn_{0.95}Fe_{0.05}O₃, and Rh-CaMn_{0.75}Fe_{0.25}O₃ were reduced at 3, 5, and 7 minutes and oxidized for 1, 1.5, 3 and 5 minutes to

identify optimal redox times (equivalently oxidation state range, also see Figure B.5 and B.6). These experiments showed optimal redox times of: 5 minutes reduction and 3 minutes oxidation for Rh-CaMnO₃, and 3 minutes oxidation and 5 minutes reduction for Rh-CaMn_{0.95}Fe_{0.05}O₃ and CaMn_{0.75}Fe_{0.25}O₃.

These optimal oxidation and reduction times were also used at 650°C and 700°C. These experiments are expected to result in higher methane conversion, due to higher amounts of oxygen release by the redox catalyst. Figure 4.8a summarizes the effect of operating temperature whereas Figure 4.8b illustrates the effect to space velocity at 600°C. The most notable observation is that the iron substituted samples reached CH₄ conversions near 100% at 700°C. Rh-CaMnO₃, on the other hand, seems to reach a limit around 70%. The increase in CH₄ conversion is accompanied by a decrease in selectivity in all cases. Despite this, there was an increase in yield with Rh-CaMn_{0.95}Fe_{0.05}O₃ and Rh-CaMn_{0.75}Fe_{0.25}O₃ showing a yield over 70%. An alternative approach to increasing methane conversion and syngas yield is by decreasing gas hourly space velocity. As shown in Figure 4.8b, 73% syngas yield was obtained using Rh-CaMn_{0.75}Fe_{0.25}O₃ at 6000 hr⁻¹. In comparison, CaMnO₃ showed a syngas yield of 54%.

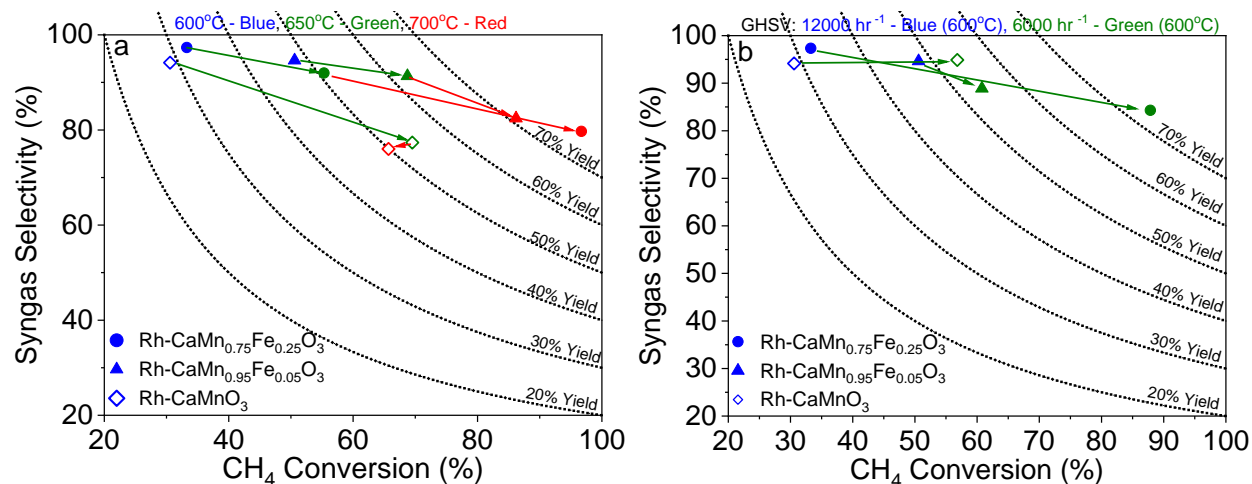


Figure 4.8: a) Effect of temperature and b) GHSV on syngas selectivity, CH₄ conversion, and yield for Rh promoted CaMn_{0.75}Fe_{0.25}O₃, Ca_{0.75}Sr_{0.25}MnO₃, and CaMnO₃. Rh-CaMn_{0.75}Fe_{0.25}O₃ and Rh-CaMn_{0.95}Fe_{0.05}O₃ are oxidized for 5 minutes and reduced for 3 minutes. Rh-CaMnO₃ is oxidized for 3 minutes and reduced for 5 minutes.

To demonstrate the redox stability of Rh-CaMn_{0.75}Fe_{0.25}O₃, mass spec results from a 50 redox cycles experiments are summarized in Figure 4.9, with the concentration of CH₄, CO₂, CO, and H₂ during the reduction half cycles illustrated. It is clear that the results are stable across all 50 cycles, with only a slight increase in syngas yield production. This could be related to a drift in mass spectrometry sensitivity, with calibrations taken after cycle 50. With this sample being cycled 100+ times prior to the experiment and these reaction conditions being repeatable across 50 cycles, the results indicate the sample will exhibit excellent long term stability.

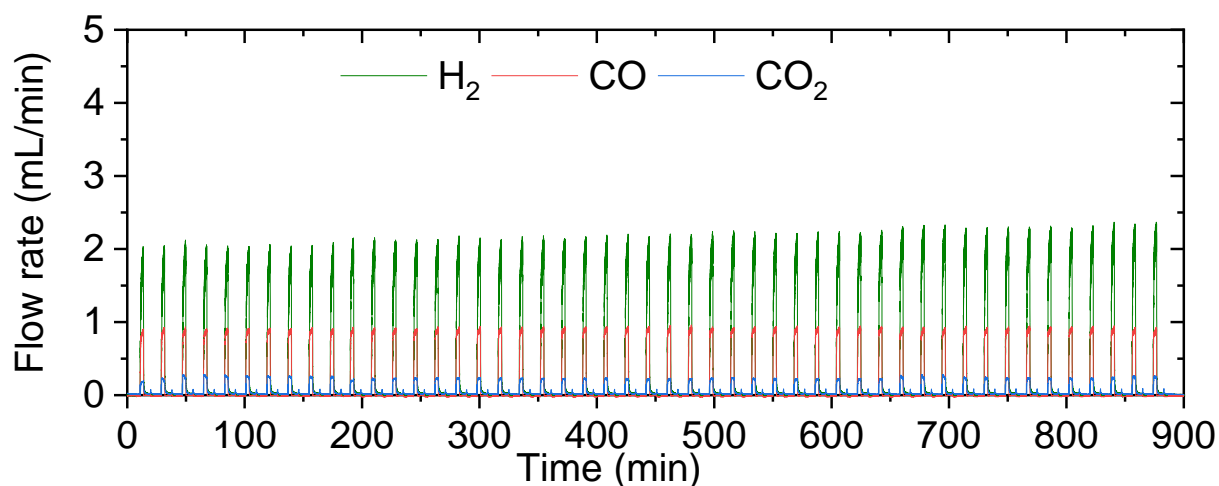


Figure 4.9: CH₄ conversion and syngas selectivity across all 50 cycles for Rh-CaMn_{0.75}Fe_{0.25}O₃. GHSV is 6000 hr⁻¹, temperature is 600°C, 5 minutes of oxidation and 3 minutes of reduction are used.

4.4 Conclusions

This article investigates the low temperature application of Rh promoted Ca_xA_{1-x}Mn_xB_{1-x}O₃ (A = Sr, B = Fe, x = 0.95 or 0.75) as a standalone redox catalysts for methane partial oxidation as well as an oxygen source in the sequential bed chemical looping reforming scheme, where these redox catalysts are combined with a secondary reforming bed. As a standalone redox catalyst, Rh promoted CaMnO₃ showed syngas selectivity of 81% at 600°C. Fe doping resulted in a redox catalyst with syngas selectivity below 5% and Sr doping resulted in syngas selectivity between 40

and 45%. TPD experiments indicate that redox catalysts with increased tendency for spontaneous oxygen release correspond to lower syngas selectivity when used as a standalone redox catalyst. When a reforming catalyst bed composed of Rh promoted Al_2O_3 , was placed downstream of these redox catalysts, significant increase in syngas selectivity and product yield were observed for all the redox catalyst samples. The effect of this sequential bed scheme was most pronounced with use of Rh promoted $\text{CaMn}_{0.95}\text{Fe}_{0.05}\text{O}_3$. CH_4 conversion increased from 10% to 39% and syngas selectivity increased from 1% to 95%. The significant increase in CH_4 conversion was attributed to the high oxygen capacity (4.5 wt.%) and redox activity of Rh promoted $\text{CaMn}_{0.95}\text{Fe}_{0.05}\text{O}_3$. Further optimization of Rh- $\text{CaMn}_{0.75}\text{Fe}_{0.25}\text{O}_3$, by adjusting the operating conditions resulted in over 70% syngas yield at 600°C . This study showed Rh promotion of CaMnO_3 based redox catalysts will result in a highly active material and when utilized in a sequential bed chemical looping reforming scheme, significant syngas yields can be achieved at a relatively operating low temperature.

4.5 References

1. U.S. Crude Oil, Natural Gas, and Natural Gas Proved Reserves, Year-end 2015 <https://www.eia.gov/naturalgas/crudeoilreserves/> (accessed Sep 26, 2018).
2. U.S. Dry Natural Gas Expected Future Production (Billion Cubic Feet) https://www.eia.gov/dnav/ng/hist/rngr11nus_1a.htm (accessed Sep 26, 2018).
3. How much carbon dioxide is produced when different fuels are burned? - FAQ - U.S. Energy Information Administration (EIA) <https://www.eia.gov/tools/faqs/faq.php?id=73&t=11> (accessed Oct 28, 2018).
4. Rostrup-Nielsen, J. R. Syngas in Perspective. *Catalysis Today* **2002**, *71* (3), 243–247. [https://doi.org/10.1016/S0920-5861\(01\)00454-0](https://doi.org/10.1016/S0920-5861(01)00454-0).
5. Wilhelm, D. J.; Simbeck, D. R.; Karp, A. D.; Dickenson, R. L. Syngas Production for Gas-to-Liquids Applications: Technologies, Issues and Outlook. *Fuel Processing Technology* **2001**, *71* (1), 139–148. [https://doi.org/10.1016/S0378-3820\(01\)00140-0](https://doi.org/10.1016/S0378-3820(01)00140-0).
6. Takeshita, T.; Yamaji, K. Important Roles of Fischer–Tropsch Synfuels in the Global Energy Future. *Energy Policy* **2008**, *36* (8), 2773–2784. <https://doi.org/10.1016/j.enpol.2008.02.044>.
7. Agrafiotis, C.; von Storch, H.; Roeb, M.; Sattler, C. Solar Thermal Reforming of Methane Feedstocks for Hydrogen and Syngas Production—A Review. *Renewable and Sustainable Energy Reviews* **2014**, *29*, 656–682. <https://doi.org/10.1016/j.rser.2013.08.050>.
8. Abatzoglou, N.; Fauteux-Lefebvre, C. Review of Catalytic Syngas Production through Steam or Dry Reforming and Partial Oxidation of Studied Liquid Compounds. *Wiley Interdisciplinary Reviews: Energy and Environment* **2016**, *5* (2), 169–187. <https://doi.org/10.1002/wene.167>.
9. Adanez, J.; Abad, A.; Garcia-Labiano, F.; Gayan, P.; de Diego, L. F. Progress in Chemical-Looping Combustion and Reforming Technologies. *Progress in Energy and Combustion Science* **2012**, *38* (2), 215–282. <https://doi.org/10.1016/j.pecs.2011.09.001>.
10. Tang, M.; Xu, L.; Fan, M. Progress in Oxygen Carrier Development of Methane-Based Chemical-Looping Reforming: A Review. *Applied Energy* **2015**, *151*, 143–156. <https://doi.org/10.1016/j.apenergy.2015.04.017>.
11. Zafar, Q.; Mattisson, T.; Gevert, B. Integrated Hydrogen and Power Production with CO₂ Capture Using Chemical-Looping Reforming Redox Reactivity of Particles of CuO, Mn₂O₃, NiO, and Fe₂O₃ Using SiO₂ as a Support. *Ind. Eng. Chem. Res.* **2005**, *44* (10), 3485–3496. <https://doi.org/10.1021/ie048978i>.

12. Rydén, M.; Lyngfelt, A.; Mattisson, T.; Chen, D.; Holmen, A.; Bjørgum, E. Novel Oxygen-Carrier Materials for Chemical-Looping Combustion and Chemical-Looping Reforming; $\text{La}_x\text{Sr}_{1-x}\text{Fe}_y\text{Co}_{1-y}\text{O}_{3-\delta}$ Perovskites and Mixed-Metal Oxides of NiO, Fe_2O_3 and Mn_3O_4 . *International Journal of Greenhouse Gas Control* **2008**, *2* (1), 21–36. [https://doi.org/10.1016/S1750-5836\(07\)00107-7](https://doi.org/10.1016/S1750-5836(07)00107-7).
13. Forutan, H. R.; Karimi, E.; Hafizi, A.; Rahimpour, M. R.; Keshavarz, P. Expert Representation Chemical Looping Reforming: A Comparative Study of Fe, Mn, Co and Cu as Oxygen Carriers Supported on Al_2O_3 . *Journal of Industrial and Engineering Chemistry* **2015**, *21*, 900–911. <https://doi.org/10.1016/j.jiec.2014.04.031>.
14. Rydén, M.; Lyngfelt, A.; Mattisson, T.; Chen, D.; Holmen, A.; Bjørgum, E. Novel Oxygen-Carrier Materials for Chemical-Looping Combustion and Chemical-Looping Reforming; $\text{La}_x\text{Sr}_{1-x}\text{Fe}_y\text{Co}_{1-y}\text{O}_{3-\delta}$ Perovskites and Mixed-Metal Oxides of NiO, Fe_2O_3 and Mn_3O_4 . *International Journal of Greenhouse Gas Control* **2008**, *2* (1), 21–36. [https://doi.org/10.1016/S1750-5836\(07\)00107-7](https://doi.org/10.1016/S1750-5836(07)00107-7).
15. Zafar, Q.; Mattisson, T.; Gevert, B. Integrated Hydrogen and Power Production with CO_2 Capture Using Chemical-Looping Reforming Redox Reactivity of Particles of CuO , Mn_2O_3 , NiO, and Fe_2O_3 Using SiO_2 as a Support. *Ind. Eng. Chem. Res.* **2005**, *44* (10), 3485–3496. <https://doi.org/10.1021/ie048978i>.
16. Rydén, M.; Lyngfelt, A.; Mattisson, T. Chemical-Looping Combustion and Chemical-Looping Reforming in a Circulating Fluidized-Bed Reactor Using Ni-Based Oxygen Carriers. *Energy Fuels* **2008**, *22* (4), 2585–2597. <https://doi.org/10.1021/ef800065m>.
17. Shafieifarhood, A.; Galinsky, N.; Huang, Y.; Chen, Y.; Li, F. $\text{Fe}_2\text{O}_3@ \text{La}_x\text{Sr}_{1-x}\text{FeO}_3$ Core-Shell Redox Catalyst for Methane Partial Oxidation. *ChemCatChem* **2014**, *6* (3), 790–799. <https://doi.org/10.1002/cctc.201301104>.
18. Mattisson, T.; Johansson, M.; Lyngfelt, A. The Use of NiO as an Oxygen Carrier in Chemical-Looping Combustion. *Fuel* **2006**, *85* (5), 736–747. <https://doi.org/10.1016/j.fuel.2005.07.021>.
19. Oller, A. R.; Costa, M.; Oberdörster, G. Carcinogenicity Assessment of Selected Nickel Compounds. *Toxicology and Applied Pharmacology* **1997**, *143* (1), 152–166. <https://doi.org/10.1006/taap.1996.8075>.
20. Yusuf, S.; Neal, L. M.; Li, F. Effect of Promoters on Manganese-Containing Mixed Metal Oxides for Oxidative Dehydrogenation of Ethane via a Cyclic Redox Scheme. *ACS Catal.* **2017**, *7* (8), 5163–5173. <https://doi.org/10.1021/acscatal.7b02004>.
21. Shulman, A.; Cleverstam, E.; Mattisson, T.; Lyngfelt, A. Manganese/Iron, Manganese/Nickel, and Manganese/Silicon Oxides Used in Chemical-Looping With Oxygen Uncoupling (CLOU) for Combustion of Methane. *Energy Fuels* **2009**, *23* (10), 5269–5275. <https://doi.org/10.1021/ef9005466>.

22. Cho, P.; Mattisson, T.; Lyngfelt, A. Comparison of Iron-, Nickel-, Copper- and Manganese-Based Oxygen Carriers for Chemical-Looping Combustion. *Fuel* **2004**, *83* (9), 1215–1225. <https://doi.org/10.1016/j.fuel.2003.11.013>.
23. Mihai, O.; Chen, D.; Holmen, A. Catalytic Consequence of Oxygen of Lanthanum Ferrite Perovskite in Chemical Looping Reforming of Methane. *Ind. Eng. Chem. Res.* **2011**, *50* (5), 2613–2621. <https://doi.org/10.1021/ie100651d>.
24. He, F.; Zhao, K.; Huang, Z.; Li, X.; Wei, G.; Li, H. Synthesis of Three-Dimensionally Ordered Macroporous LaFeO₃ Perovskites and Their Performance for Chemical-Looping Reforming of Methane. *Chinese Journal of Catalysis* **2013**, *34* (6), 1242–1249. [https://doi.org/10.1016/S1872-2067\(12\)60563-4](https://doi.org/10.1016/S1872-2067(12)60563-4).
25. Mishra, A.; Galinsky, N.; He, F.; E. Santiso, E.; Li, F. Perovskite-Structured AM_n x B_{1-x} O₃ (A = Ca or Ba; B = Fe or Ni) Redox Catalysts for Partial Oxidation of Methane. *Catalysis Science & Technology* **2016**, *6* (12), 4535–4544. <https://doi.org/10.1039/C5CY02186C>.
26. Haribal, V. P.; He, F.; Mishra, A.; Li, F. Iron-Doped BaMnO₃ for Hybrid Water Splitting and Syngas Generation. *ChemSusChem* **2017**, *10* (17), 3402–3408. <https://doi.org/10.1002/cssc.201700699>.
27. Shen, Q.; Huang, F.; Tian, M.; Zhu, Y.; Li, L.; Wang, J.; Wang, X. Effect of Regeneration Period on the Selectivity of Synthesis Gas of Ba-Hexaaluminates in Chemical Looping Partial Oxidation of Methane. *ACS Catal.* **2019**, *9* (1), 722–731. <https://doi.org/10.1021/acscatal.8b03855>.
28. Zhang, J.; Haribal, V.; Li, F. Perovskite Nanocomposites as Effective CO₂-Splitting Agents in a Cyclic Redox Scheme. *Science Advances* **2017**, *3* (8), e1701184. <https://doi.org/10.1126/sciadv.1701184>.
29. Rydén, M.; Lyngfelt, A.; Mattisson, T. Synthesis Gas Generation by Chemical-Looping Reforming in a Continuously Operating Laboratory Reactor. *Fuel* **2006**, *85* (12), 1631–1641. <https://doi.org/10.1016/j.fuel.2006.02.004>.
30. Rydén, M.; Lyngfelt, A.; Mattisson, T. Chemical-Looping Combustion and Chemical-Looping Reforming in a Circulating Fluidized-Bed Reactor Using Ni-Based Oxygen Carriers. *Energy Fuels* **2008**, *22* (4), 2585–2597. <https://doi.org/10.1021/ef800065m>.
31. Rydén, M.; Lyngfelt, A.; Mattisson, T.; Chen, D.; Holmen, A.; Bjørgum, E. Novel Oxygen-Carrier Materials for Chemical-Looping Combustion and Chemical-Looping Reforming; La_xSr_{1-x}Fe_yCo_{1-y}O_{3-δ} Perovskites and Mixed-Metal Oxides of NiO, Fe₂O₃ and Mn₃O₄. *International Journal of Greenhouse Gas Control* **2008**, *2* (1), 21–36. [https://doi.org/10.1016/S1750-5836\(07\)00107-7](https://doi.org/10.1016/S1750-5836(07)00107-7).

32. Shafiefarhood, A.; Zhang, J.; Michael Neal, L.; Li, F. Rh-Promoted Mixed Oxides for “Low-Temperature” Methane Partial Oxidation in the Absence of Gaseous Oxidants. *Journal of Materials Chemistry A* **2017**, *5* (23), 11930–11939. <https://doi.org/10.1039/C7TA01398A>.
33. Hallberg, P.; Rydén, M.; Mattisson, T.; Lyngfelt, A. CaMnO_{3-δ} Made from Low Cost Material Examined as Oxygen Carrier in Chemical-Looping Combustion. *Energy Procedia* **2014**, *63*, 80–86. <https://doi.org/10.1016/j.egypro.2014.11.009>.
34. Rydén, M.; Leion, H.; Mattisson, T.; Lyngfelt, A. Combined Oxides as Oxygen-Carrier Material for Chemical-Looping with Oxygen Uncoupling. *Applied Energy* **2014**, *113*, 1924–1932. <https://doi.org/10.1016/j.apenergy.2013.06.016>.
35. Mishra, A.; Li, T.; Li, F.; Santiso, E. E. Oxygen Vacancy Creation Energy in Mn-Containing Perovskites: An Effective Indicator for Chemical Looping with Oxygen Uncoupling. *Chem. Mater.* **2018**. <https://doi.org/10.1021/acs.chemmater.8b03187>.
36. Palcheva, R.; Olsbye, U.; Palcut, M.; Rauwel, P.; Tyuliev, G.; Velinov, N.; Fjellvåg, H. H. Rh Promoted La_{0.75}Sr_{0.25}(Fe_{0.8}Co_{0.2})_{1-x}Ga_xO_{3-δ} Perovskite Catalysts: Characterization and Catalytic Performance for Methane Partial Oxidation to Synthesis Gas. *Applied Surface Science* **2015**, *357*, 45–54. <https://doi.org/10.1016/j.apsusc.2015.08.237>.
37. Galinsky, N.; Sendi, M.; Bowers, L.; Li, F. CaMn_{1-x}B_xO_{3-δ} (B = Al, V, Fe, Co, and Ni) Perovskite Based Oxygen Carriers for Chemical Looping with Oxygen Uncoupling (CLOU). *Applied Energy* **2016**, *174*, 80–87. <https://doi.org/10.1016/j.apenergy.2016.04.046>.
38. Galinsky, N.; Mishra, A.; Zhang, J.; Li, F. Ca_{1-x}A_xMnO₃ (A = Sr and Ba) Perovskite Based Oxygen Carriers for Chemical Looping with Oxygen Uncoupling (CLOU). *Applied Energy* **2015**, *157*, 358–367. <https://doi.org/10.1016/j.apenergy.2015.04.020>.
39. Poeppelmeier, K. R.; Leonowicz, M. E.; Scanlon, J. C.; Longo, J. M.; Yelon, W. B. Structure Determination of CaMnO₃ and CaMnO_{2.5} by X-Ray and Neutron Methods. *Journal of Solid State Chemistry* **1982**, *45* (1), 71–79. [https://doi.org/10.1016/0022-4596\(82\)90292-4](https://doi.org/10.1016/0022-4596(82)90292-4).
40. Richardson, J. T.; Paripatyadar, S. A. Carbon Dioxide Reforming of Methane with Supported Rhodium. *Applied Catalysis* **1990**, *61* (1), 293–309. [https://doi.org/10.1016/S0166-9834\(00\)82152-1](https://doi.org/10.1016/S0166-9834(00)82152-1).
41. Erdohelyi, A.; Cserenyi, J.; Solymosi, F. Activation of CH₄ and Its Reaction with CO₂ over Supported Rh Catalysts. *Journal of Catalysis* **1993**, *141* (1), 287–299. <https://doi.org/10.1006/jcat.1993.1136>.

42. Wang, G.; Chen, M.; Zhou, M. Activation of Methane by Rh(0): Evidence for Direct Insertion of Rhodium into the C–H Bond at Cryogenic Temperatures. *Chemical Physics Letters* **2005**, *412* (1), 46–49. <https://doi.org/10.1016/j.cplett.2005.05.115>.
43. Rida, K.; Benabbas, A.; Bouremmad, F.; Peña, M. A.; Martínez-Arias, A. Surface Properties and Catalytic Performance of La_{1-x}Sr_xCrO₃ Perovskite-Type Oxides for CO and C₃H₆ Combustion. *Catalysis Communications* **2006**, *7* (12), 963–968. <https://doi.org/10.1016/j.catcom.2006.04.011>.
44. J. Crumlin, E.; Mutoro, E.; Liu, Z.; E. Grass, M.; D. Biegalski, M.; Lee, Y.-L.; Morgan, D.; M. Christen, H.; Bluhm, H.; Shao-Horn, Y. Surface Strontium Enrichment on Highly Active Perovskites for Oxygen Electrocatalysis in Solid Oxide Fuel Cells. *Energy & Environmental Science* **2012**, *5* (3), 6081–6088. <https://doi.org/10.1039/C2EE03397F>.
45. Zhu, X.; Li, K.; Neal, L.; Li, F. Perovskites as Geo-Inspired Oxygen Storage Materials for Chemical Looping and Three-Way Catalysis: A Perspective. *ACS Catal.* **2018**, *8* (9), 8213–8236. <https://doi.org/10.1021/acscatal.8b01973>.
46. Gao, Y.; Haeri, F.; He, F.; Li, F. Alkali Metal-Promoted La_xSr_{2-x}FeO_{4-δ} Redox Catalysts for Chemical Looping Oxidative Dehydrogenation of Ethane. *ACS Catal.* **2018**, *8* (3), 1757–1766. <https://doi.org/10.1021/acscatal.7b03928>.
47. Gao, Y.; Neal, L. M.; Li, F. Li-Promoted La_xSr_{2-x}FeO_{4-δ} Core–Shell Redox Catalysts for Oxidative Dehydrogenation of Ethane under a Cyclic Redox Scheme. *ACS Catal.* **2016**, *6* (11), 7293–7302. <https://doi.org/10.1021/acscatal.6b01399>.

Chapter 5: Spinel Oxides as a Coke Resistant Support for NiO Based Oxygen Carriers in Chemical Looping Combustion

5.1 Abstract

Nickel oxides are among the most extensively investigated oxygen carrier materials for chemical looping combustion and reforming of methane due to their high activity for methane activation and redox reactions. However, coke formation remains to be a key challenge for Ni containing oxygen carriers. The current study investigates the effect of reducible spinel-structured supports to provide coke resistance of NiO based oxygen carriers. Specifically, NiFe_2O_4 , MgFe_2O_4 , and BaFe_2O_4 are investigated as coke resistant supports for NiO due to their ability to provide active lattice oxygen in typical coking regimes. Inert MgAl_2O_4 supported NiO reduces in less two minutes. In contrast, the active spinel oxides provide lattice oxygen over 45 minutes. Under redox cycling, NiO supported on NiFe_2O_4 , MgFe_2O_4 , or BaFe_2O_4 did not show any signs of coke formation. Additionally, $\text{NiFe}_2\text{O}_4 + 0.5\text{NiO}$ displayed similar maximum oxygen capacity to $\text{MgAl}_2\text{O}_4 + 0.25\text{NiO}$ (2.5 wt.%/min vs. 2.3 wt.%/min). This indicates high methane conversion rates and coke resistance can be achieved with active spinel oxides. In-situ XRD studies revealed that initial weight loss in $\text{NiFe}_2\text{O}_4 + 0.5\text{NiO}$ is associated with formation of Ni and Fe_3O_4 . Subsequent coke inhibition was attributed to the slow reduction of Fe_3O_4 . While NiFe_2O_4 supported NiO shows signs of deactivation, MgFe_2O_4 and BaFe_2O_4 supported NiO emerged as a stable alternatives.

5.2 Introduction

As an active metal in heterogeneous catalysis, nickel has been studied for over a century due to its affinity with carbon and ability to break C-C and C-H¹⁻⁷. Notably, the methane activation energies on Ni foils has been reported to be similar to palladium and platinum foils⁷. In an era of

abundant natural gas^{8,9}, nickel's ability to activate methane is increasingly important and has subjected to extensively investigations. Two of the most commonly studied routes for methane utilization involving nickel containing heterogeneous catalysts are dry and steam reforming, where CO₂ or H₂O is used to convert methane to syngas.¹⁰⁻²⁰ Although catalysts with excellent activities have been developed and commercially utilized for steam methane reforming (SMR), coke formation and subsequent deactivation remain to be an important challenge that affects the catalyst stability and lifetime.²¹⁻²⁵ This is particularly the case of dry reforming. Various strategies have been investigated to inhibit coke formation for Ni based catalysts such as varying supports (e.g. Al₂O₃¹⁰, SiO₂^{10-12,20}, spinels^{10,13}, etc), promoters²⁶⁻²⁹, preparation methods³⁰⁻³², and enclosing Ni into core-shell structures.³³⁻³⁵ Although some of these studies have rendered highly promising catalysts, complete avoidance of coke formation is still a challenge.

More recently, nickel oxide has been studied for carbon capture from methane via chemical looping combustion (CLC).^{21,36-42} In CLC, methane is indirectly combusted, by the lattice oxygen of a metal oxide based oxygen carrier, in a two-step redox process. The first step involves methane oxidation (combustion) by the metal oxide. As a result, the metal oxide is reduced. The second step re-oxidizes the reduced metal oxide with air to complete the redox loop. As such, the metal oxide functions as an oxygen carrier to separate oxygen from air and to prevent N₂ dilution of the combustion flue gas, thereby mitigating the separation cost for carbon dioxide capture. While CLC is a promising concept and nickel oxide based oxygen carriers have shown excellent redox kinetics³⁶, coke formation still represents a major challenge for the Ni containing oxygen carriers. For instance, fluidized bed study of NiO supported on NiAl₂O₄ indicated that 18.7% of gaseous methane was converted to coke within 3 minutes of reaction time at 950°C.²¹ Such a high yield of coke can lead to decreased process efficiency and carbon capture. Many attempts have been made

to take advantage of the high activity of nickel oxides while avoiding coke formation, mostly through the use of supports such as Al_2O_3 , NiAl_2O_4 , MgAl_2O_4 , and YSZ^{22,36,43–47}. Of these supports, spinel oxides have shown promising results due to their strong interaction with nickel^{43,46,48}, with nickel being partially or fully incorporated into the spinel structure. However, co-feeding steam in chemical looping operations at a $\text{CH}_4:\text{H}_2\text{O}$ ratio of at least 1:1 was nevertheless required to fully avoid coke formation during reduction of nickel oxide^{43,46,48}. Coke formation in chemical looping is typically seen during the later stages of metal oxide reduction^{21,49}. We note that coke formation typically occur towards the later stage of the metal oxide reduction. Cho et al.²¹ showed that the onset of coke formation on nickel corresponds to when 80% of nickel oxide lattice oxygen is consumed. Similarly, Neal et al.⁴⁹ and Shafieifarhood et al.⁵⁰ showed reduction of $\text{Fe}_2\text{O}_3@ \text{La}_{0.8}\text{Sr}_{0.2}\text{FeO}_3$ can be divided in four consecutive regions, wherein the last region is dominated by methane decomposition to H_2 and coke due to depletion of lattice oxygen. As such, an “active” support that can provide a steady yet slow flux of lattice oxygen can potentially inhibit coke formation on the active metal oxides such as NiO or FeO_x . In particular, spinel oxides with reducible cations are capable of slow release of oxygen over long periods of time^{51–54}. Using NiFe_2O_4 as an example, it required roughly 10 times longer than NiO to reach 90% conversion of the metal oxide⁵¹.

The aim of this study is to evaluate the effect of active lattice oxygen in spinel oxides on coke resistance. We investigated NiFe_2O_4 , BaFe_2O_4 , and MgFe_2O_4 as active spinel supports to inhibit coke formation since they were all reported contain active lattice oxygen^{51,53,54}. For comparison purpose, inert MgAl_2O_4 support is also studied. The oxygen carriers are prepared as $\text{AB}_2\text{O}_4 + x\text{NiO}$ ($x = 0.25, 0.5$) and evaluated with redox cycling. The phase behavior of $\text{NiFe}_2\text{O}_4 + 0.5\text{NiO}$ is examined in detail to elucidate the phase-transition behavior of redox cycling. Our

results indicate that NiFe_2O_4 , MgFe_2O_4 , and BaFe_2O_4 supports inhibit coke formation at all the investigated NiO loadings. In comparison, significant coke forms on MgAl_2O_4 supported oxygen carrier after 2.5 minutes of reduction. NiFe_2O_4 and BaFe_2O_4 supported NiO showed similar maximum oxygen release rate at 2.5 – 2.8 wt.%/min when compared to that for $\text{MgAl}_2\text{O}_4 + 0.25\text{NiO}$ (2.3 wt.%/min). $\text{NiFe}_2\text{O}_4 + 0.5\text{NiO}$ showed the highest oxygen capacity at 19 wt.%. However, it exhibited deactivation. MgFe_2O_4 supported NiO displayed a moderated amount of oxygen capacity at 16 wt.% and redox stability.

5.3 Experimental

5.3.1 Oxygen Carrier Synthesis

A modified Pechini method was used to prepare the aforementioned oxygen carriers. Stoichiometric amounts of metal nitrates, *e.g.* $\text{Ni}(\text{NO}_3)_2 \cdot 6\text{H}_2\text{O}$ and $\text{Fe}(\text{NO}_3)_3 \cdot 9\text{H}_2\text{O}$ for NiFe_2O_4 , were dissolved in deionized water. Next, citric acid (CA, Sigma Aldrich) was added at a molar ratio of 2.5:1 to the total amount of metal cations and the solution was heated to 50°C and held at this temperature for 30 minutes. This results in a mixed-metal citric acid complex with good dispersion of metal ions. Ethylene glycol (EG, Sigma Aldrich) was added next at a molar ratio of 1.5:1 to the moles of citric acid at 80°C until a gel formed. This gel was dried in an oven at slightly above boiling temperature of water to remove any moisture. Finally, the sample was sintered at 1200°C for 12 hours to ensure proper phase formation. The oxygen carriers are nominally prepared as $\text{NiFe}_2\text{O}_4 + x\text{NiO}$ ($x = 0, 0.25, 0.5$), $\text{MgFe}_2\text{O}_4 + x\text{NiO}$ ($x = 0, 0.25, 0.5$), $\text{BaFe}_2\text{O}_4 + x\text{NiO}$ ($x = 0, 0.25, 0.5$), and $\text{MgAl}_2\text{O}_4 + 0.25\text{NiO}$. Commercial MgAl_2O_4 (Noah Technologies) was used, when the spinel alone was tested.

5.3.2 Phase Characterization

X-ray powder diffraction (XRD) was used to identify the crystalline phases present in each sample. The XRD pattern was obtained using a Rigaku SmartLab X-ray diffractometer with CuK_α ($\lambda = .1542$) radiation operating at 40kV and 44mA. Scanning was conducted in a step-wise approach with a step size of 0.1° over 2θ range of $20\text{--}80^\circ$ and a scan time of 4.5s at each step. HighScore Plus[®] software was used for phase matching.

An additional x-ray diffraction pattern of $\text{NiFe}_2\text{O}_4 + 0.5\text{NiO}$ was obtained using a PANalytical Empyrean diffractometer under CuK_α radiation from a sealed tube generator at 45kV and 40mA, with PIXcel1D detector at room temperature. Measurement was taken under Bragg-Brentano configuration using a spinning sample stage over a 2θ range of $10\text{--}100^\circ$ at 0.0263° step size and 4.0s per step. The phases of freshly prepared samples were confirmed by XRD and shown in Figure 5.7 and C.10-C.12.

5.3.3 In-Situ Phase Characterization

Diffraction patterns were also collected during a temperature programmed reduction (TPR) using a PANalytical Empyrean diffractometer and a XRK900 Stage. A CuK_α radiation from a sealed tube generator at 45kV and 40mA was used. A ramping rate of $10^\circ\text{C}/\text{min}$ was used from room temperature to 500°C and a ramping rate of $2^\circ\text{C}/\text{min}$ was used from 500°C to 900°C . Each scan was five minutes long over a 2θ range of $40\text{--}65^\circ$ and used a step size of 0.013° . The reactive gas used was a 3% H_2 with balance argon (5.0 grade) using a flow rate of 30 sccm. To calculate the weight loss of the oxygen carriers, during reduction, the weight during the purge step before cycle 2 was used at 100% of the oxygen carrier weight.

5.3.4 Redox and Reaction Testing.

Redox testing was also tested at 900°C in a SETARAM SETSYS Evolution Thermal Gravimetric Analyzer (TGA) with reactant gases delivered from a computer controlled gas-mixing panel. 50 mg of sample was used. Reduction and oxidation steps were performed in 10% methane (5.0 grade) and 10% oxygen (extra dry grade) respectively with helium (5.0 grade) as the inert gas. The total gas flow rate during these steps was 200 mL/min to remove external mass transfer resistance. Redox tests consisted of 10 cycles with reduction lasting 15 minutes and oxidation lasting 20 minutes. 10 minutes of purging with 180 mL/min with argon was used between reduction and oxidation steps. 50 mg of redox catalyst with a particle size below 150 microns was used.

Long term reduction studies were conducted at 900°C in a SETARAM SETSYS Evolution Thermal Gravimetric Analyzer (TGA) with reactant gases delivered from a computer controlled gas-mixing panel. Spinel oxides (NiFe_2O_4 , BaFe_2O_4 , MgFe_2O_4 , and MgAl_2O_4) were reduced for 45 minutes to compare their oxygen release vs time. 50 mg of sample was used. Reduction was performed in 10% methane (5.0 grade) with helium (5.0 grade) as the inert gas. The total gas flow rate during these steps was 200 mL/min to remove external mass transfer resistance. Before the long term reduction, the samples were cycled once according to the redox testing procedure.

The oxygen capacity is represented as a weight percent of the fully oxidized oxygen carrier. To calculate the oxygen capacity of the oxygen carriers, during reduction, the weight during the purge step before cycle 2 was used at 100% of the oxygen carrier weight. In Figure C.1, a blank experiment is shown, verifying the weight under purging and reducing conditions are indistinguishable. The weight change between purge and oxidizing conditions are 0.17 mg, and was expected to change depending on the crucible. While this was negligible compared to the

overall weight change during oxidization of oxygen carriers, the weight during oxidization was only compared between cycles and not oxygen carriers. A quadrupole mass spectrometer (QMS, MKS Cirrus II) was used to measure the products of the reduction and oxidation steps. A set of calibrations was applied to the signals obtained from the QMS. Production of CO, CO₂, and H₂ was calculated by integrating the calibrated signals of CO and CO₂, and H₂. CO₂ produced during oxidation of the redox catalyst were used to quantify coke formation during redox and long term reduction as shown below.

Hydrogen (5.0 Grade) TPR was conducted using a TGA (TA SDT Q600) with 3% hydrogen balance helium or argon (5.0 grade) at a total flowrate of 200 sccm and a ramp rate of 2°C/min to 900°C. 20mg of sample was used.

5.4 Results and discussion

5.4.1 Spinel Oxides Selection and Redox Behavior

A key performance parameter of an oxygen carrier is its activity. Therefore, a desirable support should enhance the redox activity of NiO. We note that NiFe₂O₄, MgFe₂O₄, and BaFe₂O₄ supports are redox active^{51,53,54}. It is therefore important to establish the relative redox activities of the supports. We note that the maximum theoretical oxygen capacities of NiFe₂O₄, MgFe₂O₄, and BaFe₂O₄ are 27.3 wt.%, 24.0 wt.%, and 15.3 wt.%, respectively. In addition, magnesium and barium are not reducible whereas Ni²⁺ can reduce to a metallic phase. These differences are expected to affect lattice oxygen activity and therefore support performance. To provide understanding of this, these support materials were reduced with methane. Reduction was conducted using 10% CH₄ at 900°C over 45 minutes. Oxygen capacity at 3, 15, and 40 minutes are shown in Figure 5.1a. At 3 and 15 minutes NiFe₂O₄ showed the highest oxygen capacity and at 40 minutes it showed the second most oxygen capacity. MgFe₂O₄ showed the most oxygen

capacity at 40 minute and the second most oxygen capacity at 3 and 15 minutes. During re-oxidation, MgFe_2O_4 and BaFe_2O_4 showed coke formation and integration of CO_2 products gives coke formation of 6.7 wt.% and 0.68 wt.% However, coke formation is likely to have occurred during the last five minutes of reduction, as there is a noticeable increase in H_2 production (shown in Figure C.2). This was also accompanied by a large depletion of lattice oxygen. At 40 minutes, the oxygen capacity of MgFe_2O_4 and BaFe_2O_4 was 19.7 wt% and 11.4 wt%, corresponding to 82% and 75% of active lattice oxygen. This is consistent with the findings of Neal et al⁴⁹, where depletion of lattice oxygen led to coking. However, since the typical contact time for methane CLC is in the order of minutes, these active supports would have plenty of active lattice oxygen to inhibit coking. Additionally, all of three supports regained their lattice oxygen during oxidation (shown in Figure C.2). Figure 5.1b shows the rate of oxygen capacity of MgFe_2O_4 , NiFe_2O_4 , and BaFe_2O_4 at different points during reduction. The maximum oxygen release rate of MgFe_2O_4 , NiFe_2O_4 , and BaFe_2O_4 are 3.5 wt./min, 2.5 wt./min, and 0.5 wt./min. With the reduction half cycle likely to be limited to short reduction times, the oxygen capacity during early stages of reduction times is particularly important. At both 3 and 15 minutes, NiFe_2O_4 showed the highest oxygen capacity. As such, NiFe_2O_4 , as a substrate, is likely to be most robust in inhibition of coke.

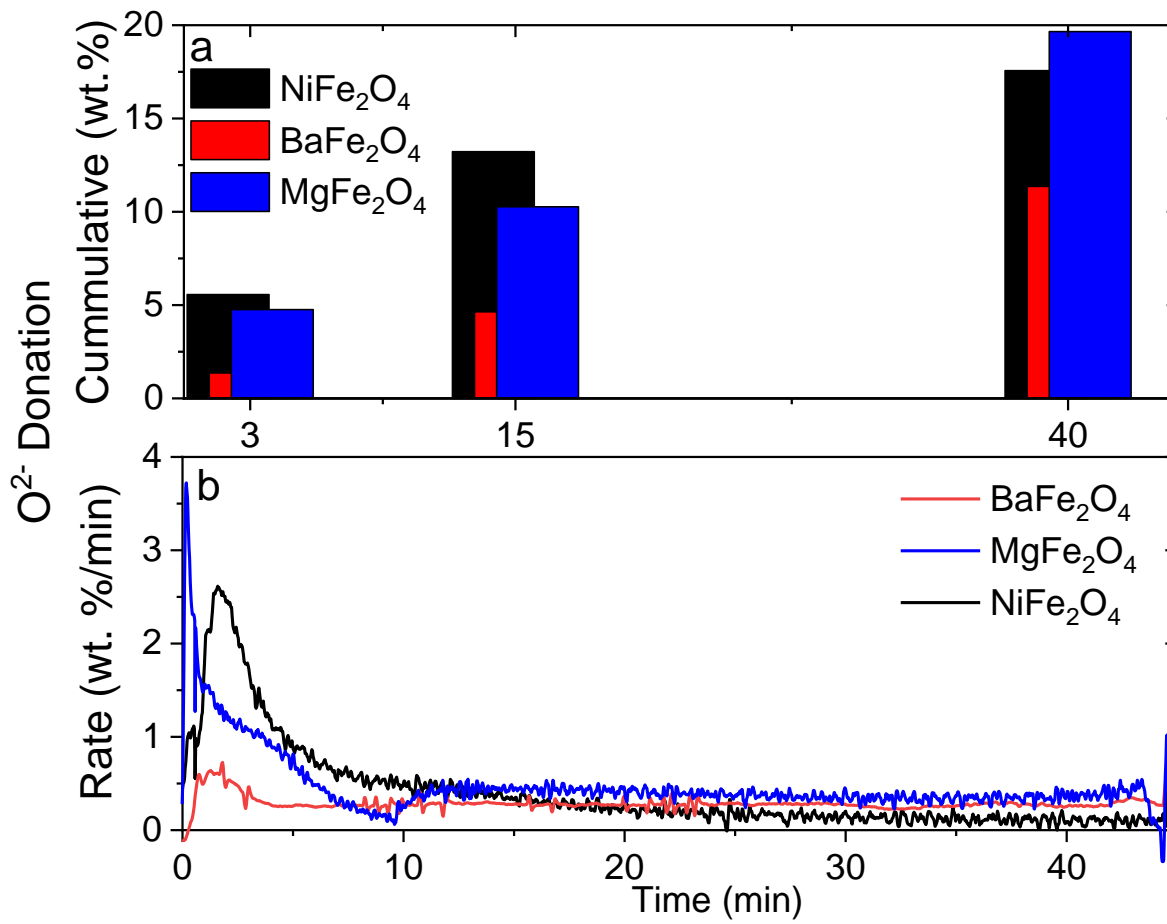


Figure 5.1: a) Cumulative oxygen donation (capacity) from MgAl₂O₄, BaFe₂O₄, MgFe₂O₄, and NiFe₂O₄ at 3, 15, and 40 mins and b) oxygen release rate of BaFe₂O₄, MgFe₂O₄, and NiFe₂O₄ under during reduction in 10% CH₄ at 900°C over 45 minutes.

5.4.2 Active Spinel Oxides as Supports for Coke Inhibition

Oxygen carriers prepared as AB₂O₄ + 0.25NiO are tested for coke resistance at 900°C with 15 minutes of reduction using 10% CH₄. MgAl₂O₄ + 0.25NiO is used as a reference for NiO reduction kinetics under an inert support. The oxygen capacity at 3, 9, and 15 minutes is shown in Figure 5.2a for NiFe₂O₄ + 0.25NiO, MgFe₂O₄ + 0.25NiO, and BaFe₂O₄ + 0.25NiO. The oxygen capacity of MgAl₂O₄ + 0.25NiO was not shown because separating weight change into oxygen capacity and coking was not possible. There was rapid weight loss in the first 0.7 minutes and weight gain starting at 2.5 minutes (shown in S3). Integration of CO₂ during oxidation showed the

overall amount of coke was 1.64 wt.%. In contrast, active supports showed no signs of CO₂ during oxidation (shown in Figure C.4, C.6, and C.8), demonstrating their ability for coke resistance. At 3, 9, and 15 minutes, NiFe₂O₄ + 0.25NiO had the most oxygen capacity, BaFe₂O₄ + 0.25NiO has the second most oxygen capacity, and MgFe₂O₄ + 0.25NiO has the third most oxygen capacity. Oxygen release rate is shown in Figure 5.2b. With NiO exhibiting fast reduction kinetics, the maximum oxygen release rate will be particularly important. MgAl₂O₄ + 0.25NiO shows a maximum oxygen release rate of 2.3 wt%/min. NiFe₂O₄ + 0.25NiO displayed an oxygen release rate of 2.8 wt%/min. This was marginally higher than the oxygen release rate of NiFe₂O₄. BaFe₂O₄ + 0.25NiO displayed an oxygen release maximum of 2.6 wt%/min. Addition of NiO had a noticeable effect on the oxygen release maximum of BaFe₂O₄, with peak intensity increasing from 0.5 wt% to 2.8 wt%. MgFe₂O₄, on the other hand, did have a defined peak. It is also noteworthy that NiFe₂O₄ + 0.25NiO and BaFe₂O₄ + 0.25NiO had similar peak intensities to MgAl₂O₄ + 0.25NiO. In comparison to an inert support, this indicates an active support will not hinder the reduction kinetics.

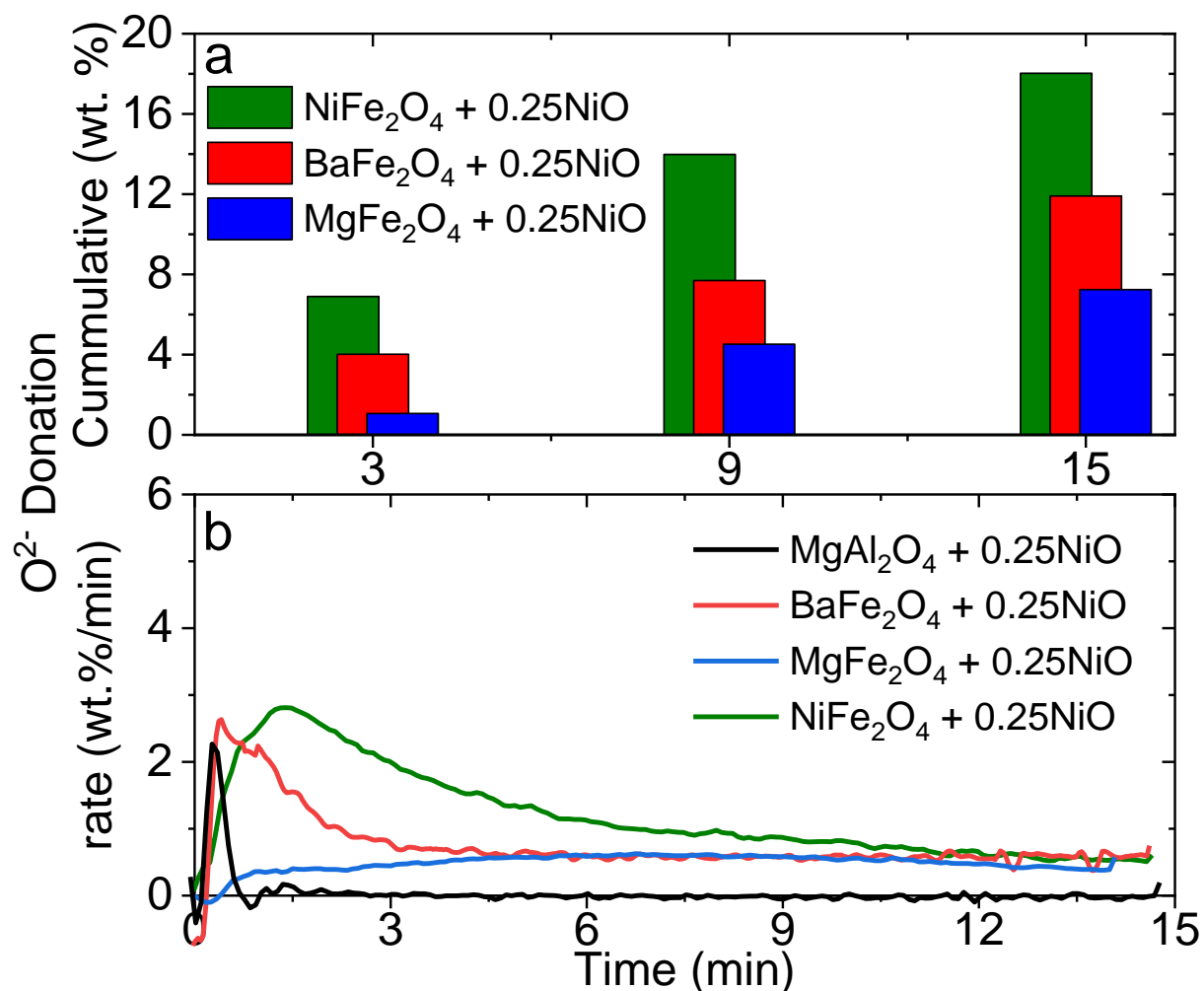


Figure 5.2: a) Oxygen donation (capacity) during reduction and oxidation and b) Oxygen release rate during reduction of MgAl₂O₄ + 0.25NiO, BaFe₂O₄ + 0.25NiO, MgFe₂O₄ + 0.25NiO, and NiFe₂O₄ + 0.25NiO. Reduction is under 10% CH₄ and oxidation is under 10% O₂. All results are at 900°C.

Higher loadings of NiO on the active support were also tested for coke resistance. The oxygen capacity at minutes 3, 9, and 15 are shown in Figure 5.3a for BaFe₂O₄ + 0.5NiO, MgFe₂O₄ + 0.5NiO, and NiFe₂O₄ + 0.5NiO. NiFe₂O₄ + 0.5NiO showed the highest amount of oxygen extraction at minute 3 and 9. There were no signs of coke formation in any of these oxygen carriers, with no CO₂ formation during oxidation (shown in Figure C.5, C.7, and C.9), demonstrating the robustness of the active support. Rate of oxygen release is shown in Figure 5.3b. NiFe₂O₄ + 0.5NiO and BaFe₂O₄ + 0.5NiO show maximum oxygen release rates of 2.5 wt.%/min. MgFe₂O₄ + 0.5NiO

shows two peaks; with the first peak having an intensity of 1.5 wt%/min and the second peak having an intensity of 2.5 wt%/min. Increasing NiO to support ratio from 0.25 to 0.5 did not result in more intense peaks, except in the case of MgFe_2O_4 . Nonetheless, these findings show that the support are robust in coke inhibition and can provide a high rate of oxygen release. This is particular noteworthy with NiFe_2O_4 , where it provides a higher amount of oxygen in the first three minutes and the rate of oxygen release slowly declines after the maximum oxygen release rate. This indicates NiFe_2O_4 is the most useless for coke inhibition. To shed light on this we carefully evaluated the phases $\text{NiFe}_2\text{O}_4 + 0.5\text{NiO}$ during reduction in the following section to further understand the process of coke inhibition.

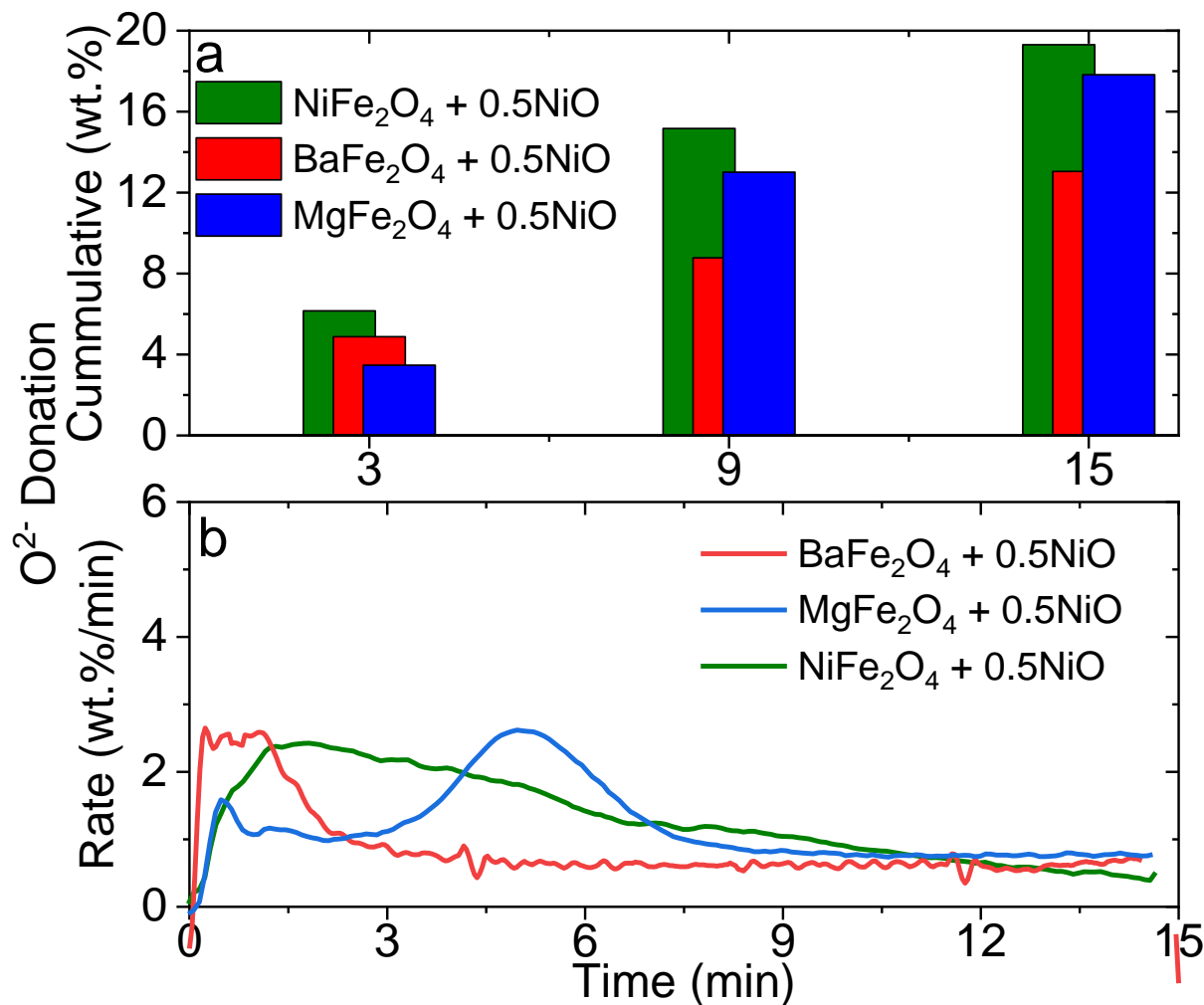


Figure 5.3: a) Weight during reduction and oxidation and b) DTG during reduction of BaFe₂O₄ + 0.5NiO, MgFe₂O₄ + 0.5NiO, and NiFe₂O₄ + 0.5NiO. Reduction is under 10% CH₄ and oxidation is under 10% O₂. All results are at 900°C.

5.4.3 Reduction Pathway of NiFe₂O₄ Supported NiO

Since NiFe₂O₄ supported oxygen carriers exhibited the highest oxygen capacity, phase transitions of NiFe₂O₄ supported NiO during the reduction reaction is further investigated with XRD and in-situ XRD. In Figure 5.4a, XRD of as prepared NiFe₂O₄, NiFe₂O₄ + 0.25NiO, and NiFe₂O₄ + 0.5NiO is shown, with reference patterns of NiO and NiFe₂O₄ shown for comparison. Diffraction peaks of NiFe₂O₄ + 0.25NiO and NiFe₂O₄ + 0.5NiO corresponded to either NiFe₂O₄ or NiO. However, the reference patterns of NiO and NiFe₂O₄ appear at very similar 2θ values (e.g.

37.3°, 43.3°, and 63°). Radiation from $\text{CuK}_{\alpha 1}$ and $\text{CuK}_{\alpha 2}$ will often result in two peaks, particularly at higher 2θ values. Thus, at least three peaks is needed to conclude the existence of two phases. Using our standard XRD conditions (step size = 0.1°, 4.5 seconds/step), three peaks were not seen at the aforementioned 2θ values (37.3°, 43.3°, and 63°). A more detailed scan (step size = 0.026°, 4.0 seconds/step) was conducted for $\text{NiFe}_2\text{O}_4 + 0.5\text{NiO}$. These results are shown in Figure 5.4b for the 2θ range: 43-44°. The results show three peaks, confirming both NiFe_2O_4 and NiO are present. With the NiFe_2O_4 reference showing a peak at a slightly lower 2θ value than NiO , the first peak is associated with a NiFe_2O_4 peak from $\text{CuK}_{\alpha 1}$ radiation. The second peak is associated with the overlap of a NiFe_2O_4 peak from $\text{CuK}_{\alpha 2}$ radiation and a NiO peak from $\text{CuK}_{\alpha 1}$ radiation. The last peak is associated with a NiO peak from $\text{CuK}_{\alpha 2}$ radiation. It should also be noted that MgFe_2O_4 and NiO have diffraction peaks at similar 2θ values and using a more detailed scan would be required to confirm the existence of two phases in MgFe_2O_4 supported oxygen carriers.

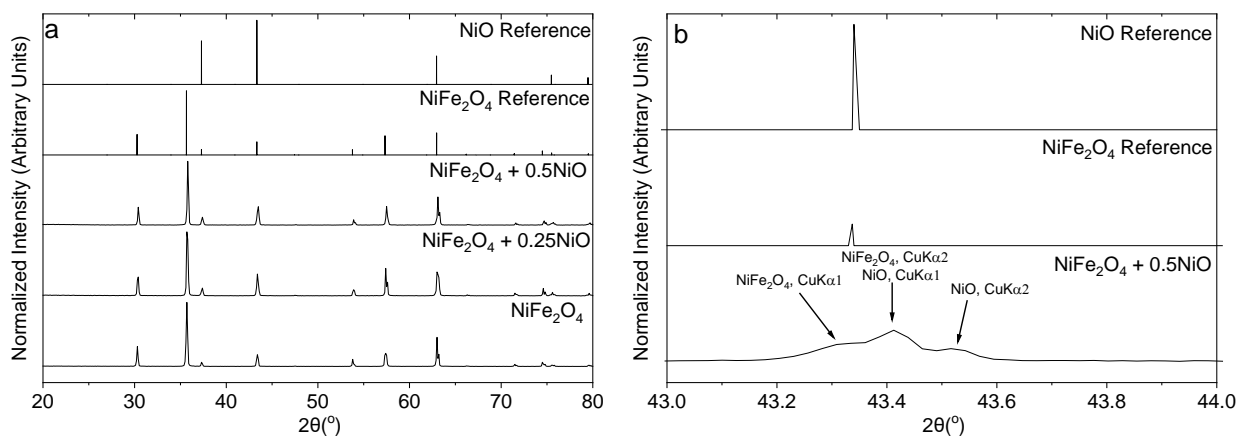


Figure 5.4: a) XRD of NiFe_2O_4 , $\text{NiFe}_2\text{O}_4 + 0.25\text{NiO}$, $\text{NiFe}_2\text{O}_4 + 0.5\text{NiO}$, b) Detailed Scan of $\text{NiFe}_2\text{O}_4 + 0.5\text{NiO}$ in the 43-44°.

Having determined both NiFe₂O₄ and NiO phases are present in NiFe₂O₄ + 0.5NiO, it was desired to understand how these phases changes under reduction. In-situ XRD with H₂ temperature-programmed reduction was used to determine these phase changes. Results of this experiment are shown in Figure 5.5 as a contour plot. As expected there are multiple phase occurring at different temperatures. These changes in the diffraction pattern are summarized below in Table 5.1. The changes in the diffraction pattern are labeled 1-6.

Table 5.1: Peak Phenomena during H₂ TPR in-Situ XRD (3% H₂) of NiFe₂O₄ + 0.5NiO.

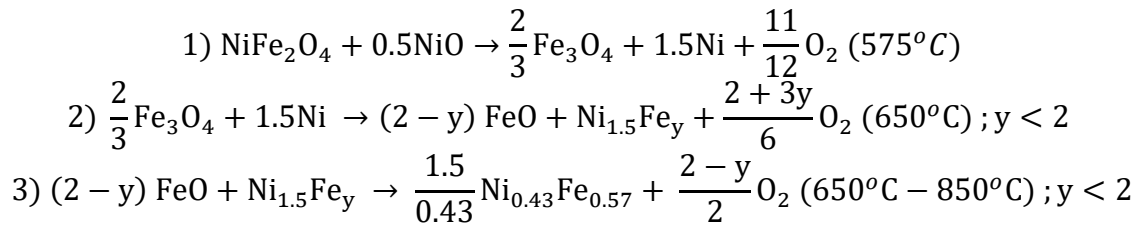
Temperature Range	2θ/° of Peaks	Phenomena
100-575°C	43.3, 54, 57.5, 63	Shift towards lower 2θ, and disappear at 575°C (1)
575°C	42.8, 43.7, 50.9, 56.8, 62.3	Peaks appear (2)
650°C	42.8, 56.8, 62.3	Peaks disappear (3)
650°C	43.7, 50.9	Shift towards lower 2θ and increase in intensity (4)
650°C	41.7, 60.4	Peaks appear (5)
650°C – 800°C	41.7, 60.4	Lose intensity and disappear at 800°C (6)

In Figure C.13, diffraction patterns at 40°C, 487°C, 604°C, 725°C, and 896°C are shown, with comparison to reference patterns of NiFe₂O₄, NiO, Fe₃O₄, FeO, Ni, Fe, and a NiFe alloy. These temperatures were chosen for phase identification because they will illustrate the phases before and after the phase transition, rather than during the phase transition. Analysis of these patterns indicated the following phases changes (Table 5.2):

Table 5.2: Phase Transitions during H₂ TPR in-Situ XRD (3% H₂) of NiFe₂O₄ + 0.5NiO.

Temperature Range (Associated Peak Phenomena)	Phase Change
100-575°C (1)	Thermal Expansion/Non-stoichiometric oxygen release of NiFe ₂ O ₄ + 0.5NiO
575°C (2)	Decomposition into Fe ₃ O ₄ and Ni
650°C (3)	Fe ₃ O ₄ decomposes
650°C (4)	FeO appears
650°C (5)	Incorporation of Fe into Ni
650°C – 800°C (6)	FeO decomposes, Fe fully incorporates into Ni

In literature, the non-stoichiometric oxygen loss during reduction was shown to be less than 0.1% by weight^{55,56}. As such, the peak shift between 100°C to 575°C was associated to thermal expansion. However, the amount of Fe that incorporates into Ni from phase decomposition of Fe₃O₄ is a function of the degree of reduction. Leaving this as variable (y), in-situ XRD indicates the phase transitions are:



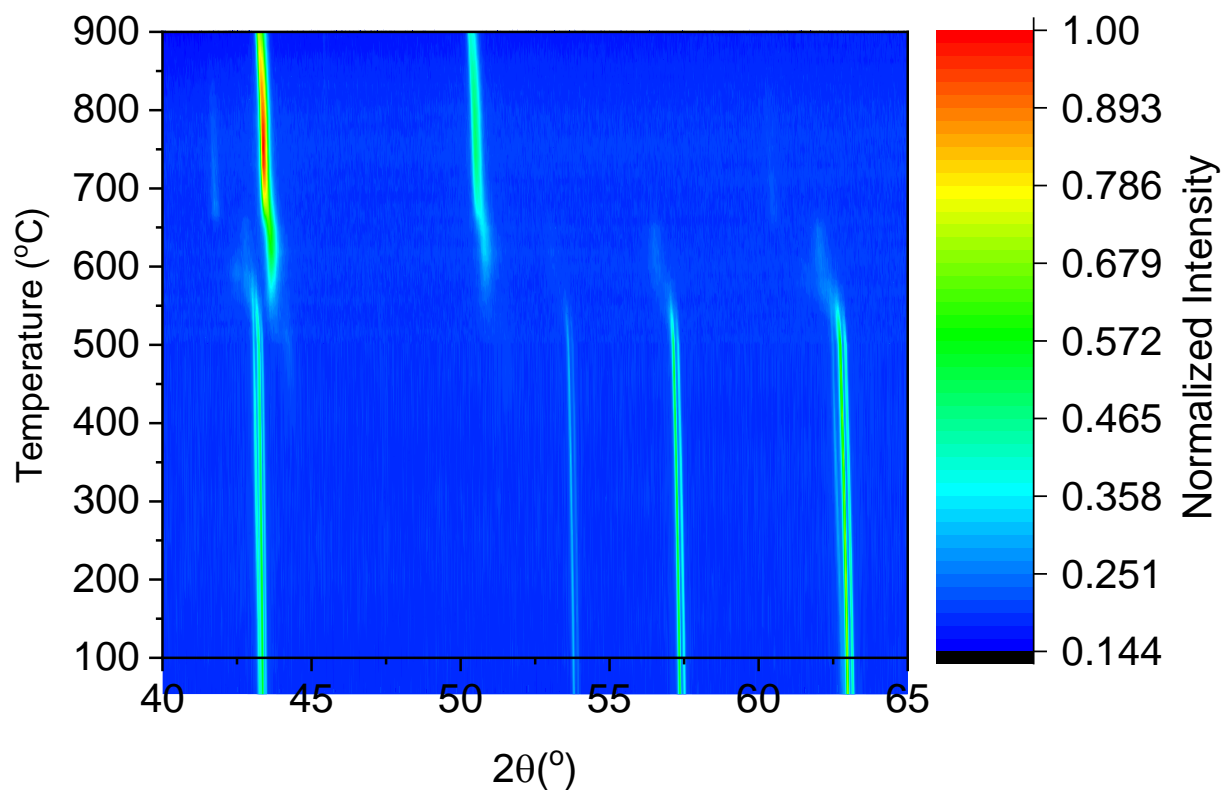


Figure 5.5: In-Situ XRD of $\text{NiFe}_2\text{O}_4 + 0.5\text{NiO}$ from 100-900°C under 3% H_2 (total flow rate: 30 mL/min). Ramping rate to 500°C was at 10°C/min and ramping from 500°C to 900°C was at 2°C/min.

Having outlined the phase transitions of $\text{NiFe}_2\text{O}_4 + 0.5\text{NiO}$ during reduction, thermogravimetric analysis was used during an H_2 -TPR for further elucidation of the nature of coke inhibition in $\text{NiFe}_2\text{O}_4 + 0.5\text{NiO}$. It should be noted that gas hourly space velocity and ramping rate below 500°C are different and will prevent a direct comparison of weight changes to phase transitions. The oxygen capacity rate is shown in Figure 5.6, with each peak labeled with the phases that are present. Cumulative oxygen capacity during this experiment is shown in Figure C.14, respectively. Oxygen release rate shows three distinct peaks (at 384°C, 600°C, and 635°C), confirming the three phase changes. Furthermore, the overall oxygen capacity is 26.8%, which is

very similar to the overall theoretical oxygen capacity. The overall oxygen capacity of $\text{NiFe}_2\text{O}_4 + 0.5\text{NiO}$ after 15 minutes of reduction in CH_4 was 19%. This corresponds to 625°C and is between the second and third DTG peak. This indicates that the decomposition of Fe_3O_4 is a significant factor in coke inhibition during redox cycling. An ideal support will release lattice oxygen independently of NiO . However, the decomposition of Fe_3O_4 is not independent of the nickel phase, as evidenced by the formation of a nickel-iron alloy. This solid state reaction suggests the support does not release oxygen independently of NiO .

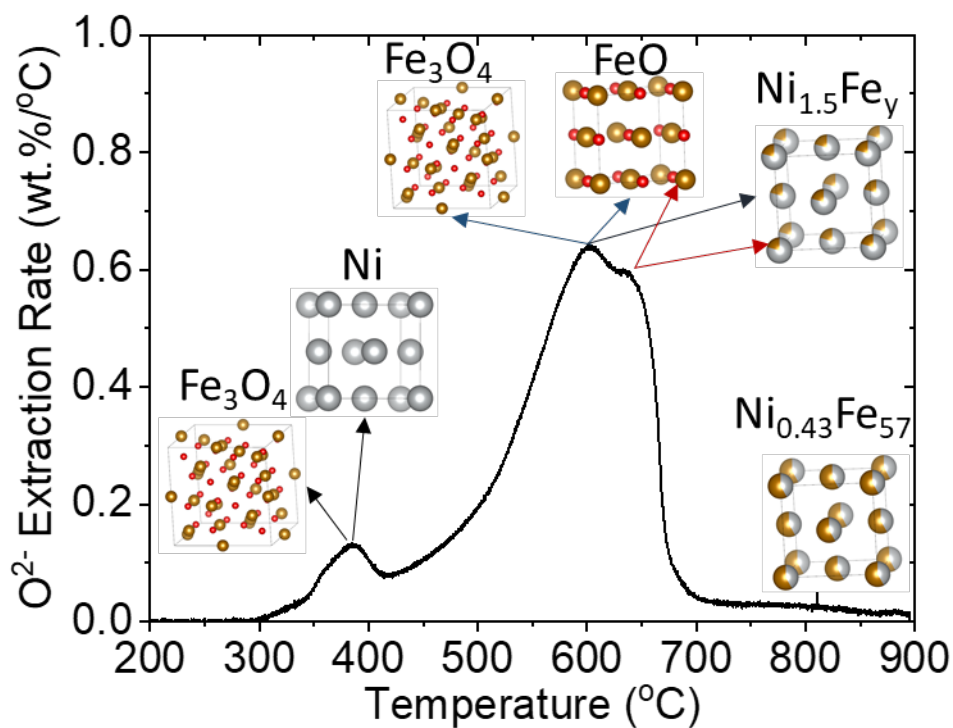


Figure 5.6: TPR under 3% H_2 at $2^\circ\text{C}/\text{min}$.

5.4.4 Redox Stabilities of the Oxygen Carriers

Performance during redox cycling is investigated here using a 10 cycle redox experiment, with cycle 2 and 10 of redox cycling analyzed in this section. Oxygen capacity during reduction is shown for $\text{NiFe}_2\text{O}_4 + 0.25\text{NiO}$, $\text{BaFe}_2\text{O}_4 + 0.25\text{NiO}$, and $\text{MgFe}_2\text{O}_4 + 0.25\text{NiO}$ in Figure 5.7a. The overall oxygen capacity for cycle 10 of $\text{NiFe}_2\text{O}_4 + 0.25\text{NiO}$, $\text{BaFe}_2\text{O}_4 + 0.25\text{NiO}$, and $\text{MgFe}_2\text{O}_4 + 0.25\text{NiO}$ was 17.2%, 8%, and 5.7%. In comparison to cycle 2, $\text{BaFe}_2\text{O}_4 + 0.25\text{NiO}$ showed a decrease in oxygen capacity from 11% to 8%. The oxygen release rates of these oxygen carriers during reduction is shown in Figure C.15 for cycle 2 and cycle 10. For $\text{BaFe}_2\text{O}_4 + 0.25\text{NiO}$ there was a marginal decrease in maximum oxygen release rate, decreasing from 2.6 wt.%/min to 2.2 wt.%/min. The maximum oxygen release rate of $\text{NiFe}_2\text{O}_4 + 0.25\text{NiO}$ decreased from 2.5 wt.%/min to 2.1 wt.%/min. $\text{MgFe}_2\text{O}_4 + 0.25\text{NiO}$ did not show any decrease in maximum oxygen release. The oxygen gain during oxidation is shown in Figure 5.7b for cycle 2 and cycle 10. The most notable feature is the large decrease in oxidization kinetics from cycle 2 to cycle 10 for $\text{NiFe}_2\text{O}_4 + 0.25\text{NiO}$. While the weight gain in cycle 2 and cycle 10 are comparable, cycle 10 required an extra 10 minutes to regain the oxygen lost during reduction.

Performance under redox cycling is also investigated for the higher NiO loadings, with cycle 2 and 10 analyzed in this section. Oxygen capacity as a function of time during reduction is shown in Figure 5.7c. In comparison to cycle 2, $\text{NiFe}_2\text{O}_4 + 0.5\text{NiO}$ shows the most serious signs of deactivation, with overall oxygen capacity decreasing from 19% to 8%. $\text{BaFe}_2\text{O}_4 + 0.5\text{NiO}$ showed a marginal decrease in oxygen capacity, decreasing from 12% to 10%. MgFe_2O_4 also showed a marginal decrease in oxygen capacity, decreasing from 16.5% to 15%. Oxygen release rate during reduction is shown for these oxygen carriers in Figure C.15 from cycle 2 to cycle 10. From cycle 2 to cycle 10, the maximum oxygen release rate of $\text{NiFe}_2\text{O}_4 + 0.5\text{NiO}$ during reduction

decreased from 2.5 wt./min to 2.0 wt./min. For $\text{BaFe}_2\text{O}_4 + 0.5\text{NiO}$, the maximum oxygen release rate decreased from 2.5 wt./min to 2.0 wt./min. $\text{MgFe}_2\text{O}_4 + 0.5\text{NiO}$ did not show any decrease in maximum oxygen release rate. The oxygen gain during oxidization is shown in Figure 5.7d. The most notable feature is the change in oxidization of $\text{NiFe}_2\text{O}_4 + 0.5\text{NiO}$ with cycling. Not only is oxidization much slower at cycle 10, the weight gain was almost 10 wt.% less at cycle 10. This suggests deactivation is occurring with NiFe_2O_4 supported NiO. However, MgFe_2O_4 and BaFe_2O_4 supported oxygen carriers show marginal changes from cycle 2 to cycle 10. The long term stability of these oxygen carriers is investigated in the next section.

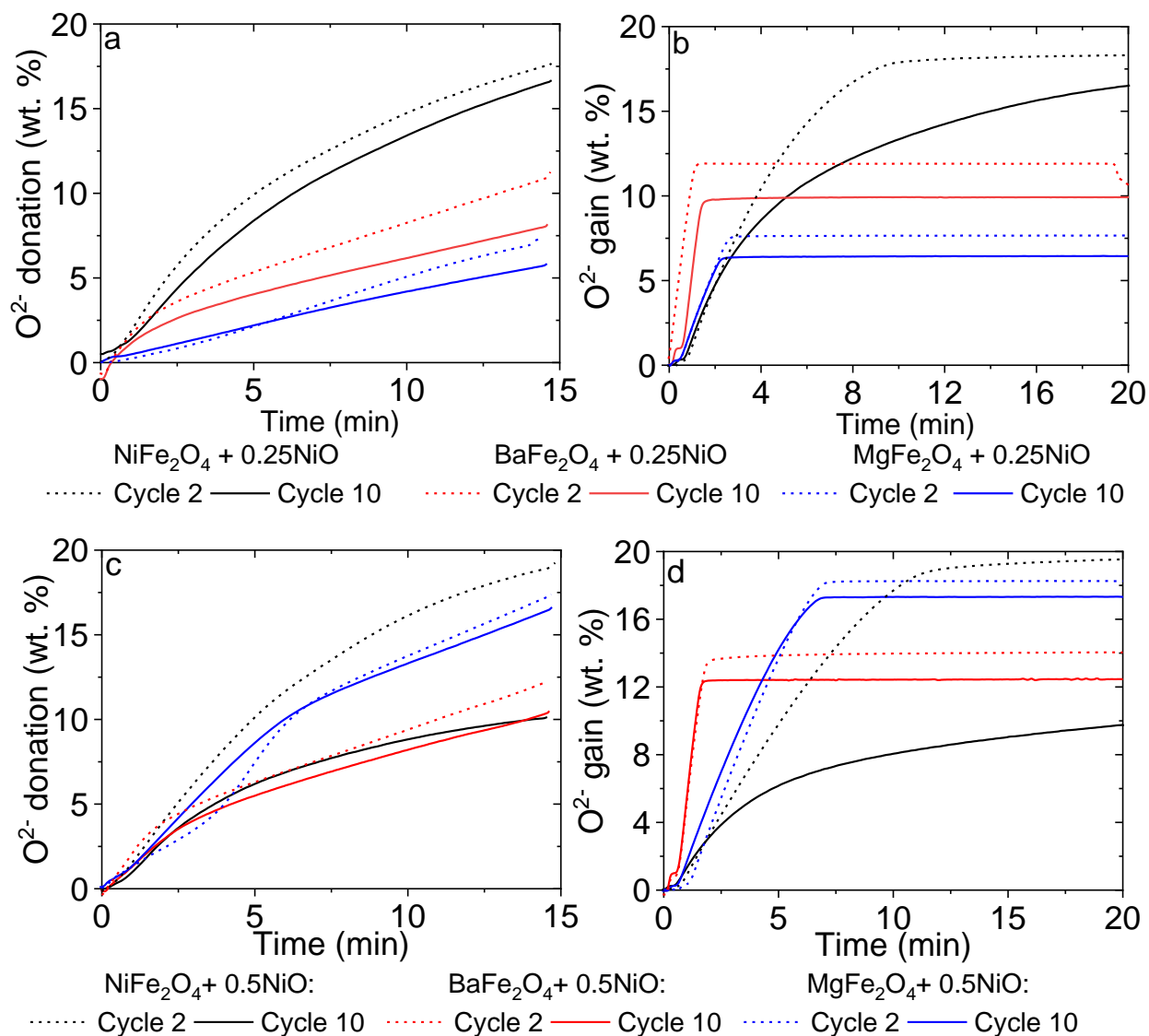


Figure 5.7: a) oxygen donation (capacity) during reduction and b) oxygen gain during oxidation with 0.25NiO and c) oxygen donation (capacity) during reduction and d) oxygen gain during oxidation with 0.5NiO. Reduction is under 10% CH_4 and oxidation is under 10% O_2 . All results are at 900°C.

5.4.5 Long Term Redox Stability of $MgFe_2O_4$ and $BaFe_2O_4$ supported Oxygen Carriers

30 cycle redox of $MgFe_2O_4 + 0.5NiO$ and $BaFe_2O_4 + NiO$ was used to test the long term stability of $MgFe_2O_4$ and $BaFe_2O_4$ supported oxygen carriers. The cumulative oxygen capacity during cycle 2, 10, and 30 of $MgFe_2O_4 + 0.5NiO$ is shown in Figure 5.8a and the weight with

respect to time is shown for all 30 cycles in Figure 5.8b. The decrease in overall oxygen capacity in cycle 10 and cycle 30 are nearly identical at 16 wt.%. The rate of oxygen capacity is shown in Figure C.16, and cycle 10 and cycle 30 are also nearly identical. This shows MgFe_2O_4 will provide a stable and active oxygen carrier. The cumulative oxygen capacity during cycle 2, 10, and 30 of $\text{BaFe}_2\text{O}_4 + 0.5\text{NiO}$ is shown in Figure C.17. The overall oxygen capacity at cycle 10 and 30 are identical at 10 wt.%. The rate of oxygen capacity is shown in Figure C.16, with rates of oxygen capacity once again being identical. This shows that BaFe_2O_4 is a stable and active support for NiO.

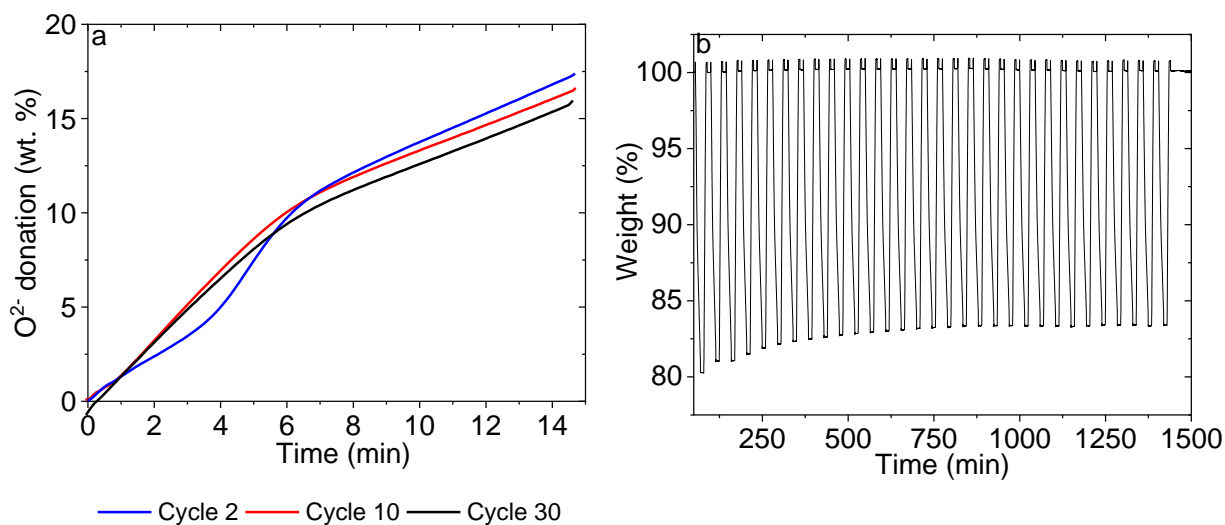


Figure 5.8: a) Oxygen donation (capacity) of $\text{MgFe}_2\text{O}_4 + 0.5\text{NiO}$ during cycles 2, 10, and 30, b) Weight of the oxygen carrier during a 30 cycle redox.

5.5 Conclusion

The current study investigates the ability of active spinel oxides to inhibit coke formation on nickel in chemical looping combustion. In particular, BaFe_2O_4 , MgFe_2O_4 , and NiFe_2O_4 were investigated because they are known to provide slow oxygen release. These materials demonstrated oxygen release over 45 minutes while $\text{MgAl}_2\text{O}_4 + 0.25\text{NiO}$ reduces within 2 minutes

and shortly after shows coke formation. $\text{BaFe}_2\text{O}_4 + x\text{NiO}$, $\text{MgFe}_2\text{O}_4 + x\text{NiO}$, and $\text{NiFe}_2\text{O}_4 + x\text{NiO}$ ($x = 0.25, 0.5$) were studied under redox cycling with 15 minutes of reduction. In these experiments, there were no signs of coke formation. Additionally NiO addition to BaFe_2O_4 and NiFe_2O_4 , increased rates of reduction. The rates of reduction was also similar to $\text{MgAl}_2\text{O}_4 + 0.25\text{NiO}$. This suggests there is a synergetic effect between NiO and active spinel oxides; active spinel oxides inhibit coke formation on nickel and nickel can possibly increase the rate of reduction for spinel oxides. In-situ XRD and H_2 TPR of $\text{NiFe}_2\text{O}_4 + 0.5\text{NiO}$ showed three phase transitions: 1) first spinel oxide and nickel oxide reduction to magnetite and nickel 2) then magnetite reduction to a combination of wustite and metallic iron and 3) finally wustite reduction, giving pure metallic phases. Comparing to redox cycling, we concluded that reduction starts with formation of nickel and magnetite and ends with formation of combination of wustite and iron. The combination of findings from redox cycling, in-situ XRD, and weight loss under H_2 TPR suggest that the synergetic effect between NiFe_2O_4 and NiO is a result of oxygen capacity from NiFe_2O_4 rather than incorporation of Ni into the spinel. While $\text{NiFe}_2\text{O}_4 + x\text{NiO}$ ($x = 0.25, 0.5$) showed a high amount of oxygen capacity and subsequently coke resistance, cycling showed deactivation. Both MgFe_2O_4 and BaFe_2O_4 supported oxygen carriers show long term activity and stability.

5.6 References

1. Ananikov, V. P. Nickel: The “Spirited Horse” of Transition Metal Catalysis. *ACS Catal.* **5**, 1964–1971 (2015).
2. Tasker, S. Z., Standley, E. A. & Jamison, T. F. Recent advances in homogeneous nickel catalysis. *Nature* **509**, 299–309 (2014).
3. Wilke, G. Contributions to Organo-Nickel Chemistry. *Angew. Chem. Int. Ed. Engl.* **27**, 185–206 (1988).
4. Crabtree, R. H. Organometallic alkane CH activation. *J. Organomet. Chem.* **689**, 4083–4091 (2004).
5. Kulkarni, A. A. & Daugulis, O. Direct Conversion of Carbon-Hydrogen into Carbon-Carbon Bonds by First-Row Transition-Metal Catalysis. *Synthesis* **2009**, 4087–4109 (2009).
6. Blomberg, M. R. A., Siegbahn, P. E. M., Nagashima, U. & Wennerberg, J. Theoretical study of the activation of alkane carbon-hydrogen and carbon-carbon bonds by different transition metals. *J. Am. Chem. Soc.* **113**, 424–433 (1991).
7. Aryafar, M. & Zaera, F. Kinetic study of the catalytic oxidation of alkanes over nickel, palladium, and platinum foils. *Catal. Lett.* **48**, 173–183 (1997).
8. U.S. Crude Oil, Natural Gas, and Natural Gas Proved Reserves, Year-end 2015. Available at: <https://www.eia.gov/naturalgas/crudeoilreserves/>. (Accessed: 26th September 2018)
9. U.S. Dry Natural Gas Expected Future Production (Billion Cubic Feet). Available at: https://www.eia.gov/dnav/ng/hist/rngr11nus_1a.htm. (Accessed: 26th September 2018)
10. Nieva, M. A., Villaverde, M. M., Monzón, A., Garetto, T. F. & Marchi, A. J. Steam-methane reforming at low temperature on nickel-based catalysts. *Chem. Eng. J.* **235**, 158–166 (2014).
11. Bradford, M. C. J. & Vannice, M. A. Catalytic reforming of methane with carbon dioxide over nickel catalysts II. Reaction kinetics. *Appl. Catal. Gen.* **142**, 97–122 (1996).
12. Bradford, M. C. J. & Vannice, M. A. Catalytic reforming of methane with carbon dioxide over nickel catalysts I. Catalyst characterization and activity. *Appl. Catal. Gen.* **142**, 73–96 (1996).
13. Mette, K. *et al.* Stable Performance of Ni Catalysts in the Dry Reforming of Methane at High Temperatures for the Efficient Conversion of CO₂ into Syngas. *ChemCatChem* **6**, 100–104 (2014).

14. Sokolov, S., Kondratenko, E. V., Pohl, M.-M., Barkschat, A. & Rodemerck, U. Stable low-temperature dry reforming of methane over mesoporous La₂O₃-ZrO₂ supported Ni catalyst. *Appl. Catal. B Environ.* **113–114**, 19–30 (2012).
15. San-José-Alonso, D., Juan-Juan, J., Illán-Gómez, M. J. & Román-Martínez, M. C. Ni, Co and bimetallic Ni–Co catalysts for the dry reforming of methane. *Appl. Catal. Gen.* **371**, 54–59 (2009).
16. Ruckenstein, E. & Hu, Y. H. Carbon dioxide reforming of methane over nickel/alkaline earth metal oxide catalysts. *Appl. Catal. Gen.* **133**, 149–161 (1995).
17. Choudhary, V. R., Rajput, A. M. & Prabhakar, B. Low temperature oxidative conversion of methane to syngas over NiO–CaO catalyst. *Catal. Lett.* **15**, 363–370 (1992).
18. Ruckenstein, E. & Hang Hu, Y. Methane partial oxidation over NiO/MgO solid solution catalysts. *Appl. Catal. Gen.* **183**, 85–92 (1999).
19. Choudhary, V. R., Rane, V. H. & Rajput, A. M. Selective oxidation of methane to CO and H₂ over unreduced NiO–rare earth oxide catalysts. *Catal. Lett.* **22**, 289–297 (1993).
20. Zhang, J. & Li, F. Coke-resistant Ni@SiO₂ catalyst for dry reforming of methane. *Appl. Catal. B Environ.* **176–177**, 513–521 (2015).
21. Cho, P., Mattisson, T. & Lyngfelt, A. Carbon Formation on Nickel and Iron Oxide-Containing Oxygen Carriers for Chemical-Looping Combustion. *Ind. Eng. Chem. Res.* **44**, 668–676 (2005).
22. Ishida, M., Jin, H. & Okamoto, T. Kinetic Behavior of Solid Particle in Chemical-Looping Combustion: Suppressing Carbon Deposition in Reduction. *Energy Fuels* **12**, 223–229 (1998).
23. Claridge, J. B. *et al.* A study of carbon deposition on catalysts during the partial oxidation of methane to synthesis gas. *Catal. Lett.* **22**, 299–305 (1993).
24. Sokolov, S., Kondratenko, E. V., Pohl, M.-M., Barkschat, A. & Rodemerck, U. Stable low-temperature dry reforming of methane over mesoporous La₂O₃-ZrO₂ supported Ni catalyst. *Appl. Catal. B Environ.* **113–114**, 19–30 (2012).
25. Liu, C., Ye, J., Jiang, J. & Pan, Y. Progresses in the Preparation of Coke Resistant Ni-based Catalyst for Steam and CO₂ Reforming of Methane. *ChemCatChem* **3**, 529–541 (2011).
26. Wang, S. & (Max) Lu, G. Q. Role of CeO₂ in Ni/CeO₂–Al₂O₃ catalysts for carbon dioxide reforming of methane. *Appl. Catal. B Environ.* **19**, 267–277 (1998).

27. Wang, J. B., Tai, Y.-L., Dow, W.-P. & Huang, T.-J. Study of ceria-supported nickel catalyst and effect of yttria doping on carbon dioxide reforming of methane. *Appl. Catal. Gen.* **218**, 69–79 (2001).
28. Kim, G. J., Cho, D.-S., Kim, K.-H. & Kim, J.-H. The reaction of CO₂ with CH₄ to synthesize H₂ and CO over nickel-loaded Y-zeolites. *Catal. Lett.* **28**, 41–52 (1994).
29. Chang, J.-S., Park, S.-E., Yoo, J. W. & Park, J.-N. Catalytic Behavior of Supported KNiCa Catalyst and Mechanistic Consideration for Carbon Dioxide Reforming of Methane. *J. Catal.* **195**, 1–11 (2000).
30. Wang, S. & Lu, G. Q. Reforming of methane with carbon dioxide over Ni/Al₂O₃ catalysts: Effect of nickel precursor. *Appl. Catal. Gen.* **169**, 271–280 (1998).
31. Lemonidou, A. A., Goula, M. A. & Vasalos, I. A. Carbon dioxide reforming of methane over 5wt.% nickel calcium aluminate catalysts – effect of preparation method. *Catal. Today* **46**, 175–183 (1998).
32. Wang, S. & Lu, G. Q. M. CO₂ reforming of methane on Ni catalysts: Effects of the support phase and preparation technique. *Appl. Catal. B Environ.* **16**, 269–277 (1998).
33. Li, Z., Mo, L., Kathiraser, Y. & Kawi, S. Yolk–Satellite–Shell Structured Ni–Yolk@Ni@SiO₂ Nanocomposite: Superb Catalyst toward Methane CO₂ Reforming Reaction. *ACS Catal.* **4**, 1526–1536 (2014).
34. Kim, H.-W., Kang, K.-M., Kwak, H.-Y. & Kim, J. H. Preparation of supported Ni catalysts on various metal oxides with core/shell structures and their tests for the steam reforming of methane. *Chem. Eng. J.* **168**, 775–783 (2011).
35. Kang, K.-M., Kim, H.-W., Shim, I.-W. & Kwak, H.-Y. Catalytic test of supported Ni catalysts with core/shell structure for dry reforming of methane. *Fuel Process. Technol.* **92**, 1236–1243 (2011).
36. Zhou, Z., Han, L. & Bollas, G. M. Kinetics of NiO reduction by H₂ and Ni oxidation at conditions relevant to chemical-looping combustion and reforming. *Int. J. Hydrog. Energy* **39**, 8535–8556 (2014).
37. Dueso, C. *et al.* Reduction and oxidation kinetics of nickel-based oxygen-carriers for chemical-looping combustion and chemical-looping reforming. *Chem. Eng. J.* **188**, 142–154 (2012).
38. Adanez, J., Abad, A., Garcia-Labiano, F., Gayan, P. & de Diego, L. F. Progress in Chemical-Looping Combustion and Reforming technologies. *Prog. Energy Combust. Sci.* **38**, 215–282 (2012).

39. Mattisson, T., Järðnäs, A. & Lyngfelt, A. Reactivity of Some Metal Oxides Supported on Alumina with Alternating Methane and Oxygen Application for Chemical-Looping Combustion. *Energy Fuels* **17**, 643–651 (2003).
40. Cho, P., Mattisson, T. & Lyngfelt, A. Comparison of iron-, nickel-, copper- and manganese-based oxygen carriers for chemical-looping combustion. *Fuel* **83**, 1215–1225 (2004).
41. Pröll, T., Kolbitsch, P., Bolhàr-Nordenkamp, J. & Hofbauer, H. A novel dual circulating fluidized bed system for chemical looping processes. *AIChE J.* **55**, 3255–3266 (2009).
42. Hossain, M. M. & de Lasa, H. I. Chemical-looping combustion (CLC) for inherent CO₂ separations—a review. *Chem. Eng. Sci.* **63**, 4433–4451 (2008).
43. Jin, H., Okamoto, T. & Ishida, M. Development of a Novel Chemical-Looping Combustion: Synthesis of a Solid Looping Material of NiO/NiAl₂O₄. *Ind. Eng. Chem. Res.* **38**, 126–132 (1999).
44. Jin, H., Okamoto, T. & Ishida, M. Development of a Novel Chemical-Looping Combustion: Synthesis of a Looping Material with a Double Metal Oxide of CoO–NiO. *Energy Fuels* **12**, 1272–1277 (1998).
45. Ishida, M. & Jin, H. CO₂ recovery in a power plant with chemical looping combustion. *Energy Convers. Manag.* **38**, S187–S192 (1997).
46. Gayán, P. *et al.* Effect of support on reactivity and selectivity of Ni-based oxygen carriers for chemical-looping combustion. *Fuel* **87**, 2641–2650 (2008).
47. Salhi, N., Boulahouache, A., Petit, C., Kiennemann, A. & Rabia, C. Steam reforming of methane to syngas over NiAl₂O₄ spinel catalysts. *Int. J. Hydrog. Energy* **36**, 11433–11439 (2011).
48. Zafar, Q., Abad, A., Mattisson, T. & Gevert, B. Reaction Kinetics of Freeze-Granulated NiO/MgAl₂O₄ Oxygen Carrier Particles for Chemical-Looping Combustion. *Energy Fuels* **21**, 610–618 (2007).
49. Neal, L. M., Shafiefarhood, A. & Li, F. Dynamic Methane Partial Oxidation Using a Fe₂O₃@La_{0.8}Sr_{0.2}FeO_{3-δ} Core–Shell Redox Catalyst in the Absence of Gaseous Oxygen. *ACS Catal.* **4**, 3560–3569 (2014).
50. Shafiefarhood, A., Hamill, J. C., Neal, L. M. & Li, F. Methane partial oxidation using FeO_x@La_{0.8}Sr_{0.2}FeO_{3-δ} core–shell catalyst – transient pulse studies. *Phys. Chem. Chem. Phys.* **17**, 31297–31307 (2015).

51. Kuo, Y.-L., Hsu, W.-M., Chiu, P.-C., Tseng, Y.-H. & Ku, Y. Assessment of redox behavior of nickel ferrite as oxygen carriers for chemical looping process. *Ceram. Int.* **39**, 5459–5465 (2013).
52. Lambert, A., Briault, P. & Comte, E. Spinel mixed oxides as oxygen carriers for chemical looping combustion. *Energy Procedia* **4**, 318–323 (2011).
53. Bhavsar, S. & Vesper, G. Bimetallic Fe–Ni Oxygen Carriers for Chemical Looping Combustion. *Ind. Eng. Chem. Res.* **52**, 15342–15352 (2013).
54. Fan, Y. & Siriwardane, R. Novel New Oxygen Carriers for Chemical Looping Combustion of Solid Fuels. *Energy Fuels* **28**, 2248–2257 (2014).
55. Paladino, A. E. Phase Equilibria in the Ferrite Region of the System Fe-Ni-O. *J. Am. Ceram. Soc.* **42**, 168–175 (1959).
56. O'bryan, H. M., Monforte, F. R. & Blair, R. Oxygen Content of Nickel Ferrites at 1300°C. *J. Am. Ceram. Soc.* **48**, 577–580 (1965).

Chapter 6: Conclusions and Future Work

6.1 Conclusions

Chemical looping is a novel process in the field of fossil fuel conversion, where the lattice oxygen of a metal oxide oxidizes a fuel in an efficient route, through a two-step redox process where *in-situ* air separation is accomplished. In the context of combustion, this results in facile CO₂ capture. The first step of this process is reduction of the metal oxide (i.e. oxygen carrier or redox catalyst) with a carbonaceous fuel and the second step is re-oxidation of the metal oxide with a gaseous oxidant. Chemical looping combustion and chemical looping reforming are applications of chemical looping that have become increasingly studied. In chemical looping combustion, a fossil fuel is combusted for energy and in chemical looping reforming methane is converted to syngas. In both processes, air is used as the gaseous oxidant. A subset of chemical looping combustion is chemical looping with oxygen uncoupling, where gaseous oxygen is released from the metal oxide to combust a solid fuel. The metal oxide in chemical looping combustion is commonly referred to as an oxygen carrier and the metal oxide in chemical looping reforming is referred to as a redox catalyst. Performance of the oxygen carrier/redox catalyst is key to success of chemical looping. Hundreds of oxygen carriers/redox catalysts have been examined for this process. Commonly studied oxygen carriers/redox catalysts for these applications are transition metal oxides with an inert support. Iron oxide has emerged as a promising candidate for chemical looping combustion. However, it exhibits low reactivity and agglomeration. Use of CuO and NiO, while being highly reactive, has met challenges, namely defluidization and coke formation. Discovery of a suitable redox catalyst for chemical looping reforming has been more difficult due to requirement for both high activity and selectivity towards partial oxidation products (syngas).

The energy of oxygen vacancy creation, calculated through density functional theory, was used as a screening tool for Mn-containing perovskites as oxygen carriers for chemical looping with oxygen uncoupling, a subset of chemical looping combustion where solid fuels are converted through gaseous oxygen produced by the oxygen carrier. The energy of oxygen vacancy creation was used to predict the relative amounts of “uncoupled” oxygen. The energy of oxygen vacancy creation showed the trend: $\text{BaMnO}_{3-\delta} > \text{CaMnO}_{3-\delta} > \text{Ca}_{0.75}\text{Sr}_{0.25}\text{MnO}_{3-\delta} > \text{CaMn}_{0.75}\text{Fe}_{0.25}\text{O}_{3-\delta}$. This trend was unaffected by the use of the Hubbard U parameter. This predicts the amount of uncoupled oxygen will follow the trend: $\text{CaMn}_{0.75}\text{Fe}_{0.25}\text{O}_{3-\delta} > \text{Ca}_{0.75}\text{Sr}_{0.25}\text{MnO}_{3-\delta} > \text{CaMnO}_{3-\delta} > \text{BaMnO}_{3-\delta}$. Thermogravimetric experiments confirmed this trend when oxygen nonstoichiometry (δ) is less than 0.023. At higher oxygen nonstoichiometry it is expected a more complete model will be needed to predict these trends, taking into account entropic effects and vacancy-vacancy interaction. Using $\text{CaMnO}_{3-\delta}$, $\text{Ca}_{0.75}\text{Sr}_{0.25}\text{MnO}_{3-\delta}$, and $\text{CaMn}_{0.75}\text{Fe}_{0.25}\text{O}_{3-\delta}$ for coal char conversion experiments showed that strontium and iron doping increase the coal char conversion past 85%.

$\text{AMn}_x\text{B}_{1-x}\text{O}_3$ (A = Ca or Ba, B = Fe or Ni) was investigated as a redox catalyst for chemical looping reforming of methane. The parent structure of BaMnO_3 led to considerable improvement of syngas selectivity, in comparison to CaMnO_3 . For instance, all $\text{BaMn}_x\text{B}_{1-x}\text{O}_3$ (B = Fe or Ni) redox catalysts showed CO selectivity over 85% whereas the highest CO selectivity obtained from $\text{CaMn}_x\text{B}_{1-x}\text{O}_3$ (B = Fe or Ni) based redox catalysts was 68%. Temperature programmed desorption/reaction and findings from the previous Chapter 2, indicated this may be a result of more tightly bound lattice oxygen. $\text{BaMn}_{1-x}\text{B}_{1-x}\text{O}_3$ based redox catalysts also exhibited coke resistance. This is attributed to the BaO surface termination. While Ni and Fe did not improve selectivity of the BaMnO_3 parent structure, they improved the oxygen capacity of the parent structure. While $\text{BaMn}_{0.5}\text{Fe}_{0.5}\text{O}_3$ showed the high oxygen carrying capacity, there were signs of

deactivation due to sintering in the reoxidation step with air. When air as an oxidant is replaced with steam, long term stability was achieved.

Rh promoted $\text{Ca}_x\text{A}_{1-x}\text{Mn}_x\text{B}_{1-x}\text{O}_3$ ($\text{A} = \text{Sr}$, $\text{B} = \text{Fe}$, $x = 0.95$ or 0.75) was investigated as a redox catalyst for low temperature (600°C) methane conversion to syngas. Results from Chapter 2 show $\text{Ca}_x\text{A}_{1-x}\text{Mn}_x\text{B}_{1-x}\text{O}_3$ ($\text{A} = \text{Sr}$, $\text{B} = \text{Fe}$, $x = 0.95$ or 0.75) are capable of CLOU and will give combustion products. However, the use of Rh surface promotion can promote syngas formation. This was witnessed with Rh promoted CaMnO_3 , where CO selectivity is above 80%. Rh promoted $\text{Ca}_x\text{Sr}_{1-x}\text{MnO}_3$ ($x = 0.95$ or 0.75) resulted in roughly an even split between combustion and selective products. Rh promoted $\text{CaMn}_x\text{Fe}_{1-x}\text{O}_3$ ($x = 0.95$ or 0.75) results in complete combustion of methane. All Rh promoted redox catalysts show significant activity, displaying 2.2 – 4.5 wt.% oxygen extraction. To utilize the high oxygen extraction, Rh promoted Al_2O_3 was placed downstream of the redox catalyst and utilized as a traditional reforming catalyst, converting the unselective products. Redox testing of this scheme resulted in syngas selectivity of at least 88% and CH_4 conversion of at least 17%. This scheme was shown to be the most effective for Rh- $\text{CaMn}_{0.95}\text{Fe}_{0.05}\text{O}_3$, where CH_4 conversion was improved from 10% to 40% and syngas selectivity was improved from 1% to 95%. This is attributed to the high oxygen donation from the redox catalyst (4.5 wt.%), compared to other non-selective redox catalysts (≤ 3.0 wt%). Syngas yield was optimized by varying redox times, temperature, and residence time. This led to syngas yield above 70% at 600°C and 700°C .

In literature it has been shown that use of NiO as an oxygen carrier results in significant coke formation. Many inert supports have been tested to alleviate this, while utilizing the fast reduction kinetics of NiO. However, a gaseous oxidant is needed to completely remove coke formation. Coke formation is associated with depletion of active lattice oxygen. As an alternative

to inert substrates, MgFe_2O_4 , NiFe_2O_4 , and BaFe_2O_4 are explored as active substrates. The use of an active substrate was shown to prevent coke formation during a 15 minute reduction. In contrast when MgAl_2O_4 , an inert substrate is used, coke formation occurs after two minutes. Additionally NiFe_2O_4 and BaFe_2O_4 supported NiO is shown to have maximum reduction rates (oxygen release maxima) similar to MgAl_2O_4 supported NiO. *In-situ* XRD of $\text{NiFe}_2\text{O}_4 + 0.5\text{NiO}$ shows this substrates prevents coke formation by the slow phase decomposition of Fe_3O_4 . Long term redox cycling shows MgFe_2O_4 and BaFe_2O_4 supported NiO are stable, with MgFe_2O_4 supported NiO showed little deactivation from cycle 2 to cycle 30.

6.2 Future Work

In this work, a neutral oxygen vacancy was assumed for calculating the energy of oxygen vacancy formation. However, this assumption was used for convenience and charge defects are likely to exist. Including charged defects, the energy of oxygen vacancy formation can be written as¹:

$$\text{Eq. 6.1: } \Delta E_{vacancy}^q = E_{defect,supercell}^q - E_{pristine,supercell} - \mu_O + qE_F + E_{corr}$$

In this equation, $E_{defected,supercell}^q$ is the energy of the defected supercell with charge state q, E_F is the fermi energy referenced to the valence band minimum, and E_{corr} is a correction term for the electrostatic interaction of the charge defects with its periodic images. One method to determining E_{corr} is to separate the electrostatic interaction into long range and short-range terms. The long-range component is the interaction beyond supercell boundaries and is evaluated by assigning a point charge to the defect and its periodic images² and using a dielectric constant to screen this interaction³. The short-range component (interaction within the supercell) is evaluated by taking the difference in electrostatic potential between the pristine and defective supercell¹. This is considered an alignment term such that the short-range electrostatic interactions decay to

zero far from the defect. As such, $E_{corr} = E_{PC} - q\Delta V$, where E_{PC} is the electrostatic energy from the long-range interactions and ΔV is the alignment term. Literature has shown that, for metal oxides, the defect is likely to be in the +2 ($q = 2$) charge state^{4,5} at $E_F = 0$. Accurate extension of this calculation to transition metal oxides is likely to require hybrid functionals to measure the band gap, because the PBE and PBE+U functionals are likely to underpredict the band gap^{6,7}. An illustration of how $\Delta E_{vacancy}$ changes across the Fermi energy is shown in Figure 6.1. A comparison of results found in Chapter 2 with those for charged defects will provide further understanding of the oxygen vacancy creation energies as an indicator for CLOU capabilities.

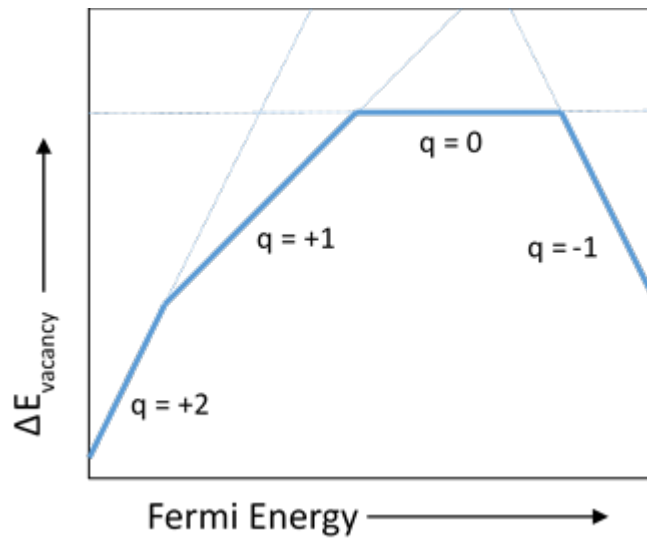


Figure 6.1: Schematic illustration of the vacancy formation energy with respect to the Fermi energy. The solid blue lines represent the most favorable charge state and dotted blue lines correspond to formation energy defined by equation 6.1.

In addition to these calculations, investigation of the recently developed SCAN meta-GGA for its application to oxygen vacancy calculations can provide insight into efficiently using DFT as a predictive tool for chemical looping applications. This functional has shown significant improvements over PBE functionals^{4,5}, with 6-7 times more computational cost (a relatively

moderate increase). For example the band gap of NiO, CoO, FeO, and MnO is under predicted by PBE+U by 37.5-55% while SCAN under predicts band gap by 12.5-42.5%⁵.

6.3 References

1. Van de Walle, C. G.; Neugebauer, J. First-Principles Calculations for Defects and Impurities: Applications to III-Nitrides. *J. Appl. Phys.* **2004**, *95* (8), 3851–3879. <https://doi.org/10.1063/1.1682673>.
2. Kumagai, Y.; Oba, F. Electrostatics-Based Finite-Size Corrections for First-Principles Point Defect Calculations. *Phys. Rev. B* **2014**, *89* (19), 195205. <https://doi.org/10.1103/PhysRevB.89.195205>.
3. Freysoldt, C.; Neugebauer, J.; Van de Walle, C. G. Fully Ab Initio Finite-Size Corrections for Charged-Defect Supercell Calculations. *Phys. Rev. Lett.* **2009**, *102* (1), 016402. <https://doi.org/10.1103/PhysRevLett.102.016402>.
4. Hine, N. D. M.; Frensch, K.; Foulkes, W. M. C.; Finnis, M. W. Supercell Size Scaling of Density Functional Theory Formation Energies of Charged Defects. *Phys. Rev. B* **2009**, *79* (2), 024112. <https://doi.org/10.1103/PhysRevB.79.024112>.
5. Maiti, D.; Cairns, J.; Kuhn, J. N.; Bhethanabotla, V. R. Interface Engineering of Metal Oxynitride Lateral Heterojunctions for Photocatalytic and Optoelectronic Applications. *J. Phys. Chem. C* **2018**, *122* (39), 22504–22511. <https://doi.org/10.1021/acs.jpcc.8b06100>.
6. Zhang, Y.; Sun, J.; Perdew, J. P.; Wu, X. Comparative First-Principles Studies of Prototypical Ferroelectric Materials by LDA, GGA, and SCAN Meta-GGA. *Phys. Rev. B* **2017**, *96* (3), 035143. <https://doi.org/10.1103/PhysRevB.96.035143>.
7. Peng, H.; Perdew, J. P. Synergy of van Der Waals and Self-Interaction Corrections in Transition Metal Monoxides. *Phys. Rev. B* **2017**, *96* (10), 100101. <https://doi.org/10.1103/PhysRevB.96.100101>.

APPENDICES

Appendix A. Supplementary Information for Chapter 2

Methods

Sensitivity Analysis of Hubbard U

A sensitivity analysis was conducted to determine the response of the energy of vacancy formation with respect to a change in Hubbard U. An 80-atom unit cell of CaMnO_3 and BaMnO_3 was used as the reference materials for the sensitivity analysis. Hubbard U was applied to Mn and varied from 2.5 to 6 eV in increments of 0.5 eV and implemented as described by Dudarev¹ using VASP²⁻⁵. G-type antiferromagnetic spin ordering was used for BaMnO_3 and Ferromagnetic was used for CaMnO_3 . K-point mesh was used according to the main text. The response of the energy of vacancy formation with respect to a change in Hubbard U was found by the slope of a linear fit of energy of vacancy formation (y) versus Hubbard U (x).

X-Ray Diffraction

X-Ray Diffraction was performed for $\text{Ca}_{0.75}\text{Sr}_{0.25}\text{MnO}_3$, $\text{CaMn}_{0.75}\text{Fe}_{0.25}\text{O}_3$, and CaMnO_3 . All samples showed diffraction patterns matching CaMnO_3 showing proper phase formation of CaMnO_3 as well as proper doping of strontium and iron in the CaMnO_3 structure. This is shown in S1.

Char Conversion Experiments

A quartz fluidized-bed reactor is with an outer diameter was used. An oxygen carrier weight of 15g is used for CaMnO_3 and $\text{CaMn}_{0.95}\text{Fe}_{0.05}\text{O}_3$ and a sample weight of 17g was used for $\text{Ca}_{0.75}\text{Sr}_{0.25}\text{MnO}_3$. 10 mg of char converted from Pittsburg #8 coal is used. The temperature is 850°C. 800 mL/min nitrogen (grade 5.0), 280 mL/min helium (grade 5.0) (char reduction) and 120 mL/min oxygen (extra dry grade, during oxidation only) was used.

CO₂ yield was defined as the char conversion multiplied by the CO₂ selectivity reported in the paper.

Results

Sensitivity Analysis

The results of the sensitivity analysis are shown in Figure A.1, with BaMnO₃ having a slope of -0.31 ($\Delta E_{\text{vacancy}}/\text{Hubbard } U$) and CaMnO₃ having a slope of -0.35 ($\Delta E_{\text{vacancy}}/\text{Hubbard } U$), showing a change in Hubbard U of 1 eV will having change of 0.31 and 0.35 eV for BaMnO₃ and CaMnO₃, respectively.

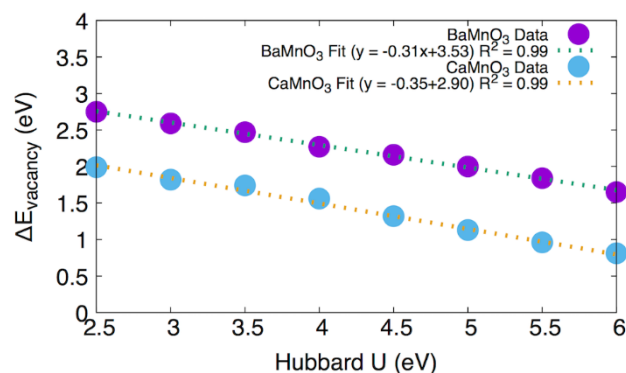


Figure A.1: Sensitivity Analysis of CaMnO₃ and BaMnO₃ using various Hubbard U values (2.5, 3.0, 3.5, 4.0, 4.5, 5.0, 5.5 and 6.0 eV) with a linear fit of the data. An 80-atom supercell is used.

Cation Shells and Corresponding Energies of Vacancy Formation for Ca_{0.75}Sr_{0.25}MnO₃

All eight cation shells and the corresponding energies of vacancy formation are shown below for Ca_{0.75}Sr_{0.25}MnO₃.

Table A1.1: Convergence test with respect to cutoff energy (CaMnO_3 , $\text{Ca}_{0.75}\text{Sr}_{0.25}\text{MnO}_3$, $\text{CaMn}_{0.75}\text{Fe}_{0.25}\text{O}_3$ values are shown using a 40 atom supercell and BaMnO_3 uses an 80 atom supercell. The perfect and defected supercells are relaxed with variable lattice parameters).

Material	$E_{\text{vac}}(\text{eV})$, Cutoff = 425 eV	$E_{\text{vac}}(\text{eV})$, Cutoff = 450 eV	Difference (eV/atom)
CaMnO_3 (site 1)	2.63	2.52	0.002
BaMnO_3	3.22	3.20	0.0002
$\text{Ca}_{0.75}\text{Sr}_{0.25}\text{MnO}_3$ (site 5)	2.27	2.26	0.0001
$\text{CaMn}_{0.75}\text{Fe}_{0.25}\text{MnO}_3$ (Site 3)	1.61	1.61	0.0000

Table A.2: Cation Shells and Corresponding Energies of Vacancy Formation for $\text{CaMn}_{0.75}\text{Fe}_{0.25}\text{O}_{3-\delta}$. Radial Distances for the cation neighbors shown here are found using DFT.

Site	Neighbor 1 (Å)	Neighbor 2 (Å)	Neighbor 3 (Å)	Neighbor 4 (Å)	Neighbor 5 (Å)	DFT Energy (eV)	DFT + U Energy (eV)
1	Mn (1.91)	Fe (1.92)	Ca (2.33)	Ca (2.57)	Ca (2.59)	1.74	0.43
2	Mn (1.91)	Mn (1.91)	Ca (2.32)	Ca (2.40)		2.38	0.90
3	Mn (1.89)	Fe (1.92)	Ca (2.32)	Ca (2.42)		1.61	0.59
4	Mn (1.91)	Mn (1.92)	Ca (2.33)	Ca (2.54)	Ca (2.59)	2.4	0.93

Table A.3: Cation Shells and Corresponding Energies of Vacancy Formation for $\text{Ca}_{0.75}\text{Sr}_{0.25}\text{MnO}_{3-\delta}$. Radial Distances for the cation neighbors shown here are found using DFT.

Site	Neighbor 1 (Å)	Neighbor 2 (Å)	Neighbor 3 (Å)	Neighbor 4 (Å)	Neighbor 5 (Å)	DFT Energy (eV)	DFT + U Energy (eV)
1a	Mn (1.93)	Mn (1.93)	Ca (2.34)	Sr (2.59)		2.77	1.45
1b	Mn (1.92)	Mn (1.92)	Ca (2.42)	Sr (2.43)		2.56	1.26
2a	Mn (1.89)	Mn (1.89)	Ca (2.33)	Ca (2.48)		2.26	0.92
2b	Mn (1.90)	Mn (1.90)	Ca (2.34)	Ca (2.43)		2.45	1.13
3a	Mn (1.91)	Mn (1.92)	Ca (2.35)	Ca (2.60)	Ca (2.63)	2.51	1.32
3b	Mn (1.91)	Mn (1.92)	Ca (2.35)	Ca (2.60)	Sr (2.63)	2.62	1.42
4	Mn (1.92)	Mn (1.92)	Ca (2.36)	Ca (2.53)	Ca (2.66)	2.54	1.43
5	Mn (1.89)	Mn (1.90)	Ca (2.44)	Sr (2.58)	Ca (2.59)	2.36	1.16

X-Ray Diffraction

Results of XRD are shown in A1.1 with CaMnO_3 , $\text{CaMn}_{0.75}\text{Fe}_{0.25}\text{O}_3$, and $\text{Ca}_{0.75}\text{Sr}_{0.25}\text{MnO}_3$ showing a good match with CaMnO_3 indicating good phase formation.

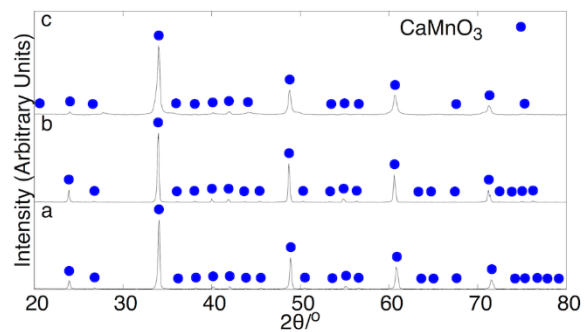


Figure A.2: XRD Pattern of a) CaMnO_3 , b) $\text{CaMn}_{0.75}\text{Fe}_{0.25}\text{O}_3$, and c) $\text{Ca}_{0.75}\text{Sr}_{0.25}\text{MnO}_3$.

XRD used for rietveld refinement is shown below in S3.

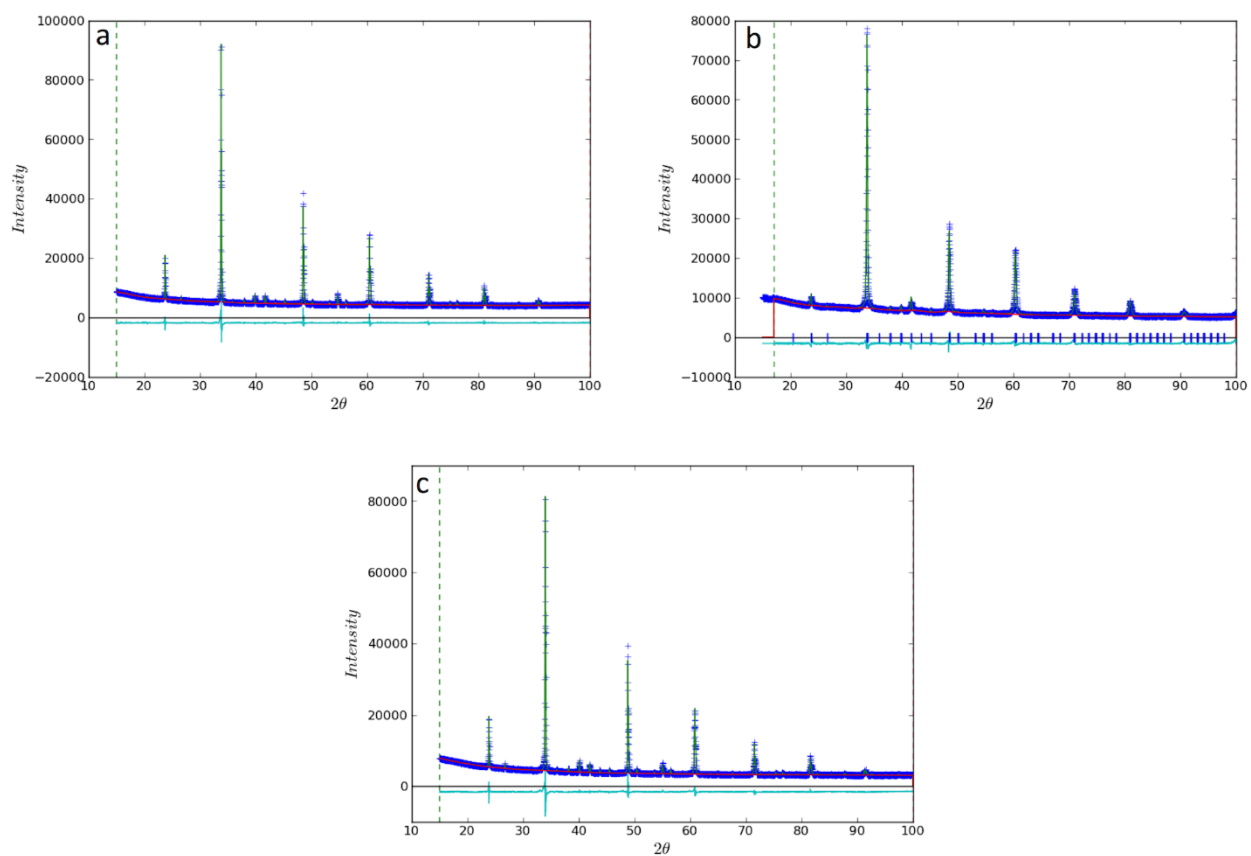


Figure A.3: XRD used for rietveld refinement, fit, and the experimental difference for a) $\text{CaMn}_{0.75}\text{Fe}_{0.25}\text{O}_3$ b) $\text{Ca}_{0.75}\text{Sr}_{0.25}\text{MnO}_3$ and c) CaMnO_3 .

Lattice parameters of pristine CaMnO₃ and BaMnO₃ with respect to magnetic ordering

Table A.4: Deviation in lattice parameters and unit cell volume from experimental values for CaMnO₃ (using DFT).

	a (% diff.)	b (% diff.)	c (% diff)	Vol. (% diff)
GAF	-0.44	-0.03	-1.90	0.47
AF-100	-0.28	-0.40	-0.10	0.57
AF-010	-0.93	-0.19	-0.05	0.79
F	-0.93	-0.26	-0.07	1.26

Table A.5: Deviation in lattice parameters and unit cell volume from experimental values for BaMnO₃ (using DFT).

	a (% diff.)	b (% diff.)	c (% diff)	Vol. (% diff)
GAF	-0.54	-0.54	-0.01	1.08
AF-001	-0.55	-0.55	-0.03	1.08
AF-010	-0.33	-0.30	-2.06	2.69
F	-0.31	-0.31	-2.00	2.63

Table A.6: Deviation in lattice parameters and unit cell volume from experimental values for CaMnO₃ (using DFT+U).

	a (% diff.)	b (% diff.)	c (% diff)	Vol. (% diff)
GAF	-1.10	-0.63	-0.55	2.29
AF-100	-1.00	-0.62	-0.47	2.10
AF-010	-1.49	-0.51	-0.57	2.59
F	-1.62	-0.82	-0.62	3.08

Table A.7: Deviation in lattice parameters and unit cell volume from experimental values for BaMnO₃ (using DFT+U).

	a (% diff.)	b (% diff.)	c (% diff)	Vol. (% diff)
GAF	-0.72	-0.72	-1.95	3.42
AF-001	-0.73	-0.73	-1.94	3.44
AF-010	-0.59	-0.58	-2.89	4.11
F	-1.62	-0.82	-0.62	3.08

Table A.8: Refinement Results for CaMnO_3 , $\text{Ca}_{0.75}\text{Sr}_{0.25}\text{MnO}_3$, and $\text{CaMn}_{0.75}\text{Fe}_{0.25}\text{O}_3$.

	CaMnO_3	$\text{Ca}_{0.75}\text{Sr}_{0.25}\text{MnO}_3$	$\text{CaMn}_{0.75}\text{Fe}_{0.25}\text{O}_3$
Z	4	4	4
Space Group	Pnma	Pnma	Pnma
a (Å)	5.28081(11)	5.3049(4)	5.30731(11)
b (Å)	7.45521(15)	7.4995(6)	7.49777(15)
c (Å)	5.26725(11)	5.3168(5)	5.30054(10)
V (Å³)	207.369(12)	211.52(5)	210.924(11)
R	0.023	0.020	0.040
wR	0.036	0.031	0.031
R_B	0.058	0.044	0.053
wR_B	0.080	0.061	0.079

Table A.9: Lattice Parameters of CaMnO_3 at 750°C, under different reducing environments.

P_{O2}	0.025 atm	0.01 atm	Inert
a (Å)	5.325(1)	5.325 (1)	5.333(1)
b (Å)	7.529 (1)	7.527 (1)	7.535(1)
c (Å)	5.323 (2)	5.324 (1)	5.330(1)
V (Å³)	213.4	213.4	214.2

Table A.10: Lattice Parameters of $\text{CaMn}_{0.75}\text{Fe}_{0.25}\text{O}_3$ at 750°C, under different reducing environments.

P_{O2}	0.025 atm	0.01 atm	Inert
a (Å)	5.356(1)	5.359 (1)	5.364 (1)
b (Å)	7.576 (1)	7.579 (1)	7.585 (1)
c (Å)	5.201 (1)	5.204 (1)	5.209 (1)
V (Å³)	211.1	211.4	211.9

Table A.11: Lattice Parameters of $\text{Ca}_{0.75}\text{Sr}_{0.25}\text{MnO}_3$ at 750°C, under different reducing environments.

P_{O2}	0.025 atm	0.01 atm	Inert
a (Å)	5.376 (1)	5.376 (1)	5.374 (1)
b (Å)	7.588 (1)	7.589 (1)	7.597 (1)
c (Å)	5.368 (1)	5.369 (1)	5.379 (1)
V (Å³)	219.0	219.1	219.6

Table A.12: Lattice Parameters for Pristine and Defective Supercell of CaMnO_3 , including both oxygen types.

P_{O_2}	Defect – Type 1	Defect – Type 2	Inert
a (Å)	5.30	5.32	5.30
b (Å)	7.49	7.46	7.46
c (Å)	5.26	5.29	5.27
V (Å ³)	208.98	209.86	208.3

Table A.13: Lattice Parameters for Pristine and Defective Supercell of $\text{Ca}_{0.75}\text{Sr}_{0.25}\text{MnO}_3$, including oxygen types discussed in the main text.

P_{O_2}	Defect – Type 2a	Defect – Type 2b	Defect – Type 5	Inert
a (Å)	5.32	5.31	5.33	5.32
b (Å)	7.54	7.54	7.51	7.51
c (Å)	5.30	5.31	5.33	5.31
V (Å ³)	212.60	212.71	213.51	212.1

Table A.14: Lattice Parameters for Pristine and Defective Supercell of $\text{CaMn}_{0.75}\text{Fe}_{0.25}\text{O}_3$, including oxygen types discussed in the main text

P_{O_2}	Defect – Type 1	Defect – Type 3	Inert
a (Å)	5.34	5.33	5.32
b (Å)	7.47	7.51	7.48
c (Å)	5.30	5.27	5.26
V (Å ³)	211.32	210.71	209.49

Table A.15: Octahedral Bond Distortion from experiments (Rietveld Refinement), DFT, and DFT+U for CaMnO_3 , $\text{Ca}_{0.75}\text{Sr}_{0.25}\text{MnO}_3$, and $\text{CaMn}_{0.75}\text{Fe}_{0.25}\text{O}_3$.

	CaMnO_3	$\text{Ca}_{0.75}\text{Sr}_{0.25}\text{MnO}_3$	$\text{CaMn}_{0.75}\text{Fe}_{0.25}\text{O}_3$
Experiment	8.64E-5	2.79E-4	2.12E-4
DFT	5.67E-6	7.74E-6	4.93E-6
DFT+U	6.67E-6	2.84E-5	1.61E-5

Equilibrium partial pressure of oxygen of Mn – containing perovskites during

The equilibrium P_{O_2} range between reduction and oxidation of $\text{BaMnO}_{3-\delta}$, $\text{CaMnO}_{3-\delta}$, $\text{Ca}_{0.75}\text{Sr}_{0.25}\text{MnO}_{3-\delta}$, and $\text{CaMn}_{0.75}\text{Fe}_{0.25}\text{O}_{3-\delta}$ is shown below. Reduction is at 650°C with an oxygen non-stoichiometry of $\delta = 0.25$ and oxidation is at 950°C with an oxygen non-stoichiometry of $\delta = 0.05$, according to the equation below, with $\Delta E_{\text{vacancy}}$ taken from DFT+U calculations using the

largest simulated supercell. P_{O_2} is the partial pressure of oxygen and P^0 is the reference partial pressure (1 atm)

$$C_v = \frac{\delta}{3} = \exp\left(\frac{-\Delta E_{vacancy}}{RT}\right) * \frac{P_{O_2}}{P^0}$$

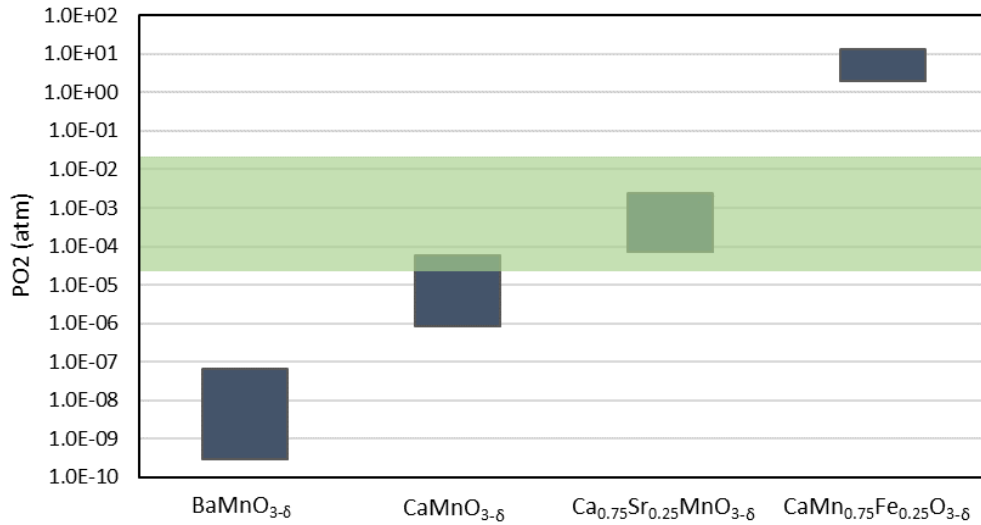


Figure A.4: Equilibrium P_{O_2} between 650°C, $\delta = 0.25$ and 950°C, $\delta = 0.05$. The desired P_{O_2} range is shaded in green.

Extra Figures

Magnetic Spin Ordering

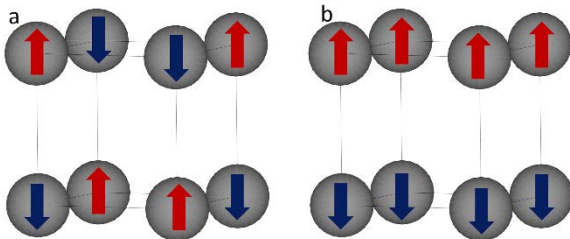


Figure A.5: Diagram of spin ordering for a) g-type antiferromagnetic and b) a-type antiferromagnetic. Grey spheres represent site of spin ordering.

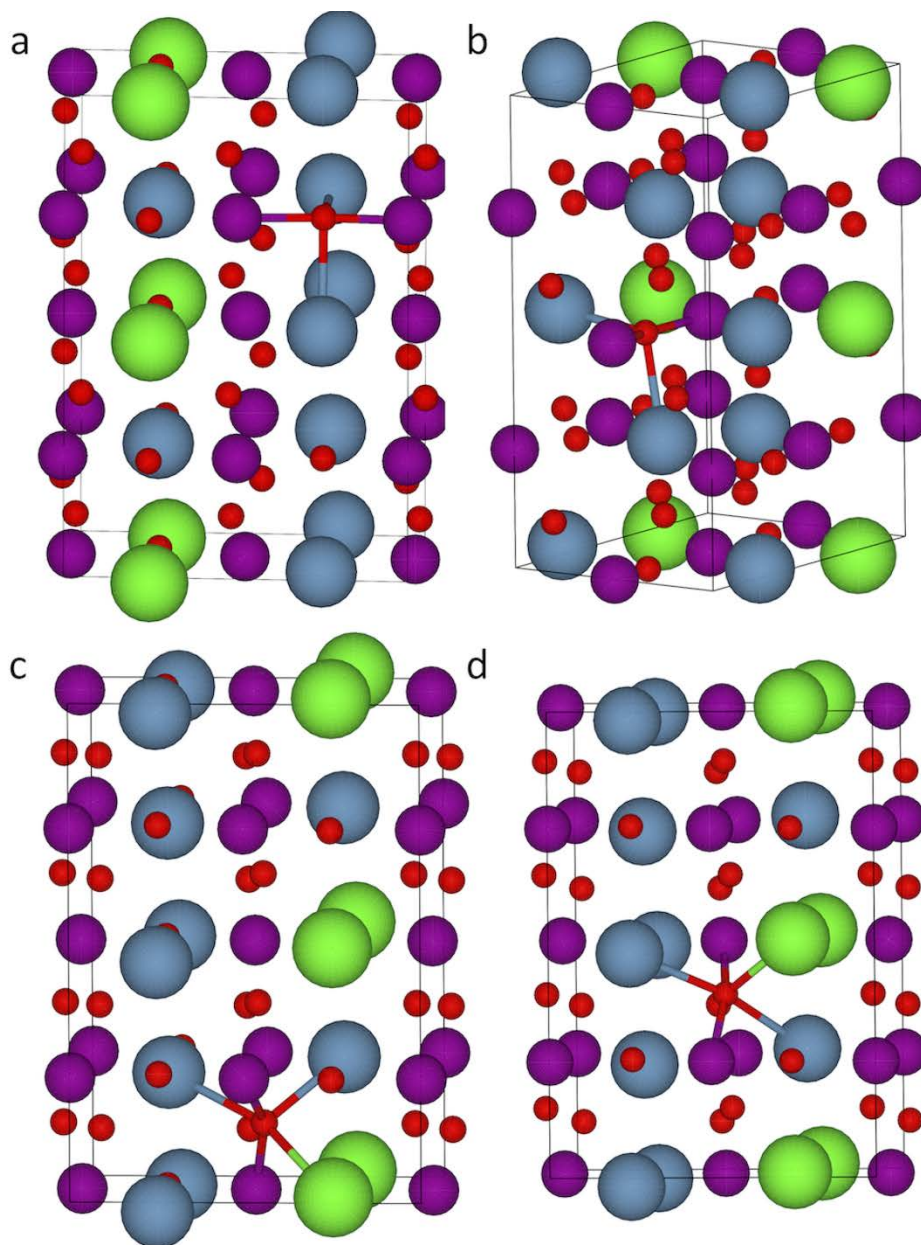


Figure A.6: Oxygen Sites for $\text{CaMn}_{0.75}\text{Fe}_{0.25}\text{O}_{3-\delta}$: a) Site 2a b) Site 2b c) Site 3a and d) Site 5.

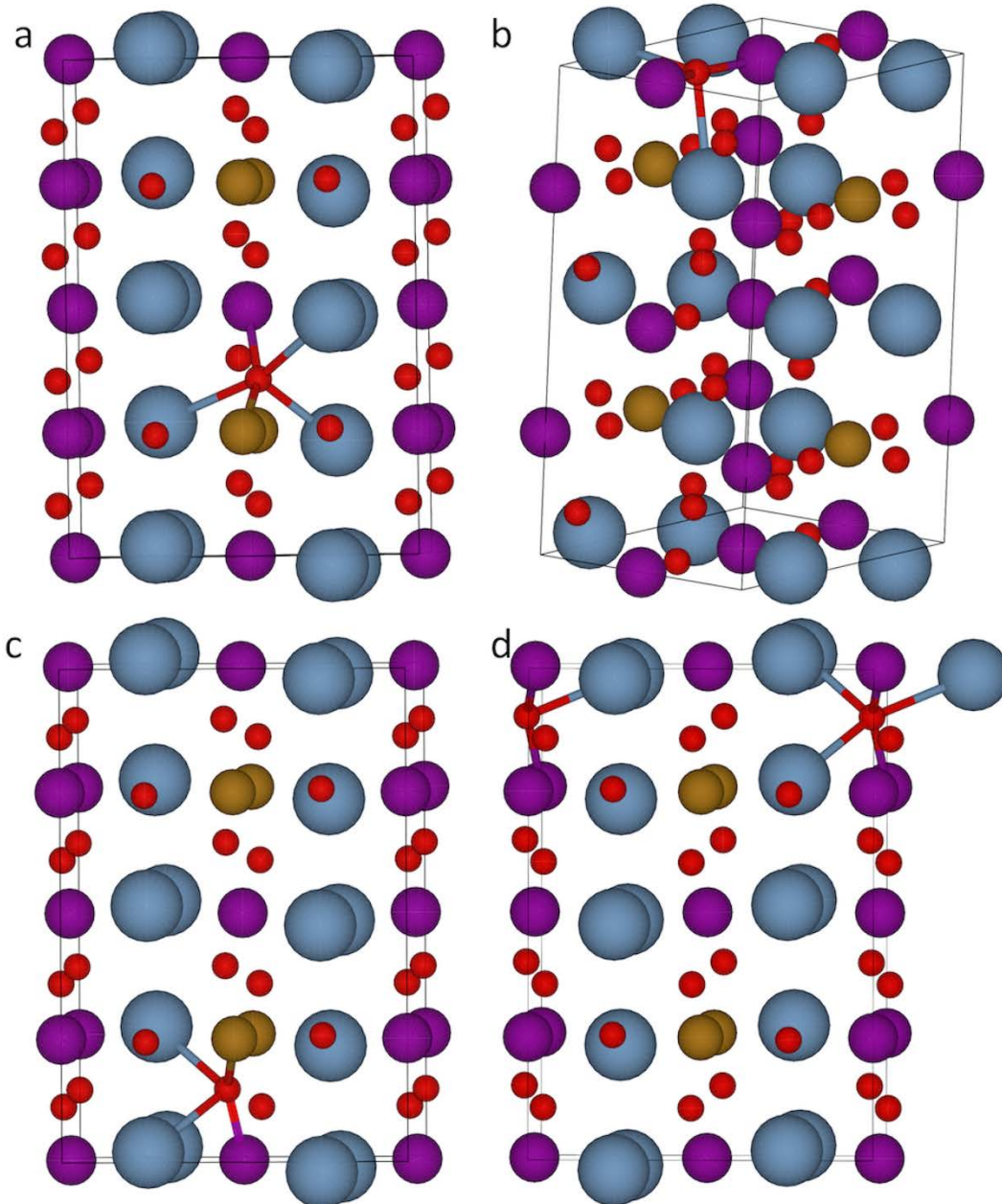


Figure A.7: Oxygen Sites for $\text{CaMn}_{0.75}\text{Fe}_{0.25}\text{O}_{3-\delta}$: a) Site 1 b) Site 2 c) Site 3 and d) Site 4.

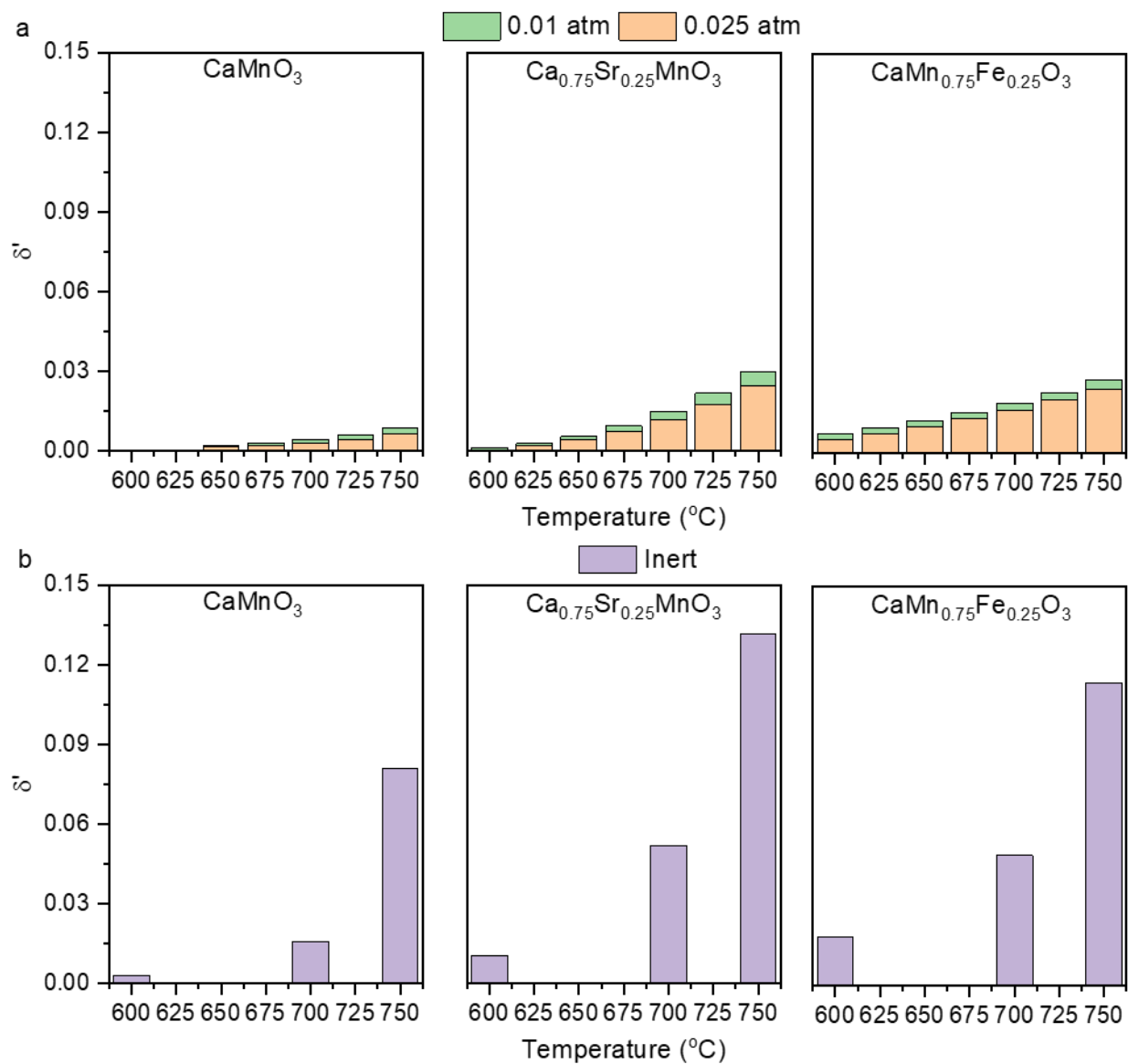


Figure A.8: Non-stoichiometry of $CaMnO_{3-\delta'}$, $Ca_{0.75}Sr_{0.25}MnO_{3-\delta'}$, and $CaMn_{0.75}Fe_{0.25}O_{3-\delta'}$ (with respect to sample at room temperature after pretreatment) as function of partial pressure of oxygen and temperature for a) $P_{O_2} = 0.01$ atm and 0.025 atm and b) Inert. δ' refers to oxygen non-stoichiometry in $ABO_{3-\delta'}$ perovskite. Pretreatment was with 20% O_2 at 1000 $^{\circ}C$.

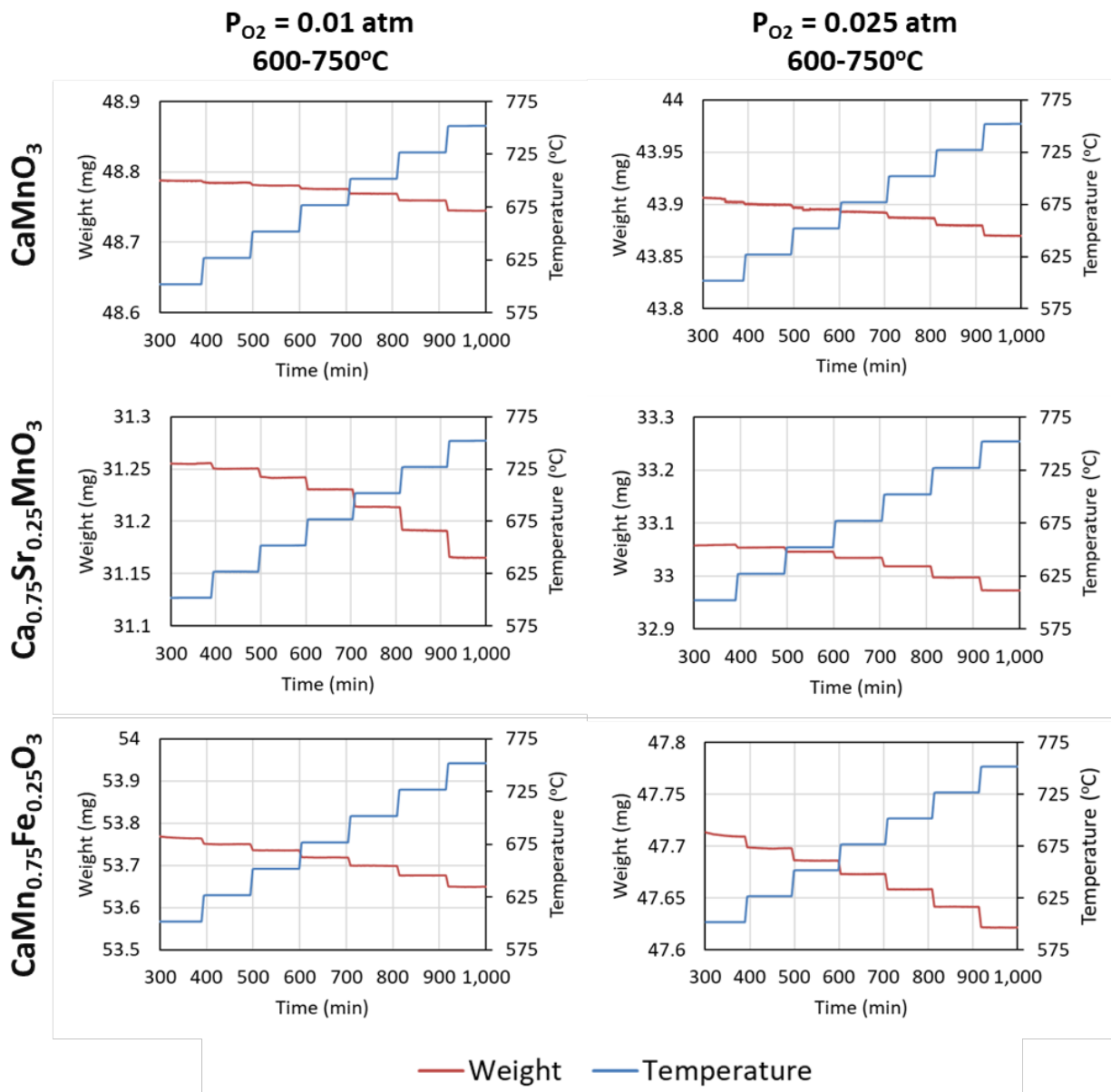


Figure A.9: Thermogravimetric curves of reductions of under either a P_{O_2} of 0.01 atm or 0.025 atm between 600-750 $^{\circ}\text{C}$ at 25 $^{\circ}\text{C}/\text{min}$ increments.

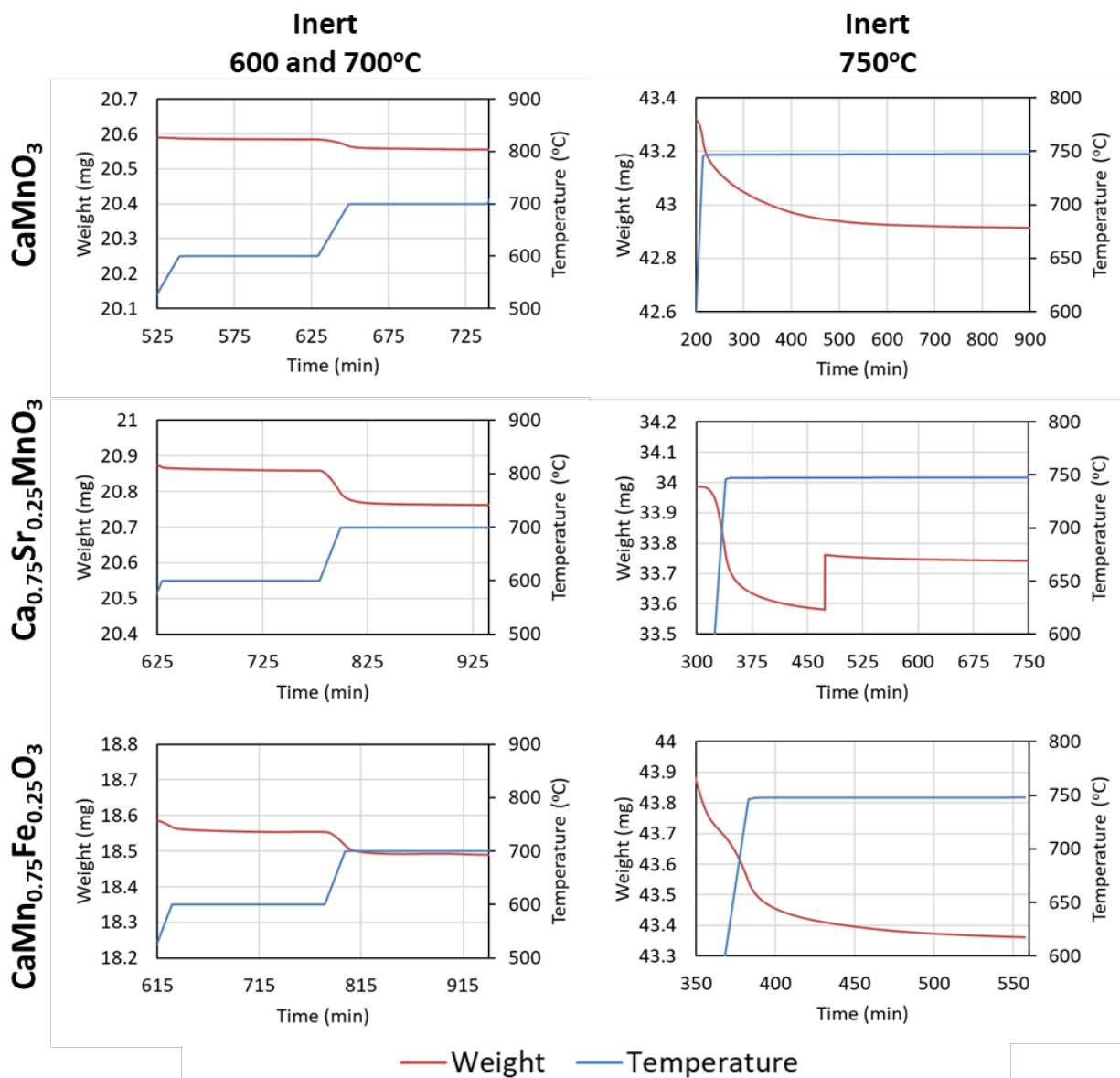


Figure A.10: Thermogravimetric curves of reduction in an inert environment at 600, 700, and 750°C.

The sudden increase in weight for $\text{Ca}_{0.75}\text{Sr}_{0.25}\text{MnO}_3$ at 750°C is a result of instrument fluctuation, due to an external force on the instrument.

References:

1. Dudarev, S. L.; Botton, G. A.; Savrasov, S. Y.; Humphreys, C. J.; Sutton, A. P. Electron-Energy-Loss Spectra and the Structural Stability of Nickel Oxide: An LSDA+U Study. *Phys. Rev. B* **1998**, *57* (3), 1505–1509. <https://doi.org/10.1103/PhysRevB.57.1505>.
2. Kresse, G.; Furthmuller, J. Efficiency of Ab-Initio Total Energy Calculations for Metals and Semiconductors Using a Plane-Wave Basis Set. *Comput. Mater. Sci.* **1996**, *6* (1), 15–50. [https://doi.org/10.1016/0927-0256\(96\)00008-0](https://doi.org/10.1016/0927-0256(96)00008-0).
3. Kresse, G.; Hafner, J. \textit{Ab Initio} Molecular Dynamics for Liquid Metals. *Phys. Rev. B* **1993**, *47* (1), 558–561. <https://doi.org/10.1103/PhysRevB.47.558>.
4. Kresse, G.; Hafner, J. \textit{Ab Initio} Molecular-Dynamics Simulation of the Liquid-Metal\char21{ }amorphous-Semiconductor Transition in Germanium. *Phys. Rev. B* **1994**, *49* (20), 14251–14269. <https://doi.org/10.1103/PhysRevB.49.14251>.
5. Kresse, G.; Furthmuller, J. Efficient Iterative Schemes for Ab Initio Total-Energy Calculations Using a Plane-Wave Basis Set. *Phys. Rev. B* **1996**, *54* (16), 11169–11186. <https://doi.org/10.1103/PhysRevB.54.11169>.

Appendix B. Supplementary Information for Chapter 4

Method for calculating equilibrium products

The equilibrium compositions of products, resulting from methane reaction with redox catalysts was found using a mixture of oxygen extracted from the redox catalysts and methane fed to redox catalysts. The total amount of oxygen was calculated from oxygen containing products including CO, CO₂, and H₂O, while the amount of CH₄ was calculated from the carbons in CO, CO₂, and CH₄. The equilibrium composition was simulated using an Rgibbs reactor in AspenPlus.

Results

XRD

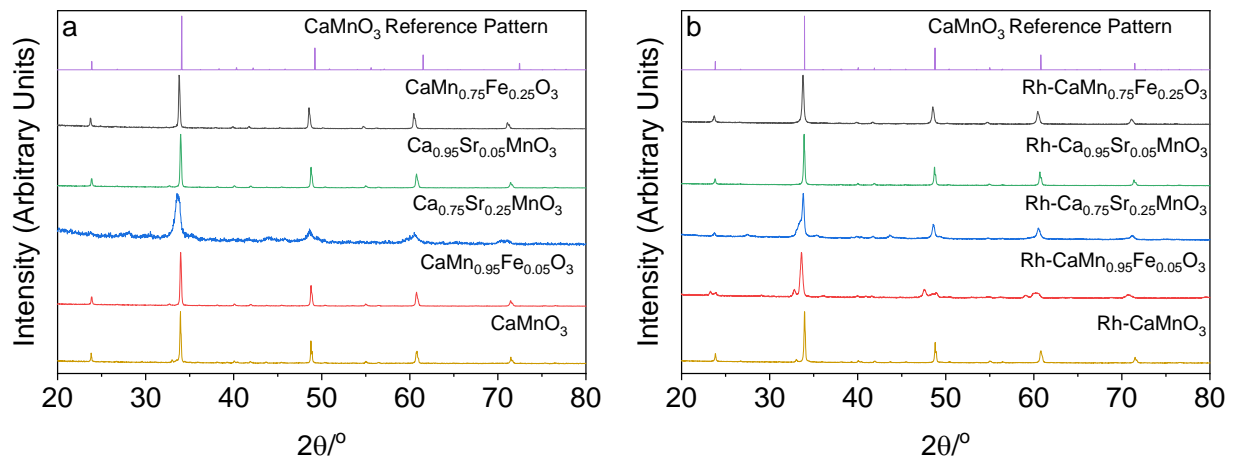


Figure B.1: XRD patterns of a) unpromoted CaMnO₃, CaMn_{0.95}Fe_{0.05}MnO₃, Ca_{0.75}Sr_{0.25}MnO₃, Ca_{0.95}Sr_{0.05}MnO₃, and CaMn_{0.75}Fe_{0.25}O₃ and b) Rh promoted Rh-CaMnO₃, Rh-CaMn_{0.95}Fe_{0.05}MnO₃, Rh-Ca_{0.75}Sr_{0.25}MnO₃, Rh-Ca_{0.95}Sr_{0.05}MnO₃, and Rh-CaMn_{0.75}Fe_{0.25}O₃ redox catalysts.

CH₄ TPR

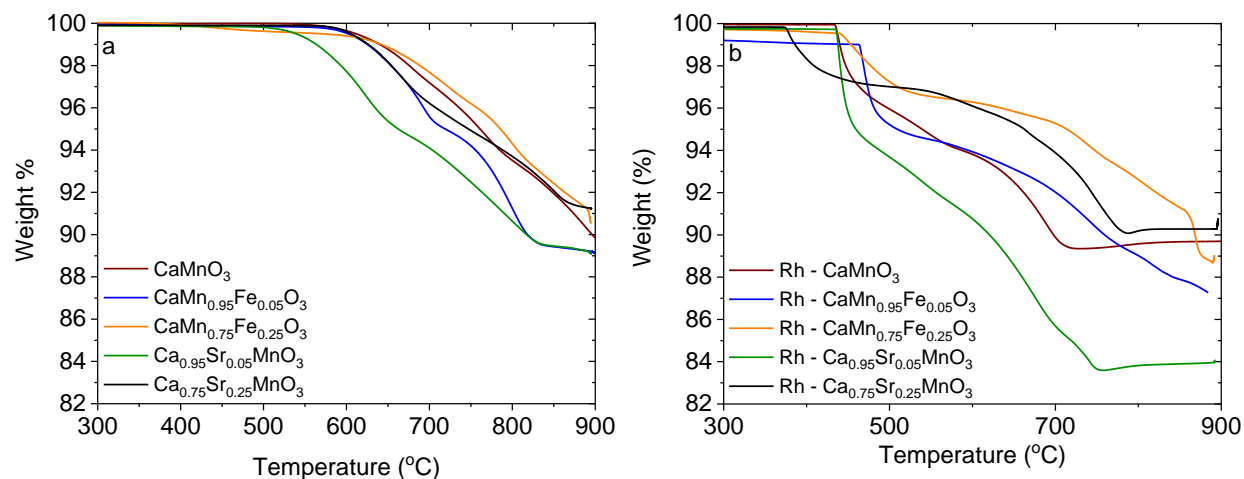


Figure B.2: Weight loss of a) unpromoted and b) promoted redox catalysts during CH₄ – TPR. The redox catalysts were reduced in 10% CH₄ by heating to 900°C at a ramp rate of 20°C/min.

Oxygen TPD

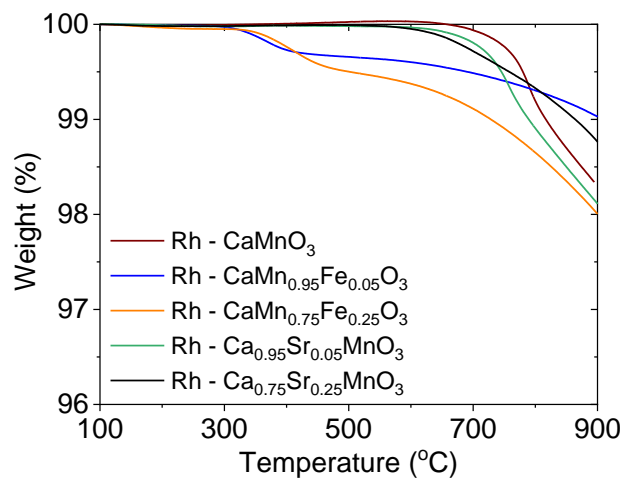


Figure B.3: Weight loss of promoted redox catalysts during O₂-TPD.

Instantaneous CH₄ conversion and Syngas Selectivity

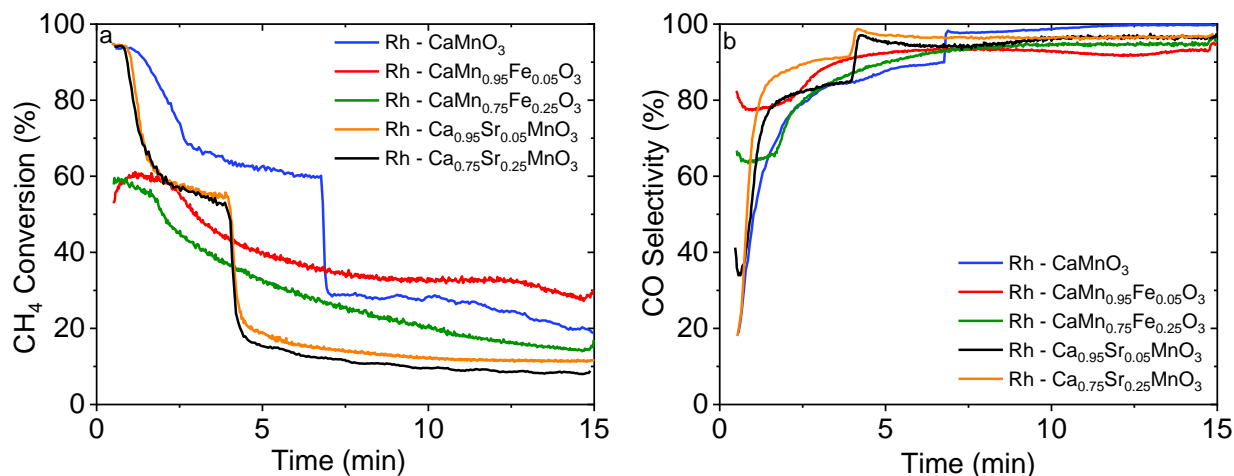


Figure B.4: a) Instantaneous CH₄ conversion and b) Instantaneous CO Selectivity of Rh - CaMnO₃, Rh - CaMn_{0.75}Fe_{0.25}O₃, Rh - CaMn_{0.95}Fe_{0.05}O₃, Rh - Ca_{0.75}Sr_{0.25}MnO₃, and Rh - Ca_{0.95}Sr_{0.05}MnO₃ during dual bed experiments. Reaction condition: 5% CH₄, GHSV = 12000 h⁻¹, 600°C, 15 min reduction, and 10 min oxidation.

Optimization of Redox Time

Effects of oxidation time on methane conversion and syngas yield are shown in Figure S5, using five minutes of reduction. For Rh-CaMn_{0.95}Fe_{0.05}O₃ redox catalyst, the CH₄ conversion increased significantly with increasing oxidation time from 1 to 3 minutes. Further increasing oxidation time to 5 min only slightly improved methane conversion from 46% to 51%. Rh-CaMn_{0.75}Fe_{0.25}O₃ showed an increase in CH₄ conversion initially with increasing oxidation time up to 1.5 minutes, while reaching a plateau with longer oxidation time. The increase in CH₄ conversion was accompanied by a similar increase in syngas yield. This finding showed that 5 minutes of oxidation resulted in high methane conversion and/or syngas yield, which was used to further optimize the reaction conditions for Rh-CaMn_{0.75}Fe_{0.25}O₃ and Rh-CaMn_{0.95}Fe_{0.05}O₃ catalysts. For Rh-CaMnO₃, there was an increase in CH₄ conversion across all oxidation times, and maximum syngas yield was achieved with 3 minutes of oxidation. Therefore, we chose 3 minutes of oxidation for further optimization of Rh-CaMnO₃.

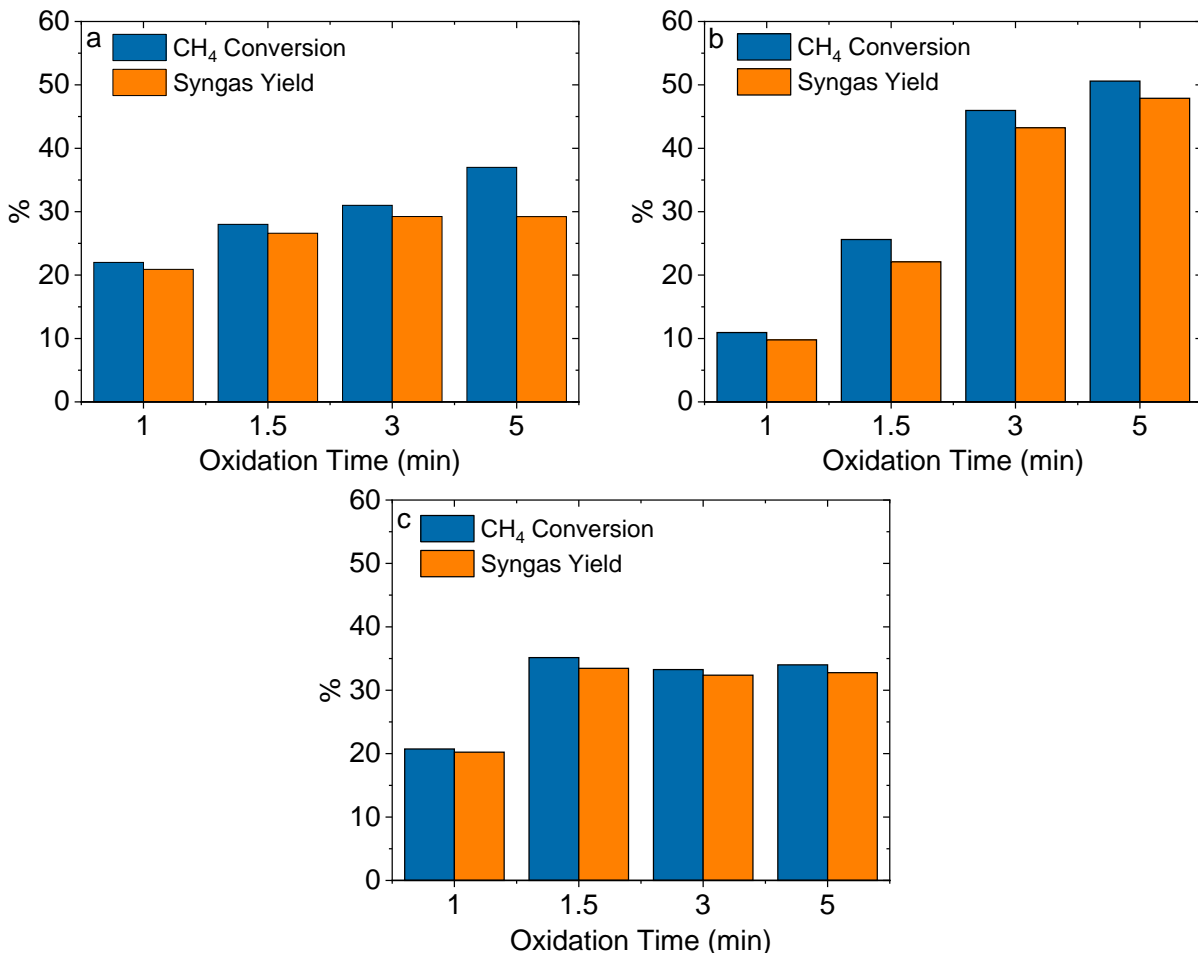


Figure B.5: CH₄ conversion and syngas yield for varying oxidation time between 1 and 5 minutes for a) Rh-CaMnO₃, b) Rh-CaMn_{0.95}Fe_{0.05}O₃, c) CaMn_{0.75}Fe_{0.25}O₃. All results shown here use 5 minutes reduction at 600°C with 5% CH₄ during reduction and 5.8% O during oxidation at a GHSV of 12000 h⁻¹.

Further optimization was conducted by varying reduction time from 3 to 7 min, as shown in Figure S6. Rh-CaMn_{0.75}Fe_{0.25}O₃ showed 8% higher methane conversion by shortening the reduction time to three minutes. It also showed an increase in syngas yield of 7%. Rh-CaMn_{0.95}Fe_{0.05}O₃ showed the highest methane conversion with 3 or 5 minutes of reduction. As such, future experiments used 3 minutes of reduction and 5 minutes of oxidation for Fe doped redox catalysts.

Rh-CaMnO₃ showed an increase in methane conversion and syngas yield of 7% and 4.5%, respectively, when reduction time was shortened to three minutes. As previously discussed, Rh-

CaMnO₃ showed a two stage behavior of i) high methane conversion, low selectivity and ii) high selectivity, low methane conversion. It is most desirable to have an even split of these two regions so syngas yield can be optimized. At higher temperatures and lower residence times, the first region is expected to be emphasized due to higher oxidation. Subsequently, three minutes of reduction may not display the second region. With only a marginal increase in methane conversion occurring by decreasing reduction time to three minutes, future experiments used five minutes of reduction.

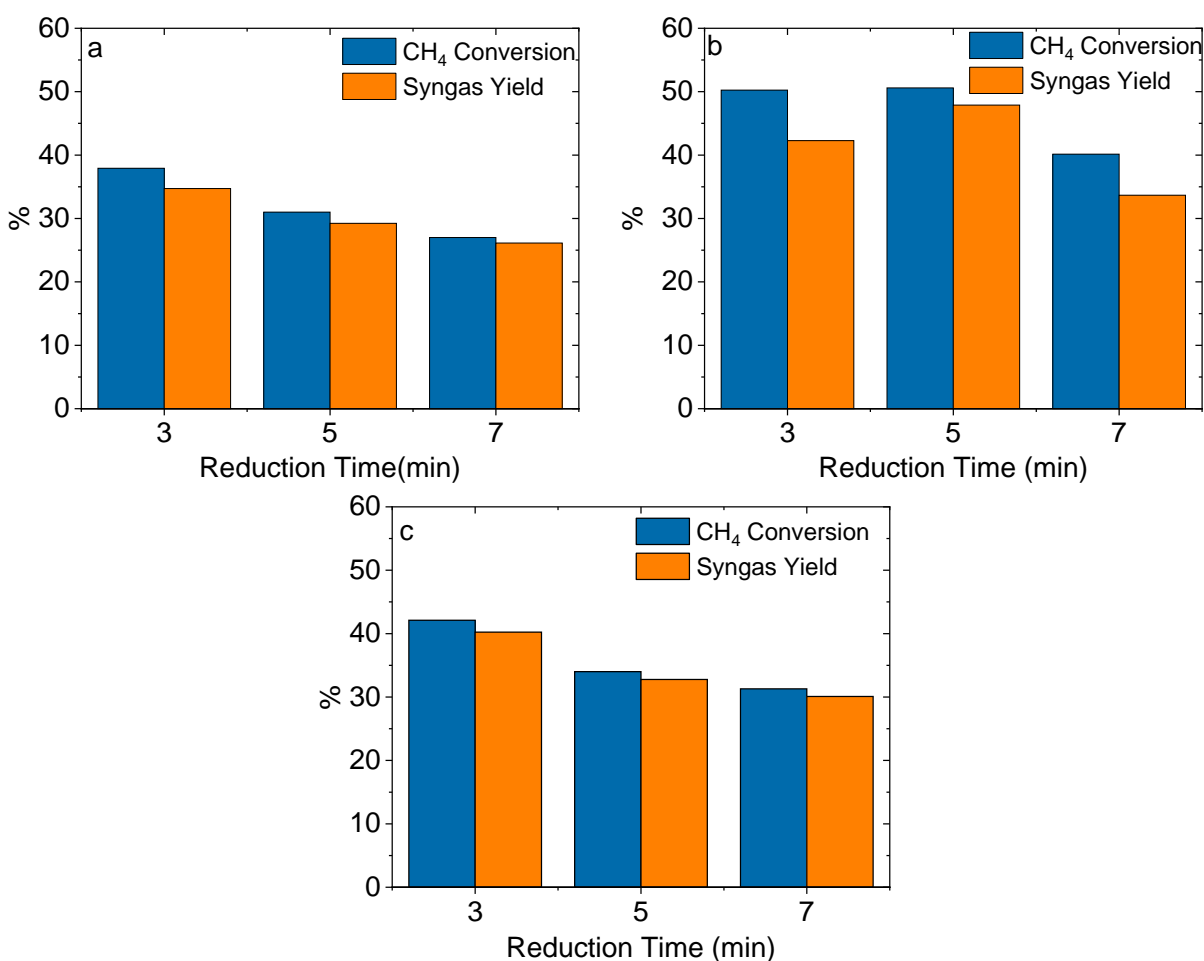


Figure B.6: CH₄ conversion and syngas yield for varying reduction time between 3 and 7 minutes for a) Rh-CaMnO₃, b) Rh-CaMn_{0.95}Fe_{0.05}O₃, c) Rh-CaMn_{0.75}Fe_{0.25}O₃. Rh-CaMnO₃ used 3 minutes oxidation. Rh-CaMn_{0.95}Fe_{0.05}O₃ and Rh-CaMn_{0.75}Fe_{0.25}O₃ used 5 minutes of oxidation. All results here are at 600°C with 5% CH₄ during reduction and 5.8% O during oxidation at a GHSV of 12000 h⁻¹.

Appendix C. Supplementary Information for Chapter 5

Results

Blank Redox Experiment

A blank redox experiment showed the weight of an empty crucible during reduction and inert (purge) steps are equal. The momentary weight increase was a result of gas switching and lasted less than one minute. The weight change due to switching from inert to oxidizing conditions was roughly 0.17mg. The weight difference between inert and oxidizing was expected to be change between crucible, but is expected to be negligible in comparison to overall weight change of the oxygen carrier during oxidization. Nonetheless, the weight during oxidization was only compared between cycles and not oxygen carriers.

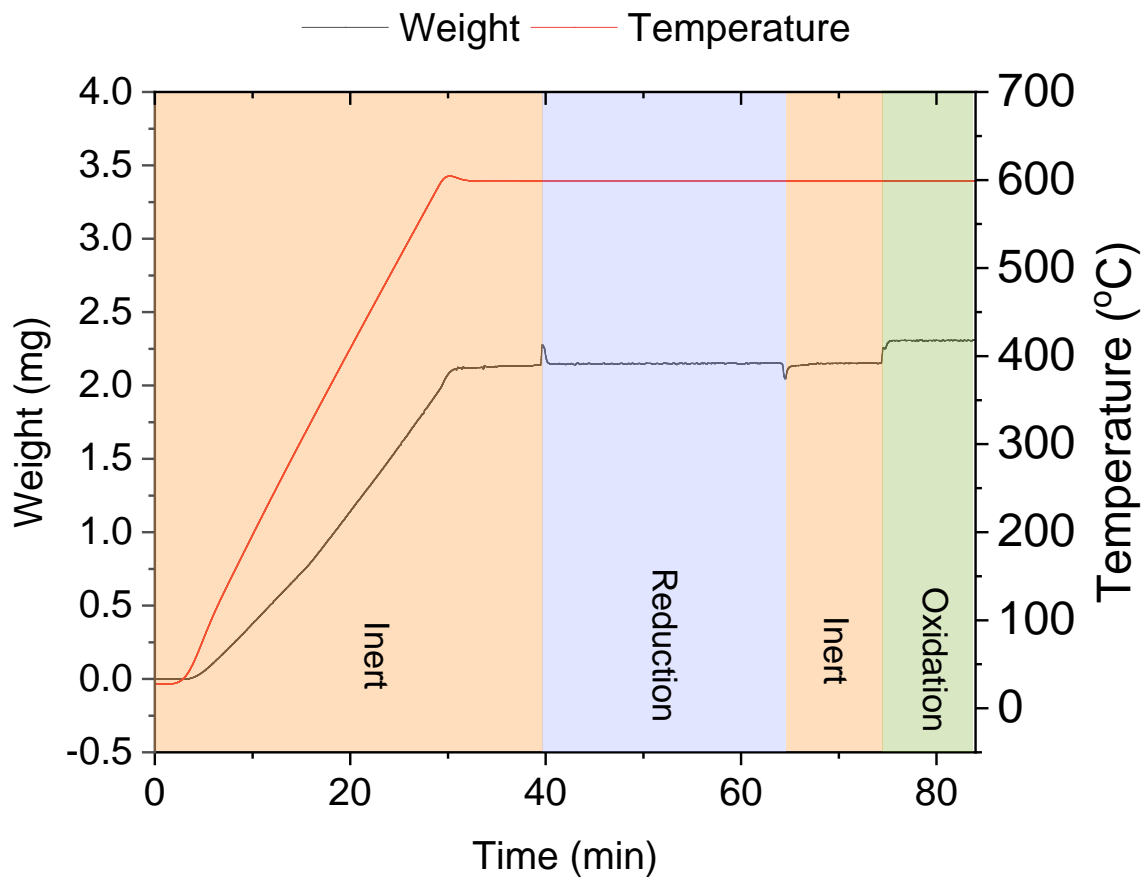


Figure C.1: Weight of an empty crucible during inert (180 mL/min He), reduction (180 mL/min He, 20 mL/min CH₄), and oxidation (180 mL/min He, 20 mL/min O₂) at 900°C.

Long Term Reduction of Spinel

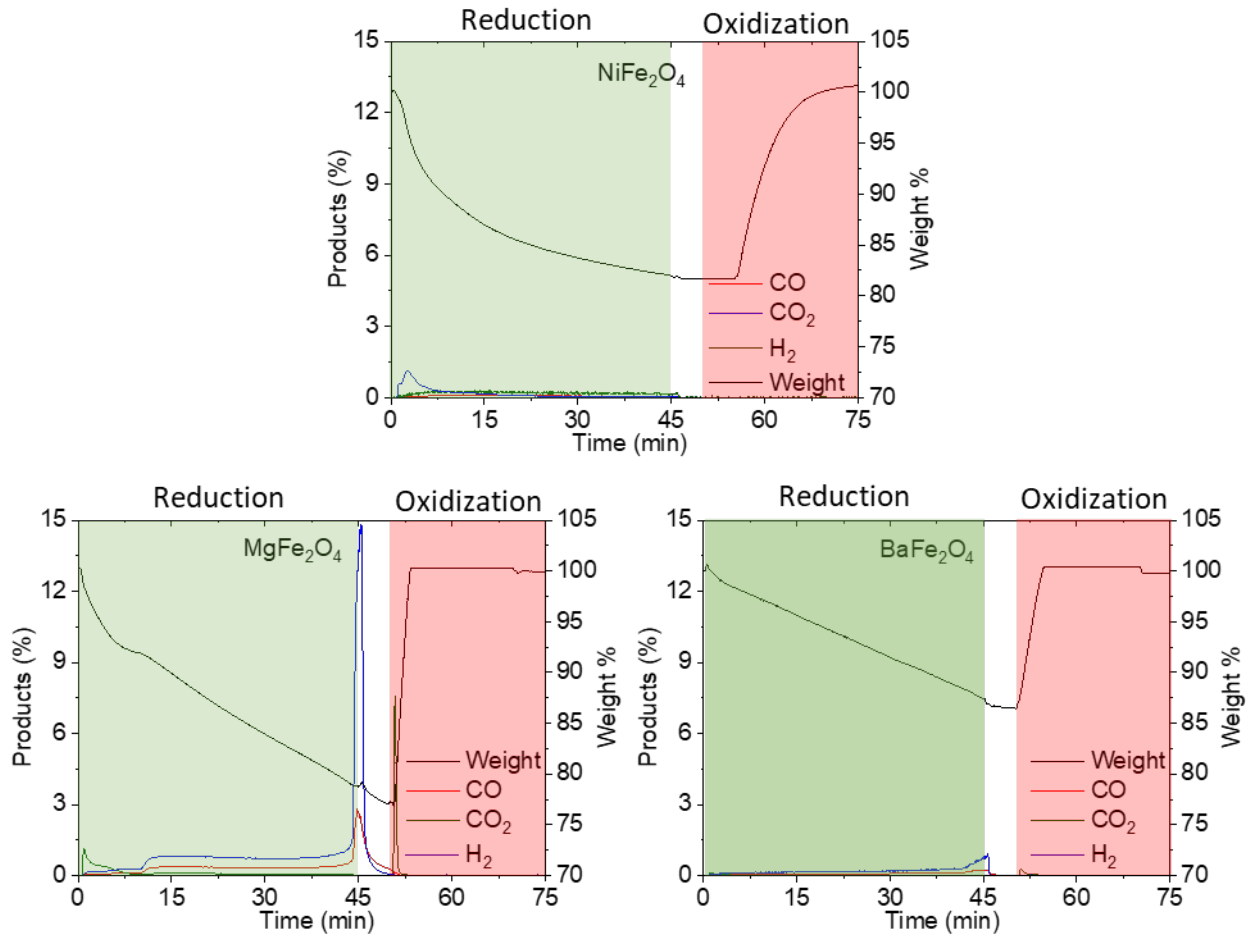


Figure C.2: Products during long term reduction and re-oxidization of MgFe₂O₄, NiFe₂O₄, and BaFe₂O₄.

Redox Cycling

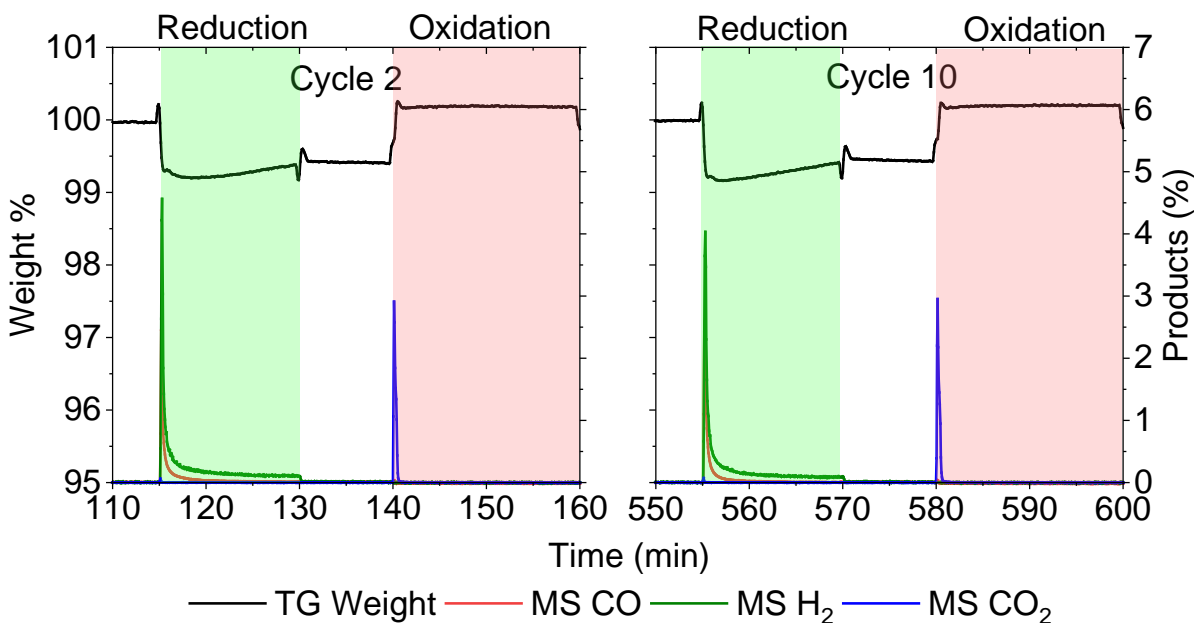


Figure C.3: Redox cycling of $\text{MgAl}_2\text{O}_4 + 0.25\text{NiO}$ under at 900°C . Reduction is with 180 mL/min He and 20 mL/min CH_4 . Oxidation is with 180 mL/min He and 20 mL/min O_2 . Purge is with 180 mL/min He.

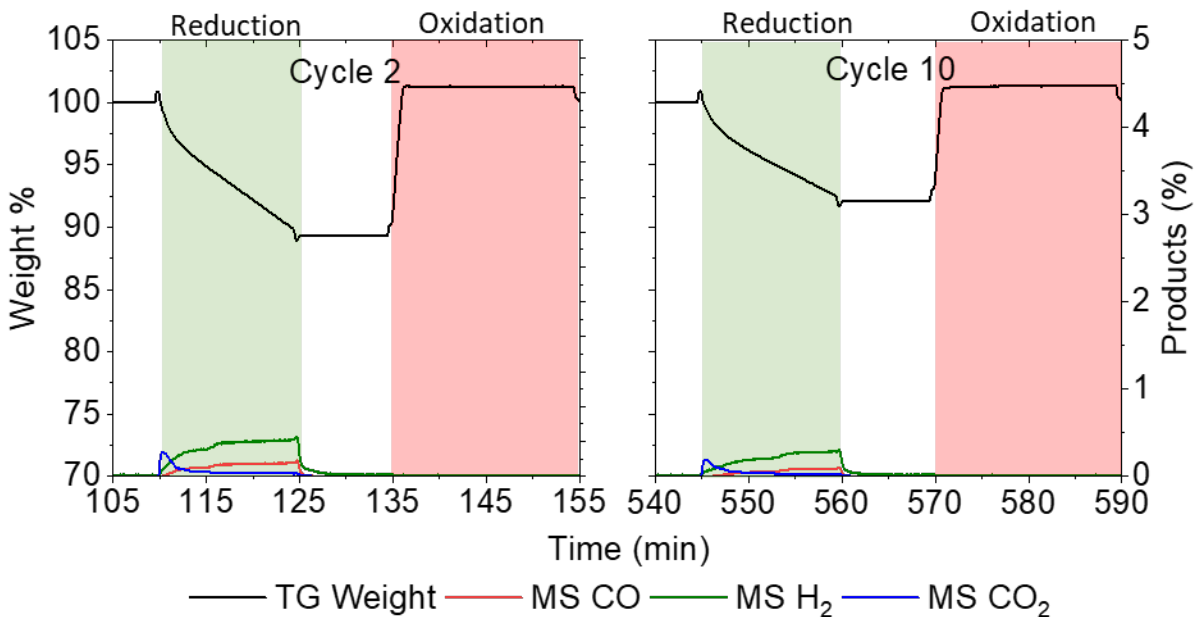


Figure C.4: Redox cycling of $\text{BaFe}_2\text{O}_4 + 0.25\text{NiO}$ under at 900°C . Reduction is with 180 mL/min He and 20 mL/min CH_4 . Oxidation is with 180 mL/min He and 20 mL/min O_2 . Purge is with 180 mL/min He.

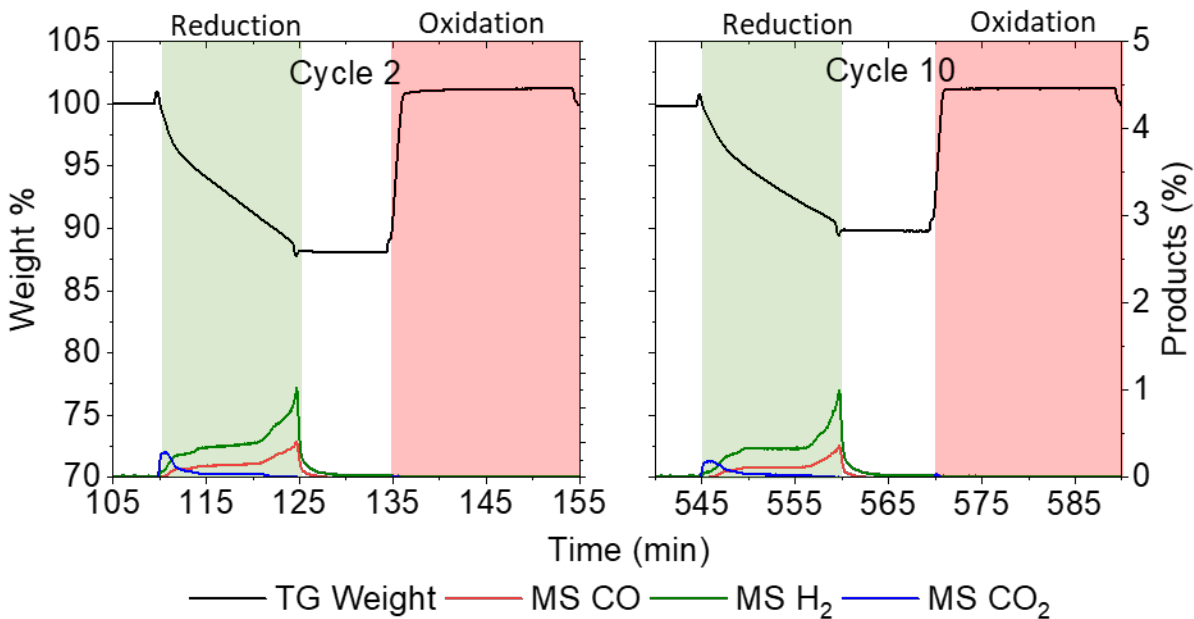


Figure C.5: Redox cycling of BaFe₂O₄ + 0.5NiO under at 900°C. Reduction is with 180 mL/min He and 20 mL/min CH₄. Oxidation is with 180 mL/min He and 20mL/min O₂. Purge is with 180 mL/min He.

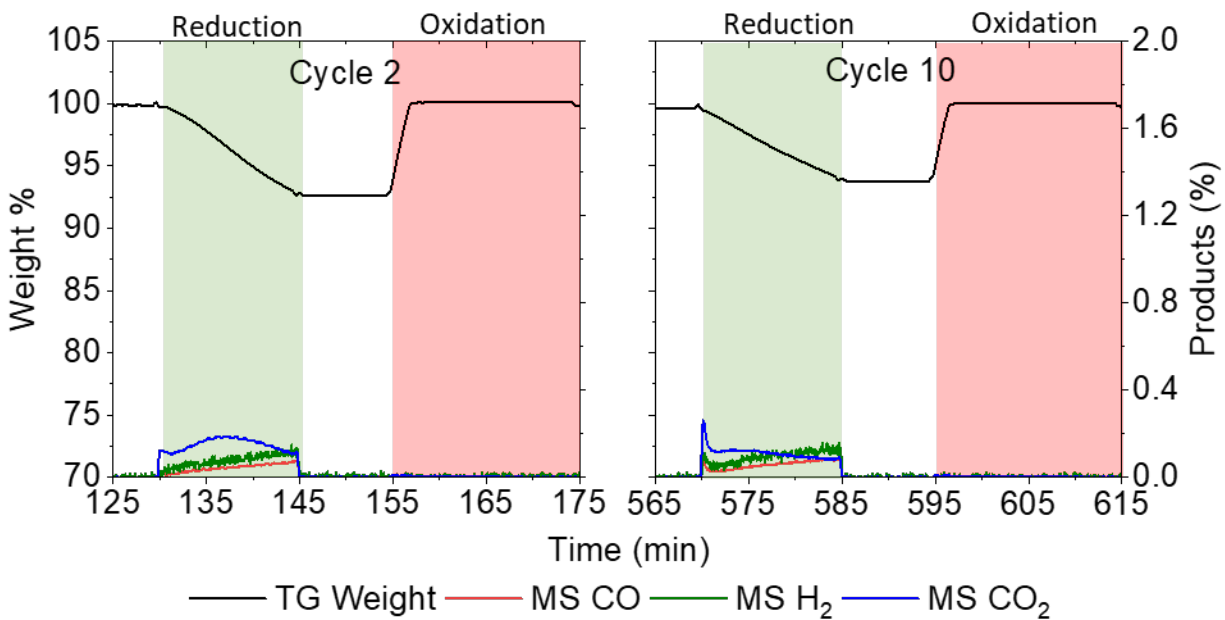


Figure C.6: Redox cycling of MgFe₂O₄ + 0.25NiO under at 900°C. Reduction is with 180 mL/min He and 20 mL/min CH₄. Oxidation is with 180 mL/min He and 20mL/min O₂. Purge is with 180 mL/min He.

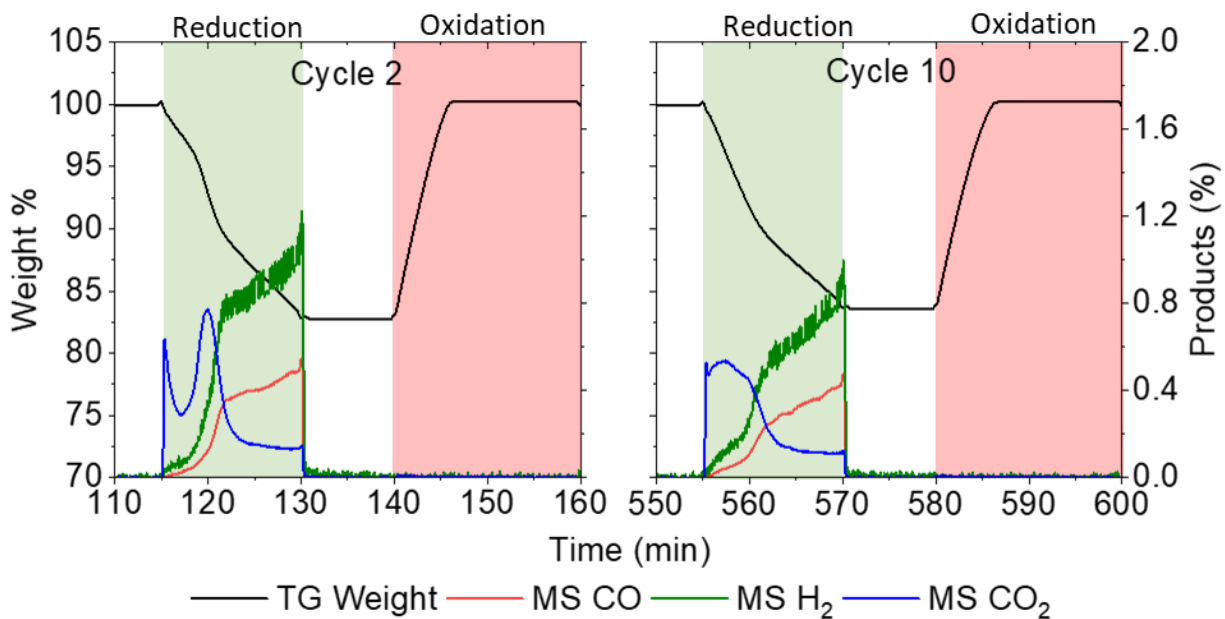


Figure C.7: Redox cycling of $\text{MgFe}_2\text{O}_4 + 0.5\text{NiO}$ under at 900°C . Reduction is with 180 mL/min He and 20 mL/min CH_4 . Oxidation is with 180 mL/min He and 20mL/min O_2 . Purge is with 180 mL/min He.

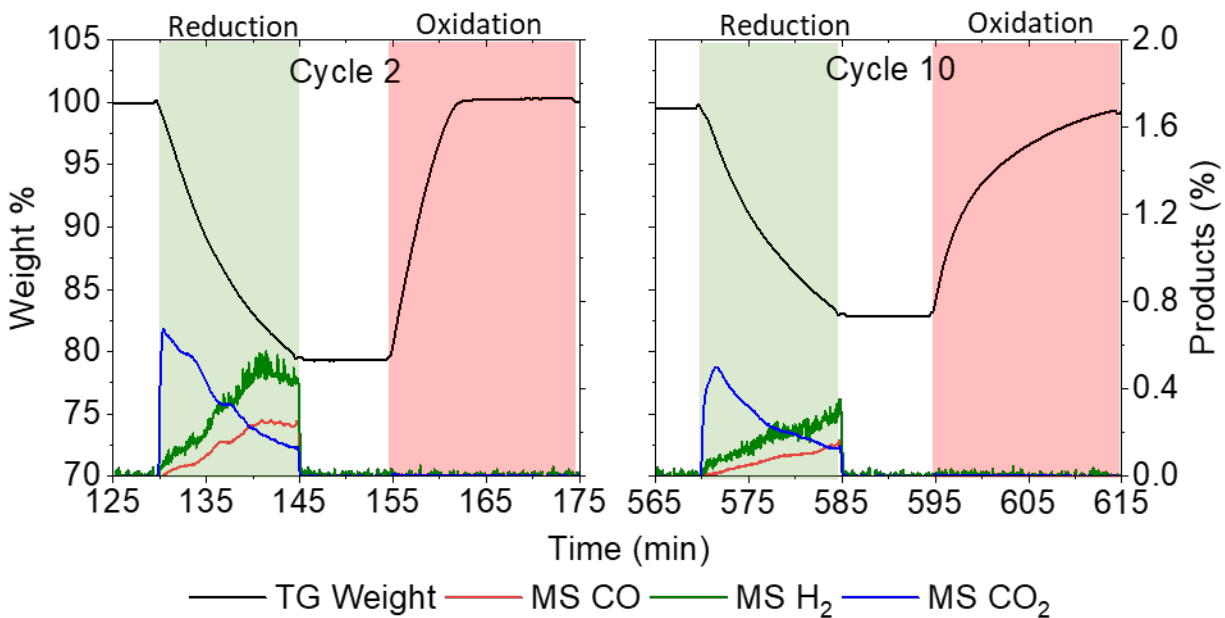


Figure C.8: Redox cycling of $\text{NiFe}_2\text{O}_4 + 0.25\text{NiO}$ under at 900°C . Reduction is with 180 mL/min He and 20 mL/min CH_4 . Oxidation is with 180 mL/min He and 20mL/min O_2 . Purge is with 180 mL/min He.

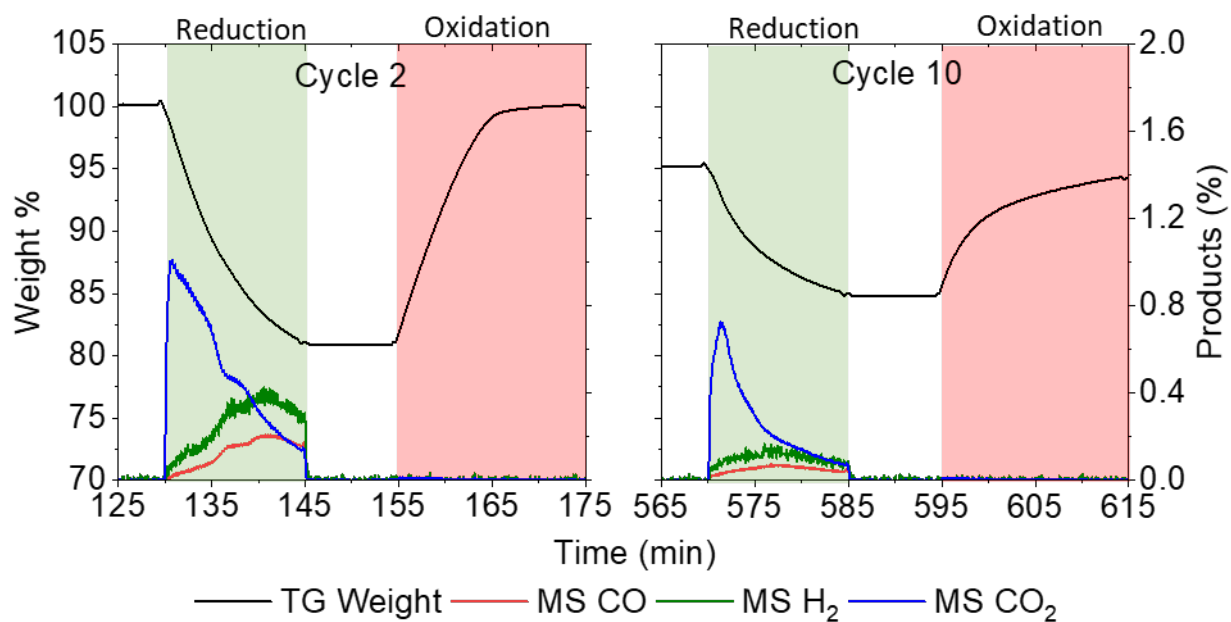


Figure C.9: Redox cycling of $\text{NiFe}_2\text{O}_4 + 0.5\text{NiO}$ under at 900°C . Reduction is with 180 mL/min He and 20 mL/min CH_4 . Oxidation is with 180 mL/min He and 20mL/min O_2 . Purge is with 180 mL/min He.

XRD

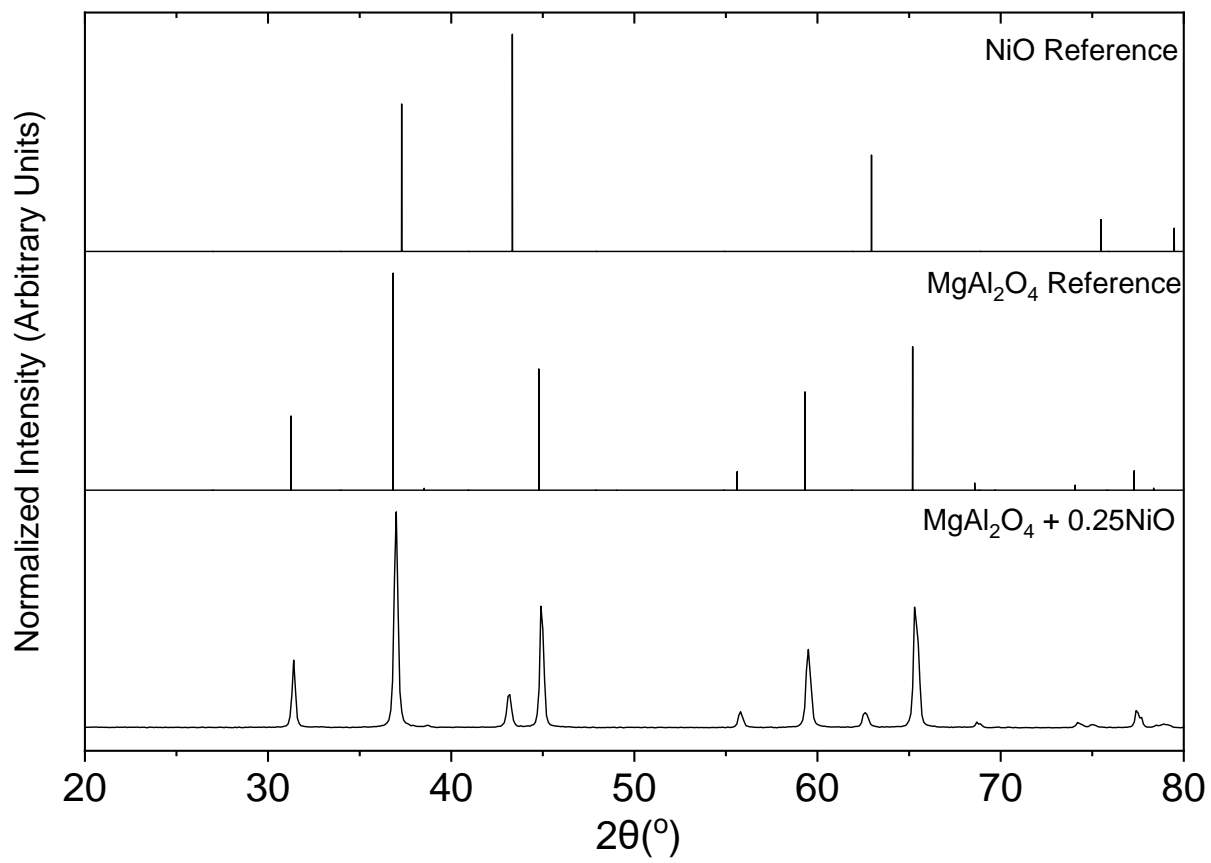


Figure C.10: XRD of MgAl₂O₄ + 0.5NiO with reference patterns of MgAl₂O₄ and NiO shown for comparison.

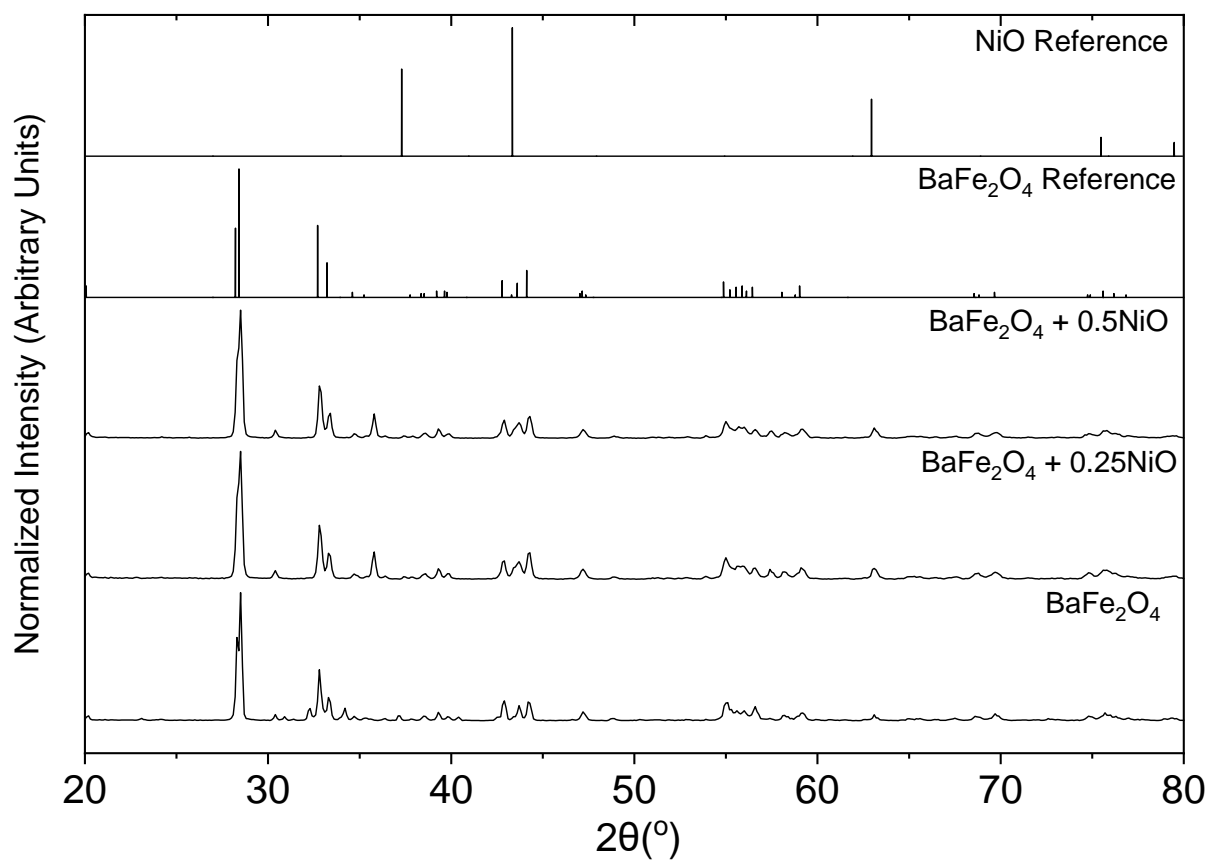


Figure C.11: XRD of BaFe₂O₄ + xNiO (x = 0, 0.25, 0.5) with reference patterns of BaFe₂O₄ and NiO shown for reference.

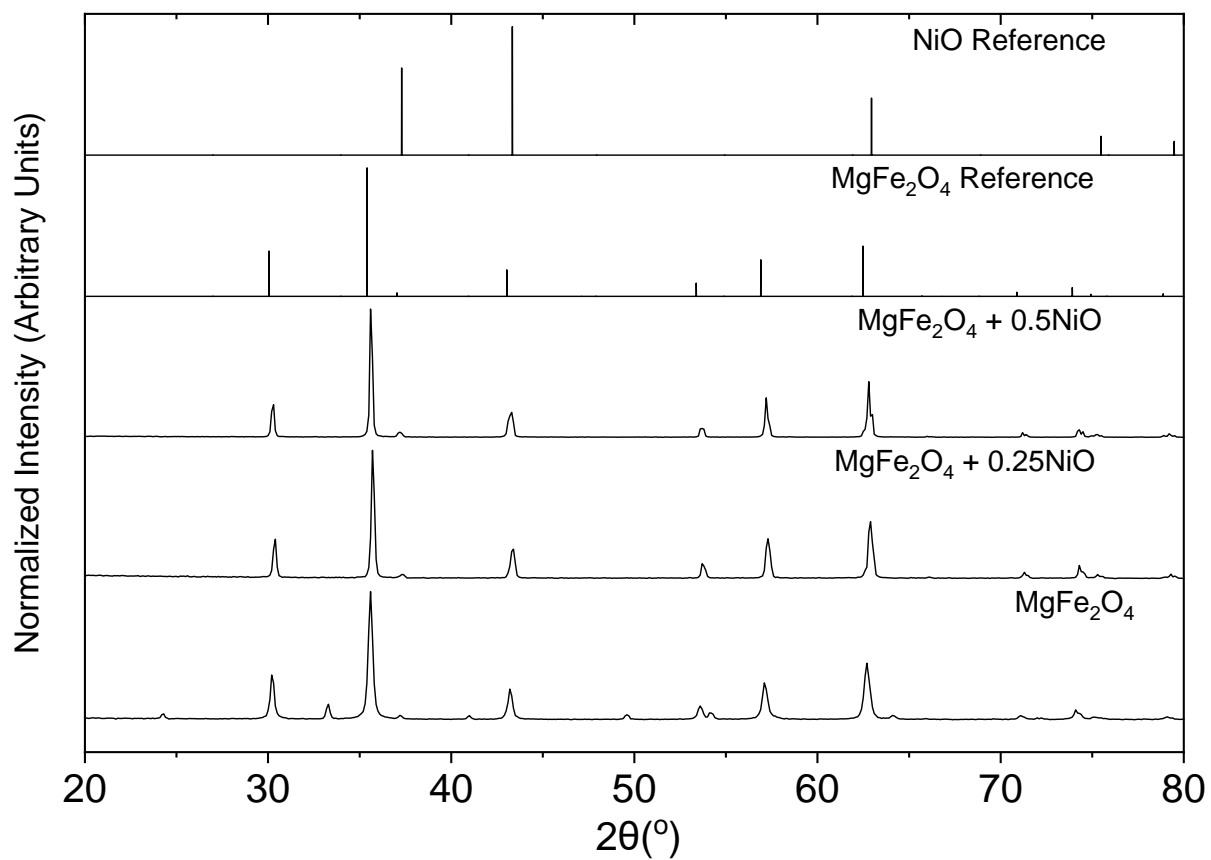


Figure C.12: XRD of $\text{MgFe}_2\text{O}_4 + x\text{NiO}$ ($x = 0, 0.25, 0.5$) with reference patterns of MgFe_2O_4 and NiO shown for reference.

In-Situ XRD

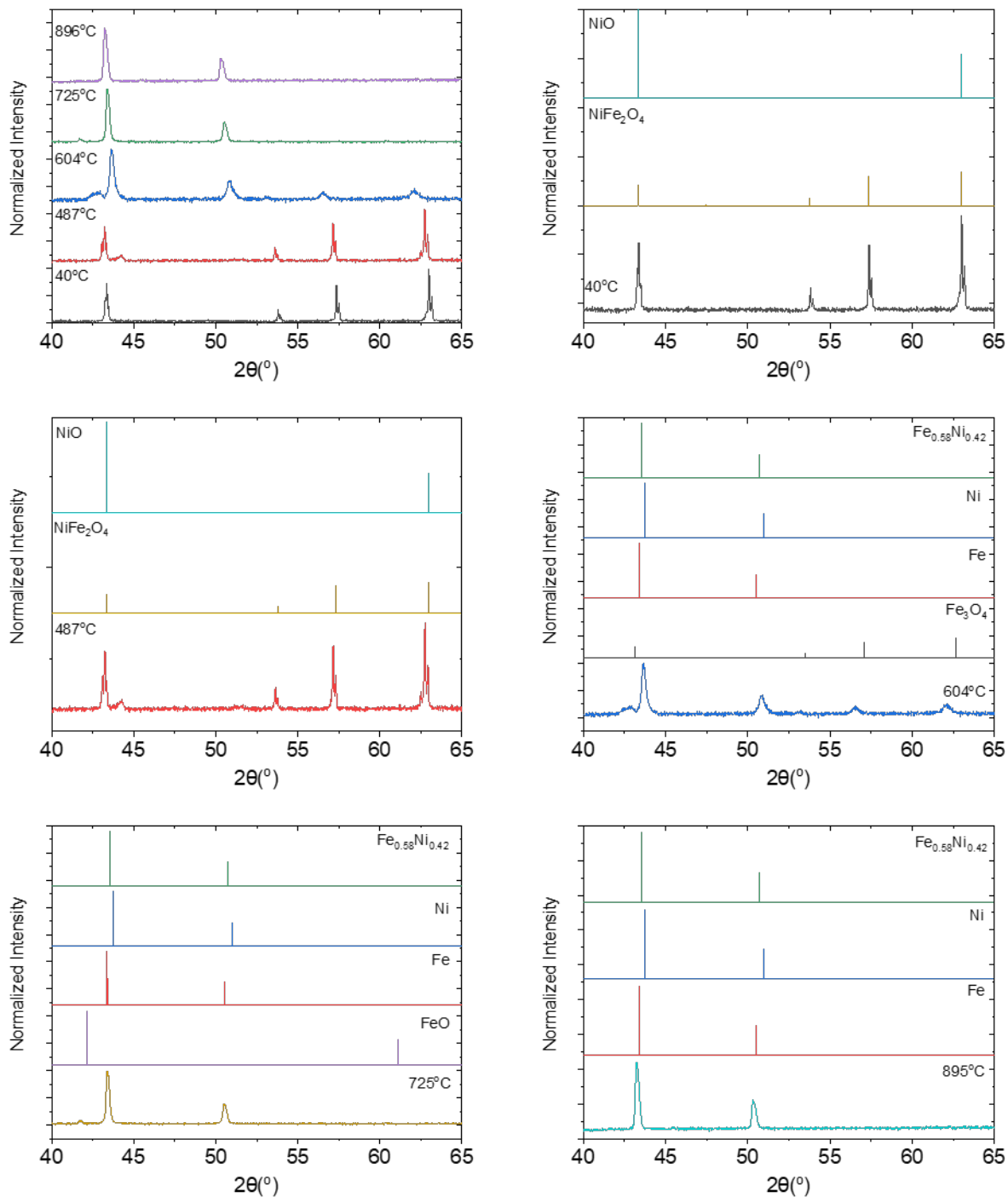


Figure C.13: In-situ XRD results at 40°C, 487°C, 604°C, 725°C, 895°C. Reference patterns of NiO, NiFe₂O₄, Fe₃O₄, FeO, Ni, Fe, and Fe_{0.58}Ni_{0.42} are shown for comparison.

H₂ TPR

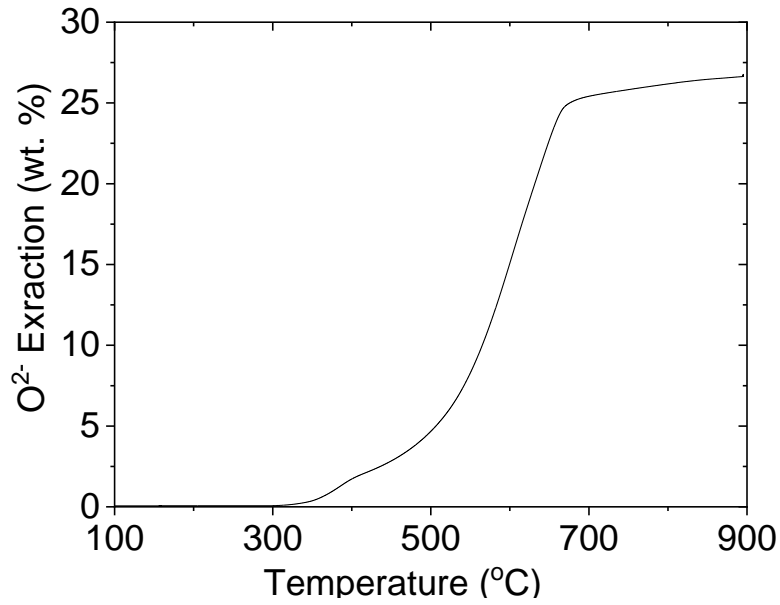


Figure C.14: O²⁻ Extraction (wt. %) during H₂-TPR.

Redox Stability of Oxygen Carriers

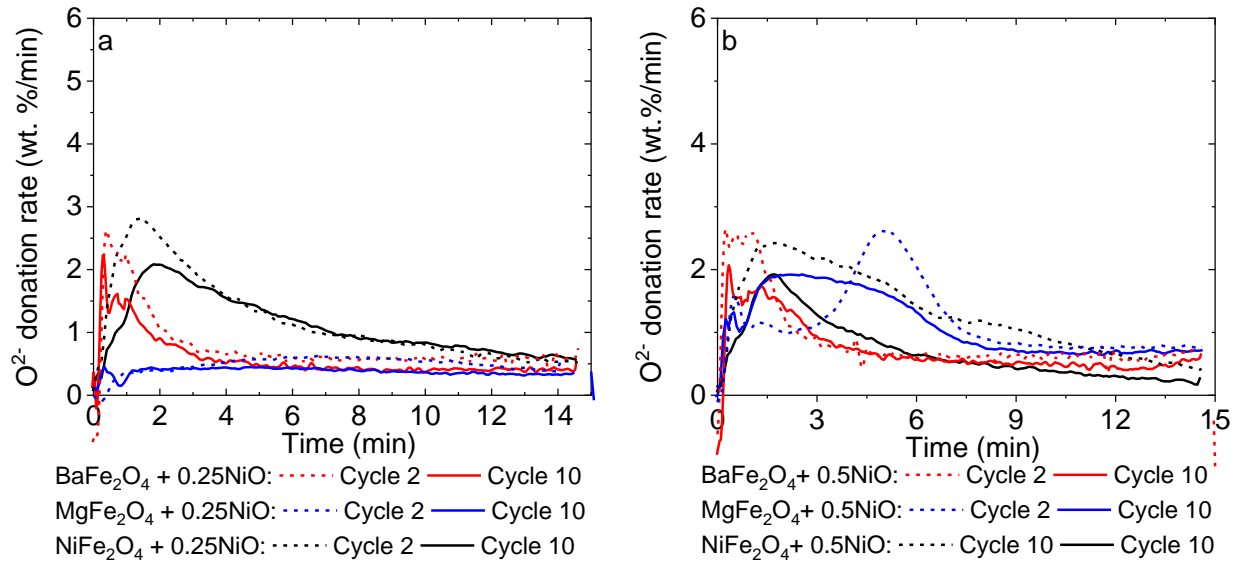


Figure C.15: O²⁻ donation rate (wt. %/min) during reduction of cycle 2 and cycle 10.

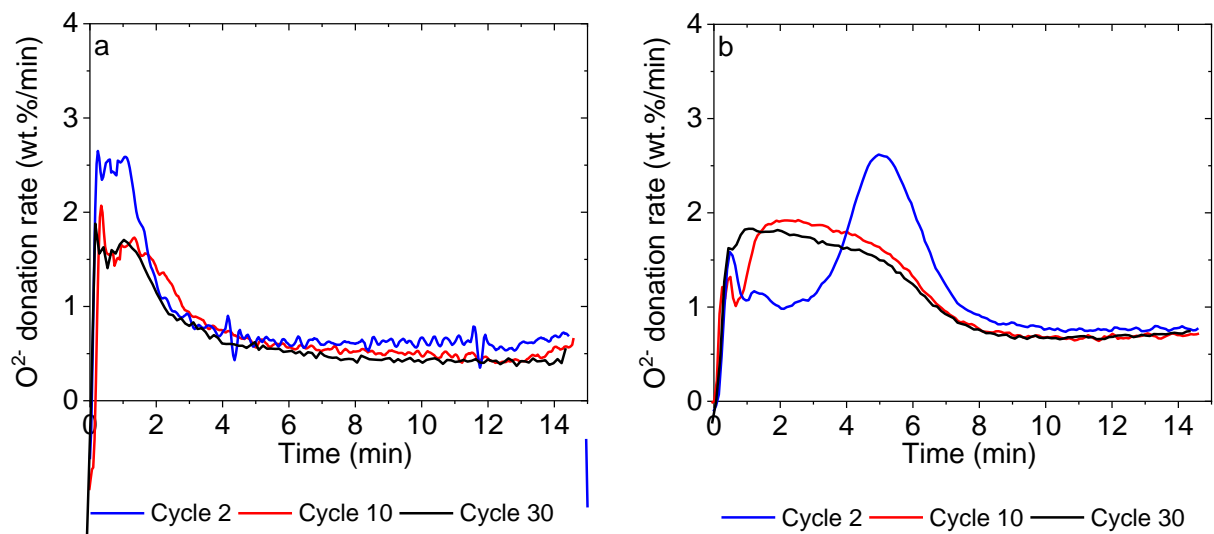


Figure C.16: Oxygen release rates of a) BaFe₂O₄ + 0.5NiO and b) MgFe₂O₄ + 0.5NiO during redox cycling.

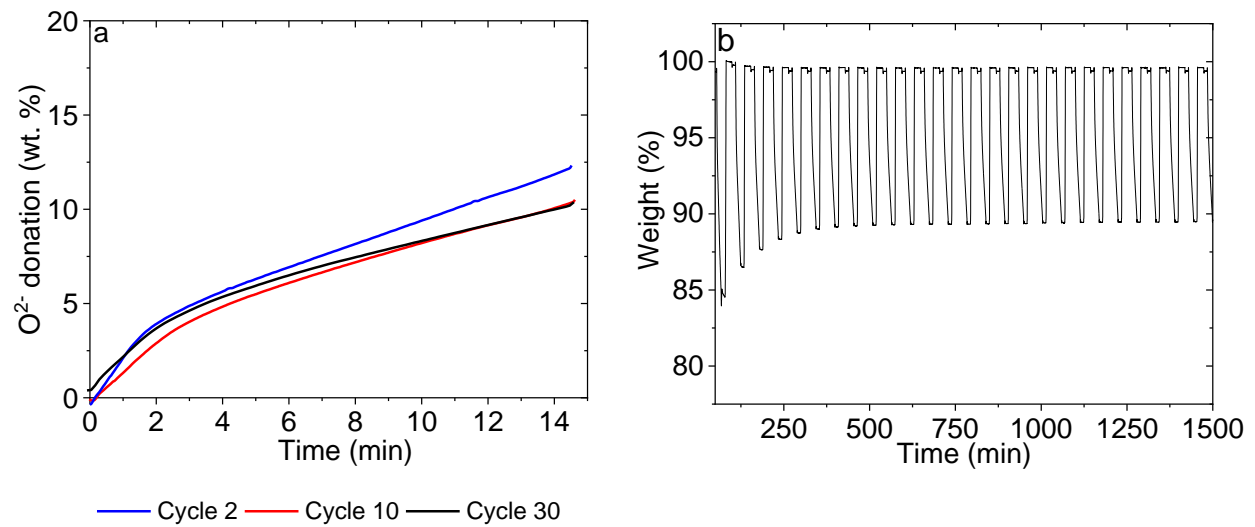


Figure C.17: a) Oxygen donation (capacity) of MgFe₂O₄ + 0.5NiO during cycles 2, 10, and 30, b) Weight of the oxygen carrier during cycling.